Modelling and Control of Small-Scale Helicopter on a Test Platform

by

Gilbert M. Y. Lai

A thesis
presented to the University of Waterloo
in fulfilment of the
thesis requirement for the degree of
Doctor of Philosophy
in
Electrical and Computer Engineering

Waterloo, Ontario, Canada, 2008

AUTHOR'S DECLARATION FOR ELECTRONIC SUBMISSION OF A THESIS

I hereby declare that I am the sole author of this thesis. This is a true copy of the thesis, including any required final revisions, as accepted by my examiners.

I understand that my thesis may be made electronically available to the public.

Abstract

The helicopter is a Multiple-Input Multiple-Output (MIMO) system with highly coupled characteristics, which increases the complexity of the system dynamics. In addition, the system dynamics of the helicopter are unstable [1], referring to its tendency to deviate from an equilibrium when disturbed. Despite the complexity in its modelling and control, the benefit of using a helicopter for unmanned, autonomous applications can be tremendous. One particular application that motivates this research is the use of an unmanned small-scale helicopter in an autonomous survey mission over an area struck by disaster, such as an earthquake.

The work presented in this thesis provides a framework for utilizing a platform system for research and development of small-scale helicopter systems. A platform system enables testing and analysis to be performed indoor in a controlled environment. This can provide a more convenient mean for helicopter research since the system is not affected by environmental elements, such as wind, rain or snow condition. However, the presence of the platform linkages poses challenges for analysis and controller design as it alters the helicopter system flight dynamics.

Through a six degree-of-freedom (6 DOF) platform model derived in this research, the criteria for matching the trim conditions between the platform system and a stand alone helicopter have been identified. With the matched trim conditions, linearization is applied to perform analysis on the effects that the platform has on the system dynamics. The results of the analysis provide insights into both the limitations and benefits of utilizing the platform system for helicopter research.

Finally, a Virtual Joint Control scheme is proposed as an unified control strategy for both the platform and the stand alone helicopter systems. Having a consistent control scheme between the two systems allows for comparisons between simulation and experimental results for the two systems to be made more readily. Furthermore, the Virtual Joint Control scheme represents a novel flight control strategy for stand alone helicopter systems.

Acknowledgements

It has been a long journey getting to this point. Throughout this time, I have been very fortunate to have received support, encouragement and assistance from a lot of individuals. There is not enough space in all of the pages in this thesis to express my gratitude towards all of these individuals. To them, I offer a heartfelt *thank you!* I would like to thank my co-supervisors Prof. David Wang and Prof. Glenn Heppler for their guidance, support, and friendship. Their encouragements, insights and patience with me throughout this journey are greatly appreciated.

I would like to thank the other members of my thesis committee: Prof. Samuel Asokanthan, who acted as my external examiner, Prof. Jan Huissoon, Prof. Andrew Heunis, Prof. Eric Kubica, and Prof. William Wilson for their valuable advise and feedback.

I would like to thank Prof. Anthony Vax and Prof. Rob Gorbet for allowing me to work on the test platform system that they have started building. I would like to acknowledge the generosity of Mr. Paul Salchak from CasalCorp and Dr. Mark Tischler from NASA Ames Research Center for allowing me to evaluate their CIFER® software for my research. I would also like to acknowledge the financial support I received for this research in the form of scholarships from the Natural Sciences and Engineering Research Council (NSERC) and the University of Waterloo.

I would like to extend special thanks to my colleagues Kamyar Ziaei, Thambirajan Ravichandran, Kingsley Fregene, Matthew Black and Luke Kupczyk for the many hours of discussions, interactions and collaborations. My appreciation also goes to Dr. Laurent Bernardin, Dr. Tom Lee and Dr. Jan Bakus from Maplesoft for allowing me to take leave of absence from work so I can finish up my thesis work.

I would like to express my gratitude to my family, whom had provided me unconditional support and countless encouragements. Without them, this work would never have come to completion.

Finally, I am forever indebted to my wife, Daria, for her faith in me, her patience with me, her understanding throughout the years, her constant encouragement, her unwavering support and her unconditional love. I am very grateful to be able to share this experience with my partner for life.

Contents

List of Tables

List of Figures

Chapter 1

Introduction

There are many reasons for studying helicopter dynamics and flight control. Search-and-rescue, surveillance, reconnaissance, and air-ambulance are examples of missions in which helicopters play a significant role [2]. The importance of helicopters in these roles increases the desire to improve their performance through better models and controllers.

There is also interest from the Autonomous Unmanned Vehicle (AUV) community in helicopter research [3, 4, 5, 6, 7]. Although the history of helicopter research can be dated back to about a century ago [2], the focus in autonomous helicopter research is a recent trend. Early helicopter research focused more on the design aspect; for example, the objectives of researchers such as Igor Sikorsky were to design and build a flying machine that was capable of vertical take-off and landing and hovering [2]. It is only recently, with the increased availability of computing power and the increased understanding of helicopter aerodynamics, that autonomous helicopter research is becoming more popular. Without human pilots, helicopters can be made smaller. This will potentially reduce the operating cost. In addition, autonomous helicopters can be sent to places that would otherwise be too dangerous for human-piloted aircraft to go. For example, autonomous helicopters are better for tasks such as surveying over an active volcano, fire-fighting and geophysical surveying in remote areas. Autonomy also has an advantage in repetitive tasks, such as patrolling borders. As a result, many helicopter applications can benefit from the use of controllers that allow autonomous flight.

Despite the many advantages of small-scale helicopters over full-sized ones, small model helicopters are considerably harder to control than their full-sized counterparts since they are

easily affected by aerodynamic disturbances [8]. Furthermore, as autonomous helicopter control is a relative new area, only limited results are available in the literature, particularly in the areas of flight path control strategies. Therefore, the focus of the research presented in this thesis is on modelling and controller design for small-scale helicopters in order to formulate generic techniques that will improve their capabilities and performance in autonomous tasks.

1.1 Background

A typical small-scale helicopter is shown in Figure 1.1[1]. The main rotor provides lift as well as the controls necessary, such as roll and pitch, for the helicopter to navigate in three-dimensional (3-D) space. The tail rotor provides heading control by generating a yaw counter torque that prevents the helicopter from spinning due to the reaction force and torque from the main rotor.

Figure 1.1: UAV

The dynamics of a helicopter are nonlinear and highly coupled between its axes of motion, making it difficult to control. For example, when the engine throttle is increased to make a vertical climb, the helicopter will tend to yaw due to the increased rotor reaction torque. To compensate, the tail rotor thrust must be increased, which will increase the side force acting on the body. As a result, the vertical motion of the helicopter is coupled with both the yaw and the lateral movements. For control design and analysis, an effective way to capture such complex dynamics is required.

In addition to being coupled and nonlinear, the helicopter dynamics are also inherently unstable. This poses significant challenges in performing experiments to obtain the system model. For instance, an experienced pilot is required to provide stable in-flight experimentation for data collection. The complex and lengthy process for both prior and post flight maintenance are costly and time consuming, especially if crashes have occurred. Furthermore, favourable environment conditions, such as calm sunny days, are required to provide quality experimentation data. All of these factors motivate the use of an indoor facility in the form of a platform experiment

[1]Courtesy of the Waterloo Aerial Robotics Group (WARG)

to provide an efficient environment for research and development. The challenge in applying such platform system for UAV research lies in the effect of the linkage over the system dynamics. This necessitates the derivation of the platform system model to characterize the platform linkage influence. Because of the difference in the system dynamics, alternate control scheme from the conventional flight control strategies are needed for the platform system. The model of one such platform system will be presented in this thesis, together with a proposed Virtual Joint Control strategy that is applicable to both the platform system and its free-flying stand-alone helicopter counterpart. The following section will provide a basic introduction to existing research issues in the areas of helicopter modelling and control.

1.2 Literature Review

1.2.1 Modelling

Modelling complexity varies with the intended applications. A general approach in obtaining a suitable flight mechanics model is to apply physical laws and principles such as Momentum Theory and Blade Element Theory [9, 10, 1]. These models can be classified into three levels according to their complexity [11, 12]. Level 1 models represent the simplest set of models that are adequate in describing the system behaviour whereas Level 3 models consist of the most detailed and complex set of models, which can accurately predict the system responses. In Level 1 models, the helicopter structure is approximated as a rigid body and the rotor dynamics are either ignored or simplified with rigid blade approximations. In contrast, Level 3 models incorporate detailed modelling of the rotor, the blade and structural vibration modes and the nonlinear aerodynamic airflow effects [12]. The complexity of Level 2 models fits in-between that of Level 1 and Level 3 models. Level 2 models include limited nonlinear aerodynamic effects and rotor blade vibration mode characteristics.

Within the autonomous helicopter research literature, Level 1 models (i.e. rigid body models) are among the most common because of their manageable complexity. A typical rigid body model is nonlinear and has the position, orientation, linear and angular velocities as states, resulting in a 12^{th} order system model [13]. Depending on the application, researchers have either simplified or enhanced this basic model by adjusting the model order. For example, to provide better

approximation of the system dynamics, Koo *et al.* [14] increase the number of states to 16 to account for the rotor dynamics. Weilenmann *et al.* [15] and Walker *et al.* [16] further increase the number of states to 18 and 19 respectively to include the dynamics of the DC motor of their helicopter. Conversely, since their main focus is on attitude control only, Corban *et al.* [7] and Prasad *et al.* [17] reduce the number of states in their linear model to 7 by including only the linear and angular rates, together with the collective control signal.

Other alternatives in simplifying the system dynamics include using only the roll angle, pitch angle, the linear and the angular rates as the states (8^{th} order) [18]; using the linear and angular rates together with the orientation as the states (9^{th} order) [19]; and using the simplified 8^{th} or 9^{th} order model in combination with the rotor dynamics (10^{th} or 11^{th} order) [4, 8, 20, 21].

Because of their complexity, Level 2 and Level 3 models are rarely used for control purposes. They are primarily used in the area of system (mechanical) design and simulation analysis (e.g. training flight simulator), where effects such as rotor airflow and blade vibrations are significant. In contrast, for a typical control application operating with slow, simple manoeuvres such as hover, these higher order effects are less significant [12]. For the purpose of this research, a Level 1 rigid body model for the platform system will be derived.

1.2.2 Flight Control

There are many different controllers proposed in the literature for autonomous helicopters. The type and complexity of the controller depend largely on the intended application. For instance, to obtain precision hovering over some marked targets, Rock *et al.* [22] proposed a vision-based controller. Through the images of the target taken from a camera on-board the helicopter, hovering is maintained by keeping constant the relative orientation between the helicopter and the target as seen in the image. The three typical layers of control are navigation, path/trajectory and attitude control.

Navigational Control

The function of navigation controller for helicopters is to oversee the operation of the system with the aim to reach the intended mission target. Navigation tasks include path and trajectory planning, object and collision avoidance and multi-vehicle cooperation. Often, a navigation con-

trol strategy is divided into a hierarchical structure with the upper-most level composed of some decision-making directives and the lower-most level being the stabilization system, i.e. position and attitude control. For example, the hierarchical structure proposed by Sanders *et al.* [4] consists of a navigation filter, an inner-loop hover control system, a way-point guidance system, and a ground-based flight manager. Similarly, the system described by Lai *et al.* [23] contains a navigation manager, a flight path controller and an attitude/height stabilizing controller. In both cases, the navigational control is usually on the highest level.

Naturally, the emphasis in navigational control is on the design of the overall control structure (the hierarchy) as well as the high level intelligence that is responsible for the planning actions. Since the motion of the helicopter body is typically much slower than the rotor blades responses [9], the guidance and intelligent system usually operates at a much slower rate than the stabilization system. This difference in time scale means that a navigational control system is inherently a hybrid system consisting of fast and slow components. Koo *et al.* [3] propose a control system that explicitly addressed such hybrid control issues. Frazzoli *et al.* [24, 25] also propose a hybrid control system that is suitable for aggressive manoeuvring of autonomous helicopters. Both Koo *et al.* [3] and Frazzoli *et al.* [24, 25] provide only preliminary simulation results of their systems.

Position Control

Position or path control differs from navigational control in that position control focuses on the *tracking* of a path or trajectory by the vehicle instead of the *generation* of the path. An example situation where path following is important is when a helicopter is used in assisting fire-fighting. The helicopter has to move to the location of the fire and unload either water or fire-extinguishing chemicals directly onto the fire. In such a case, the path that the helicopter has to follow is predefined by the fire location.

One approach to handling this problem is to design a feedback linearization controller based on the rigid-body system dynamics around the equilibrium (hover) position [14]. However, the exact input-output feedback linearized system obtained from exact input-output linearization has non-minimum phase zero dynamics, meaning that the system is not asymptotically stable. Koo and Sastry [14] show that although tracking control based on exact linearization can stabi-

lize the position outputs (achieving tracking performance), such a control approach resulted in undesirable internal dynamics, such as oscillations in the roll and pitch angles. To address this, Koo and Sastry [14] use an approximate linearization approach instead of the exact linearization. They approximately linearize the system by neglecting the couplings between the rolling (pitching) moments and lateral (longitudinal) accelerations which are the cause of the non-minimum phase characteristic exhibited by the exactly linearized system. The approximate control law is shown, in simulation, to be able to stabilize the system internal dynamics. Experimental implementation is not included.

Mahony and Lozano [26] also look at the non-minimum phase zero dynamics problem and propose a different solution. Instead of performing linearization on the helicopter rigid body model directly, Mahony and Lozano first simplify the system model. The reduced model is then linearized. By doing so, the resulting linearized model does not contain non-minimum phase zero dynamics. Hence, arbitrarily accurate tracking performance can be achieved with high gain control, provided the tracking manoeuvres are slow. The restriction on the speed of motion comes from the assumptions that the actuator and rotor dynamics are significantly faster than the rigid body dynamics. There is no experimental result reported for verification.

In addition to system dynamics, characteristics of the desired trajectory are also important factors in path controller design. Frezza [27] proposes a flight path controller that takes into account the feasible trajectories of the system in coordinated flight. Control signals are generated as a constrained problem. First, a connecting contour that would connect the current location of the helicopter and the desired trajectory is identified from within the set of feasible trajectories. Then, control signals are computed to achieve exact tracking of the connecting contour. No experimental results are presented in regards to the performance of such a control strategy.

Attitude Control

The objective in attitude control is to regulate the orientation of the helicopter. Attitude control is the lowest layer of control among the three levels. Because of this, attitude control has been studied most extensively by researchers, as compared to navigational and path control. Among the different orientations, hover is the most common attitude to be achieved by autonomous helicopter controllers as it provides a complex, unstable, nonlinear and coupled, yet manageable

problem for control case studies [28, 29, 30, 31]. There are two general themes in designing attitude controllers: model-based and non model-based. In model-based control design, the rigid body model is commonly used. A rigid body model considers the net force and moment acting on the centre of gravity of the helicopter. As a result, individual blade and rotor dynamics are ignored in the rigid body model. This can be done because the aerodynamic time constants of the blades and the rotors are much faster than those of the rigid body dynamics (body roll, pitch and yaw motions) [9]. Also, by including the aerodynamic forces and moments implicitly as net force and moment, the resulting rigid body model is simpler and easier to handle, albeit still nonlinear. With a nonlinear rigid body model, controllers are then designed using various control design techniques.

Lee *et al.* [8] linearize the nonlinear rigid body model and design a state feedback Linear Quadratic Gaussian (LQG) attitude controller. They apply the attitude controller to a small-scale helicopter attached to a stand that allowed 3 degree-of-freedom (DOF) motions. Experimental results show the attitude controller is successful in stabilizing the model helicopter and further tuning of the controller promised to improve performance. Similar to the approach proposed by Lee *et al.* [8], Morris *et al.* [28] also design a LQG controller with set-point tracking for a small-scale helicopter on a stand and yielded similar results. However, neither group of researchers provide suggestion on how to relate and extend their results to a stand alone helicopter system.

Instead of designing controllers for the linearized system, Rebeschieß and Roloff [32] design a feedback linearization controller for angular pitch control from the nonlinear model. The feedback linearization controller linearizes the system, then the linearized system is controlled by a linear Proportional-Integral (PI) controller to achieve the desired angular control. Another nonlinear control strategy is proposed by Mahony *et al.* [30], who propose a Lyapunov control law for hover control. The Lyapunov control law is designed using the backstepping technique, which is an iterative procedure that generates, at each step, a *virtual* state feedback control input such that a candidate Lyapunov function can be found to guarantee stability [33]. No simulation or experimental results with respect to the performance of the Lyapunov controller are given.

Shim *et al.* [34] examine and compare three different control strategies: linear robust multivariable control, fuzzy logic control with evolutionary tuning and nonlinear tracking control.

Of these methods, both the linear robust controller and the nonlinear tracking controller use a model-based approach, whereas the fuzzy logic controller is non model-based. The linear robust controller is generated with the μ-synthesis technique on the linearized model dynamics. The nonlinear controller is obtained using an approximate input-output linearization technique similar to the one presented by Koo and Sastry [14]. The fuzzy controller is based on PID-type rules and its gain factors are initially tuned manually. An evolutionary algorithm is then implemented to adjust the gains to optimize the performance. All three of these controllers are applied to a nonlinear helicopter model in simulations. Simulation results show that all three controllers were capable, to a certain extent, of handling uncertainties and disturbances. Both the linear robust controller and the fuzzy controller are limited to a relatively small operating range, namely near-hover conditions. On the other hand, although the nonlinear controller covers a substantially wider range of the flight envelopes, it requires significantly more accurate knowledge about the system. This situation represents a typical trade-off between complexity and performance in controller design.

The second theme in attitude control design addresses the problem of handling complex helicopter dynamics by applying non model-based intelligent control techniques, such as the fuzzy controller presented by Shim *et al.* [34]. These types of controllers typically require some set of training data and their performance is directly related to how good the training data is in describing the system dynamics. For instance, the neural network yaw controller presented by Ma *et al.* [35] uses two neural networks (NN). The first NN, the NN model, simulates the system dynamics (in this case, the yaw dynamics) through training with input-output data collected during test flights. Once trained, this NN model would approximate the outputs of a real helicopter given the same input. After that, a second neural network, the NN controller, is cascaded with the NN model. The NN controller is then trained with the NN model using backpropagation learning rules in order to stabilize the closed-loop system. The resulting NN controller is shown to perform reasonably well when applied back to the original system.

A neural network, in general, is a function estimator [36]. It approximates the dynamics of a helicopter as a nonlinear function, such as the NN model presented by Ma *et al.* [35] mentioned above. With this in mind, Montgomery and Bekey [6] present a fuzzy-neural controller that mimicked a human pilot (the teacher) in controlling the helicopter instead of the helicopter dynamics. It is similar to the NN controller presented by Ma *et al.* [35]. The difference is that

Ma *et al.* [35] train the NN controller with the objective of stabilizing the closed-loop system, whereas Montgomery and Bekey [6] train the NN controller to mimic the behaviour of a human pilot. Simulation results show that this *teaching by showing* controller is able to perform within expectation levels, i.e. it is doing as good as the teacher pilot.

Neural Network controllers are trained with training data sets. These NN controllers can handle the flying conditions that are captured in the training data very well (as those conditions were the only information available to the NN controllers). Unfortunately, when an unexpected situation occurs, such as a sudden wind gust, the NN controllers will have a hard time handling the situation if the training data does not include such flying condition. A common solution is to train the neural network on-line instead of *a priori*. For instance, the nonlinear controller presented by Corban *et al.* [7] uses a neural network to adjust the parameters of the feedback linearization controller to compensate for modelling error in the linearization process. Prasad *et al.* [17] present a similar strategy. The learning fuzzy logic controller presented by Sasaki *et al.* [37] is another way of achieving non model-based learning control. Here, a learning algorithm, based on the gradient descent method, is applied to adjust the weights of consequence in different fuzzy rules. The idea is to vary the weights of consequence to accommodate any changes in the system dynamics that are unforeseen during the fuzzy rule design.

Although the non model-based approach is simple and easy to implement, it provides little insights into the behaviour of the system for analysis. For the purpose of utilizing the platform system as an experimentation tool for the stand-alone helicopter, since there is significant difference in the dynamics between the two systems, a model-based control approach is selected for the research presented in this thesis.

1.3 Research Overview

The work presented in this thesis provides a framework for utilizing a platform system for research and development of small-scale helicopter systems. The six degree-of-freedom (6 DOF) nonlinear rigid body model with quasi-steady rotor dynamics [12] (a Level 1 model) of the Platform system (capital P refers to the particular platform system that is used for this research) is derived through the Principle of Virtual Power [38]. From the Platform model, the relationship between the Platform model and a stand alone helicopter, to be referred to as the Unmanned Aerial

Vehicle (UAV), model is presented through Theorem 2.1 and Lemma 2.1.

Through the results obtained from Theorem 2.1 and Lemma 2.1, the expression for the non-dimensional *apparent payload* is derived. The *apparent payload* expression provides the condition for matching the operating trim condition between the Platform and the UAV models. This forms the basis for direct comparisons between the results obtained from these two systems. Furthermore, different Platform configurations can be defined based on the *apparent payload* expression to study the effects of various aspects of the Platform on the system dynamic behaviour. Two examples of such analysis, adjusting the Platform linkage mass and the rotor operating speed, are presented. From these analysis, it is shown that direct equivalence between the Platform and UAV systems are not achievable without active controls at the Platform joints. An extension to the Platform system for achieving dynamic equivalence to UAV systems are proposed in Theorem 5.1 in Chapter 5 as one of the possible future research topics.

Finally, the Virtual Joint Control scheme is derived. The Virtual Joint Control scheme is designed to be applicable to both the Platform and the UAV systems to facilitate comparisons and research between them. It also provides an explicit mechanism for selecting the trade-off between Attitude Tracking and Position Tracking performance. The Virtual Joint Control scheme is extendable through the use of different stable joint control strategies. Two variant forms of the Virtual Joint Control scheme are presented. Simulation results show both forms of the Virtual Joint Control scheme are capable of stable control for both the Platform and the UAV systems.

1.4 Thesis Outline

The remaining chapters of this thesis are organized as follows:

Chapter 2 introduces the six degree-of-freedom (6 DOF) nonlinear rigid body model with quasi-steady rotor dynamics for both the Platform and the UAV systems. The relationships between these two systems are derived.

Chapter 3 examines the Platform system model. The *apparent payload* expression is derived. Different configurations for the Platform system setup based on the *apparent*

payload expression are introduced and analyzed through linearization around the hover trim condition.

Chapter 4 presents the proposed Virtual Joint Control scheme for the Platform and the UAV systems. Two variant forms of the proposed control scheme are presented. Simulation results show stable control for both the Platform and the UAV systems under these control algorithms.

Chapter 5 summarizes the contributions in this research. Possible extensions to the current research are presented as future work.

Appendix A describes the convention employed in this thesis for the definition of the rotational transformation matrices.

Appendix B contains derivation of the helicopter rotor dynamics.

Appendix C contains the detailed kinematics relationships of the Platform linkages.

Appendix D contains the system matrices, such as the mass and inertial matrix, of the Platform model.

Appendix E contains a list of helicopter parameter and controller gains values used in the simulation results presented in Chapter 4.

Chapter 2

Modelling

In this chapter, the Platform system utilized in this research will be introduced. Its dynamic model, together with that of a stand-alone small-scale helicopter, will be derived. The small-scale helicopter is referred to as an Unmanned Aerial Vehicle (UAV). A photo of a typical UAV is shown in Figure 1.1. The relationship between the two models will be established through the derivation of a nonlinear mapping. This nonlinear mapping provides an important research contribution as it allows a comparison to be made between the UAV model and the platform system model. Such a comparative analysis will be demonstrated in subsequent chapters.

2.1 Helicopter Rigid Body Model

The dynamic model of a stand alone small-scale helicopter (UAV) will be derived in this section. The model derivation will be divided into four subsections. First, the flight mechanism model for a helicopter will be introduced. The net force and moment acting on the helicopter rigid body will be derived next. This is followed by the derivation of the rotor dynamics equations. Finally, the rigid body dynamic model for the UAV system will be obtained by applying the Newton-Euler Method [39].

2.1.1 Flight Mechanism

In a conventional helicopter, flight is achieved through the combined action of two rotors: a main rotor primarily responsible for generating lifting thrust and a tail rotor for controlling the

heading direction [2]. In the process of thrust generation, each of the rotors also exerts reaction torques along the corresponding axis of rotation on the helicopter body due to the motion of the blades. Furthermore, side forces are also generated by the rotors to facilitate helicopter motion in the air. For the purpose of modelling, these rotor forces and moments can be described by a set of four non-dimensional quantities: the thrust coefficient $\hat{C}_{\mathrm{T}}$, the longitudinal planar force coefficient $\hat{C}_{\mathrm{lon}}$, the lateral planar force coefficient $\hat{C}_{\mathrm{lat}}$, and the torque coefficient $\hat{C}_{\mathrm{Q}}$. Figure 2.1 illustrates the relative direction of these quantities with respect to the main rotor. The corresponding quantities for the tail rotor are defined in a similar fashion relative to the rotor orientation and are denoted as $\hat{C}_{T_{\mathrm{tail}}}$, $\hat{C}_{lon_{\mathrm{tail}}}$, $\hat{C}_{lat_{\mathrm{tail}}}$, and $\hat{C}_{Q_{\mathrm{tail}}}$ respectively. The *hat* symbol ($\hat{}$) denotes normalized quantities. For simplicity, the rolling and pitching moment generated by the rotors, such as those from the gyroscopic effect [39], are assumed to be negligible and are not included as part of this rotor force and moment description. Such an assumption can be justified by the use of a fully articulated rotor with a small hinge offset [2, 9, 10, 1], where the presence of hub hinges allows the blades to flap in response to the moments generated; thereby no moment (or very little moment through the hinge offset) is transmitted to the helicopter body through the rotor hub [2, 1, 10].

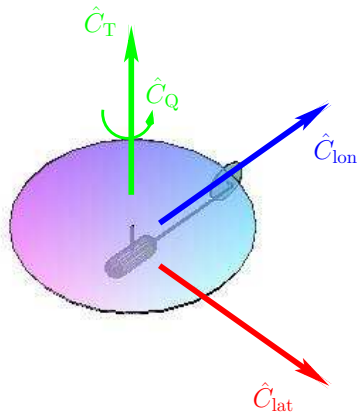

Figure 2.1: Helicopter Rotor Force

The use of non-dimensional coefficients to represent the force and moment generated by the rotors facilitates analysis independent of rotor size [10]. The non-dimensional coefficients are defined by dividing the magnitude of the force and moment quantities by the non-dimensional factors. The non-dimensional factor for force is given by $\rho A_{\mathrm{disc}}(\Omega R)^2$, where ρ is the air volume density with unit $\frac{\mathrm{kg}}{\mathrm{m}^3}$, R is the main rotor radius with unit m, Ω is the main rotor rotation speed with unit $\frac{\mathrm{rad}}{\mathrm{s}}$, and $A_{\mathrm{disc}} = \pi R^2$ is the area of the main rotor disc with unit m^2 [10, 12]. The corresponding non-dimensional factor for the torque is given by $\rho A_{\mathrm{disc}}(\Omega R)^2 R$. Using the magnitude of the thrust T_{main} and T_{tail} generated by the main and tail rotor respectively, the corresponding thrust coef-

ficients are given by:

$$\hat{C}_{\mathrm{T}} = \frac{T_{\mathrm{main}}}{\rho A_{\mathrm{disc}}(\Omega R)^2} \qquad \hat{C}_{T_{\mathrm{tail}}} = \frac{T_{\mathrm{tail}}}{\rho A_{disc_{\mathrm{tail}}}(\Omega_{\mathrm{tail}} R_{\mathrm{tail}})^2} \tag{2.1}$$

Notice that the direction of the thrust vectors T_{main} and T_{tail} are perpendicular (normal) to the tip-path-plane (TPP) of the corresponding rotors. The TPP is the plane traced out by the tip of the rotor blades as they rotate [10]. Recall the direction of the non-dimensional coefficients are defined with respect to the helicopter body, as shown in Figure 2.1. As such, the relationships defined in (2.1) are purely scalar, instead of, vector relationships.

The non-dimensional factor for the tail rotor is defined with respect to its corresponding quantities: tail radius R_{tail}, tail rotor speed Ω_{tail}, and tail rotor area $A_{disc_{\mathrm{tail}}} = \pi R_{\mathrm{tail}}^2$. For dimensional analysis, however, it is important to normalize the quantities with respect to the same dimensional factor. As such, for subsequent sections, the normalized tail thrust is expressed as:

$$\hat{T}_{\mathrm{tail}} = \frac{T_{\mathrm{tail}}}{\rho A_{\mathrm{disc}}(\Omega R)^2} = \hat{A}(\hat{\Omega}\hat{R})^2 \hat{C}_{T_{\mathrm{tail}}} \tag{2.2}$$

where

$$\hat{R} = \frac{R_{\mathrm{tail}}}{R} \qquad \hat{\Omega} = \frac{\Omega_{\mathrm{tail}}}{\Omega} \qquad \hat{A} = \frac{A_{disc_{\mathrm{tail}}}}{A_{\mathrm{disc}}} \tag{2.3}$$

are the ratios between the radius, speed and disc area of the two rotors.

The longitudinal and lateral force coefficients for the main rotor are defined as:

$$\hat{C}_{\mathrm{lon}} = \frac{F_{\mathrm{lon}}}{\rho A_{\mathrm{disc}}(\Omega R)^2} \qquad \hat{C}_{\mathrm{lat}} = \frac{F_{\mathrm{lat}}}{\rho A_{\mathrm{disc}}(\Omega R)^2} \tag{2.4}$$

where F_{lon} and F_{lat} are the main rotor longitudinal and lateral force respectively. The corresponding coefficients for the tail rotor are defined as:

$$\hat{C}_{lon_{\mathrm{tail}}} = \frac{F_{lon_{\mathrm{tail}}}}{\rho A_{disc_{\mathrm{tail}}}(\Omega_{\mathrm{tail}} R_{\mathrm{tail}})^2} \qquad \hat{C}_{lat_{\mathrm{tail}}} = \frac{F_{lat_{\mathrm{tail}}}}{\rho A_{disc_{\mathrm{tail}}}(\Omega_{\mathrm{tail}} R_{\mathrm{tail}})^2} \tag{2.5}$$

Similar to the normalized thrust, when normalized with respect to the main rotor, the normalized tail forces are expressed in terms of their coefficients as:

$$\hat{F}_{lon_{\text{tail}}} = \frac{F_{lon_{\text{tail}}}}{\rho A_{\text{disc}}(\Omega R)^2} = \hat{A}(\hat{\Omega}\hat{R})^2 \hat{C}_{lon_{\text{tail}}} \qquad \hat{F}_{lat_{\text{tail}}} = \frac{F_{lat_{\text{tail}}}}{\rho A_{\text{disc}}(\Omega R)^2} = \hat{A}(\hat{\Omega}\hat{R})^2 \hat{C}_{lat_{\text{tail}}} \tag{2.6}$$

Finally, the rotor torque coefficients are defined as:

$$\hat{C}_{\text{Q}} = \frac{Q_{\text{main}}}{\rho A_{\text{disc}}(\Omega R)^2 R} \qquad \hat{C}_{Q_{\text{tail}}} = \frac{Q_{\text{tail}}}{\rho A_{disc_{\text{tail}}}(\Omega_{\text{tail}} R_{\text{tail}})^2 R_{\text{tail}}} \tag{2.7}$$

where the rotor torques Q_{main} and Q_{tail} are defined along the normal axis to the TPP. The normalized tail torque with respect to the main rotor defined as:

$$\hat{Q}_{\text{tail}} = \frac{Q_{\text{tail}}}{\rho A_{\text{disc}}(\Omega R)^2 R} = \hat{A}(\hat{\Omega}\hat{R})^2 \hat{R} \hat{C}_{Q_{\text{tail}}} \tag{2.8}$$

The rotor force and moment are controlled by four rotor inputs [2, 1, 10]. For the main rotor, there are three inputs: the collective θ_0, the longitudinal cyclic B_1 and the lateral cyclic A_1. The collective θ_0 primarily controls the magnitude of the thrust for the main rotor; whereas the cyclic inputs B_1 and A_1 are responsible mainly for the longitudinal and lateral side force respectively. The longitudinal force corresponds to motion in the back and forth direction; while the lateral force corresponds to motion in the sideways direction. However, because of the coupling nature in the rotor aerodynamics, these inputs also have additional auxiliary effects. For example, since thrust is generated by rotating blades, the magnitude of the thrust and the torque are coupled. As a result, in addition to the thrust coefficient $\hat{C}_{\text{T}}$, the collective θ_0 also affects the torque coefficient $\hat{C}_{\text{Q}}$. As for the tail rotor, there is only one input, the rudder θ_{tail}. The tail rudder θ_{tail} control is analogous to the collective θ_0 control for the main rotor. It is responsible for controlling the magnitude of the thrust generated by the tail rotor. There is no cyclic control for the tail rotor because the primary function of the tail rotor is to provide counter torque for heading control. Collecting these rotor inputs together, the input vector $\vec{\boldsymbol{u}}$ for the helicopter system can be defined as:

$$\vec{\boldsymbol{u}} = \begin{bmatrix} \theta_0 & A_1 & B_1 & \theta_{\text{tail}} \end{bmatrix}^T \tag{2.9}$$

A helicopter is then controlled by setting appropriate values to the input vector $\vec{\boldsymbol{u}}$, which then generates the necessary rotor force and moment (as represented by the rotor coefficients) to

achieve flight:

$$(\theta_0, A_1, B_1, \theta_{\text{tail}}) \longrightarrow (\hat{C}_{\text{T}}, \hat{C}_{\text{lon}}, \hat{C}_{\text{lat}}, \hat{C}_{\text{Q}}, \hat{C}_{T_{\text{tail}}}, \hat{C}_{lon_{\text{tail}}}, \hat{C}_{lat_{\text{tail}}}, \hat{C}_{Q_{\text{tail}}})$$

2.1.2 Body Force and Moment

The net force and moment acting on the helicopter rigid body consists of two components: rotor effect and gravitational force.

$$\tilde{\boldsymbol{\tau}} = \tilde{\boldsymbol{\tau}}_{g_{\text{b}}} + \tilde{\boldsymbol{\tau}}_{\text{R}} \tag{2.10}$$

The rotor effect $\tilde{\boldsymbol{\tau}}_{\text{R}}$, which is composed of actions from both the main and the tail rotor, will be derived first. This is followed by the derivation of the gravitational component $\tilde{\boldsymbol{\tau}}_{g_{\text{b}}}$. Other body force and moment such as fuselage drag and aerodynamic moments from the fuselage, the vertical and horizontal tail fins are assumed to be negligible. This assumption can be justified for specific flight conditions such as in hover or flight with slow velocities, both of which are typical under the platform system.

Rotor Effect

The rotor coefficients introduced in the previous section are defined with respect to the individual rotor hub coordinates. The net rotor force and moment exerted on the helicopter body can be obtained by combining the main and tail rotor force and moment in the body-fixed frame. The normalized main and tail rotor force vectors in the body-fixed frame, expressed in terms of the non-dimensional rotor coefficients, are defined as:

$$\hat{\tilde{\boldsymbol{F}}}_{\text{main}} \triangleq \begin{bmatrix} \hat{X}_{\text{M}} \\ \hat{Y}_{\text{M}} \\ \hat{Z}_{\text{M}} \end{bmatrix} = \begin{bmatrix} -\hat{C}_{\text{lon}} \\ -\hat{C}_{\text{lat}} \\ -\hat{C}_{\text{T}} \end{bmatrix} \qquad \hat{\tilde{\boldsymbol{F}}}_{\text{tail}} \triangleq \begin{bmatrix} \hat{X}_{\text{T}} \\ \hat{Y}_{\text{T}} \\ \hat{Z}_{\text{T}} \end{bmatrix} = \hat{A}(\hat{\Omega}\hat{R})^2 \begin{bmatrix} -\hat{C}_{lon_{\text{tail}}} \\ -\hat{C}_{T_{\text{tail}}} \\ \hat{C}_{lat_{\text{tail}}} \end{bmatrix} \tag{2.11}$$

where the *tilde* symbol ($\tilde{}$) denotes quantities expressed with respect to the body-fixed frame.

A diagram showing the body-fixed frame attached to the centre of gravity of the helicopter is shown in Figure 2.2. The main rotor is offset from the centre of gravity by l_M along the body-fixed x axis and by h_M along the body-fixed z axis; while the tail rotor is offset by l_T and

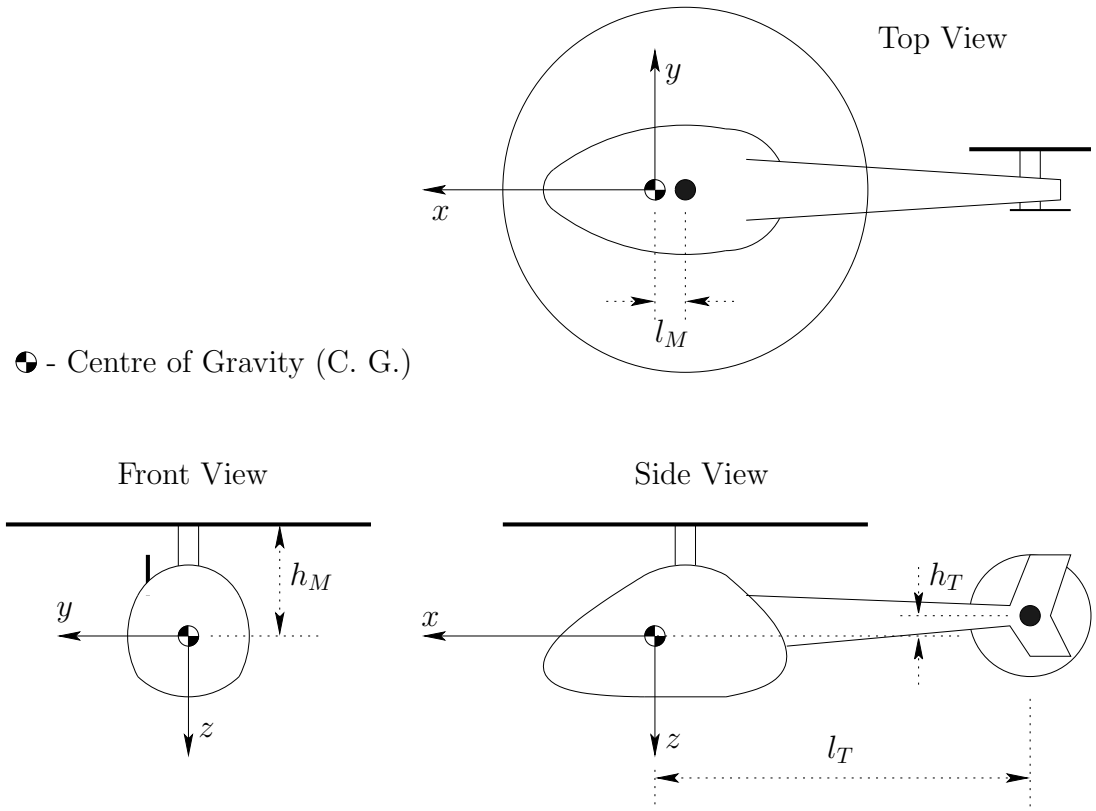

Figure 2.2: Helicopter Body-Fixed Reference Frame

h_T respectively. The helicopter configuration shown in Figure 2.2 assumes that there is no offset between the two rotors along the body y axis. It is convenient to normalize these parameters by the main rotor radius R:

$$\hat{h}_M = \frac{h_M}{R} \qquad \hat{l}_M = \frac{l_M}{R} \qquad \hat{h}_T = \frac{h_T}{R} \qquad \hat{l}_T = \frac{l_T}{R} \tag{2.12}$$

From Figure 2.2, the normalized rotor offset vectors can be defined with respect to the body-fixed frame as:

$$\hat{\hat{\boldsymbol{r}}}_{\text{main}} = \begin{bmatrix} -\hat{l_M} \\ 0 \\ -\hat{h_M} \end{bmatrix} \qquad \hat{\hat{\boldsymbol{r}}}_{\text{tail}} = \begin{bmatrix} -\hat{l_T} \\ 0 \\ -\hat{h_T} \end{bmatrix} \tag{2.13}$$

The normalized rotor moment acting on the centre of gravity of the helicopter can be expressed in terms of these normalized rotor offset vectors:

$$\hat{\hat{\boldsymbol{M}}}_{\text{main}} = \begin{bmatrix} 0 \\ 0 \\ -\hat{C}_{\text{Q}} \end{bmatrix} + \hat{\hat{\boldsymbol{r}}}_{\text{main}} \times \hat{\hat{\boldsymbol{F}}}_{\text{main}} \qquad \hat{\hat{\boldsymbol{M}}}_{\text{tail}} = \begin{bmatrix} 0 \\ \hat{A}(\hat{\Omega}\hat{R})^2 \hat{R} \hat{C}_{Q_{\text{tail}}} \\ 0 \end{bmatrix} + \hat{\hat{\boldsymbol{r}}}_{\text{tail}} \times \hat{\hat{\boldsymbol{F}}}_{\text{tail}} \tag{2.14}$$

A generalized force vector $\hat{\hat{\boldsymbol{\tau}}}$ can be defined by augmenting the force and moment vectors together. The normalized generalized force vector for the main and tail rotor expressed in the body-fixed frame can be written as:

$$\hat{\hat{\boldsymbol{\tau}}}_{\text{M}} \triangleq \begin{bmatrix} \hat{\hat{\boldsymbol{F}}}_{\text{main}} \\ \hat{\hat{\boldsymbol{M}}}_{\text{main}} \end{bmatrix} \qquad \hat{\hat{\boldsymbol{\tau}}}_{\text{T}} \triangleq \begin{bmatrix} \hat{\hat{\boldsymbol{F}}}_{\text{tail}} \\ \hat{\hat{\boldsymbol{M}}}_{\text{tail}} \end{bmatrix} \tag{2.15}$$

where the top half are the linear force along axes of the body-fixed frame and the bottom half represent the corresponding moments about those axes. The net normalized generalized force acting on the helicopter body generated by the rotors is obtained by adding up the effects from

both rotors:

$$\begin{aligned}\hat{\tilde{\boldsymbol{\tau}}}_{\mathrm{R}} &= \hat{\tilde{\boldsymbol{\tau}}}_{\mathrm{M}} + \hat{\tilde{\boldsymbol{\tau}}}_{\mathrm{T}} \\ &\triangleq \begin{bmatrix} \hat{X}_{\mathrm{R}} \\ \hat{Y}_{\mathrm{R}} \\ \hat{Z}_{\mathrm{R}} \\ \hat{L}_{\mathrm{R}} \\ \hat{M}_{\mathrm{R}} \\ \hat{N}_{\mathrm{R}} \end{bmatrix} = \begin{bmatrix} -\hat{C}_{\mathrm{lon}} - \hat{A}(\hat{\Omega}\hat{R})^2\hat{C}_{lon_{\mathrm{tail}}} \\ -\hat{C}_{\mathrm{lat}} - \hat{A}(\hat{\Omega}\hat{R})^2\hat{C}_{T_{\mathrm{tail}}} \\ -\hat{C}_{\mathrm{T}} + \hat{A}(\hat{\Omega}\hat{R})^2\hat{C}_{lat_{\mathrm{tail}}} \\ -\hat{h}_M\hat{C}_{\mathrm{lat}} - \hat{A}(\hat{\Omega}\hat{R})^2\hat{h}_T\hat{C}_{T_{\mathrm{tail}}} \\ \hat{h}_M\hat{C}_{\mathrm{lon}} - \hat{l}_M\hat{C}_{\mathrm{T}} + \hat{A}(\hat{\Omega}\hat{R})^2(\hat{h}_T\hat{C}_{lon_{\mathrm{tail}}} + \hat{l}_T\hat{C}_{lat_{\mathrm{tail}}} - \hat{R}\hat{C}_{Q_{\mathrm{tail}}}) \\ \hat{l}_M\hat{C}_{\mathrm{lat}} - \hat{C}_{\mathrm{Q}} + \hat{A}(\hat{\Omega}\hat{R})^2\hat{l}_T\hat{C}_{T_{\mathrm{tail}}} \end{bmatrix} \end{aligned} \tag{2.16}$$

The actual generalized rotor force acting on the helicopter rigid body ($\tilde{\boldsymbol{\tau}}_{\mathrm{R}}$) can be computed by multiplying (2.16) with the dimensional factors:

$$\tilde{\boldsymbol{\tau}}_{\mathrm{R}} = \begin{bmatrix} \rho A_{\mathrm{disc}}(\Omega R)^2 \boldsymbol{I}_{3\times3} & \mathbf{0}_{3\times3} \\ \mathbf{0}_{3\times3} & \rho A_{\mathrm{disc}}(\Omega R)^2 R \boldsymbol{I}_{3\times3} \end{bmatrix} \hat{\tilde{\boldsymbol{\tau}}}_{\mathrm{R}} \tag{2.17}$$

where $\boldsymbol{I}_{3\times3}$ and $\mathbf{0}_{3\times3}$ are the identity and zero matrices of dimension 3×3 respectively.

Given the rotor coefficients, the body force and moment generated by the rotors can be obtained from (2.16) and (2.17):

$$\begin{pmatrix} \hat{C}_{\mathrm{T}}, \hat{C}_{\mathrm{lon}}, \hat{C}_{\mathrm{lat}}, \hat{C}_{\mathrm{Q}}, \\ \hat{C}_{T_{\mathrm{tail}}}, \hat{C}_{lon_{\mathrm{tail}}}, \hat{C}_{lat_{\mathrm{tail}}}, \hat{C}_{Q_{\mathrm{tail}}} \end{pmatrix} \longrightarrow (\hat{X}_{\mathrm{R}}, \hat{Y}_{\mathrm{R}}, \hat{Z}_{\mathrm{R}}, \hat{L}_{\mathrm{R}}, \hat{M}_{\mathrm{R}}, \hat{N}_{\mathrm{R}}) \longrightarrow (X_{\mathrm{R}}, Y_{\mathrm{R}}, Z_{\mathrm{R}}, L_{\mathrm{R}}, M_{\mathrm{R}}, N_{\mathrm{R}})$$

where the rotor forces X_{R}, Y_{R} and Z_{R} are the dimensional counterpart to the normalized generalized forces $\hat{X}_{\mathrm{R}}$, $\hat{Y}_{\mathrm{R}}$ and $\hat{Z}_{\mathrm{R}}$. These dimensional force quantities can be obtained by multiplying their non-dimensional counterparts with the non-dimensional force factor $\rho A_{\mathrm{disc}}(\Omega R)^2$. Similarly, the dimensional rotor moments L_{R}, M_{R} and N_{R} are obtained by multiplying their non-dimensional counterparts ($\hat{L}_{\mathrm{R}}$, $\hat{M}_{\mathrm{R}}$ and $\hat{N}_{\mathrm{R}}$) with the non-dimensional torque factor $\rho A_{\mathrm{disc}}(\Omega R)^2 R$.

Gravity

Let the inertial frame be defined with z axis pointing downward positive, as is defined in the body-fixed frame (see Figure 2.2). The horizontal axes are defined in such a way that the

body-fixed x and y axes would align with the corresponding axes of the inertial frame when the helicopter has zero roll, pitch and yaw ($\phi = 0$, $\theta = 0$, and $\psi = 0$). The gravity vector acting on the helicopter rigid body can conveniently be expressed in the inertial frame as:

$$\vec{\boldsymbol{F}}_{g_\mathrm{b}} = \begin{bmatrix} 0 \\ 0 \\ m_b g \end{bmatrix} \tag{2.18}$$

where m_b is the mass of the helicopter body and g is the gravitational acceleration. The inertial gravity vector in (2.18) can be transformed into the body-fixed frame by multiplying with the transpose of the rotation matrix $\boldsymbol{R}^{\mathrm{body}}_{\mathrm{inertial}} = \boldsymbol{R}_{\psi,\theta,\phi}$ between the inertial and the body-fixed frame:

$$\tilde{\boldsymbol{F}}_{g_\mathrm{b}} = \left(\boldsymbol{R}^{\mathrm{body}}_{\mathrm{inertial}}\right)^T \vec{\boldsymbol{F}}_{g_\mathrm{b}} = \begin{bmatrix} -m_b g \sin(\theta) \\ m_b g \cos(\theta)\sin(\phi) \\ m_b g \cos(\theta)\cos(\phi) \end{bmatrix} \tag{2.19}$$

The rotation matrix $\boldsymbol{R}_{\psi,\theta,\phi}$ is defined in (A.6). A generalized gravity force vector $\tilde{\boldsymbol{\tau}}_{g_\mathrm{b}}$ can be defined with respect to the body-fixed frame similar to the rotor generalized vector $\tilde{\boldsymbol{\tau}}_{\mathrm{R}}$ in (2.17):

$$\tilde{\boldsymbol{\tau}}_{g_\mathrm{b}} = \begin{bmatrix} -m_b g \sin(\theta) \\ m_b g \cos(\theta)\sin(\phi) \\ m_b g \cos(\theta)\cos(\phi) \\ 0 \\ 0 \\ 0 \end{bmatrix} \tag{2.20}$$

The normalized form of the generalized gravity vector is given as:

$$\hat{\tilde{\boldsymbol{\tau}}}_{g_\mathrm{b}} = \begin{bmatrix} \frac{-m_b g \sin(\theta)}{\rho A_{\mathrm{disc}} (\Omega R)^2} \\ \frac{m_b g \cos(\theta)\sin(\phi)}{\rho A_{\mathrm{disc}} (\Omega R)^2} \\ \frac{m_b g \cos(\theta)\cos(\phi)}{\rho A_{\mathrm{disc}} (\Omega R)^2} \\ 0 \\ 0 \\ 0 \end{bmatrix} = \begin{bmatrix} -\hat{m}_b \hat{g} \sin(\theta) \\ \hat{m}_b \hat{g} \cos(\theta)\sin(\phi) \\ \hat{m}_b \hat{g} \cos(\theta)\cos(\phi) \\ 0 \\ 0 \\ 0 \end{bmatrix} \tag{2.21}$$

where $\hat{m}_b$ and $\hat{g}$ are the normalized helicopter mass and the normalized gravitational acceleration respectively. They are defined as:

$$\hat{m}_b = \frac{m_b}{\rho A_{\text{disc}} R} \qquad \hat{g} = \frac{g}{\Omega^2 R} \tag{2.22}$$

2.1.3 Rotor Dynamics

In the most basic view, a helicopter rotor can be modelled as an actuator disc that generates the thrust required for flight by accelerating air through the rotating blades. The amount of thrust generated by a rotor is dependent on several factors. In addition to the physical dimensions such as the rotor radius (blade length), the width of the blade (chord length) and the type of air foil (shape of the blade), the amount of thrust generated by the rotor also depends on the rotation speed of the rotor, the relative movement of the rotor in the air and the relative angle between the rotor blade and the incoming air stream (also known as the angle of attack of the blade). For simplicity, the rotor rotation speed (denoted as Ω) is assumed to be constant [1, 10]. This is justified through the use of a speed governor. Furthermore, since both the main and tail rotor are often driven by a single engine through some transmission mechanism, the speed of the tail rotor Ω_{tail} is linked to the main rotor speed through a constant gear ratio $\hat{\Omega}$:

$$\Omega_{\text{tail}} = \hat{\Omega}\Omega \tag{2.23}$$

As the basic thrust generation mechanism between the main and tail rotor are the same, the dynamics of the main rotor will be derived first through the use of the momentum theory and the blade element method [10]. Then the dynamics of the tail rotor will be obtained by modifying the main rotor equations accordingly.

Main Rotor Dynamics

Referring to Figure 2.3, the position of the blade around the rotor (the azimuth angle) is denoted as Ψ. By convention, $\Psi = 0^\circ$ is when the blade is at the aft (backward) position of the helicopter; while $\Psi = 180^\circ$ is at the fore (forward) position of the helicopter [10, 1, 9, 12]. The direction of Ψ is defined by the direction of rotation of the rotor blades. The blade rotation shown in Figure 2.3 is positive in the clockwise direction when viewed from above. That is the

direction of the rotor blade rotation for the test platform helicopter. This means $\Psi = 90°$ is on the left hand side; while $\Psi = 270°$ is on the right hand side of the helicopter. A blade element at a distance r_s away from the rotor hub is marked in the diagram.

Recall the three inputs of the main rotor are the collective θ_0, the longitudinal cyclic B_1 and the lateral cyclic A_1. These inputs affect the pitch angle of the blade as it rotates around the azimuth. The collective input changes the rotor blade pitch evenly around the rotor disc. This has a net effect of changing the magnitude of the rotor thrust ($\hat{C}_T$). In contrast, the cyclic inputs vary the blade pitch as the blade travels around the rotor. This has a net effect of altering the direction of the thrust vector which generates side forces ($\hat{C}_{lon}$ and $\hat{C}_{lat}$) responsible for body rotation and side movement of the helicopter. Combing the collective and the cyclic effects, the blade pitch θ can be expressed as a periodic function of the azimuth angle Ψ [10]:

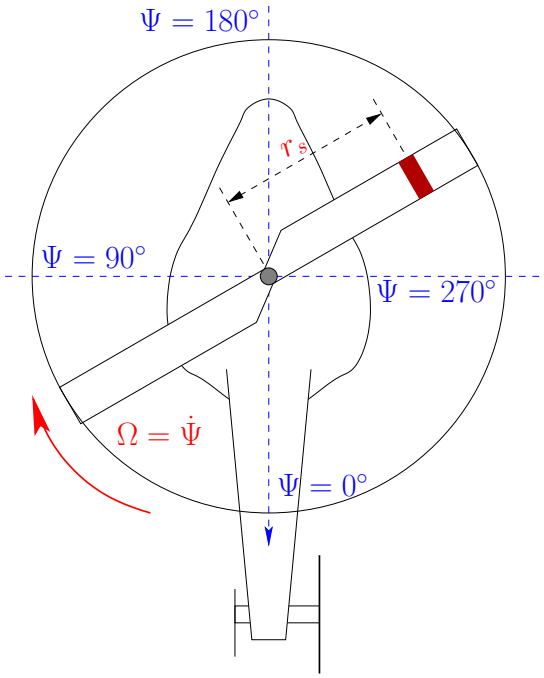

Figure 2.3: Rotor Rotation Coordinates

$$\theta = \theta_0 - A_1 \cos(\Psi) - B_1 \sin(\Psi) \tag{2.24}$$

The collective pitch θ_0 is the nominal pitch of the blade. The longitudinal cyclic pitch B_1 represents the pitch of the blade when it is at $\Psi = 270°$ and $\Psi = 90°$; whereas the lateral cyclic pitch A_1 represents the blade pitch as $\Psi = 180°$ and $\Psi = 0°$. As the lift generated by the rotor blade is proportional to the blade pitch [10], the longitudinal cyclic pitch B_1 causes the maximum and minimum lift to be applied at $\Psi = 270°$ and $\Psi = 90°$ respectively. The variation in lift experienced by the blade results in a steady state once-per-revolution out-of-plane (perpendicular to the rotor disc) motion called flapping [10, 1]. For a rotor with flapping hinges (that is, the blades are mounted to the rotor hub through the hinges to allow the blade to flap up and down

freely), the flapping motion represents a harmonic response to a periodic excitation (the cyclic pitch) [9]. Recall the plane traced out by the tip of the blades is called the tip-path-plane (TPP). The net rotor thrust vector is defined as normal to the TPP [10]. Focusing only on the first order harmonic, the blade flapping angle (β) can be expressed in a form similar to (2.24):

$$\beta = a_0 - a_{1,\mathrm{s}} \cos(\Psi) + b_{1,\mathrm{s}} \sin(\Psi) \tag{2.25}$$

where a_0 is the coning angle, $a_{1,\mathrm{s}}$ is the longitudinal flapping/tilt angle and $b_{1,\mathrm{s}}$ is the lateral flapping/tilt angle. The coning angle a_0 is the angle at which the moment generated about the flapping hinge by the forces acting on the rotor blade, such as the centrifugal force, lift and gravity, equals to zero (in equilibrium) [1]. The longitudinal flapping angle $a_{1,\mathrm{s}}$ represents the maximum and minimum flapping at $\Psi = 180^\circ$ and $\Psi = 0^\circ$ respectively; whereas $b_{1,\mathrm{s}}$ represents the maximum and minimum flapping at $\Psi = 90^\circ$ and $\Psi = 270^\circ$ respectively.

The flapping harmonic motion is characterized by a 90° phase lag in the response. In the case of the longitudinal pitch B_1, the maximum (and minimum) lift at $\Psi = 270^\circ$ (and $\Psi = 90^\circ$) results in maximum (and minimum) flapping 90° later at $\Psi = 0^\circ$ (and $\Psi = 180^\circ$). For steady state harmonic motion, the amount of flapping is equal to the amount of cyclic blade angle [9]. In other words, one degree of cyclic pitch results in one degree of flapping [10]:

$$a_{1,\mathrm{s}} = -B_1 \qquad\qquad b_{1,\mathrm{s}} = -A_1 \tag{2.26}$$

The blade pitch is typically achieved through the action of servo motors. The inputs to the servo motors are denoted as δ_{coll}, δ_{lon} and δ_{lat}. The blades are connected to the servo motors through the control rods and the swashplate [12] in such a way that δ_{coll} controls the collective pitch θ_0, δ_{lon} controls the longitudinal cyclic pitch B_1, and δ_{lat} controls the lateral cyclic pitch A_1. These connections are shown in Figure 2.4.

Under normal flight condition (such as hover), the rigid body dynamics of the helicopter is significantly slower than the servo dynamics [30] so that the servo dynamics can usually be ignored. This simplifies the blade pitch to be proportional to the servo inputs:

$$\theta_0 = K_{\mathrm{coll}}\delta_{\mathrm{coll}} \qquad B_1 = K_{\mathrm{lon}}\delta_{\mathrm{lon}} \qquad A_1 = K_{\mathrm{lat}}\delta_{\mathrm{lat}} \tag{2.27}$$

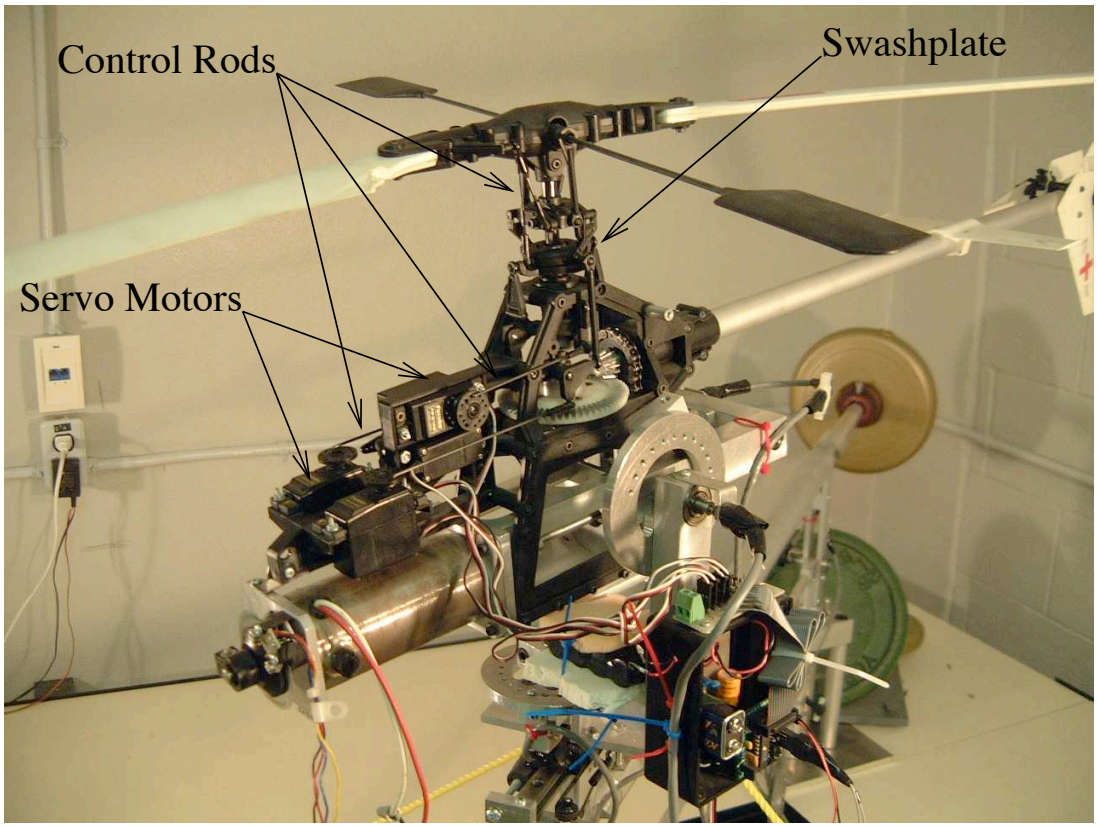

Figure 2.4: Helicopter

Therefore, for simplicity, θ_0, B_1 and A_1 will be taken as the input for the main rotor directly, as well as the collective pitch of the tail rotor θ_{tail} (recall (2.9)):

$$\vec{\boldsymbol{u}} = \begin{bmatrix} \theta_0 & A_1 & B_1 & \theta_{\text{tail}} \end{bmatrix}^T$$

For a rotor disc operating in hover, the average speed of air v_1 passing through as a result of thrust generation can be related to the thrust T by applying the momentum theory and the principle of conservation of energy [1] (see Appendix B.1 for details):

$$T = 2\rho A_{\text{disc}} v_1^2 \qquad \text{or} \qquad v_1 = \sqrt{\frac{T}{2\rho A_{\text{disc}}}} \tag{2.28}$$

The velocity v_1 is called the induced velocity. The implicit assumption here is that both the thrust and the induced velocity are uniformly distributed across the rotor disc. For a general

flight condition, the relationship between T and v_1 is modified to include the rotor velocity through air due to the motion of the helicopter [12]:

$$T = 2\rho A_{\text{disc}} V_{\text{air}} v_1 \qquad \text{or} \qquad v_1 = \frac{T}{2\rho A_{\text{disc}} V_{\text{air}}} \tag{2.29}$$

where V_{air} is the rotor velocity through air given by:

$$V_{\text{air}} = \sqrt{V_{\text{horizontal}}^2 + (v_1 + V_{\text{vertical}})^2} \tag{2.30}$$

The component of the rotor velocity that lies in the plane of rotation of the blades is denoted as $V_{\text{horizontal}}$; while the perpendicular component is denoted V_{vertical}.

The horizontal velocity of the rotor disc is composed of both the linear and angular velocity component of the helicopter rigid body motion projected along the direction of motion through the side slip angle η_m:

$$V_{\text{horizontal}} = u\cos(\eta_m) + v\sin(\eta_m) + h_M\left[p\sin(\eta_m) - q\cos(\eta_m)\right] - l_M r\sin(\eta_m) \tag{2.31}$$

where u, v, and w are the x, y, and z axis component of the linear velocity of the helicopter $\vec{\boldsymbol{v}}_b$ expressed in the body-fixed frame respectively; while p, q, and r are the corresponding component for the angular velocity vector $\vec{\boldsymbol{\omega}}_b$ expressed in the body-fixed frame:

$$\tilde{\boldsymbol{v}}_b = \begin{bmatrix} u \\ v \\ w \end{bmatrix} \qquad\qquad \tilde{\boldsymbol{\omega}}_b = \begin{bmatrix} p \\ q \\ r \end{bmatrix} \tag{2.32}$$

The side slip angle η_m of the main rotor represents the ratio between the forward and the sideways motion of the rotor and is defined as:

$$\eta_m = \arctan\left(\frac{v - l_{\text{M}} r + h_{\text{M}} p}{u - h_{\text{M}} q}\right) \tag{2.33}$$

The vertical velocity component of the rotor disc is defined as:

$$V_{\text{vertical}} = -(w + l_M q) \tag{2.34}$$

Notice that the direction of V_{vertical} is defined with the same positive direction as the induced velocity v_1, which is opposite to the body z axis.

The horizontal $V_{\text{horizontal}}$ and vertical V_{vertical} velocity of the main rotor disc, as well as the averaged induced velocity v_1 at the rotor, can be divided by the rotor tip speed ΩR to obtain the non-dimensional velocities μ (also referred to as the advanced ratio), λ_{z} and λ_1 (also known as the inflow factor):

$$\mu = \frac{V_{\text{horizontal}}}{\Omega R} \qquad \lambda_{\text{z}} = \frac{V_{\text{vertical}}}{\Omega R} \qquad \lambda_1 = \frac{v_1}{\Omega R} \tag{2.35}$$

Similarly, the components of the angular velocity of the helicopter body can also be normalized as:

$$\upsilon_{\text{x}} = \frac{p}{\Omega} \qquad \upsilon_{\text{y}} = \frac{q}{\Omega} \qquad \upsilon_{\text{z}} = \frac{r}{\Omega} \tag{2.36}$$

The net thrust T generated by the rotor can be obtained by integrating the incremental thrust generated by a small blade element based on its local conditions, such as local relative speed and angle of attack. This method is referred to as the blade element method [1, 10]. For a rotor with N_b number of blades in hover, the thrust, T, computed from applying the blade element method is given by (see Appendix B.2 for details):

$$T = \frac{1}{2}\rho N_b c R (\Omega R)^2 a_L \left(\frac{1}{3}\theta_0 - \frac{1}{2}\frac{v_1}{\Omega R}\right) \tag{2.37}$$

where c is the blade chord length and a_L is the lift curve coefficient whose value is dependent on the shape of the air foil of the blades [1].

The thrust coefficient $\hat{C}_{\text{T}}$ for the main rotor in hover can be obtained by dividing (2.37) by the non-dimensional factor according to (2.1):

$$\hat{C}_{\text{T}} = \frac{\sigma a_L}{4}\left(\frac{2}{3}\theta_0 - \lambda_1\right) \tag{2.38}$$

where σ is the solidity, defined as the ratio between the total blade area $A_{\text{b}} = N_b c R$ and the

rotor disc area $A_{\text{disc}} = \pi R^2$ [10]:

$$\sigma = \frac{A_{\text{b}}}{A_{\text{disc}}} = \frac{N_b c R}{\pi R^2} = \frac{N_b c}{\pi R} \tag{2.39}$$

Although the thrust coefficient $\hat{C}_{\text{T}}$ defined in (2.38) might appear to be affine in the collective input θ_0, examination of the definition for the inflow factor λ_1 given in (2.35) and (2.28) reveals otherwise.

For general flight, the thrust coefficient becomes (see Appendix B.2):

$$\hat{C}_{\text{T}} = \frac{\sigma a_L}{4}\left[\frac{2}{3}\theta_0\left(1+\frac{3}{2}\mu^2\right) - (\lambda_1 + \lambda_{\text{z}} + \mu\hat{B}_1) - \frac{\mu \upsilon_{\text{x}}}{2}\right] \tag{2.40}$$

where the longitudinal cyclic pitch input $\hat{B}_1$ is defined with respect to the hub-wind frame. The hub-wind frame is obtained by rotating the main rotor hub frame by the side-slip angle η_m about the hub z axis [9]. The main rotor hub frame has the same orientation as the body-fixed frame except it is attached to the main rotor hub instead of the rigid body centre of gravity. The relationship between the cyclic inputs defined previously in (2.9) and the rotated inputs can be obtained through the rotation matrix between the hub and hub-wind frame (see Appendix A):

$$\hat{A}_1 = \sin(\eta_m)B_1 + \cos(\eta_m)A_1 \qquad\qquad \hat{B}_1 = \cos(\eta_m)B_1 - \sin(\eta_m)A_1 \tag{2.41}$$

Notice that when the side slip angle is zero ($\eta_m = 0$), such as when the helicopter is in hover or forward flight, the cyclic inputs defined in (2.9) and (2.41) would be aligned and have the same values.

In addition to the thrust, when the helicopter is in motion (such as in forward flight), the asymmetry in the local angle of attack of the blades also produces net force within the disc plane. The resulting longitudinal and lateral side forces, referred to as the planar Horizontal Force (H-Force) [10], can be obtained by integrating the incremental drag force generated by the

blade element analogous to those for the thrust (see Appendix B.2) [10]:

$$\begin{aligned}\hat{C}_{\text{lon}} = &\frac{\mu\sigma}{4}c_{\text{D}} + a_{1,\text{s}}\hat{C}_{\text{T}} + \frac{a_L\sigma}{4}\Bigg((\lambda_1 + \lambda_{\text{z}} - a_{1,\text{s}}\mu)\left[\theta_0\mu - \frac{1}{2}(a_{1,\text{s}} + \hat{B}_1) - \upsilon_{\text{x}}\right] \\ &+ (b_{1,\text{s}} + \hat{A}_1)\left[\frac{a_0}{3} - \frac{\mu}{8}(K\lambda_1 - \upsilon_{\text{y}})\right] + a_0\left[\frac{\mu a_0}{2} + \frac{1}{3}(K\lambda_1 - \upsilon_{\text{y}})\right] \\ &+ \upsilon_{\text{x}}\left[\frac{\theta_0}{3} - \frac{3}{8}\mu(a_{1,\text{s}} + \hat{B}_1)\right]\Bigg) \qquad (2.42)\end{aligned}$$

$$\begin{aligned}\hat{C}_{\text{lat}} = &- b_{1,\text{s}}\hat{C}_{\text{T}} + \frac{a_L\sigma}{4}\Bigg((\lambda_1 + \lambda_{\text{z}} - a_{1,\text{s}}\mu)\left[3a_0\mu + (K\lambda_1 - \upsilon_{\text{y}}) + \frac{1}{2}(b_{1,\text{s}} + \hat{A}_1)\right] \\ &+ (a_{1,\text{s}} + \hat{B}_1)\left[\frac{a_0}{3} + \frac{\mu}{8}(K\lambda_1 - \upsilon_{\text{y}}) + a_0\mu^2\right] - \theta_0\left[\frac{3}{2}a_0\mu + \frac{1}{3}(K\lambda_1 - \upsilon_{\text{y}})\right] \\ &+ \upsilon_{\text{x}}\left[\frac{a_0}{3} + \frac{\mu}{8}(b_{1,\text{s}} + \hat{A}_1)\right]\Bigg) \qquad (2.43)\end{aligned}$$

The expressions for the coning angle (a_0), the flapping coefficients ($a_{1,\text{s}}$ and $b_{1,\text{s}}$) and the inflow distribution factor K can be found in Appendix B.2. The drag coefficient c_{D} is another air foil dependent property similar to a_L [10].

The longitudinal and lateral force coefficients in (2.42) and (2.43) are defined with respect to the rotor hub-wind frame, which is rotated from the body-fixed frame by the side slip angle η_m about the vertical axis. This means the longitudinal direction here is along the direction of the incoming air stream; while the lateral direction is defined as perpendicular to the longitudinal direction.

Finally, carrying out the same process for the torque in hover, the torque coefficient for the main rotor $\hat{C}_{\text{Q}}$ can be obtained (see Appendix B.2):

$$\hat{C}_{\text{Q}} = \frac{\sigma}{8}c_{\text{D}} + \frac{1}{\sqrt{2}}\hat{C}_{\text{T}}^{3/2} \qquad (2.44)$$

The corresponding expression for general flight is:

$$\hat{C}_{\text{Q}} = \frac{\sigma}{8}c_{\text{D}}(1 + 3\mu^2) + (\lambda_1 + \lambda_{\text{z}})\hat{C}_{\text{T}} - \mu\hat{C}_{\text{lon}} + \frac{a_L\sigma}{\gamma_L}(a_{1,\text{s}}\upsilon_{\text{y}} + b_{1,\text{s}}\upsilon_{\text{x}} + K\lambda_1\upsilon_{\text{x}}) \qquad (2.45)$$

where γ_L is the Lock number [10, 12] defined as:

$$\gamma_L = \frac{\rho c a_L R^4}{I_{\text{blade}}}$$

with I_{blade} representing the blade flapping inertia.

The rotor dynamics derived in this section is referred to as the *quasi-steady* rotor model [12] for the assumption that the blade flapping response is fast relative to the rigid body dynamics of the rest of the system. The implication is that the rotor blade flapping dynamics can be represented by the steady-state response (the flapping coefficients a_0, $a_{1,\text{s}}$, and $b_{1,\text{s}}$, see Appendix B.2).

Tail Rotor Dynamics

By taking into account the difference between the two rotors, the expressions for the tail rotor coefficients can be obtained by modifying the corresponding main rotor equations. First, only the collective control is available in the tail rotor. So, to obtain the expressions for the tail rotor, the cyclic control inputs $\hat{A}_1$ and $\hat{B}_1$ are set to zero; while the collective θ_0 is replaced with θ_{tail} instead of θ_0. Second, the velocities the tail rotor experienced due to the motion of the helicopter rigid body will be different from that of the main rotor because of the difference in position and orientation of the tail rotor. Finally, the rotor parameter values for the tail rotor, such as the rotor speed Ω_{tail}, are used instead of those for the main rotor. A list of updated parameter values for the tail rotor is shown below:

$$\mu_{\text{tail}} = \frac{u\cos(\eta_t) - w\sin(\eta_t) - q\big[l_T\sin(\eta_t) + h_T\cos(\eta_t)\big]}{\Omega_{\text{tail}} R_{\text{tail}}} \tag{2.46}$$

$$\lambda_{z_{\text{tail}}} = \frac{-v + l_T r - h_T p}{\Omega_{\text{tail}} R_{\text{tail}}} \tag{2.47}$$

$$\upsilon_{x_{\text{tail}}} = \frac{p\cos(\eta_t) - r\sin(\eta_t)}{\Omega_{\text{tail}}} \tag{2.48}$$

$$\upsilon_{y_{\text{tail}}} = -\left[\frac{p\sin(\eta_t) + r\cos(\eta_t)}{\Omega_{\text{tail}}}\right] \tag{2.49}$$

$$\sigma_{\text{tail}} = \frac{A_{b_{\text{tail}}}}{A_{disc_{\text{tail}}}} \tag{2.50}$$

where the side slip angle η_t for the tail rotor is defined as:

$$\eta_t = \arctan\left(\frac{w + l_T q}{-u + h_T q}\right) \tag{2.51}$$

Updated Body Force and Moment Equations

Recall the rotor coefficient expressions derived in the previous sections were defined with respect to the rotor hub-wind axis, while the expressions for the body force and moment in (2.16) are defined with the assumption that the hub-wind frame be aligned with the body-fixed frame, such as during hover or forward flight. For general flight, (2.16) needs to be updated by taking into account the effect of the side slip angles η_m and η_t experienced by the two rotors.

$$\hat{X}_{\mathrm{R}} = -\cos(\eta_m)\hat{C}_{\mathrm{lon}} + \sin(\eta_m)\hat{C}_{\mathrm{lat}} + \hat{A}(\hat{\Omega}\hat{R})^2\big[\sin(\eta_t)\hat{C}_{lat_{\mathrm{tail}}} - \cos(\eta_t)\hat{C}_{lon_{\mathrm{tail}}}\big] \tag{2.52}$$

$$\hat{Y}_{\mathrm{R}} = -\cos(\eta_m)\hat{C}_{\mathrm{lat}} - \sin(\eta_m)\hat{C}_{\mathrm{lon}} - \hat{A}(\hat{\Omega}\hat{R})^2\hat{C}_{T_{\mathrm{tail}}} \tag{2.53}$$

$$\hat{Z}_{\mathrm{R}} = -\hat{C}_{\mathrm{T}} + \hat{A}(\hat{\Omega}\hat{R})^2\big[\cos(\eta_t)\hat{C}_{lat_{\mathrm{tail}}} + \sin(\eta_t)\hat{C}_{lon_{\mathrm{tail}}}\big] \tag{2.54}$$

$$\hat{L}_{\mathrm{R}} = -\hat{h}_M\big[\cos(\eta_m)\hat{C}_{\mathrm{lat}} + \sin(\eta_m)\hat{C}_{\mathrm{lon}}\big] - \hat{A}(\hat{\Omega}\hat{R})^2\hat{h}_T\hat{C}_{T_{\mathrm{tail}}} \tag{2.55}$$

$$\begin{aligned}\hat{M}_{\mathrm{R}} = {} & \hat{h}_M\big[\cos(\eta_m)\hat{C}_{\mathrm{lon}} - \sin(\eta_m)\hat{C}_{\mathrm{lat}}\big] - \hat{l}_M\hat{C}_{\mathrm{T}} + \hat{A}(\hat{\Omega}\hat{R})^2\Big(\\ & \big[\hat{h}_T\cos(\eta_t) + \hat{l}_T\sin(\eta_t)\big]\hat{C}_{lon_{\mathrm{tail}}} + \big[\hat{l}_T\cos(\eta_t) - \hat{h}_T\sin(\eta_t)\big]\hat{C}_{lat_{\mathrm{tail}}} - \hat{R}\hat{C}_{Q_{\mathrm{tail}}}\Big)\end{aligned} \tag{2.56}$$

$$\hat{N}_{\mathrm{R}} = \hat{l}_M\big[\cos(\eta_t)\hat{C}_{\mathrm{lat}} + \sin(\eta_t)\hat{C}_{\mathrm{lon}}\big] - \hat{C}_{\mathrm{Q}} + \hat{A}(\hat{\Omega}\hat{R})^2\hat{l}_T\hat{C}_{T_{\mathrm{tail}}} \tag{2.57}$$

where the planar force coefficients $\hat{C}_{\mathrm{lon}}$, $\hat{C}_{\mathrm{lat}}$, $\hat{C}_{lon_{\mathrm{tail}}}$ and $\hat{C}_{lat_{\mathrm{tail}}}$ are defined with reference to their respective hub-wind frame. Notice that although the relations between the control inputs (θ_0, A_1, B_1 and θ_{tail}) and the rotor coefficients are nonlinear (see comment on (2.38) above), the expressions for the generalized rotor forces shown in (2.52)-(2.57) are affine in the rotor coefficients. This observation will be exploited in the proposed Virtual Joint Control scheme presented in Chapter 4.

2.1.4 Rigid Body Dynamics

The rigid body dynamics of a stand alone helicopter (UAV) can be obtained by applying the Newton-Euler formulation [12, 39]:

$$\tilde{\boldsymbol{F}}_b^a = m_b \left(\frac{\partial \tilde{\boldsymbol{v}}_b}{\partial t} + \tilde{\boldsymbol{\omega}}_b \times \tilde{\boldsymbol{v}}_b \right) \qquad \tilde{\boldsymbol{M}}_b^a = \frac{\partial \tilde{\boldsymbol{H}}_b}{\partial t} + \tilde{\boldsymbol{\omega}}_b \times \tilde{\boldsymbol{H}}_b \tag{2.58}$$

where $\tilde{\boldsymbol{F}}_b^a$ and $\tilde{\boldsymbol{M}}_b^a$ are the net force and moment acting on the centre of gravity of the helicopter rigid body:

$$\tilde{\boldsymbol{F}}_b^a = \begin{bmatrix} X \\ Y \\ Z \end{bmatrix} = \tilde{\boldsymbol{F}}_{g_\mathrm{b}} + \tilde{\boldsymbol{F}}_\mathrm{R} \qquad \tilde{\boldsymbol{M}}_b^a = \begin{bmatrix} L \\ M \\ N \end{bmatrix} = \tilde{\boldsymbol{M}}_{g_\mathrm{b}} + \tilde{\boldsymbol{M}}_\mathrm{R} \tag{2.59}$$

and $\tilde{\boldsymbol{H}}_b$ is the angular momentum about the centre of gravity (C.G.) of the helicopter rigid body. It is defined as the product between the inertia matrix $\boldsymbol{I}_\mathrm{b}$ about the C.G. and the rigid body angular velocity $\tilde{\boldsymbol{\omega}}_\mathrm{b}$ expressed in the body-fixed frame [39]:

$$\tilde{\boldsymbol{H}}_b = \boldsymbol{I}_\mathrm{b} \tilde{\boldsymbol{\omega}}_\mathrm{b} \tag{2.60}$$

The inertia matrix $\boldsymbol{I}_\mathrm{b}$ is defined with respect to the body-fixed frame:

$$\boldsymbol{I}_\mathrm{b} = \begin{bmatrix} I_{xx_\mathrm{b}} & -I_{xy_\mathrm{b}} & -I_{xz_\mathrm{b}} \\ -I_{xy_\mathrm{b}} & I_{yy_\mathrm{b}} & -I_{yz_\mathrm{b}} \\ -I_{xz_\mathrm{b}} & -I_{yz_\mathrm{b}} & I_{zz_\mathrm{b}} \end{bmatrix} \tag{2.61}$$

where I_{xx_b}, I_{yy_b}, and I_{zz_b} are the mass moment of inertia of the helicopter rigid body; while I_{xz_b}, I_{xy_b}, and I_{yz_b} are the products of inertia [39].

The form of the Newton-Euler equation of motions stated in (2.58) is expressed with respect to the reference frame attached to the centre of gravity of the helicopter rigid body, referred to as the body-fixed frame (see Figure 2.2). The use of this moving body-fixed frame as the reference frame gives rise to the cross-product terms in (2.58) [38, 39]. Expanding (2.58), the resulting

force and moment equations expressed with respect to the body-fixed frame are given by:

$$\begin{aligned} m_b(\dot{u} - rv + qw) &= X \\ m_b(\dot{v} - pw + ru) &= Y \\ m_b(\dot{w} - qu + pv) &= Z \end{aligned} \tag{2.62}$$

and

$$\begin{aligned} I_{xx_b}\dot{p} - (I_{yy_b} - I_{zz_b})qr + I_{xy_b}(pr - \dot{q}) - I_{xz_b}(pq + \dot{r}) + I_{yz_b}(r^2 - q^2) &= L \\ I_{yy_b}\dot{q} + (I_{xx_b} - I_{zz_b})pr + I_{yz_b}(pq - \dot{r}) + I_{xz_b}(p^2 - r^2) - I_{xy_b}(qr + \dot{p}) &= M \\ I_{zz_b}\dot{r} - (I_{xx_b} - I_{yy_b})pq - I_{yz_b}(pr + \dot{q}) + I_{xz_b}(qr - \dot{p}) + I_{xy_b}(q^2 + p^2) &= N \end{aligned} \tag{2.63}$$

Equation (2.63) can be simplified if there is symmetry about the x–z plane of the body-fixed coordinate. In most helicopters, this assumption is approximately true, with the exception in the slight asymmetry in the tail due to the tail rotor arrangement. In the case where symmetry applies, both the I_{xy} and I_{yz} product of inertia become zero [12], resulting in:

$$\begin{aligned} I_{xx_b}\dot{p} - (I_{yy_b} - I_{zz_b})qr - I_{xz_b}(pq + \dot{r}) &= L \\ I_{yy_b}\dot{q} + (I_{xx_b} - I_{zz_b})pr + I_{xz_b}(p^2 - r^2) &= M \\ I_{zz_b}\dot{r} - (I_{xx_b} - I_{yy_b})pq + I_{xz_b}(qr - \dot{p}) &= N \end{aligned} \tag{2.64}$$

The dynamic model for the helicopter rigid body defined in (2.62) and (2.64) can be combined into a matrix equation form:

$$\tilde{\boldsymbol{M}}\ddot{\tilde{\boldsymbol{\Phi}}} + \tilde{\boldsymbol{h}}(\dot{\tilde{\boldsymbol{\Phi}}}) = \tilde{\boldsymbol{\tau}}(\vec{\boldsymbol{\Theta}}, \dot{\tilde{\boldsymbol{\Phi}}}, \vec{\boldsymbol{u}}) \tag{2.65}$$

where $\dot{\tilde{\boldsymbol{\Phi}}}$ is the generalized body rate vector with the body-fixed linear and angular velocity as its component:

$$\dot{\tilde{\boldsymbol{\Phi}}} = \begin{bmatrix} u & v & w & p & q & r \end{bmatrix}^T \tag{2.66}$$

The vector $\vec{\boldsymbol{\Theta}}$ is the generalized position vector of the C.G. of the helicopter. It contains the position, expressed in terms of the inertial frame coordinates, and the attitude, expressed in

terms of Euler angles, of the helicopter body:

$$\vec{\boldsymbol{\Theta}} = \begin{bmatrix} x & y & z & \phi & \theta & \psi \end{bmatrix}^T \tag{2.67}$$

The generalized body rate vector $\dot{\vec{\boldsymbol{\Phi}}}$ can be expressed in terms of the rate of change of the generalized position vector $\dot{\vec{\boldsymbol{\Theta}}}$ through the rotation matrix $\boldsymbol{R}_{\text{body}}^{\text{inertial}}$ between the inertial and body-fixed frame and the Euler rate mapping matrix $\boldsymbol{R}_{\text{Euler}}$ (see Appendix A.1.1 for details):

$$\begin{bmatrix} u \\ v \\ w \\ p \\ q \\ r \end{bmatrix} = \begin{bmatrix} \boldsymbol{R}_{\text{body}}^{\text{inertial}} & \boldsymbol{0}_{3\times3} \\ \boldsymbol{0}_{3\times3} & \boldsymbol{R}_{\text{Euler}} \end{bmatrix} \begin{bmatrix} \dot{x} \\ \dot{y} \\ \dot{z} \\ \dot{\phi} \\ \dot{\theta} \\ \dot{\psi} \end{bmatrix} \tag{2.68}$$

The mass-inertia matrix $\tilde{\boldsymbol{M}}$ is defined as:

$$\tilde{\boldsymbol{M}} = \begin{bmatrix} m_b & 0 & 0 & 0 & 0 & 0 \\ 0 & m_b & 0 & 0 & 0 & 0 \\ 0 & 0 & m_b & 0 & 0 & 0 \\ 0 & 0 & 0 & I_{xx_{\text{b}}} & 0 & -I_{xz_{\text{b}}} \\ 0 & 0 & 0 & 0 & I_{yy_{\text{b}}} & 0 \\ 0 & 0 & 0 & -I_{xz_{\text{b}}} & 0 & I_{zz_{\text{b}}} \end{bmatrix} \tag{2.69}$$

For the UAV model, the mass-inertia matrix is constant as it is expressed with respect to the body-fixed frame.

The Coriolis and centrifugal terms $\tilde{\boldsymbol{h}}(\dot{\vec{\boldsymbol{\Phi}}})$ can be expressed as a product with the body rate

vector $\tilde{\boldsymbol{h}}(\dot{\tilde{\boldsymbol{\Phi}}}) = \tilde{\boldsymbol{C}}(\dot{\tilde{\boldsymbol{\Phi}}})\dot{\tilde{\boldsymbol{\Phi}}}$ with the matrix $\tilde{\boldsymbol{C}}(\dot{\tilde{\boldsymbol{\Phi}}})$ being defined as:

$$\tilde{\boldsymbol{C}}(\dot{\tilde{\boldsymbol{\Phi}}}) = \begin{bmatrix} 0 & -m_b r & m_b q & 0 & 0 & 0 \\ m_b r & 0 & -m_b p & 0 & 0 & 0 \\ -m_b q & m_b p & 0 & 0 & 0 & 0 \\ 0 & 0 & 0 & -I_{xz_\mathrm{b}} q & -I_{yy_\mathrm{b}} r & I_{zz_\mathrm{b}} q \\ 0 & 0 & 0 & I_{xx_\mathrm{b}} r + I_{xz_\mathrm{b}} p & 0 & -(I_{zz_\mathrm{b}} p + I_{xz_\mathrm{b}} r) \\ 0 & 0 & 0 & -I_{xx_\mathrm{b}} q & I_{yy_\mathrm{b}} p & I_{xz_\mathrm{b}} q \end{bmatrix} \tag{2.70}$$

Notice that the definition of $\tilde{\boldsymbol{C}}(\dot{\tilde{\boldsymbol{\Phi}}})$ is not unique. Here, it is defined as

$$\tilde{\boldsymbol{C}}(\dot{\tilde{\boldsymbol{\Phi}}}) = \begin{bmatrix} m_b \boldsymbol{S}(\tilde{\boldsymbol{\omega}}_b) & \mathbf{0}_{3\times 3} \\ \mathbf{0}_{3\times 3} & \boldsymbol{S}(\tilde{\boldsymbol{\omega}}_b)\boldsymbol{I}_\mathrm{b} \end{bmatrix}$$

where $\boldsymbol{S}(\tilde{\boldsymbol{\omega}}_b)$ is the skew symmetric matrix for the angular velocity vector $\tilde{\boldsymbol{\omega}}_b$ [40]:

$$\boldsymbol{S}(\tilde{\boldsymbol{\omega}}_b) = \begin{bmatrix} 0 & -r & q \\ r & 0 & -p \\ -q & p & 0 \end{bmatrix} \tag{2.71}$$

As derived in the previous sections, the generalized body force vector $\tilde{\boldsymbol{\tau}}$ defined in (2.10) consists of effects generated from gravity and rotor dynamics. Therefore it is dependent on the rotor input vector $\vec{\boldsymbol{u}}$, the generalized body rate vector $\dot{\tilde{\boldsymbol{\Phi}}}$, and the generalized positive vector $\vec{\boldsymbol{\Theta}}$.

Just as the generalized force vector can be normalized, the matrix dynamic equation in (2.65) can be non-dimensionalized as:

$$\hat{\tilde{\boldsymbol{M}}}\ddot{\hat{\tilde{\boldsymbol{\Phi}}}} + \hat{\tilde{\boldsymbol{C}}}(\dot{\hat{\tilde{\boldsymbol{\Phi}}}})\dot{\hat{\tilde{\boldsymbol{\Phi}}}} = \hat{\tilde{\boldsymbol{\tau}}}(\hat{\vec{\boldsymbol{\Theta}}}, \dot{\hat{\tilde{\boldsymbol{\Phi}}}}, \vec{\boldsymbol{u}}) \tag{2.72}$$

The normalized mass-inertial matrix $\hat{\hat{\boldsymbol{M}}}$ is defined as:

$$\hat{\hat{\boldsymbol{M}}} = \begin{bmatrix} \hat{m}_b & 0 & 0 & 0 & 0 & 0 \\ 0 & \hat{m}_b & 0 & 0 & 0 & 0 \\ 0 & 0 & \hat{m}_b & 0 & 0 & 0 \\ 0 & 0 & 0 & \hat{I}_{xx_\mathrm{b}} & 0 & -\hat{I}_{xz_\mathrm{b}} \\ 0 & 0 & 0 & 0 & \hat{I}_{yy_\mathrm{b}} & 0 \\ 0 & 0 & 0 & -\hat{I}_{xz_\mathrm{b}} & 0 & -\hat{I}_{zz_\mathrm{b}} \end{bmatrix} \tag{2.73}$$

where the normalized helicopter mass $\hat{m}_b$ is defined in (2.22) and the normalized moment and product of inertia are defined as:

$$\hat{I}_{xx_\mathrm{b}} = \frac{I_{xx_\mathrm{b}}}{\rho A_{\mathrm{disc}} R^3} \qquad \hat{I}_{yy_\mathrm{b}} = \frac{I_{yy_\mathrm{b}}}{\rho A_{\mathrm{disc}} R^3} \qquad \hat{I}_{zz_\mathrm{b}} = \frac{I_{zz_\mathrm{b}}}{\rho A_{\mathrm{disc}} R^3} \qquad \hat{I}_{xz_\mathrm{b}} = \frac{I_{xz_\mathrm{b}}}{\rho A_{\mathrm{disc}} R^3} \tag{2.74}$$

The normalized generalized position and body rate vectors are defined as:

$$\hat{\vec{\boldsymbol{\Theta}}} = \begin{bmatrix} \frac{x}{R} \\ \frac{y}{R} \\ \frac{z}{R} \\ \phi \\ \theta \\ \psi \end{bmatrix} \qquad \dot{\hat{\vec{\boldsymbol{\Phi}}}} = \begin{bmatrix} \frac{u}{\Omega R} \\ \frac{v}{\Omega R} \\ \frac{w}{\Omega R} \\ \frac{p}{\Omega} \\ \frac{q}{\Omega} \\ \frac{r}{\Omega} \end{bmatrix} \tag{2.75}$$

Finally, the normalized $\hat{\hat{\boldsymbol{C}}}(\dot{\hat{\vec{\boldsymbol{\Phi}}}})$ matrix is given by:

$$\hat{\hat{\boldsymbol{C}}}(\dot{\hat{\vec{\boldsymbol{\Phi}}}}) = \begin{bmatrix} \hat{m}_b \hat{\boldsymbol{S}}(\hat{\vec{\boldsymbol{\omega}}}_b) & \boldsymbol{0}_{3\times 3} \\ \boldsymbol{0}_{3\times 3} & \hat{\boldsymbol{S}}(\hat{\vec{\boldsymbol{\omega}}}_b)\hat{\boldsymbol{I}}_\mathrm{b} \end{bmatrix} \tag{2.76}$$

2.2 Platform Description

The Helicopter Test Platform used in this research consists of a small helicopter powered by an electric motor and a 6 Degree-Of-Freedom (DOF) linkage platform. The helicopter is mounted at the end of the 6 DOF platform, shown in Figure 2.5. The motion of the helicopter is constrained

to the workspace of the platform linkage. This arrangement allows the helicopter to be operated safely indoors.

Figure 2.5: Helicopter Test Platform

The airframe of the helicopter used on the platform is a Kyosho Concept 30 SE model R-C (Remote-Controlled) helicopter. It is refitted so that it can be attached to the test platform. A simplified diagram of the test platform (with the helicopter body mounted at the end of the platform) is shown in Figure 2.6. The whole platform can be divided into five rigid bodies: the base rod (Body 1), the bottom boom (Body 2), the main boom (Body 3), the vertical bar (Body 4) and the helicopter body (Body 5). The four linkages form a parallelogram in the vertical plane. As the main and bottom boom rotates about the Elbow joint up and down in the vertical plane, the orientation of the vertical bar does not change and remains parallel to the vertical axis. The platform linkage parallelogram rotates about the base rod for horizontal movements.

The joints on the platform are not actuated. This means the motion of the platform is driven

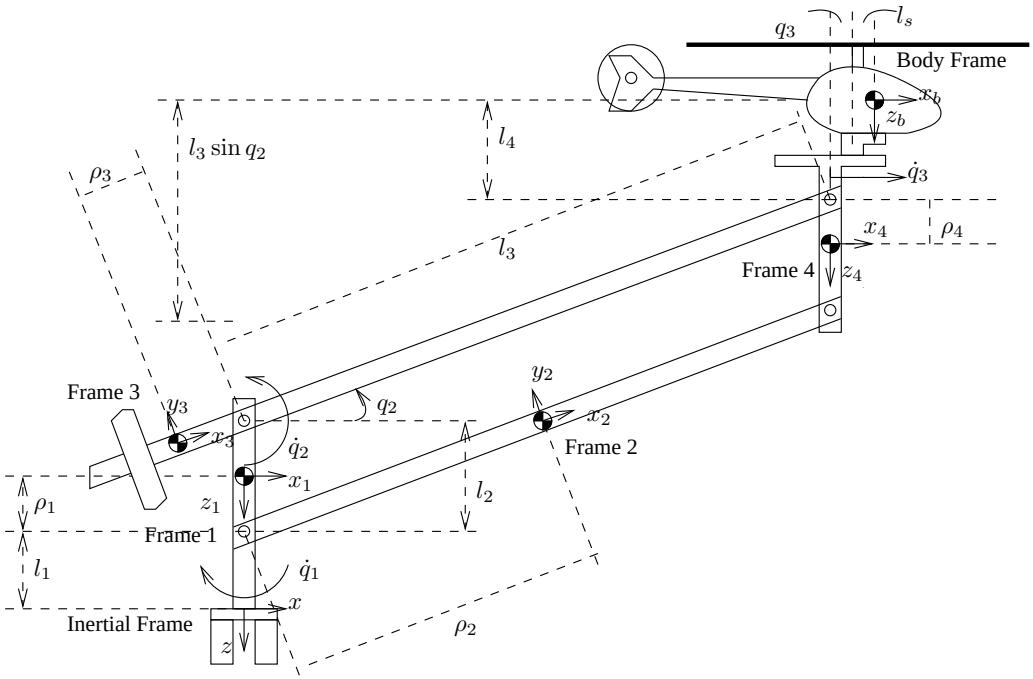

Figure 2.6: Helicopter Test Platform Diagram

through gravitational force and the rotors on the helicopter. A counter weight can be attached to the main boom for gravity balance. Since the counter weight is rigidly attached to the main boom, it is combined with the main boom into a single rigid body and is collectively referred to as the main boom. The centre of gravity of each body is marked in Figure 2.6. They are estimated based on the geometry of the platform.

The 6 DOF helicopter motion is parameterized through six joint variables on the platform linkages. The six joints are designated as the base (Joint 1), the elbow (Joint 2), the rail/slider (Joint 3), the yaw (Joint 4), the pitch (Joint 5) and the roll (Joint 6). All of the joints, except Joint 3, are revolute joints. Joint 3 is a prismatic joint [40]. The range of motion for each of the joints is adjustable, allowing testing of individual joints separately or in combination. Potentiometers are attached to the joints to measure the joint variables.

The upper three joints (the yaw, pitch and roll joints) form a spherical joint. These three joint variables are the Euler angles [41] describing the orientation (attitude) of the helicopter body with respect to the platform. The Cartesian position of the helicopter body is described through the lower three joints (the base, elbow and slider joints). The parallel linkage arrangement of

the lower three joints is similar to a typical spherical manipulator configuration [40] with one exception. The orientation of the slider joint (Joint 3) is constrained along the horizontal plane instead of rotating with the previous revolute joint (Joint 2). This results in a slightly modified workspace within which the helicopter can operate. This modified workspace is illustrated in Figure 2.7.

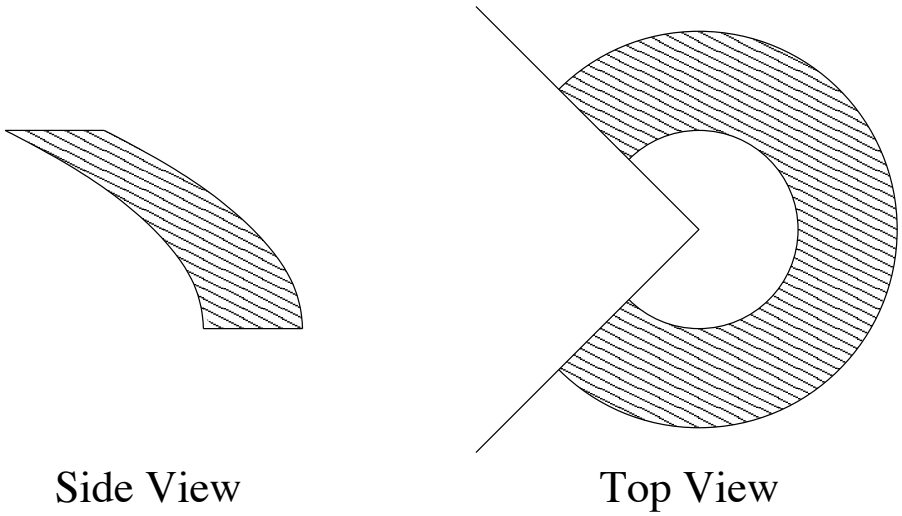

Figure 2.7: Helicopter Platform Workspace

From the geometry of the platform workspace, it can be seen that one set of singular points for the platform is defined as when the elbow joint q_2 is pointing vertically up or down ($q_2 = \pm\pi/2$). Furthermore, through the use of the Euler angles (q_4, q_5 and q_6) to represent orientation (attitude), another set of singular points is introduced at $q_5 = \pm\pi/2$ [39]. The programmed reference trajectories used for control study in this thesis are designed to avoid these singularities (see Chapter 4).

The motion of the helicopter is controlled through four Futaba FP-S148 digital servo motors, which adjust the blade pitch of both the main and tail rotors. Three of the four servo motors control the collective, longitudinal cyclic and lateral cyclic pitch of the main rotor blades; while the last servo motor controls the collective pitch of the tail rotor blades.

2.3 Platform Model

The platform system can be viewed as a multibody system actuated by the helicopter rotor force and moment. A selection of techniques such as the Newton-Euler method, the Euler-Lagrange method [39] and the Principle of Virtual Power [38] can be used for model derivation of multibody systems. Although the Principle of Virtual Power is presented in the subsequent model derivation, the Euler-Lagrange method has also been applied to obtain the same model for verification. The Principle of Virtual Power is selected for the convenience in obtaining the Jacobian matrix from the projection relationships between the helicopter body velocities and the generalized joint rates. Notice that for the Platform system, the constraints are purely geometric (holonomic) with no velocity dependence. This means the Principle of Virtual Power is equivalent to the Principle of Virtual Work when applying to the Platform system [38, 39].

For a n-link rigid body, given the mass m_i, the velocity of the centre of gravity $\vec{\boldsymbol{v}}_i$, the angular momentum $\vec{\boldsymbol{H}}_i$ about the centre of gravity, the active force $\vec{\boldsymbol{F}}_i^a$ and moment $\vec{\boldsymbol{M}}_i^a$ acting on each link, the statement of the Principle of Virtual Power for the k^{th} generalized coordinate can be expressed as [38]:

$$\sum_{i=1}^{n}\left(m_i\dot{\vec{\boldsymbol{v}}}_i - \vec{\boldsymbol{F}}_i^a\right)\cdot\vec{\boldsymbol{\beta}}_{ik} + \sum_{i=1}^{n}\left(\dot{\vec{\boldsymbol{H}}}_i - \vec{\boldsymbol{M}}_i^a\right)\cdot\vec{\boldsymbol{\gamma}}_{ik} = 0 \tag{2.77}$$

The rate projection vectors $\vec{\boldsymbol{\beta}}_{ik}$ and $\vec{\boldsymbol{\gamma}}_{ik}$ associated with the linear velocity $\vec{\boldsymbol{v}}_i$ and the angular velocity $\vec{\boldsymbol{\omega}}_i$ respectively are defined as:

$$\vec{\boldsymbol{\beta}}_{ik} = \frac{\partial\vec{\boldsymbol{v}}_i}{\partial\dot{q}_k} \qquad\qquad \vec{\boldsymbol{\gamma}}_{ik} = \frac{\partial\vec{\boldsymbol{\omega}}_i}{\partial\dot{q}_k} \tag{2.78}$$

Equation (2.77) states that the sum of both the linear and angular dynamic components projected to the k^{th} generalized coordinate through $\vec{\boldsymbol{\beta}}_{ik}$ and $\vec{\boldsymbol{\gamma}}_{ik}$ is equal to zero. In other words, the power associated with the constraint forces is zero [38].

For the helicopter platform, it is useful to rearrange (2.77) to separate out the force and moment terms from the acceleration and angular momentum terms:

$$\sum_{i=1}^{n} m_i\dot{\vec{\boldsymbol{v}}}_i\cdot\vec{\boldsymbol{\beta}}_{ik} + \sum_{i=1}^{n}\dot{\vec{\boldsymbol{H}}}_i\cdot\vec{\boldsymbol{\gamma}}_{ik} = \sum_{i=1}^{n}\vec{\boldsymbol{F}}_i^a\cdot\vec{\boldsymbol{\beta}}_{ik} + \sum_{i=1}^{n}\vec{\boldsymbol{M}}_i^a\cdot\vec{\boldsymbol{\gamma}}_{ik} \tag{2.79}$$

This represents the familiar Newton-Euler formulation projected onto the k^{th} generalized coordinate.

In the case of the test platform, the generalized coordinates are the joint variables q_k, with k going from Joint 1 (the base joint) to Joint 6 (the roll joint). The joint state vector $\bar{\boldsymbol{q}}$ is then defined as:

$$\bar{\boldsymbol{q}} = \begin{bmatrix} q_1 & q_2 & q_3 & q_4 & q_5 & q_6 \end{bmatrix}^T \tag{2.80}$$

where the *over-bar* ($\bar{}$) is used to denote quantities expressed in terms of the generalized joint space variables. The equations of motion for all six of the generalized coordinate in the platform system can be collected together into a matrix equation form:

$$\sum_{i=1}^{n} \left(\begin{bmatrix} \vec{\boldsymbol{\beta}}_{i1}^T & \vec{\boldsymbol{\gamma}}_{i1}^T \\ \vdots & \vdots \\ \vec{\boldsymbol{\beta}}_{i6}^T & \vec{\boldsymbol{\gamma}}_{i6}^T \end{bmatrix} \begin{bmatrix} m_i \dot{\vec{\boldsymbol{v}}}_i \\ \dot{\vec{\boldsymbol{H}}}_i \end{bmatrix} \right) = \sum_{i=1}^{n} \left(\begin{bmatrix} \vec{\boldsymbol{\beta}}_{i1}^T & \vec{\boldsymbol{\gamma}}_{i1}^T \\ \vdots & \vdots \\ \vec{\boldsymbol{\beta}}_{i6}^T & \vec{\boldsymbol{\gamma}}_{i6}^T \end{bmatrix} \begin{bmatrix} \vec{\boldsymbol{F}}_i^a \\ \vec{\boldsymbol{M}}_i^a \end{bmatrix} \right) \tag{2.81}$$

There are six reference frames defined in Figure 2.6. The inertial frame (Frame 0) is fixed in space, defined with the z axis as the vertical axis, positive pointing downward. Frame 1 is attached rigidly to the centre of gravity of the base rod (Joint 1) and thus rotates with it through q_1. Similarly, Frame 2 is attached to the bottom boom, Frame 3 to the main boom, Frame 4 to the vertical bar and finally, the Body Frame is attached to the helicopter body. From these frame definitions, the base joint, q_1, rotates about the vertical z axis of the inertial frame. The elbow joint, q_2, rotates both the main and bottom boom about the z_2 axis of Frame 2 (or Frame 3, these two frames has the same orientation by virtue of the parallel link structure). It is positive when the rotation brings the helicopter up (higher). The slider joint, q_3, is a linear joint constrained by the parallelogram configuration of the platform along the horizontal x_4 axis of Frame 4 (or Frame 1, which has the same orientation as Frame 4). It is positive when the helicopter body moves away from the base rod (outward direction). The rotation from Frame 4 (or Frame 1) to the helicopter Body Frame consists of a series of three current axis rotations [40]. First, the yaw joint, q_4, rotates about the vertical z_4 axis of Frame 4. It is then followed by the pitch joint rotation q_5 about the y axis of the resulting frame. Finally, the roll joint, q_6, rotates about the x axis of the resulting frame. The platform system Body Frame is defined to be consistent with the body-fixed frame defined for the UAV case. The mappings between the

UAV Euler angles and the platform joint angles are:

$$\phi = q_6 \qquad \theta = q_5 \qquad \psi = q_1 + q_4 \tag{2.82}$$

Rotation matrices are used to represent these frame rotations [40]. For example, the rotation matrix for the rotation between the inertial frame and Frame 1 is given by (see Appendix A for details):

$$\boldsymbol{R}_0^1 = \begin{bmatrix} C_{q_1} & -S_{q_1} & 0 \\ S_{q_1} & C_{q_1} & 0 \\ 0 & 0 & 1 \end{bmatrix} \tag{2.83}$$

where the short forms for the sine and cosine of the joint angles have been used:

$$S_{q_k} = \sin q_k \qquad C_{q_k} = \cos q_k \qquad k = 1, \ldots, 6 \tag{2.84}$$

The rotation matrices between the inertial frame and the rest of the frames are derived in Appendix A.3.

2.3.1 Kinematics

Position Vector

Given the rotation matrices and the geometry of the platform linkages (See Figure 2.6), the position vectors for the centre of gravity of each of the five rigid bodies can be expressed with respect to the inertial frame in terms of the joint variables. Let $\vec{\boldsymbol{r}}_i$ be the position vectors of the i^{th} rigid body with respect to the platform base (origin of the inertial frame). The position vectors for the five rigid bodies (the four platform linkages and the helicopter body) expressed

in the inertial frame are given as:

$$\vec{\boldsymbol{r}}_1 = \begin{bmatrix} 0 \\ 0 \\ -(l_1+\rho_1) \end{bmatrix} \qquad \vec{\boldsymbol{r}}_2 = \begin{bmatrix} 0 \\ 0 \\ -l_1 \end{bmatrix} + \boldsymbol{R}_0^2 \begin{bmatrix} \rho_2 \\ 0 \\ 0 \end{bmatrix} \qquad \vec{\boldsymbol{r}}_3 = \begin{bmatrix} 0 \\ 0 \\ -(l_1+l_2) \end{bmatrix} + \boldsymbol{R}_0^3 \begin{bmatrix} -\rho_3 \\ 0 \\ 0 \end{bmatrix}$$
$$\vec{\boldsymbol{r}}_4 = \begin{bmatrix} 0 \\ 0 \\ -(l_1+\rho_4) \end{bmatrix} + \boldsymbol{R}_0^2 \begin{bmatrix} l_3 \\ 0 \\ 0 \end{bmatrix} \qquad \vec{\boldsymbol{r}}_b = \begin{bmatrix} 0 \\ 0 \\ -(l_1+l_2) \end{bmatrix} + \boldsymbol{R}_0^2 \begin{bmatrix} l_3 \\ 0 \\ 0 \end{bmatrix} + \boldsymbol{R}_0^b \begin{bmatrix} l_s+q_3 \\ 0 \\ -l_4 \end{bmatrix} \tag{2.85}$$

Notice that a subscript b is used for the helicopter rigid body position instead of 5. This is done to highlight the difference between the linkage rigid bodies of the platform and the helicopter rigid body and to be consistent with the UAV case. For indexing purpose, the number of rigid bodies in the system is $n = 5$ and hence $\vec{\boldsymbol{r}}_b$ is taken as $\vec{\boldsymbol{r}}_5$ or $b = 5$. The expanded expressions for the position vectors can be found in Appendix C.1. The rotation matrix $\boldsymbol{R}_0^b$ between the inertial and body-fixed frame is the same as $\boldsymbol{R}_{\text{inertial}}^{\text{body}}$ referenced in (2.68) (see Appendix A for details).

Rate Vectors

The angular velocities $\vec{\boldsymbol{\omega}}_i$ for each rigid body can be obtained by adding up the joint rotations experienced by each body in the appropriate reference frames [39]:

$$\vec{\boldsymbol{\omega}}_1 = \begin{bmatrix} 0 \\ 0 \\ \dot{q}_1 \end{bmatrix} \qquad \vec{\boldsymbol{\omega}}_2 = \begin{bmatrix} 0 \\ 0 \\ \dot{q}_1 \end{bmatrix} + \boldsymbol{R}_0^2 \begin{bmatrix} 0 \\ 0 \\ \dot{q}_2 \end{bmatrix} \qquad \vec{\boldsymbol{\omega}}_3 = \begin{bmatrix} 0 \\ 0 \\ \dot{q}_1 \end{bmatrix} + \boldsymbol{R}_0^3 \begin{bmatrix} 0 \\ 0 \\ \dot{q}_2 \end{bmatrix}$$
$$\vec{\boldsymbol{\omega}}_4 = \begin{bmatrix} 0 \\ 0 \\ \dot{q}_1 \end{bmatrix} \qquad \vec{\boldsymbol{\omega}}_b = \begin{bmatrix} 0 \\ 0 \\ (\dot{q}_1+\dot{q}_4) \end{bmatrix} + \boldsymbol{R}_0^4 \boldsymbol{R}_{z,q_4} \left(\begin{bmatrix} 0 \\ \dot{q}_5 \\ 0 \end{bmatrix} + \boldsymbol{R}_{y,q_5} \begin{bmatrix} \dot{q}_6 \\ 0 \\ 0 \end{bmatrix} \right) \tag{2.86}$$

where $\boldsymbol{R}_{z,q_4}$ and $\boldsymbol{R}_{y,q_5}$ are the rotation matrices defined in Appendix A about the z and y axis respectively. The rate of change of the joint variables with respect to time is denoted as $\dot{q}_k = \frac{dq_k}{dt}$. The angular velocities in (2.86) are expressed in the inertial frame. For the derivation of the dynamic equations of the platform, it is convenient to transform the angular velocities into the

respective local frames attached to the rigid bodies:

$$\vec{\omega}_{l_1} = \boldsymbol{R}_1^0\vec{\omega}_1 \qquad \vec{\omega}_{l_2} = \boldsymbol{R}_2^0\vec{\omega}_2 \qquad \vec{\omega}_{l_3} = \boldsymbol{R}_3^0\vec{\omega}_3 \qquad \vec{\omega}_{l_4} = \boldsymbol{R}_4^0\vec{\omega}_4 \qquad \vec{\omega}_{l_b} = \boldsymbol{R}_b^0\vec{\omega}_b \tag{2.87}$$

where $\boldsymbol{R}_b^0 = (\boldsymbol{R}_0^b)^T$ and $\boldsymbol{R}_0^b$ is defined in Appendix A.3.3. The expanded expressions for the angular velocities can be found in Appendix C.2.2. Since the local frame for the helicopter rigid body refers to the body-fixed frame, the angular velocity $\vec{\boldsymbol{\omega}}_{l_b}$ defined here is the same as $\tilde{\boldsymbol{\omega}}_b$ defined in (2.32) for the UAV model.

Next, the rigid body velocities $\vec{\boldsymbol{v}}_i$ are obtained by taking the time derivative of the position vectors:

$$\begin{aligned}
\vec{\boldsymbol{v}}_1 &= \begin{bmatrix} 0 \\ 0 \\ 0 \end{bmatrix} \qquad \vec{\boldsymbol{v}}_2 = \dot{\boldsymbol{R}}_0^2 \begin{bmatrix} \rho_2 \\ 0 \\ 0 \end{bmatrix} \qquad \vec{\boldsymbol{v}}_3 = \dot{\boldsymbol{R}}_0^3 \begin{bmatrix} \rho_3 \\ 0 \\ 0 \end{bmatrix} \\
\vec{\boldsymbol{v}}_4 &= \dot{\boldsymbol{R}}_0^2 \begin{bmatrix} l_3 \\ 0 \\ 0 \end{bmatrix} \qquad \vec{\boldsymbol{v}}_b = \dot{\boldsymbol{R}}_0^2 \begin{bmatrix} l_3 \\ 0 \\ 0 \end{bmatrix} + \dot{\boldsymbol{R}}_0^b \begin{bmatrix} (l_s + q_3) \\ 0 \\ -l_4 \end{bmatrix} + \boldsymbol{R}_0^b \begin{bmatrix} \dot{q}_3 \\ 0 \\ 0 \end{bmatrix}
\end{aligned} \tag{2.88}$$

Similar to the angular velocities, the linear velocities can be expressed with respect to the local frames through transformation:

$$\vec{\boldsymbol{v}}_{l_1} = \begin{bmatrix} 0 \\ 0 \\ 0 \end{bmatrix} \qquad \vec{\boldsymbol{v}}_{l_2} = \boldsymbol{R}_2^0\vec{\boldsymbol{v}}_2 \qquad \vec{\boldsymbol{v}}_{l_3} = \boldsymbol{R}_3^0\vec{\boldsymbol{v}}_3 \qquad \vec{\boldsymbol{v}}_{l_4} = \boldsymbol{R}_4^0\vec{\boldsymbol{v}}_4 \qquad \vec{\boldsymbol{v}}_{l_b} = \boldsymbol{R}_b^0\vec{\boldsymbol{v}}_b \tag{2.89}$$

Appendix C.2.1 contains the expanded expressions for the linear velocities. Again, the helicopter body velocity $\vec{\boldsymbol{v}}_{l_b}$ expressed in the body-fixed frame is the same as $\tilde{\boldsymbol{v}}_b$ defined in (2.32). Both the angular and linear velocities of the rigid bodies can be expressed in the form $\boldsymbol{J}\dot{\boldsymbol{q}}$ where $\boldsymbol{J}$ is the Jacobian matrix [40] and $\dot{\boldsymbol{q}}$ is the rate of change of the joint state vector defined as:

$$\dot{\boldsymbol{q}} = \begin{bmatrix} \dot{q}_1 & \dot{q}_2 & \dot{q}_3 & \dot{q}_4 & \dot{q}_5 & \dot{q}_6 \end{bmatrix}^T \tag{2.90}$$

Expanding (2.87) with the joint state vector in (2.90) and the Jacobian matrices $\boldsymbol{J}_{\omega_i}$ of the

rigid bodies, the rigid body angular velocities $\vec{\boldsymbol{\omega}}_{l_i}$ with respect to the associated local frames can be written as:

$$\vec{\boldsymbol{\omega}}_{l_1} = \begin{bmatrix} 0 & 0 & 0 & 0 & 0 & 0 \\ 0 & 0 & 0 & 0 & 0 & 0 \\ 1 & 0 & 0 & 0 & 0 & 0 \end{bmatrix} \dot{\tilde{\boldsymbol{q}}} = \boldsymbol{J}_{\omega_1} \dot{\tilde{\boldsymbol{q}}} \qquad \vec{\boldsymbol{\omega}}_{l_4} = \boldsymbol{J}_{\omega_4} \dot{\tilde{\boldsymbol{q}}} = \boldsymbol{J}_{\omega_1} \dot{\tilde{\boldsymbol{q}}}$$

$$\vec{\boldsymbol{\omega}}_{l_2} = \begin{bmatrix} -S_{q_2} & 0 & 0 & 0 & 0 & 0 \\ -C_{q_2} & 0 & 0 & 0 & 0 & 0 \\ 0 & 1 & 0 & 0 & 0 & 0 \end{bmatrix} \dot{\tilde{\boldsymbol{q}}} = \boldsymbol{J}_{\omega_2} \dot{\tilde{\boldsymbol{q}}} \qquad \vec{\boldsymbol{\omega}}_{l_3} = \boldsymbol{J}_{\omega_3} \dot{\tilde{\boldsymbol{q}}} = \boldsymbol{J}_{\omega_2} \dot{\tilde{\boldsymbol{q}}}$$

$$\vec{\boldsymbol{\omega}}_{l_b} = \tilde{\boldsymbol{\omega}}_b = \begin{bmatrix} -S_{q_5} & 0 & 0 & -S_{q_5} & 0 & 1 \\ C_{q_5} S_{q_6} & 0 & 0 & C_{q_5} S_{q_6} & C_{q_6} & 0 \\ C_{q_5} C_{q_6} & 0 & 0 & C_{q_5} C_{q_6} & -S_{q_6} & 0 \end{bmatrix} \dot{\tilde{\boldsymbol{q}}} = \boldsymbol{J}_{\omega_b} \dot{\tilde{\boldsymbol{q}}} \tag{2.91}$$

Correspondingly, for the linear velocities in (2.89), they can be expanded, using the joint state vector in (2.90), as:

$$\vec{\boldsymbol{v}}_{l_2} = \rho_2 \begin{bmatrix} 0 & 0 & 0 & 0 & 0 & 0 \\ 0 & 1 & 0 & 0 & 0 & 0 \\ C_{q_2} & 0 & 0 & 0 & 0 & 0 \end{bmatrix} \dot{\tilde{\boldsymbol{q}}} = \rho_2 \boldsymbol{J}_{v_p} \dot{\tilde{\boldsymbol{q}}} = \boldsymbol{J}_{v_2} \dot{\tilde{\boldsymbol{q}}} \qquad \vec{\boldsymbol{v}}_{l_3} = -\rho_3 \boldsymbol{J}_{v_p} \dot{\tilde{\boldsymbol{q}}} = \boldsymbol{J}_{v_3} \dot{\tilde{\boldsymbol{q}}}$$

$$\vec{\boldsymbol{v}}_{l_4} = l_3 \begin{bmatrix} 0 & -S_{q_2} & 0 & 0 & 0 & 0 \\ C_{q_2} & 0 & 0 & 0 & 0 & 0 \\ 0 & -C_{q_2} & 0 & 0 & 0 & 0 \end{bmatrix} = \boldsymbol{J}_{v_4} \dot{\tilde{\boldsymbol{q}}} \qquad \vec{\boldsymbol{v}}_{l_1} = \begin{bmatrix} 0 \\ 0 \\ 0 \end{bmatrix}$$

$$\vec{\boldsymbol{v}}_{l_b} = \tilde{\boldsymbol{v}}_b = \boldsymbol{R}_b^4 \begin{bmatrix} 0 & -l_3 S_{q_2} & 1 & 0 & 0 & 0 \\ l_{hp} & 0 & 0 & 0 & 0 & 0 \\ 0 & -l_3 C_{q_2} & 0 & 0 & 0 & 0 \end{bmatrix} \dot{\tilde{\boldsymbol{q}}} = \boldsymbol{J}_{v_b} \dot{\tilde{\boldsymbol{q}}} \tag{2.92}$$

where $l_{hp} = (l_s + q_3 + l_3 C_{q_2})$ and $\boldsymbol{R}_b^4$ is the transpose of $\boldsymbol{R}_4^b$, which is the rotation matrix from Frame 4 to the Body Frame of the helicopter. The rotation matrix $\boldsymbol{R}_4^b$ is defined in Appendix A.3.3. Appendix C.3 contains the expanded expressions of the Jacobian matrices.

From the angular and linear velocities defined in (2.91) and (2.92), the rate projection vectors $\vec{\boldsymbol{\beta}}_{ik}$ and $\vec{\boldsymbol{\gamma}}_{ik}$, defined in (2.78), are the k^{th} column of the Jacobian matrices $\boldsymbol{J}_{v_i}$ and $\boldsymbol{J}_{\omega_i}$

respectively:

$$\boldsymbol{J}_{v_i} = \begin{bmatrix} \vec{\boldsymbol{\beta}}_{i1} & \vec{\boldsymbol{\beta}}_{i2} & \vec{\boldsymbol{\beta}}_{i3} & \vec{\boldsymbol{\beta}}_{i4} & \vec{\boldsymbol{\beta}}_{i5} & \vec{\boldsymbol{\beta}}_{i6} \end{bmatrix} \quad \boldsymbol{J}_{\omega_i} = \begin{bmatrix} \vec{\boldsymbol{\gamma}}_{i1} & \vec{\boldsymbol{\gamma}}_{i2} & \vec{\boldsymbol{\gamma}}_{i3} & \vec{\boldsymbol{\gamma}}_{i4} & \vec{\boldsymbol{\gamma}}_{i5} & \vec{\boldsymbol{\gamma}}_{i6} \end{bmatrix} \tag{2.93}$$

For example,

$$\vec{\boldsymbol{\beta}}_{b1} = \begin{bmatrix} l_{hp} S_{q_4} C_{q_5} \\ l_{hp}(S_{q_4} S_{q_5} S_{q_6} + C_{q_4} C_{q_6}) \\ l_{hp}(S_{q_4} S_{q_5} C_{q_6} - C_{q_4} S_{q_6}) \end{bmatrix} \qquad \vec{\boldsymbol{\gamma}}_{b1} = \begin{bmatrix} -S_{q_5} \\ C_{q_5} S_{q_6} \\ C_{q_5} C_{q_6} \end{bmatrix}$$

Notice that by using the linear and angular velocities ($\vec{\boldsymbol{v}}_{l_i}$ and $\vec{\boldsymbol{\omega}}_{l_i}$) expressed with respect to the local frames to define the rate projection vectors ($\vec{\boldsymbol{\beta}}_{ik}$ and $\vec{\boldsymbol{\gamma}}_{ik}$), the dot product in (2.79) will be performed with respect to the local frames as well.

The angular momentum about the centre of gravity of each rigid body $\vec{\boldsymbol{H}}_{l_i}$ is defined as the product between the inertia matrix $\boldsymbol{I}_i$ about the centre of gravity and the angular velocity $\vec{\boldsymbol{\omega}}_{l_i}$ of the rigid body expressed in the locally attached frame [39]:

$$\vec{\boldsymbol{H}}_{l_i} = \boldsymbol{I}_i \vec{\boldsymbol{\omega}}_{l_i}$$

The general form of the inertia matrix is given as:

$$\boldsymbol{I}_i = \begin{bmatrix} I_{xx_{\mathrm{i}}} & -I_{xy_{\mathrm{i}}} & -I_{xz_{\mathrm{i}}} \\ -I_{xy_{\mathrm{i}}} & I_{yy_{\mathrm{i}}} & -I_{yz_{\mathrm{i}}} \\ -I_{xz_{\mathrm{i}}} & -I_{yz_{\mathrm{i}}} & I_{zz_{\mathrm{i}}} \end{bmatrix}$$

Based on symmetry of the rigid bodies, the inertia matrix of each of the rigid bodies can be

simplified to:

$$\boldsymbol{I}_1 = \begin{bmatrix} I_{xx_1} & 0 & 0 \\ 0 & I_{yy_1} & 0 \\ 0 & 0 & I_{zz_1} \end{bmatrix} \quad \boldsymbol{I}_2 = \begin{bmatrix} I_{xx_2} & 0 & 0 \\ 0 & I_{yy_2} & 0 \\ 0 & 0 & I_{zz_2} \end{bmatrix} \quad \boldsymbol{I}_3 = \begin{bmatrix} I_{xx_3} & 0 & 0 \\ 0 & I_{yy_3} & 0 \\ 0 & 0 & I_{zz_3} \end{bmatrix}$$
$$\boldsymbol{I}_4 = \begin{bmatrix} I_{xx_4} & 0 & 0 \\ 0 & I_{yy_4} & 0 \\ 0 & 0 & I_{zz_4} \end{bmatrix} \quad \boldsymbol{I}_b = \begin{bmatrix} I_{xx_b} & 0 & -I_{xz_b} \\ 0 & I_{yy_b} & 0 \\ -I_{xz_b} & 0 & I_{zz_b} \end{bmatrix} \tag{2.94}$$

Acceleration Vectors

The linear acceleration for each of the rigid bodies are computed by taking the time derivative of the linear velocities $\vec{\boldsymbol{a}}_{l_i} = \dot{\vec{\boldsymbol{v}}}_{l_i}$:

$$\begin{aligned} \vec{\boldsymbol{a}}_{l_2} &= \rho_2 \left[\left(\boldsymbol{J}_{v_p} \ddot{\boldsymbol{q}} + \dot{\boldsymbol{J}}_{v_p} \dot{\boldsymbol{q}} \right) + \vec{\boldsymbol{\omega}}_{l_2} \times \boldsymbol{J}_{v_p} \dot{\boldsymbol{q}} \right] & \vec{\boldsymbol{a}}_{l_3} &= -\rho_3 \left[\left(\boldsymbol{J}_{v_p} \ddot{\boldsymbol{q}} + \dot{\boldsymbol{J}}_{v_p} \dot{\boldsymbol{q}} \right) + \vec{\boldsymbol{\omega}}_{l_3} \times \boldsymbol{J}_{v_p} \dot{\boldsymbol{q}} \right] \\ \vec{\boldsymbol{a}}_{l_4} &= \left(\boldsymbol{J}_{v_4} \ddot{\boldsymbol{q}} + \dot{\boldsymbol{J}}_{v_4} \dot{\boldsymbol{q}} \right) + \vec{\boldsymbol{\omega}}_{l_4} \times \boldsymbol{J}_{v_4} \dot{\boldsymbol{q}} & \vec{\boldsymbol{a}}_{l_b} &= \left(\boldsymbol{J}_{v_b} \ddot{\boldsymbol{q}} + \dot{\boldsymbol{J}}_{v_b} \dot{\boldsymbol{q}} \right) + \vec{\boldsymbol{\omega}}_{l_b} \times \boldsymbol{J}_{v_b} \dot{\boldsymbol{q}} \\ \vec{\boldsymbol{a}}_{l_1} &= \begin{bmatrix} 0 & 0 & 0 \end{bmatrix}^T \end{aligned} \tag{2.95}$$

The rate of change of the angular momentum $\dot{\vec{\boldsymbol{H}}}_{l_i}$ is computed by taking the time derivative of the angular momentum:

$$\begin{aligned} \dot{\vec{\boldsymbol{H}}}_{l_2} &= \boldsymbol{I}_2 \left(\boldsymbol{J}_{\omega_2} \ddot{\boldsymbol{q}} + \dot{\boldsymbol{J}}_{\omega_2} \dot{\boldsymbol{q}} \right) + \vec{\boldsymbol{\omega}}_{l_2} \times \boldsymbol{I}_2 \vec{\boldsymbol{\omega}}_{l_2} & \dot{\vec{\boldsymbol{H}}}_{l_1} &= \boldsymbol{I}_1 \boldsymbol{J}_{\omega_1} \ddot{\boldsymbol{q}} \\ \dot{\vec{\boldsymbol{H}}}_{l_3} &= \boldsymbol{I}_3 \left(\boldsymbol{J}_{\omega_3} \ddot{\boldsymbol{q}} + \dot{\boldsymbol{J}}_{\omega_3} \dot{\boldsymbol{q}} \right) + \vec{\boldsymbol{\omega}}_{l_3} \times \boldsymbol{I}_3 \vec{\boldsymbol{\omega}}_{l_3} & \dot{\vec{\boldsymbol{H}}}_{l_4} &= \boldsymbol{I}_4 \boldsymbol{J}_{\omega_4} \ddot{\boldsymbol{q}} \\ \dot{\vec{\boldsymbol{H}}}_{l_b} &= \boldsymbol{I}_b \left(\boldsymbol{J}_{\omega_b} \ddot{\boldsymbol{q}} + \dot{\boldsymbol{J}}_{\omega_b} \dot{\boldsymbol{q}} \right) + \vec{\boldsymbol{\omega}}_{l_b} \times \boldsymbol{I}_b \vec{\boldsymbol{\omega}}_{l_b} \end{aligned} \tag{2.96}$$

where the cross product terms $\vec{\boldsymbol{\omega}}_{l_i} \times \boldsymbol{I}_i \vec{\boldsymbol{\omega}}_{l_i}$ are the result of the angular velocities being expressed with respect to the local moving frames [39].

2.3.2 Force and Moment

The source of the forces and moments acting on the platform rigid bodies are the weight of the linkages and the aerodynamic effects generated by the rotor blades. To simplify the development

of the platform model, a projected generalized force vector $\bar{\boldsymbol{\tau}}$ is defined as:

$$\bar{\boldsymbol{\tau}} = \begin{bmatrix} \tau_1 & \tau_2 & \tau_3 & \tau_4 & \tau_5 & \tau_6 \end{bmatrix}^T \tag{2.97}$$

where each of the projected generalized force τ_k is defined as the projected force and moment terms on the right hand side of (2.79):

$$\tau_k = \sum_{i=1}^{n} \vec{\boldsymbol{F}}_i^a \cdot \vec{\boldsymbol{\beta}}_{ik} + \sum_{i=1}^{n} \vec{\boldsymbol{M}}_i^a \cdot \vec{\boldsymbol{\gamma}}_{ik} \tag{2.98}$$

The gravitational force acting on each of the linkage body on the test platform $\vec{\boldsymbol{F}}_{g_i}$ is simply the product between the link mass m_i and the gravitational acceleration g in the z direction of the inertial frame (downward direction) projected to the respective local frame:

$$\vec{\boldsymbol{F}}_{g_2} = \boldsymbol{R}_2^0 \begin{bmatrix} 0 \\ 0 \\ m_2 g \end{bmatrix} = \begin{bmatrix} -m_2 g S_{q_2} \\ -m_2 g C_{q_2} \\ 0 \end{bmatrix} \qquad \vec{\boldsymbol{F}}_{g_1} = \begin{bmatrix} 0 \\ 0 \\ m_1 g \end{bmatrix}$$

$$\vec{\boldsymbol{F}}_{g_3} = \boldsymbol{R}_3^0 \begin{bmatrix} 0 \\ 0 \\ m_3 g \end{bmatrix} = \begin{bmatrix} -m_3 g S_{q_2} \\ -m_2 g C_{q_2} \\ 0 \end{bmatrix} \qquad \vec{\boldsymbol{F}}_{g_4} = \begin{bmatrix} 0 \\ 0 \\ m_4 g \end{bmatrix}$$

$$\vec{\boldsymbol{F}}_{g_b} = \boldsymbol{R}_b^0 \begin{bmatrix} 0 \\ 0 \\ m_b g \end{bmatrix} = \begin{bmatrix} -m_6 g S_{q_5} \\ m_6 g C_{q_5} S_{q_6} \\ m_6 g C_{q_5} C_{q_6} \end{bmatrix} \tag{2.99}$$

With this, the projection of the gravity component to the generalized joint coordinate ($\bar{\boldsymbol{\tau}}$) becomes:

$$\bar{\boldsymbol{\tau}}_g = \sum_{i=1}^{4} \boldsymbol{J}_{v_i}^T \vec{\boldsymbol{F}}_{g_i} + \boldsymbol{J}_{v_b}^T \vec{\boldsymbol{F}}_{g_b} = \begin{bmatrix} 0 \\ -\left(m_2\rho_2 - m_3\rho_3 + m_4 l_3\right) g C_{q_2} \\ 0 \\ 0 \\ 0 \\ 0 \end{bmatrix} + \begin{bmatrix} 0 \\ -m_b g l_3 C_{q_2} \\ 0 \\ 0 \\ 0 \\ 0 \end{bmatrix} \tag{2.100}$$

where the subscript g denotes the gravity component.

Notice that the gravity component only has a non-zero entry in the component corresponding to that of the elbow joint (q_2). It is also independent of the slider joint variable q_3. This is the result of the modified workspace where the orientation of the slider joint is constrained to the horizontal plane. As such, the elbow joint is the only joint that would move the platform in the vertical direction.

Since none of the joints of the platform is actuated, the aerodynamic effects generated by the two rotors of the helicopter are the remaining active force and moment acting on the platform system. The rotor force and moment effects expressed in the body-fixed frame have be derived in (2.52) – (2.57). The rotor effects acting on the platform system $\bar{\boldsymbol{\tau}}_{\mathrm{R}}$ can be obtained by transforming the body-fixed effects $\tilde{\boldsymbol{\tau}}_{\mathrm{R}}$ to the generalized joint space coordinate through the Jacobian matrix $\boldsymbol{J}_b$ between the joint rates and the body-fixed rates:

$$\bar{\boldsymbol{\tau}}_{\mathrm{R}} = \boldsymbol{J}_{\mathrm{b}}^T \tilde{\boldsymbol{\tau}}_{\mathrm{R}} \tag{2.101}$$

where

$$\boldsymbol{J}_b \triangleq \begin{bmatrix} \boldsymbol{J}_{v_{\mathrm{b}}} \\ \boldsymbol{J}_{\omega_{\mathrm{b}}} \end{bmatrix} \tag{2.102}$$

This mapping is analogous to the mapping of the end-effector force to the joint torque employed in the end-effector force control method for robot manipulators [40].

2.3.3 Dynamic Equations

With the above definitions, the equations of motions for the test platform described by (2.77) can be combined into a matrix form:

$$\bar{\boldsymbol{M}}(\bar{\boldsymbol{q}})\ddot{\bar{\boldsymbol{q}}} + \bar{\boldsymbol{h}}(\bar{\boldsymbol{q}}, \dot{\bar{\boldsymbol{q}}}) = \bar{\boldsymbol{\tau}}(\bar{\boldsymbol{q}}, \dot{\bar{\boldsymbol{q}}}, \vec{\boldsymbol{u}}) \tag{2.103}$$

where $\bar{\boldsymbol{M}}(\bar{\boldsymbol{q}})$ is the mass-inertial matrix, $\bar{\boldsymbol{h}}(\bar{\boldsymbol{q}}, \dot{\bar{\boldsymbol{q}}})$ contains the terms that are due to centrifugal and Coriolis effects [40], and $\vec{\boldsymbol{u}}$ is the helicopter control input vector. Similar to the UAV case, the helicopter input vector consists of the collective θ_0, the lateral cyclic A_1 and the longitudinal cyclic B_1 pitch angles of the main rotor, and the rudder angle θ_{tail} of the tail rotor (the collective

pitch angle of the tail rotor):

$$\vec{\boldsymbol{u}} = \begin{bmatrix} \theta_0 & A_1 & B_1 & \theta_{\text{tail}} \end{bmatrix}^T \tag{2.104}$$

The mass-inertial matrix $\bar{\boldsymbol{M}}(\bar{\boldsymbol{q}})$ is symmetric and has the form:

$$\bar{\boldsymbol{M}}(\bar{\boldsymbol{q}}) = \begin{bmatrix} m_{11} & 0 & 0 & m_{44} & m_{15} & m_{16} \\ 0 & m_{22} & m_{23} & 0 & 0 & 0 \\ 0 & m_{23} & m_{33} & 0 & 0 & 0 \\ m_{44} & 0 & 0 & m_{44} & m_{15} & m_{16} \\ m_{15} & 0 & 0 & m_{15} & m_{55} & m_{56} \\ m_{16} & 0 & 0 & m_{16} & m_{56} & m_{66} \end{bmatrix} \tag{2.105}$$

Appendix D.2 and D.3 contain the expanded expressions for $\bar{\boldsymbol{M}}(\bar{\boldsymbol{q}})$ and $\bar{\boldsymbol{h}}(\bar{\boldsymbol{q}}, \dot{\bar{\boldsymbol{q}}})$ respectively. Contrary to the UAV case, the mass-inertia matrix of the platform system $\bar{\boldsymbol{M}}(\bar{\boldsymbol{q}})$ is not constant and is dependent on the joint space variable vector $\bar{\boldsymbol{q}}$.

The platform model in (2.103) can be normalized similar to the UAV case:

$$\hat{\bar{\boldsymbol{M}}}(\hat{\bar{\boldsymbol{q}}})\ddot{\hat{\bar{\boldsymbol{q}}}} + \hat{\bar{\boldsymbol{h}}}(\hat{\bar{\boldsymbol{q}}}, \dot{\hat{\bar{\boldsymbol{q}}}}) = \hat{\bar{\boldsymbol{\tau}}}(\hat{\bar{\boldsymbol{q}}}, \dot{\hat{\bar{\boldsymbol{q}}}}, \vec{\boldsymbol{u}}) \tag{2.106}$$

The joint variable vector $\bar{\boldsymbol{q}}$ can be normalized according to the type of the joint variables:

$$\hat{\bar{\boldsymbol{q}}} = \begin{bmatrix} q_1 & q_2 & \frac{q_3}{R} & q_4 & q_5 & q_6 \end{bmatrix}^T \tag{2.107}$$

where only the slider joint q_3 has dimensional length unit (m); the rest of the joints have non-dimensional angular unit (rad). The corresponding normalized rate and acceleration joint vector can be obtained as:

$$\begin{aligned} \dot{\hat{\bar{\boldsymbol{q}}}} &= \begin{bmatrix} \frac{q_1}{\Omega} & \frac{q_2}{\Omega} & \frac{q_3}{\Omega R} & \frac{q_4}{\Omega} & \frac{q_5}{\Omega} & \frac{q_6}{\Omega} \end{bmatrix}^T \\ \ddot{\hat{\bar{\boldsymbol{q}}}} &= \begin{bmatrix} \frac{\ddot{q}_1}{\Omega^2} & \frac{\ddot{q}_2}{\Omega^2} & \frac{\ddot{q}_3}{\Omega^2 R} & \frac{\ddot{q}_4}{\Omega^2} & \frac{\ddot{q}_5}{\Omega^2} & \frac{\ddot{q}_6}{\Omega^2} \end{bmatrix}^T \end{aligned} \tag{2.108}$$

Using the mass ($\rho A_{\text{disc}} R$) and inertia ($\rho A_{\text{disc}} R^3$) dimensional factors, the normalized mass-

inertia matrix for the platform system can be defined as:

$$\hat{\bar{\boldsymbol{M}}}(\hat{\bar{\boldsymbol{q}}}) = \begin{bmatrix} \hat{m}_{11} & 0 & 0 & \hat{m}_{44} & \hat{m}_{15} & \hat{m}_{16} \\ 0 & \hat{m}_{22} & \hat{m}_{23} & 0 & 0 & 0 \\ 0 & \hat{m}_{23} & \hat{m}_{33} & 0 & 0 & 0 \\ \hat{m}_{44} & 0 & 0 & \hat{m}_{44} & \hat{m}_{15} & \hat{m}_{16} \\ \hat{m}_{15} & 0 & 0 & \hat{m}_{15} & \hat{m}_{55} & \hat{m}_{56} \\ \hat{m}_{16} & 0 & 0 & \hat{m}_{16} & \hat{m}_{56} & \hat{m}_{66} \end{bmatrix} \tag{2.109}$$

where the normalized mass quantity corresponds to the slider joint q_3:

$$\hat{m}_{33} = \frac{m_{33}}{\rho A_{\text{disc}} R} \tag{2.110}$$

whereas the normalized inertia quantities correspond to the other rotatory joints:

$$\begin{aligned} \hat{m}_{11} &= \frac{m_{11}}{\rho A_{\text{disc}} R^3} & \hat{m}_{22} &= \frac{m_{22}}{\rho A_{\text{disc}} R^3} & \hat{m}_{44} &= \frac{m_{44}}{\rho A_{\text{disc}} R^3} \\ \hat{m}_{55} &= \frac{m_{55}}{\rho A_{\text{disc}} R^3} & \hat{m}_{66} &= \frac{m_{66}}{\rho A_{\text{disc}} R^3} & \hat{m}_{15} &= \frac{m_{15}}{\rho A_{\text{disc}} R^3} \\ \hat{m}_{16} &= \frac{m_{16}}{\rho A_{\text{disc}} R^3} & \hat{m}_{56} &= \frac{m_{56}}{\rho A_{\text{disc}} R^3} \end{aligned} \tag{2.111}$$

and finally, the coupled normalized entries between q_2 and q_3 joints:

$$\hat{m}_{23} = \frac{m_{23}}{\rho A_{\text{disc}} R^2} \tag{2.112}$$

The normalized $\hat{\bar{\boldsymbol{h}}}$ and $\hat{\bar{\boldsymbol{\tau}}}$ can be obtained accordingly by dividing the appropriate dimensional factors.

2.4 Platform and UAV Models Relation

Recall the platform system model in (2.103) has been developed to include the dynamics of both the platform linkage and the helicopter rigid body. In comparison, the UAV model developed in (2.65) consists only of the helicopter rigid body model. This means the UAV model is a special case of the platform model. From these observations, the following theorem is formulated:

Theorem 2.1 *Assuming it is not near its singular points, the platform model defined in* (2.103) *converges to the UAV Model defined in* (2.65) *as the mass and inertia of the platform linkages approach zero.*

Proof: Theorem 2.1

Recall the platform model in (2.103) was derived from the statement of the Principle of Virtual Power. As the mass and inertia of the platform linkage goes to zero, the matrix equation of the Principle of Virtual Power in (2.81) is reduced to:

$$\underbrace{\begin{bmatrix} \tilde{\boldsymbol{\beta}}_{b1}^T & \tilde{\boldsymbol{\gamma}}_{b1}^T \\ \vdots & \vdots \\ \tilde{\boldsymbol{\beta}}_{b6}^T & \tilde{\boldsymbol{\gamma}}_{b6}^T \end{bmatrix}}_{\boldsymbol{J}_b(\bar{\boldsymbol{q}})^T} \begin{bmatrix} m_b \dot{\tilde{\boldsymbol{v}}}_b \\ \dot{\tilde{\boldsymbol{H}}}_b \end{bmatrix} = \underbrace{\begin{bmatrix} \tilde{\boldsymbol{\beta}}_{b1}^T & \tilde{\boldsymbol{\gamma}}_{b1}^T \\ \vdots & \vdots \\ \tilde{\boldsymbol{\beta}}_{b6}^T & \tilde{\boldsymbol{\gamma}}_{b6}^T \end{bmatrix}}_{\boldsymbol{J}_b(\bar{\boldsymbol{q}})^T} \begin{bmatrix} \tilde{\boldsymbol{F}}_b^a \\ \tilde{\boldsymbol{M}}_b^a \end{bmatrix} \tag{2.113}$$

With the assumption that the helicopter is not near its singularity points, this can now be reduced to (2.65) by cancelling out $\boldsymbol{J}_b^T$ and expanding the rate, acceleration, force and moment vectors in the helicopter body fixed (local) frame. ∎

Theorem 2.1 shows that in the limit as the platform mass and inertia vanish, so will their effects on the system dynamics. In such a case, the system behaviour will be identical to that of the UAV model. However, to relate the platform and the UAV models when the platform mass and inertia are non-zero, a mapping between the two models is needed. Since the UAV model is defined with respect to the body fixed frame of the helicopter, while the platform model is defined in terms of the platform joint coordinates, a first step in relating the two cases is to express the platform model in the helicopter body fixed frame. The following Lemma gives a mapping of the platform model from the joint coordinates to the body fixed coordinates:

Lemma 2.1 *Assuming the helicopter platform system is not near its singularity points, a mapping that relates the platform model in* (2.103)*, where it is expressed in terms of the platform*

joint variables, to the one that is expressed in the body fixed frame can be defined as:

$$\begin{aligned}
\tilde{\boldsymbol{M}}(\vec{\boldsymbol{\Theta}}) &= \left[\boldsymbol{J}_b(\vec{\boldsymbol{\Theta}})^{-1}\right]^T \bar{\boldsymbol{M}}(\vec{\boldsymbol{\Theta}})\boldsymbol{J}_b(\vec{\boldsymbol{\Theta}})^{-1} \\
\tilde{\boldsymbol{h}}(\vec{\boldsymbol{\Theta}}, \dot{\vec{\boldsymbol{\Phi}}}) &= \left[\boldsymbol{J}_b(\vec{\boldsymbol{\Theta}})^{-1}\right]^T \bar{\boldsymbol{h}}(\vec{\boldsymbol{\Theta}}, \dot{\vec{\boldsymbol{\Phi}}}) - \tilde{\boldsymbol{M}}(\vec{\boldsymbol{\Theta}})\dot{\boldsymbol{J}}_b(\vec{\boldsymbol{\Theta}})\boldsymbol{J}_b(\vec{\boldsymbol{\Theta}})^{-1}\dot{\vec{\boldsymbol{\Phi}}} \\
\tilde{\boldsymbol{\tau}}(\vec{\boldsymbol{\Theta}}, \dot{\vec{\boldsymbol{\Phi}}}, \vec{\boldsymbol{u}}) &= \left[\boldsymbol{J}_b(\vec{\boldsymbol{\Theta}})^{-1}\right]^T \bar{\boldsymbol{\tau}}(\vec{\boldsymbol{\Theta}}, \dot{\vec{\boldsymbol{\Phi}}}, \vec{\boldsymbol{u}})
\end{aligned} \tag{2.114}$$

such that

$$\tilde{\boldsymbol{M}}(\vec{\boldsymbol{\Theta}})\ddot{\vec{\boldsymbol{\Phi}}} + \tilde{\boldsymbol{h}}(\vec{\boldsymbol{\Theta}}, \dot{\vec{\boldsymbol{\Phi}}}) = \tilde{\boldsymbol{\tau}}(\vec{\boldsymbol{\Theta}}, \dot{\vec{\boldsymbol{\Phi}}}, \vec{\boldsymbol{u}}) \tag{2.115}$$

where $\tilde{\boldsymbol{x}}$ denotes quantities expressed in the helicopter body frame; while $\bar{\boldsymbol{x}}$ denotes quantities expressed with respect to the generalized joint coordinates.

Proof: Lemma 2.1

The mapping between the coordinate vectors $\bar{\boldsymbol{q}}$ and $\vec{\boldsymbol{\Theta}}$ can be obtained in two steps. First, the position and attitude of the helicopter body ($\vec{\boldsymbol{\Theta}}$) is expressed in terms of the joint variables ($\bar{\boldsymbol{q}}$). Then, the desired mapping is obtained by solving for the inverse relationship to express $\bar{\boldsymbol{q}}$ in terms of $\vec{\boldsymbol{\Theta}}$. The helicopter body position is given by expanding the position vector defined in (2.85):

$$\begin{bmatrix} x \\ y \\ z \end{bmatrix} = \begin{bmatrix} (l_s + q_3 + l_3 C_{q_2}) C_{q_1} \\ (l_s + q_3 + l_3 C_{q_2}) S_{q_2} \\ -(l_1 + l_2 + l_4 + l_3 S_{q_2}) \end{bmatrix} \tag{2.116}$$

From the geometry of the platform, the Euler angles of the helicopter body are given as follows.

$$\begin{bmatrix} \phi \\ \theta \\ \psi \end{bmatrix} = \begin{bmatrix} q_6 \\ q_5 \\ q_1 + q_4 \end{bmatrix} \tag{2.117}$$

Assuming the platform is not near its singularity points, the position and attitude equations in (2.116) and (2.117) can be solved together to obtain the following inverse mapping:

$$\bar{\boldsymbol{q}} = \begin{bmatrix} q_1 \\ q_2 \\ q_3 \\ q_4 \\ q_5 \\ q_6 \end{bmatrix} = \begin{bmatrix} \arctan\left(\frac{y}{x}\right) \\ \arcsin\left(-\frac{z+l_1+l_2+l_4}{l_3}\right) \\ \sqrt{x^2+y^2} - l_s - \sqrt{l_3^2 - (z+l_1+l_2+l_4)^2} \\ \psi - \arctan\left(\frac{y}{x}\right) \\ \theta \\ \phi \end{bmatrix} \triangleq \vec{\boldsymbol{f}}(\vec{\boldsymbol{\Theta}}) \tag{2.118}$$

The mapping between the joint rates and the body rates are defined by the inverse Jacobian:

$$\dot{\bar{\boldsymbol{q}}} = \boldsymbol{J}_b^{-1} \dot{\vec{\boldsymbol{\Phi}}} \tag{2.119}$$

The rate of change of the helicopter position and attitude vector $\dot{\vec{\boldsymbol{\Theta}}}$ can be expressed in terms of the body rate vector $\dot{\vec{\boldsymbol{\Phi}}}$ by the following relationship:

$$\dot{\vec{\boldsymbol{\Theta}}} = \begin{bmatrix} \dot{x} \\ \dot{y} \\ \dot{z} \\ \dot{\phi} \\ \dot{\theta} \\ \dot{\psi} \end{bmatrix} = \begin{bmatrix} \boldsymbol{R}_0^b & \boldsymbol{0}_{3\times3} \\ \boldsymbol{0}_{3\times3} & (\boldsymbol{R}_{\text{Euler}})^{-1} \end{bmatrix} \begin{bmatrix} u \\ v \\ w \\ p \\ q \\ r \end{bmatrix} \triangleq \boldsymbol{T}(\vec{\boldsymbol{\Theta}}) \dot{\vec{\boldsymbol{\Phi}}} \tag{2.120}$$

which is derived by transforming the linear velocity in the body frame to the inertial frame through the rotation matrix $\boldsymbol{R}_0^b$ and mapping the angular body rate to the rate of change of the Euler angles through $(\boldsymbol{R}_{\text{Euler}})^{-1}$. The rotation matrix $\boldsymbol{R}_0^b$ and matrix mapping $(\boldsymbol{R}_{\text{Euler}})^{-1}$ can be found in Appendix A.3.3 and Appendix A.1.1 respectively.

The rate of change of the body rate vector $\ddot{\vec{\boldsymbol{\Phi}}}$ can be obtained from the time derivative of the Jacobian relationship:

$$\ddot{\vec{\boldsymbol{\Phi}}} = \dot{\boldsymbol{J}}_b \dot{\bar{\boldsymbol{q}}} + \boldsymbol{J}_b \ddot{\bar{\boldsymbol{q}}} \tag{2.121}$$

Substituting expressions for $\bar{\boldsymbol{q}}$, $\dot{\bar{\boldsymbol{q}}}$ and $\ddot{\bar{\boldsymbol{q}}}$ from (2.118), (2.119), and (2.103), the above expression can be re-arranged into:

$$\bar{\boldsymbol{M}}(\vec{\boldsymbol{\Theta}})\boldsymbol{J}_b(\vec{\boldsymbol{\Theta}})^{-1}\ddot{\vec{\boldsymbol{\Phi}}} + \left[\bar{\boldsymbol{h}}(\vec{\boldsymbol{\Theta}},\dot{\vec{\boldsymbol{\Phi}}}) - \boldsymbol{M}(\vec{\boldsymbol{\Theta}})\boldsymbol{J}_b(\vec{\boldsymbol{\Theta}})^{-1}\dot{\boldsymbol{J}}_b(\vec{\boldsymbol{\Theta}})\boldsymbol{J}_b(\vec{\boldsymbol{\Theta}})^{-1}\dot{\vec{\boldsymbol{\Phi}}}\right] = \bar{\boldsymbol{\tau}}(\vec{\boldsymbol{\Theta}},\dot{\vec{\boldsymbol{\Phi}}},\vec{\boldsymbol{u}}) \tag{2.122}$$

where $\bar{\boldsymbol{M}}(\vec{\boldsymbol{\Theta}})$, $\bar{\boldsymbol{h}}(\vec{\boldsymbol{\Theta}},\dot{\vec{\boldsymbol{\Phi}}})$, and $\bar{\boldsymbol{\tau}}(\vec{\boldsymbol{\Theta}},\dot{\vec{\boldsymbol{\Phi}}},\vec{\boldsymbol{u}})$ are components of the platform model expressed in joint space, with the exception that the joint variables are substituted in terms of the body position, attitude and rates according to (2.118) and (2.119).

Next, the relationship between the generalized force vectors $\bar{\boldsymbol{\tau}}(\vec{\boldsymbol{\Theta}},\dot{\vec{\boldsymbol{\Phi}}},\vec{\boldsymbol{u}})$ and $\tilde{\boldsymbol{\tau}}(\vec{\boldsymbol{\Theta}},\dot{\vec{\boldsymbol{\Phi}}},\vec{\boldsymbol{u}})$ is:

$$\bar{\boldsymbol{\tau}}(\vec{\boldsymbol{\Theta}},\dot{\vec{\boldsymbol{\Phi}}},\vec{\boldsymbol{u}}) = \boldsymbol{J}_b(\vec{\boldsymbol{\Theta}})^T\tilde{\boldsymbol{\tau}}(\vec{\boldsymbol{\Theta}},\dot{\vec{\boldsymbol{\Phi}}},\vec{\boldsymbol{u}}) \tag{2.123}$$

This relationship is obtained by interpreting the generalized force expressed in the body frame as an end-effector force applied to the platform linkage structure. Then through the use of virtual work, the above relationship between $\bar{\boldsymbol{\tau}}(\vec{\boldsymbol{\Theta}},\dot{\vec{\boldsymbol{\Phi}}},\vec{\boldsymbol{u}})$ and $\tilde{\boldsymbol{\tau}}(\vec{\boldsymbol{\Theta}},\dot{\vec{\boldsymbol{\Phi}}},\vec{\boldsymbol{u}})$ is obtained [40].

Finally, substituting (2.123) into (2.122) to get:

$$\begin{aligned}
&\left(\left[\boldsymbol{J}_b(\vec{\boldsymbol{\Theta}})^{-1}\right]^T\bar{\boldsymbol{M}}(\vec{\boldsymbol{\Theta}})\boldsymbol{J}_b(\vec{\boldsymbol{\Theta}})^{-1}\right)\ddot{\vec{\boldsymbol{\Phi}}} \\
&+\ \left[\boldsymbol{J}_b(\vec{\boldsymbol{\Theta}})^{-1}\right]^T\bar{\boldsymbol{h}}(\vec{\boldsymbol{\Theta}},\dot{\vec{\boldsymbol{\Phi}}}) - \left(\left[\boldsymbol{J}_b(\vec{\boldsymbol{\Theta}})^{-1}\right]^T\bar{\boldsymbol{M}}(\vec{\boldsymbol{\Theta}})\boldsymbol{J}_b(\vec{\boldsymbol{\Theta}})^{-1}\right)\dot{\boldsymbol{J}}_b(\vec{\boldsymbol{\Theta}})\boldsymbol{J}_b(\vec{\boldsymbol{\Theta}})^{-1}\dot{\vec{\boldsymbol{\Phi}}} \\
&\quad = \tilde{\boldsymbol{\tau}}(\vec{\boldsymbol{\Theta}},\dot{\vec{\boldsymbol{\Phi}}},\vec{\boldsymbol{u}})
\end{aligned} \tag{2.124}$$

which gives the desired mapping relationship. ∎

Lemma 2.1 provides a mapping to relate the platform model expressed in the joint space and in the body-fixed frame. According to Theorem 2.1, the body components $\tilde{\boldsymbol{M}}(\vec{\boldsymbol{\Theta}})$, $\tilde{\boldsymbol{h}}(\vec{\boldsymbol{\Theta}},\dot{\vec{\boldsymbol{\Phi}}})$, and $\tilde{\boldsymbol{\tau}}(\vec{\boldsymbol{\Theta}},\dot{\vec{\boldsymbol{\Phi}}},\vec{\boldsymbol{u}})$ defined in (2.114) will converge to those of the UAV model defined in (2.65) as the mass and inertia of the platform linkage approaches zero. This represents the scenario where a stand alone helicopter is attached to a *virtual* platform whose linkages have zero mass and inertia. Such interpretation will be used in the development of a control strategy applicable for both the UAV and the platform system. Furthermore, it will be shown that the nonlinear coordinate mapping provides a systematic method to investigate the effect of the platform linkage setup, such as counter balance configuration, on the dynamic behaviour of the platform system and

how it relates to the UAV model.

2.5 Summary

In this chapter, the rigid body model of a stand alone helicopter (UAV model) has been derived with a quasi-steady rotor model that accounts for the effect of the helicopter rigid body dynamics. In addition, the helicopter test platform used in this research has been introduced and its nonlinear 6 DOF model has been derived. Through the derivation of the dynamic models for both the UAV and the platform systems, it is shown that the platform model approaches that of the UAV system as the mass and inertia of the platform linkage are reduced to zero. Furthermore, a nonlinear mapping that transforms the platform model between joint space and body frame coordinate was derived. This allows systematic analysis and comparison between the platform model (derived in joint space) and the UAV model (derived in body frame).

In summary, the contributions presented in this chapter are:

- the nonlinear model for the platform system has been derived
- a systematic mapping between the platform and UAV model has been developed

Chapter 3

Model Analysis

In this chapter, the platform system model derived in Chapter 2 will be examined more closely. In particular, the payload equation derived from the platform system dynamic model defined in (2.103) will be analyzed. The payload equation gives rise to the investigation into the effect of the platform counter weight configuration on the system operating point. Linearization is then applied to both the UAV and the Platform system model around the same operating point for comparisons. Linearization to the Platform system model around the same operating point for the different counter weight configurations is also performed to examine the resulting mode changes in the system dynamics. In total, four Platform configurations are examined: UAV, BALANCED, REDUCED and HANGAR.

3.1 Helicopter Trim

A helicopter is referred to being at *trim* when it is operating in equilibrium (zero acceleration) with fixed (constant) control inputs [12]. Typical trim conditions include hover (zero linear velocity) and constant speed flight. Helicopter dynamic behaviour can vary significantly depending on the the condition under which it is operating, such as whether it is in hover or in forward flight [10, 12]. This makes the operating point a significant factor to consider when performing system analysis. In this thesis, only the hover condition is studied for both the Platform and the UAV systems.

For the UAV system, the hover trim condition is obtained by setting both the rate and

acceleration of the helicopter to zero:

$$\ddot{\tilde{\mathbf{\Phi}}} = \begin{bmatrix} \dot{u} & \dot{v} & \dot{w} & \dot{p} & \dot{q} & \dot{r} \end{bmatrix}^T = \vec{\mathbf{0}}_{6\times 1}, \quad \text{and} \quad \dot{\tilde{\mathbf{\Phi}}} = \begin{bmatrix} u & v & w & p & q & r \end{bmatrix}^T = \vec{\mathbf{0}}_{6\times 1}, \tag{3.1}$$

where u, v, and w are the linear and p, q, and r are the angular velocities of the helicopter, expressed with respect to the body-fixed frame. When applying the hover trim condition to the dynamic model of the UAV system in (2.65),

$$\tilde{\boldsymbol{M}}\ddot{\tilde{\mathbf{\Phi}}} + \tilde{\boldsymbol{h}}(\dot{\tilde{\mathbf{\Phi}}}) = \tilde{\boldsymbol{\tau}}(\vec{\mathbf{\Theta}}, \dot{\tilde{\mathbf{\Phi}}}, \vec{\boldsymbol{u}}), \tag{2.65}$$

the trim equations can be obtained as

$$\tilde{\boldsymbol{\tau}}_{\mathrm{e}}(\vec{\mathbf{\Theta}}_{\mathrm{e}}, \vec{\mathbf{0}}_{6\times 1}, \vec{\boldsymbol{u}}_{\mathrm{e}}) = \vec{\mathbf{0}}_{6\times 1}, \tag{3.2}$$

where $\tilde{\boldsymbol{\tau}}_{\mathrm{e}}$ is the generalized body force of the helicopter at trim (which is, by definition, equal to zero in equilibrium); $\vec{\mathbf{\Theta}}_{\mathrm{e}}$ is the position and attitude (orientation) of the helicopter at trim; and $\vec{\boldsymbol{u}}_{\mathrm{e}}$ is the rotor trim control inputs. Obtaining the hover trim conditions for the helicopter therefore involves solving the six equations represented in (3.2) for the six position and attitude variables in $\vec{\mathbf{\Theta}}_{\mathrm{e}}$ and the four rotor control input variables in $\vec{\boldsymbol{u}}_{\mathrm{e}}$:

$$\vec{\mathbf{\Theta}}_{\mathrm{e}} = \begin{bmatrix} x_{\mathrm{e}} & y_{\mathrm{e}} & z_{\mathrm{e}} & \phi_{\mathrm{e}} & \theta_{\mathrm{e}} & \psi_{\mathrm{e}} \end{bmatrix}^T, \qquad \text{and} \qquad \vec{\boldsymbol{u}}_{\mathrm{e}} = \begin{bmatrix} \theta_{0_{\mathrm{e}}} & A_{1_{\mathrm{e}}} & B_{1_{\mathrm{e}}} & \theta_{tail_{\mathrm{e}}} \end{bmatrix}^T.$$

In general, to obtain the solution to the six hover trim equations, four out of the ten unknowns are set arbitrarily. Upon examination of the trim equations in (3.2), the trim condition is independent of the position (x, y, and z) and heading (ψ) of the helicopter. This is intuitive since a helicopter is capable of hovering at arbitrary position and heading. As such, the hover trim condition for the UAV helicopter is defined by the four rotor control inputs ($\theta_{0_{\mathrm{e}}}$, $A_{1_{\mathrm{e}}}$, $B_{1_{\mathrm{e}}}$, and $\theta_{tail_{\mathrm{e}}}$), together with the roll (ϕ_{e}) and pitch (θ_{e}) angles of the helicopter rigid body.

Mapping the UAV hover trim conditions in (3.1) to that of the Platform system yields:

$$\ddot{\boldsymbol{q}} = \begin{bmatrix} \ddot{q}_1 & \ddot{q}_2 & \ddot{q}_3 & \ddot{q}_4 & \ddot{q}_5 & \ddot{q}_6 \end{bmatrix}^T = \vec{\mathbf{0}}_{6\times 1}, \quad \text{and} \quad \dot{\boldsymbol{q}} = \begin{bmatrix} \dot{q}_1 & \dot{q}_2 & \dot{q}_3 & \dot{q}_4 & \dot{q}_5 & \dot{q}_6 \end{bmatrix}^T = \vec{\mathbf{0}}_{6\times 1}. \tag{3.3}$$

Applying this hover trim condition to the corresponding dynamic model for the Platform system derived in (2.103)

$$\bar{\boldsymbol{M}}(\bar{\boldsymbol{q}})\ddot{\bar{\boldsymbol{q}}} + \bar{\boldsymbol{h}}(\bar{\boldsymbol{q}}, \dot{\bar{\boldsymbol{q}}}) = \bar{\boldsymbol{\tau}}(\bar{\boldsymbol{q}}, \dot{\bar{\boldsymbol{q}}}, \vec{\boldsymbol{u}}) \tag{2.103}$$

would result in

$$\bar{\boldsymbol{\tau}}(\bar{\boldsymbol{q}}_{\mathrm{e}}, \vec{\mathbf{0}}_{6\times 1}, \vec{\boldsymbol{u}}_{\mathrm{e}}) = \vec{\mathbf{0}}_{6\times 1}. \tag{3.4}$$

Similar to the UAV case, there are six equations with ten unknowns (six joint variables and four inputs) to solve for. In this case, the position and heading of the helicopter rigid body are represented by the lower four joints (q_1 to q_4). At first glance, the trim solution to (3.4) would be dependent on these lower joint variables. In particular, the weight effect of the platform linkage has a direct consequence on the gravity vector through the elbow joint q_2, as illustrated in (2.100). When the platform hover condition in (3.4) is expanded and re-arranged in terms of the gravity and rotor components

$$\begin{bmatrix} 0 \\ \left[\hat{m}_2\hat{\rho}_2 - \hat{m}_3\hat{\rho}_3 + (\hat{m}_4 + \hat{m}_b)\hat{l}_3\right]\hat{g}\cos(\hat{q}_2) \\ 0 \\ 0 \\ 0 \\ 0 \end{bmatrix} = \boldsymbol{J}_{\mathrm{b}}(\bar{\boldsymbol{q}})^T \begin{bmatrix} \hat{\hat{\boldsymbol{X}}}_{\mathrm{R}} \\ \hat{\hat{\boldsymbol{Y}}}_{\mathrm{R}} \\ \hat{\hat{\boldsymbol{Z}}}_{\mathrm{R}} \\ \hat{\hat{\boldsymbol{L}}}_{\mathrm{R}} \\ \hat{\hat{\boldsymbol{M}}}_{\mathrm{R}} \\ \hat{\hat{\boldsymbol{N}}}_{\mathrm{R}} \end{bmatrix}, \tag{3.5}$$

the component corresponding to the elbow joint q_2 is the only non-zero element in the gravity vector. This term represent the effective weight experienced by the helicopter rotors due to the combined weight of the platform linkages and the helicopter body. Defining the non-dimensional *apparent payload* $\hat{W}_p$ as

$$\hat{W}_p \triangleq \left[\hat{m}_2\hat{\rho}_2 - \hat{m}_3\hat{\rho}_3 + (\hat{m}_4 + \hat{m}_b)\hat{l}_3\right]\frac{\hat{g}}{\hat{l}_3}. \tag{3.6}$$

When the trim equation in (3.5) is projected to the body-fixed frame through the Jacobian

$\boldsymbol{J}_b(\bar{\boldsymbol{q}})^T$, it can be expressed in terms of the apparent payload $\hat{W}_p$ as

$$\hat{W}_p \begin{bmatrix} -\sin(q_5) \\ \cos(q_5)\sin(q_6) \\ \cos(q_5)\cos(q_6) \\ 0 \\ 0 \\ 0 \end{bmatrix} = \begin{bmatrix} \hat{\hat{\boldsymbol{X}}}_{\mathrm{R}} \\ \hat{\hat{\boldsymbol{Y}}}_{\mathrm{R}} \\ \hat{\hat{\boldsymbol{Z}}}_{\mathrm{R}} \\ \hat{\hat{\boldsymbol{L}}}_{\mathrm{R}} \\ \hat{\hat{\boldsymbol{M}}}_{\mathrm{R}} \\ \hat{\hat{\boldsymbol{N}}}_{\mathrm{R}} \end{bmatrix}, \tag{3.7}$$

where simplification has been applied assuming the Platform system is not operating near its singular points.

The generalized rotor forces represented on the right hand side of (3.7) are defined in (2.52)–(2.57) and are independent of the platform parameters. Recall the trim condition is defined by the trim inputs ($\vec{\boldsymbol{u}}$) and the roll (ϕ or q_6) and the pitch (θ or q_5) angles of the helicopter. This means that the platform effect on the trim condition can be summarized into a single term in the apparent payload $\hat{W}_p$. Since the apparent payload is also independent of the lower joint variables (q_1 to q_4), other than the restriction of not being near any of the singularities, the trim condition is also independent of the position and attitude of the helicopter, just as in the UAV case. Furthermore, for a fixed set of helicopter parameters, only the apparent payload defines the trim condition. In other words, *different platform configurations (such as moving the counter weight location or using a different counter weight for balancing) would operate at the same trim provided their apparent payload $\hat{W}_p$ are equal.* Such scenarios will be explored in more details in the subsequent sections.

3.2 Payload Equation

One of the consequences of being able to define the trim condition with the apparent payload $\hat{W}_p$ is that it gives rise to the possibility of setting up different configurations of the platform system to operate at the same trim. This allows direct comparison of the effects on the system behaviour of various parameters (such as the location of the counter weight). More importantly, it enables the potential to match the operating point of the platform system to any target UAV systems, allowing comparison as well as potential derivation of equivalence conditions.

From the result of Lemma 2.1, the UAV system model can be defined in terms of the joint space variables q_i as

$$\bar{\boldsymbol{M}}_{\mathrm{U}}(\bar{\boldsymbol{q}})\ddot{\bar{\boldsymbol{q}}} + \bar{\boldsymbol{h}}_{\mathrm{U}}(\bar{\boldsymbol{q}}, \dot{\bar{\boldsymbol{q}}}) = \bar{\boldsymbol{\tau}}_{\mathrm{U}}(\bar{\boldsymbol{q}}, \dot{\bar{\boldsymbol{q}}}, \vec{\boldsymbol{u}}), \tag{3.8}$$

where the subscript U denotes the model for the UAV system. This model is expressed in terms of the joint space coordinates $\bar{\boldsymbol{q}}$ and represents a target UAV system mounted on a *virtual* platform (which has mass-less links). As the only difference between the system in (3.8) and the one in (2.65) is the nonlinear coordinate mapping presented in Lemma 2.1, the two systems will be used interchangeably hereinafter.

In non-dimensional form, the UAV system can be expressed as

$$\hat{\bar{\boldsymbol{M}}}_{\mathrm{U}}(\bar{\boldsymbol{q}})\ddot{\bar{\boldsymbol{q}}} + \hat{\bar{\boldsymbol{h}}}_{\mathrm{U}}(\bar{\boldsymbol{q}}, \dot{\bar{\boldsymbol{q}}}) = \hat{\bar{\boldsymbol{\tau}}}_{\mathrm{U}}(\bar{\boldsymbol{q}}, \dot{\bar{\boldsymbol{q}}}, \vec{\boldsymbol{u}}). \tag{3.9}$$

The apparent payload of this UAV system is just the weight of the helicopter body

$$\hat{W}_p = \hat{m}_b \hat{g}. \tag{3.10}$$

To match the operating point of the target UAV system to that of a platform system, where the target UAV helicopter is mounted on real linkages, the two apparent payload expressions are equated to form

$$\hat{m}_b \hat{g} = \left[\hat{m}_2 \hat{\rho}_2 - \hat{m}_3 \hat{\rho}_3 + (\hat{m}_4 + \hat{m}_b)\hat{l}_3\right] \frac{\hat{g}}{\hat{l}_3}, \tag{3.11}$$

which can be simplified as

$$\hat{m}_3 \hat{\rho}_3 = \frac{1}{\hat{l}_3}(\hat{m}_2 \hat{\rho}_2 + \hat{m}_4 \hat{\rho}_4), \tag{3.12}$$

where the term $\hat{m}_3\hat{\rho}_3$, representing the counter weight configuration on a platform system, has been isolated. This gives the condition for matching the operating points between the UAV and the Platform system. In fact, any platform systems whose counter weight configuration (defined by the mass and location of the weight mounted in the main boom of the platform) satisfying (3.12) would have the same trim as the UAV system. Such a platform system configuration will be referred to as the BALANCED configuration, where the effective function of the counter weight on the main boom is to *gravity balance* the mass of the platform linkage structure. Notice that the balanced condition given in (3.12) is independent of the helicopter parameter ($\hat{m}_b$). That

is a consequence of having the same helicopter for the target UAV and the Platform system. This also means that the matching trim condition is independent of the material used for the platform linkages, as long as appropriate counter weight is setup to satisfy (3.12). Furthermore, the condition in (3.11) has been specified in term of non-dimensional parameters, allowing the platform parameters to be scaled according to the non-dimensionalize force factor $\rho A_{\text{disc}}(\Omega R)^2$. One particular scenario is the scaling through the rotor speed Ω, which would have an effect on the payload balance equation and will be examined later in this chapter.

3.2.1 Trim Values for the BALANCED Configuration

Using the parameter values for the UAV system listed in Appendix E, the trim conditions obtained by solving (3.2) are shown in Table 3.1.

Variables	Values	Variables	Values
θ_{0_e}	0.12 rad (6.9°)	θ_{tail_e}	0.21 rad (12.3°)
A_{1_e}	0.0 rad (0.0°)	B_{1_e}	−0.053 rad (−3.0°)
q_{5_e}	−0.053 rad (−3.0°)	q_{6_e}	0.053 rad (3.0°)

Table 3.1: Hover Trim Condition

With the same helicopter operating conditions as the UAV system (same rotor speed Ω and rotor radius R), the BALANCED platform configuration will have the same trim conditions as listed in Table 3.1, since (3.12) is satisfied. The model for the Platform system setup with the BALANCED configuration will be denoted with the subscript B as

$$\hat{\bar{\boldsymbol{M}}}_{\text{B}}(\hat{\bar{\boldsymbol{q}}})\ddot{\hat{\bar{\boldsymbol{q}}}} + \hat{\bar{\boldsymbol{h}}}_{\text{B}}(\hat{\bar{\boldsymbol{q}}}, \dot{\hat{\bar{\boldsymbol{q}}}}) = \hat{\bar{\boldsymbol{\tau}}}_{\text{B}}(\hat{\bar{\boldsymbol{q}}}, \dot{\hat{\bar{\boldsymbol{q}}}}, \vec{\boldsymbol{u}}) \tag{3.13}$$

hereinafter.

3.3 Linearization

For comparison, the Platform system with the BALANCED configuration and the UAV system will be linearized in this section about the hover trim conditions defined in Table 3.1 to examine their respective dynamic modes. Let the state vector $\bar{\mathbb{X}}$ be defined as consisting of the joint

variable vector $\bar{\boldsymbol{q}}$ and its rate vector $\dot{\bar{\boldsymbol{q}}}$:

$$\bar{\mathbb{X}} = \begin{bmatrix} \bar{\boldsymbol{q}} \\ \dot{\bar{\boldsymbol{q}}} \end{bmatrix}. \tag{3.14}$$

From the nonlinear models for the Platform system defined in (2.103), the rate of change of the state vector $\bar{\mathbb{X}}$ is then defined by the following vector function $\bar{\mathbb{F}}(\bar{\mathbb{X}}, \vec{\boldsymbol{u}})$:

$$\dot{\bar{\mathbb{X}}} = \bar{\mathbb{F}}(\bar{\mathbb{X}}, \vec{\boldsymbol{u}}) = \begin{bmatrix} \dot{\bar{\boldsymbol{q}}} \\ \ddot{\bar{\boldsymbol{q}}} \end{bmatrix} = \begin{bmatrix} \bar{\mathbb{F}}_1(\bar{\mathbb{X}}) \\ \bar{\mathbb{F}}_2(\bar{\mathbb{X}}, \vec{\boldsymbol{u}}) \end{bmatrix} = \begin{bmatrix} \dot{\bar{\boldsymbol{q}}} \\ \bar{\boldsymbol{M}}(\bar{\boldsymbol{q}})^{-1}\big[\bar{\boldsymbol{\tau}}(\bar{\boldsymbol{q}}, \dot{\bar{\boldsymbol{q}}}, \vec{\boldsymbol{u}}) - \bar{\boldsymbol{h}}(\bar{\boldsymbol{q}}, \dot{\bar{\boldsymbol{q}}})\big] \end{bmatrix}. \tag{3.15}$$

The linearization of the Platform model is obtained by expanding the nonlinear vector function defined in (3.15) around the hover equilibrium point ($\bar{\mathbb{X}}_{\mathrm{e}}$ and $\vec{\boldsymbol{u}}_{\mathrm{e}}$) through a Taylor series expansion [42]:

$$\dot{\bar{\mathbb{X}}}_{\mathrm{e}} + \Delta\dot{\bar{\mathbb{X}}} = \bar{\mathbb{F}}(\bar{\mathbb{X}}_{\mathrm{e}}, \vec{\boldsymbol{u}}_{\mathrm{e}}) + \left.\frac{\partial\bar{\mathbb{F}}}{\partial\bar{\mathbb{X}}}\right|_{\bar{\mathbb{X}}_{\mathrm{e}}, \vec{\boldsymbol{u}}_{\mathrm{e}}} \Delta\bar{\mathbb{X}} + \left.\frac{\partial\bar{\mathbb{F}}}{\partial\vec{\boldsymbol{u}}}\right|_{\bar{\mathbb{X}}_{\mathrm{e}}, \vec{\boldsymbol{u}}_{\mathrm{e}}} \Delta\vec{\boldsymbol{u}} + \text{Higher Order Terms}, \tag{3.16}$$

where $\Delta\bar{\mathbb{X}} = \bar{\mathbb{X}} - \bar{\mathbb{X}}_{\mathrm{e}} \triangleq \bar{\boldsymbol{\mathcal{X}}}$ and $\Delta\vec{\boldsymbol{u}} = \vec{\boldsymbol{u}} - \vec{\boldsymbol{u}}_{\mathrm{e}} \triangleq \vec{\boldsymbol{\mathcal{U}}}$. Applying the hover definition of $\dot{\bar{\mathbb{X}}} = 0$ and ignoring the higher order terms, the linearization of the Platform model becomes

$$\begin{aligned} \Delta\dot{\bar{\mathbb{X}}} &= \left.\frac{\partial\bar{\mathbb{F}}}{\partial\bar{\mathbb{X}}}\right|_{\bar{\mathbb{X}}_{\mathrm{e}}, \vec{\boldsymbol{u}}_{\mathrm{e}}} \Delta\bar{\mathbb{X}} + \left.\frac{\partial\bar{\mathbb{F}}}{\partial\vec{\boldsymbol{u}}}\right|_{\bar{\mathbb{X}}_{\mathrm{e}}, \vec{\boldsymbol{u}}_{\mathrm{e}}} \Delta\vec{\boldsymbol{u}} \\ &\triangleq \bar{\boldsymbol{A}}\bar{\boldsymbol{\mathcal{X}}} + \bar{\boldsymbol{B}}\vec{\boldsymbol{\mathcal{U}}}, \end{aligned} \tag{3.17}$$

where the system matrix $\bar{\boldsymbol{A}}$ and the input matrix $\bar{\boldsymbol{B}}$ can be partitioned into

$$\bar{\boldsymbol{A}} = \begin{bmatrix} \left.\frac{\partial\bar{\mathbb{F}}_1}{\partial\bar{\boldsymbol{q}}}\right|_{\bar{\mathbb{X}}_{\mathrm{e}}, \vec{\boldsymbol{u}}_{\mathrm{e}}} & \left.\frac{\partial\bar{\mathbb{F}}_1}{\partial\dot{\bar{\boldsymbol{q}}}}\right|_{\bar{\mathbb{X}}_{\mathrm{e}}, \vec{\boldsymbol{u}}_{\mathrm{e}}} \\ \left.\frac{\partial\bar{\mathbb{F}}_2}{\partial\bar{\boldsymbol{q}}}\right|_{\bar{\mathbb{X}}_{\mathrm{e}}, \vec{\boldsymbol{u}}_{\mathrm{e}}} & \left.\frac{\partial\bar{\mathbb{F}}_2}{\partial\dot{\bar{\boldsymbol{q}}}}\right|_{\bar{\mathbb{X}}_{\mathrm{e}}, \vec{\boldsymbol{u}}_{\mathrm{e}}} \end{bmatrix} \quad \text{and} \quad \bar{\boldsymbol{B}} = \begin{bmatrix} \left.\frac{\partial\bar{\mathbb{F}}_1}{\partial\vec{\boldsymbol{u}}}\right|_{\bar{\mathbb{X}}_{\mathrm{e}}, \vec{\boldsymbol{u}}_{\mathrm{e}}} \\ \left.\frac{\partial\bar{\mathbb{F}}_2}{\partial\vec{\boldsymbol{u}}}\right|_{\bar{\mathbb{X}}_{\mathrm{e}}, \vec{\boldsymbol{u}}_{\mathrm{e}}} \end{bmatrix}. \tag{3.18}$$

The linear model for the UAV system can be obtained similarly by applying the linearization procedure described above to the UAV model in (3.8).

The modes of a Multiple-Input Multiple-Output (MIMO) system, such as the Platform and the UAV systems, are defined by the eigenvalues of the matrix $\bar{\boldsymbol{A}}$. Substituting the parameter values for the UAV system listed in Appendix E to the linearized model, its modal frequencies

around the hover trim condition are given by

$$\text{eig}(\bar{\boldsymbol{A}}_{\text{U}}) = \begin{bmatrix} \vec{\mathbf{0}}_{4\times 1} \\ 0.42 \pm 1.08\ j \\ 0.34 \\ 0.15 \\ -4.23 \\ -2.24 \\ -1.21 \\ -0.75 \end{bmatrix}, \tag{3.19}$$

where the subscript U is used to denote the linearized model for the UAV system and $j \triangleq \sqrt{-1}$ is the imaginary number. The four poles at the origin represent the integrator dynamics associated with the position and heading of the helicopter (see Appendix F). As they do not have any effects on the flight dynamics, these modes are not usually considered by most helicopter models in the flight control literature [8, 43, 14, 31, 44, 45, 46, 47]. This results in the more common eighth order linear model instead of the twelfth order linear model represented in (3.17). Four of the eight modes remaining belong to the longitudinal modes while the rest are the lateral modes. The longitudinal modes consist of the unstable oscillatory mode in the complex pole pair at $0.42 \pm 1.08\ j$, which is typically referred to as the phugoid mode that couples the dynamics between forward speed (u) and pitching rate (q) [10, 12]. The other two longitudinal modes are the stable poles at -2.24 and -0.75, which roughly correspond to the stable damped dynamics for the pitch (θ) and heave (height) motion (w) respectively [10, 12]. The lateral modes consist of the unstable poles at 0.34 and 0.15 that roughly correspond to the unstable side slip motion that associates with the lateral velocity (v) and rolling rate (p). Finally, the two remaining stable poles at -1.21 and -4.23 are associated with the damped yaw rate (r) and roll (ϕ) responses respectively.

The linearized modal frequencies around the hover trim point for the Platform system with the BALANCED configuration at its *home* position and heading (that is $q_i = 0$ for i from 1 to

4) is given by

$$\text{eig}(\bar{\boldsymbol{A}}_{\text{B}}) = \begin{bmatrix} \vec{\mathbf{0}}_{4\times 1} \\ 0.41 \pm 1.08\, j \\ 0.2 \pm 0.05\, j \\ -4.36 \\ -2.03 \\ -1.16 \\ -0.52 \end{bmatrix}. \tag{3.20}$$

For comparison, the eigenvalues for the UAV system are plotted side-by-side with those for the BALANCED case in Figure 3.1(a) and Figure 3.1(b). Overall, the modes between the

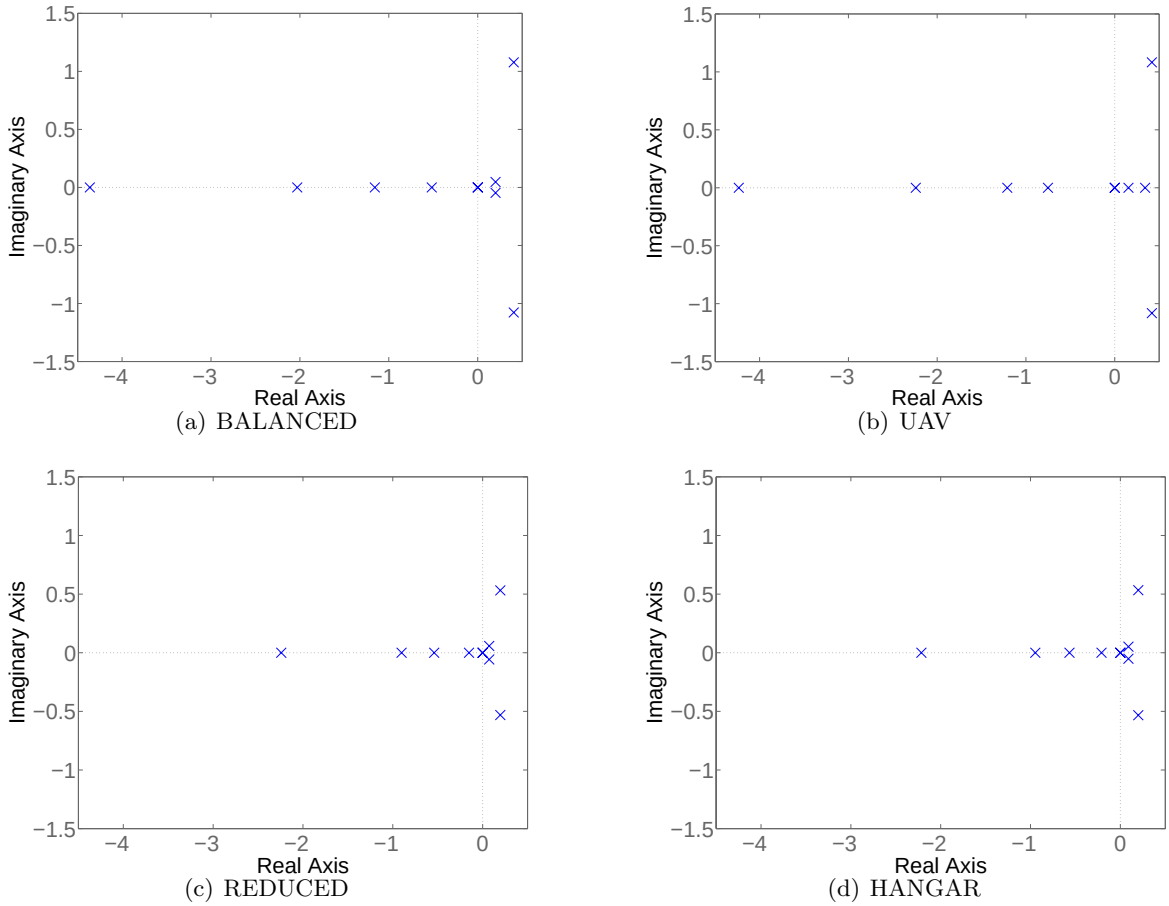

(a) BALANCED (b) UAV

(c) REDUCED (d) HANGAR

Figure 3.1: System Poles Around Hover ($q_4 = 0$)

BALANCED and the UAV systems are very similar. The primary difference between them is in

the unstable lateral modes. While the unstable lateral modes in the UAV systems are damped (at 0.34 and 0.15), the one for the BALANCED case (at $0.2 \pm 0.05\, j$) are oscillatory. This is the effect of the added mass and inertia has on the lateral dynamic due to the heading orientation of the helicopter relative to the platform (i.e. $q_4 = 0$). Contrary to the linearization of the UAV system, the linearization of the Platform system around the hover trim point is dependent on the position and heading of the helicopter because of the presence of the additional mass and inertia from the platform linkages. For instance, when the Platform system with the BALANCED configuration is linearized about $q_4 = \pi/2$, while keeping q_1, q_2, and q_3 at zero, the platform linkage effect is switched to the longitudinal modes. This is illustrated in Figure 3.2(a) and Figure 3.2(b), where the modes of the BALANCED case with $q_4 = \pi/2$ is plotted side-by-side with the ones for the UAV case.

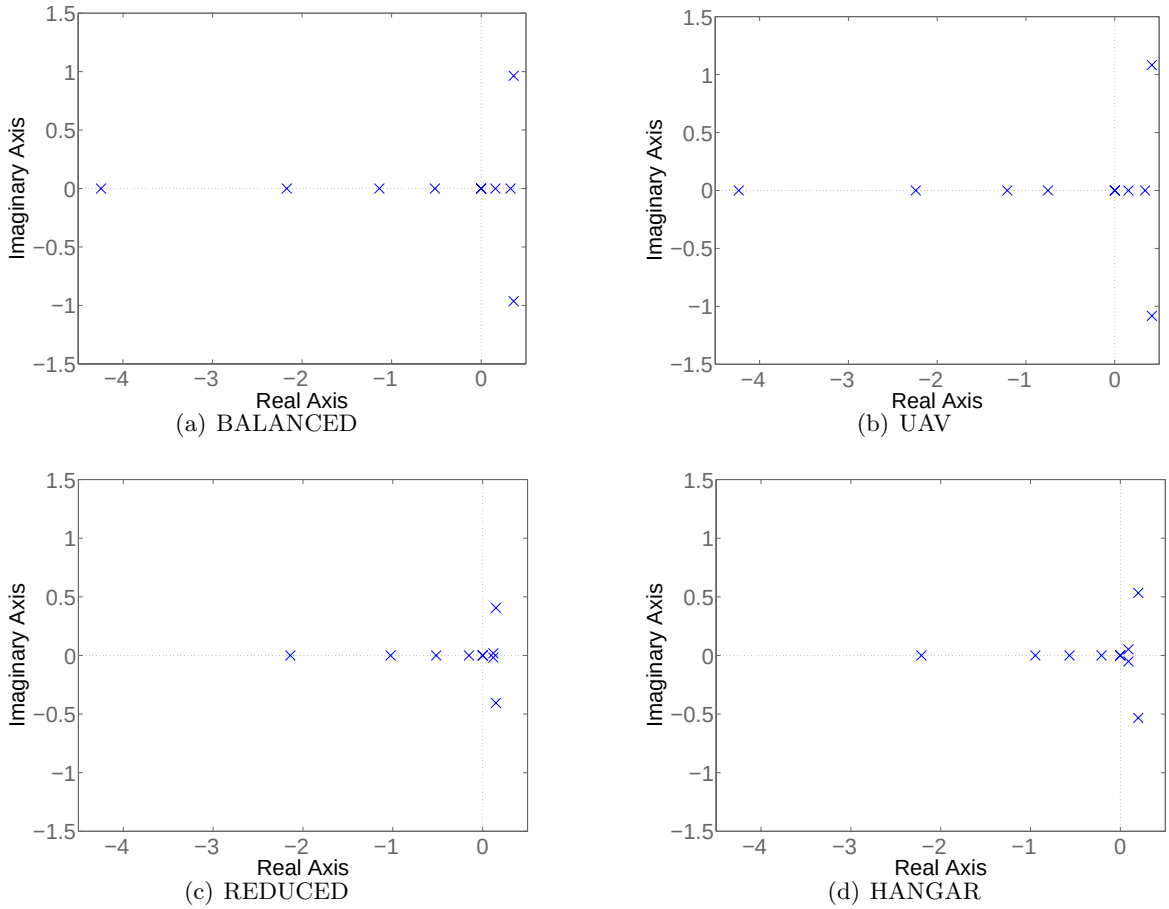

(a) BALANCED (b) UAV

(c) REDUCED (d) HANGAR

Figure 3.2: System Poles Around Hover ($q_4 = \pi/2$)

The linear modal frequencies for the BALANCED case with $q_4 = \pi/2$ is listed below:

$$\text{eig}(\bar{\boldsymbol{A}}_{\text{B}}) = \begin{bmatrix} \vec{\mathbf{0}}_{4\times 1} \\ 0.36 \pm 0.96\ j \\ 0.33 \\ 0.16 \\ -4.24 \\ -2.17 \\ -1.14 \\ -0.52 \end{bmatrix}. \tag{3.21}$$

In this case ($q_4 = \pi/2$), the primary difference with the UAV system is manifested in the longitudinal modes due to the changes in the relative orientation. In particular, the UAV longitudinal phugoid mode at $0.42 \pm 1.08\ j$ is reduced to $0.36 \pm 0.96\ j$. Also the stable damped pitch and heave mode at -2.24 and -0.75 are shifted to -2.17 and -0.52 respectively.

Additional change is observed in the yaw rate response. It went from -1.21 for the UAV system to the BALANCED system of -1.16 and -1.14 for the $q_4 = 0$ and $q_4 = \pi/2$ cases respectively. The reason the yaw rate response is affected in both of these cases is that the absolute yaw orientation ψ of the helicopter is defined as the sum of the base (q_1) and the yaw (q_4) joints of the platform:

$$\psi = q_1 + q_4.$$

As such, the effect of the platform linkage on the yaw rate response is similar regardless of the yaw joint (q_4).

The general trend of the effect of the platform linkages on the helicopter behaviour can be observed by tracing out the variations in the poles while gradually increasing the values of the link mass and inertia from zero, which corresponds to the UAV system attached to a virtual platform. Figure 3.3 shows the trace plot of the poles for both the $q_4 = 0$ and the $q_4 = \pi/2$ cases. The cross symbol ($\times$) denotes poles for the UAV system. These poles are then traced, moving towards the $\triangle$ symbol, as the mass and inertia of the platform linkages (m_i, $I_{xx_{\text{i}}}$, $I_{yy_{\text{i}}}$, and $I_{zz_{\text{i}}}$ for i from 1 to 4) are increased gradually, while satisfying the payload condition in (3.12). Notice that by satisfying (3.12), the system remains to be operating under the BALANCED

configuration, hence under the same trim condition. In the case of Figure 3.3, the platform link

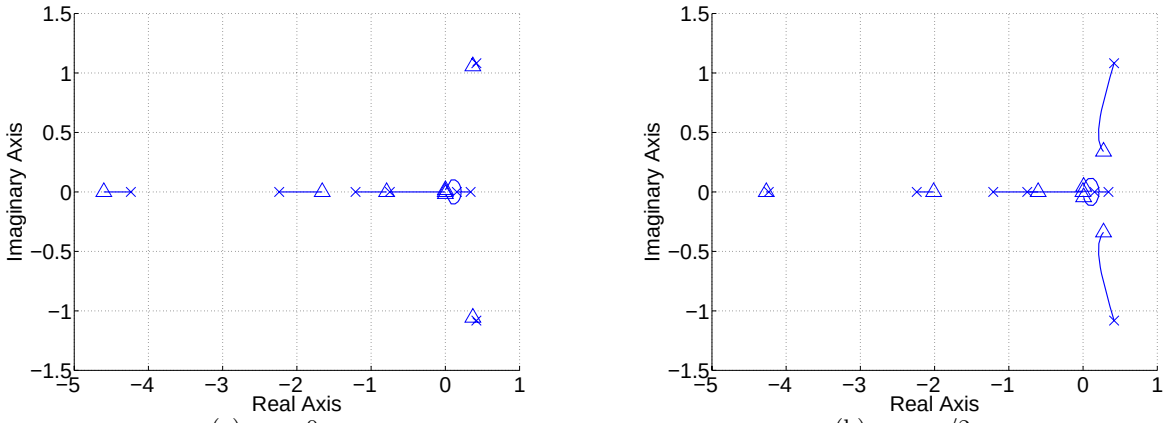

(a) $q_4 = 0$ (b) $q_4 = \pi/2$

Figure 3.3: BALANCED Pole Trace: Varying Mass and Inertia

mass and inertia are adjusted uniformly by dividing through a scaling factor ζ_p. This makes satisfying (3.12) straightforward:

$$\frac{\hat{m}_3}{\zeta_\mathrm{p}}\hat{\rho}_3 = \frac{1}{\hat{l}_3}\left(\frac{\hat{m}_2}{\zeta_\mathrm{p}}\hat{\rho}_2 + \frac{\hat{m}_4}{\zeta_\mathrm{p}}\hat{\rho}_4\right) \tag{3.22}$$

As $\zeta_\mathrm{p} \to \infty$, the mass and inertia will approach zero and the system will resemble the UAV case. On the opposite end, as ζ_p is reduced, the mass and inertia will be increased. When ζ_p is reduced to 1, the poles will correspond to those shown in Figure 3.1(a) and Figure 3.2(a). Then, as ζ_p is reduced further, it represents systems with heavier platform linkages than the target platform employed in this research (as defined by the parameter values listed under the BALANCED configuration in Appendix E). The triangle symbol ($\triangle$) represents the poles of a system with $\zeta_\mathrm{p} = 0.001$, or with links about one thousandth times more massive than the target platform in the BALANCED configuration.

From Figure 3.3, in both the $q_4 = 0$ and the $q_4 = \pi/2$ cases, as the platform linkages become more and more massive ($\zeta_\mathrm{p} \to 0$), most of the poles tend to converge towards the origin. The sole exception is for the one pole associated with the stable damped roll (ϕ) response on the far left of the complex plane, which moves towards negative infinity. This indicates that as the platform linkages become more massive, the system behaviour tends to resemble more and more to those of the integrator-like dynamics. This observation agrees with the intuition that the platform

linkages dominate the rotor response of the helicopter and become the system dynamics as their mass and inertia increases.

Figure 3.3 also illustrates how the the effect of the platform link mass and inertia on the system dynamics is dependent on the helicopter heading orientation. For $q_4 = 0$, the helicopter longitudinal direction is aligned along the platform linkage. As such, the platform effect is more significant for the lateral dynamics than for the longitudinal dynamics, as indicated in the relatively stationary phugoid mode. On the other hand, for $q_4 = \pi/2$, the longitudinal direction is perpendicular to the platform linkages. Therefore, the platform mass and inertia has a more significant impact on the longitudinal dynamics than the lateral dynamics. This is indicated by the relatively large reduction in the phugoid mode.

Finally, notice that the pole trace plots shown in Figure 3.3 are obtained by applying linearization repeatedly to the nonlinear system model as the scaling factor ζ_{p} is varied. These plots provide a systematic tool for tracking changes in the system dynamics due to changes in the system parameters. For instance, Figure 3.3 can be used to compare the dynamics between two test platforms made up of different materials provided they are set up to operate at the same trim condition.

3.4 Reduced Rotor Speed Configurations

The BALANCED configuration defined previously is assumed to have the same helicopter parameters as the UAV system. However, when operating in an indoor laboratory setting, certain limitations might need to be imposed onto the operation of the Platform system such that the helicopter parameters cannot be matched. For instance, the Platform system might need to be operating under a reduced rotor speed. Such requirement could be due to safety concern arising from the proximity of the experiment to the research personnel. Alternatively, the use of electric motor instead of gas engine for indoor operation might limit the rotor power available, requiring the operation be carried with reduced rotor speed. In this section, such a reduced main rotor speed configuration, referred to as the REDUCED configuration, will be investigated.

Recall the UAV case refers to the case with a helicopter mounted on a *virtual* platform that has the same geometrical dimensions as the platform in the BALANCED case. The UAV case represents the reference or benchmark system to which research on the Platform system would

be compared. Through the result from Lemma 2.1, it is also the theoretical equivalent to a stand alone UAV system. The BALANCED configuration represents the ideal case under which the Platform can be setup to *mimic* the UAV system behaviour. It addresses the need to have physical platform linkages for support in the quest for safe indoor operations through the use of the payload equation as the Platform setup criteria. In the REDUCED configuration, the implementation of the Platform system for UAV research is taken a step further to address the limitation in the main rotor speed within the indoor setting. It will be shown that the matching trim criteria dictates that the counter weight setup be adjusted away from the BALANCED configuration in order to compensate for the variation in the main rotor speed.

3.4.1 Main Rotor Speed/Counter Weight Trade-Off

Recall that the trim matching condition between the UAV and the Platform systems is defined by matching the apparent payload between them. The apparent payload matching condition in (3.11) is expressed in terms of non-dimensional parameters and is thus independent of helicopter dimensional quantities, such as the rotor radius R and the rotor speed Ω. This means systems with different rotor speed or rotor radius can still be configured to operate at the same trim as long as their non-dimensional apparent payload satisfy (3.11). For the REDUCED–UAV configuration matching, the apparent payload matching condition in (3.11) can be expanded explicitly in terms of the main rotor speed for the REDUCED (Ω_{D}) and the UAV (Ω_{U}) configurations as

$$\begin{aligned}&\left(\frac{m_b}{\rho A_{\mathrm{disc}} R}\right)\left(\frac{g}{\Omega_{\mathrm{U}}^2 R}\right)\\ &\qquad = \left[\left(\frac{m_2}{\rho A_{\mathrm{disc}} R}\right)\left(\frac{\rho_2}{R}\right) - \left(\frac{m_3}{\rho A_{\mathrm{disc}} R}\right)\left(\frac{\rho_3}{R}\right) + \left(\frac{m_4 + m_b}{\rho A_{\mathrm{disc}} R}\right)\left(\frac{l_3}{R}\right)\right]\left[\frac{g/(\Omega_{\mathrm{D}}^2 R)}{l_3/R}\right], \quad (3.23)\end{aligned}$$

where the rotor radius R is assumed to be the same for both cases. This can be simplified into

$$m_3\rho_3 = -m_b l_3(\check{\Omega}^2 - 1) + m_2\rho_2 + m_4 l_3, \quad (3.24)$$

where $\check{\Omega} \triangleq \Omega_{\mathrm{D}}/\Omega_{\mathrm{U}}$ is the ratio between the main rotor speed of the two configurations. The quadratic constraint represented in (3.24) between the rotor speed ratio ($\check{\Omega}$) and the counter weight configuration parameters (represented by the product $m_3\rho_3$) is illustrated in Figure 3.4.

The Platform systems that correspond to the points along the curve in Figure 3.4 would be operating under the same trim condition. When $\check{\Omega} = 1$, (3.24) reverts back to the apparent payload matching condition for the BALANCED–UAV case defined in (3.12) as expected. The condition $\check{\Omega} < 1$ represents the set of Platform systems that are set to operate at a reduced main rotor speed while maintaining the same trim condition when compared to the target UAV system. The previously defined REDUCED configuration falls within this set. As the ratio of the main rotor speed decreases, the counter weight configuration ($m_3\rho_3$) will need to be increased to compensate for the reduction in thrust in order to maintain the trim condition. In the limit when $\check{\Omega} = 0$, it represents the scenario where the counter weight configuration would have been set to completely compensate for the effect caused by both the platform linkage and the helicopter body

$$m_3\rho_3 = m_2\rho_2 + (m_4 + m_b)l_3. \tag{3.25}$$

Under such scenario, the trim condition is upheld solely by the counter weight instead of through the thrust generated by the helicopter rotor. At the other end, when $\check{\Omega} > 1$, it represents the scenario where the reduction in the counter weight effect (less gravity compensation) is offset by the increase in thrust due to the increased rotor speed. When $m_3\rho_3 = 0$, the case where no counter weight is used, the platform linkage effect is compensated completely by the increased rotor thrust.

Recall the product $m_3\rho_3$ represents the parameter for the composite body consisting of both the main boom and the counter weight on the platform (Link 3 in Figure 2.6). When discussing changes in the counter weight setting, it is more convenient to consider the effect contributed by the bare main boom and those by the counter weight separately. That is because practically, when adjusting the platform configuration, it is only the counter weight portion that is varied. The bare main boom portion would otherwise remain constant. For

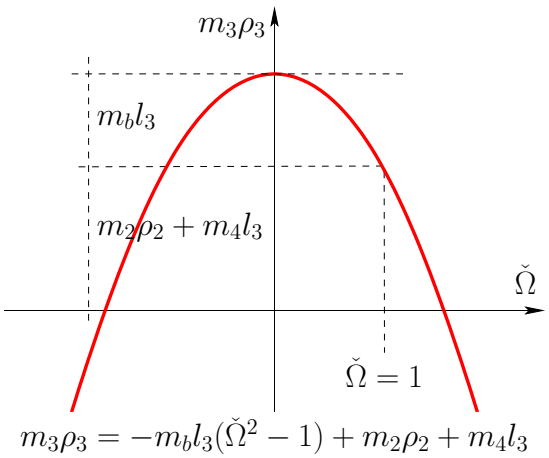

Figure 3.4: Speed/Weight Trade-Off

counter weight change discussion hereinafter, a set of parameters with subscript w, such as m_w and ρ_w, are introduced to denote quantities for the counter weight alone. Depending on the context, the parameters with subscript 3 will then be understood as denoting quantities for either the full composite main boom (including the counter weight effect) or the bare main boom only. With this change of notation, the main rotor speed and counter weight trade-off constraint in (3.24) can be updated into

$$m_w \rho_w = -m_b l_3 (\check{\Omega}^2 - 1) + m_2 \rho_2 - m_3 \rho_3 + m_4 l_3, \tag{3.26}$$

where m_w is the counter weight mass; ρ_w is the location of the centre of mass of the counter weight relative to the elbow (q_2) joint of the platform; m_3 and ρ_3 here refer to the mass and centre of mass of the bare main boom. Notice that, for consistency, the direction for the location of the centre of mass of the bare main boom ρ_3 is kept the same as defined previously, which results in ρ_3 being negative for the bare boom only case (see Appendix E).

Pole Trace Plot for Varying Main Rotor Speed

Physically, there are two ways to satisfy the rotor speed and counter weight trade-off represented by (3.26): either fixes the counter weight mass and adjusts its location; or fixes the mount location but adjusts the counter weight mass. It is more convenient to do the former since varying the mass m_w necessitates change in the inertia associated with the counter weight as well (such as $I_{xx_{\mathrm{w}}}$).

For the following analysis, the counter weight mass is assumed to be kept constant while its mount location on the main boom is adjusted. In particular, the value of $m_w = 5.7$ kg from the BALANCED configuration (see Appendix E) will be used. Figure 3.5 illustrates the trace plots for the poles of the Platform system as its main rotor speed is varied with respect to the one for the BALANCED/UAV configuration while its counter weight setting is adjusted according to (3.26). Figure 3.5(a) shows the trace plots for the $q_4 = 0$ case while Figure 3.5(b) shows the $q_4 = \pi/2$ case. As an example, when the main rotor speed ratio is set to half of that from the BALANCED/UAV configuration, that is $\check{\Omega} = 0.5$, the resulting location of the $m_w = 5.7$ kg counter weight is given by $\rho_w = 0.919$ m, with the parameter values for the BALANCED configuration substituted into (3.26). The physical limit of $m_w \rho_w = 0$ for the counter weight

setting imposes an upper bound for the main rotor speed ratio given by

$$\check{\Omega} \leq \sqrt{\frac{m_2\rho_2 - m_3\rho_3 + (m_4 + m_b)l_3}{m_b l_3}}, \tag{3.27}$$

which yields the value of $\check{\Omega} \leq 1.17$ for the BALANCED configuration parameter values from Appendix E.

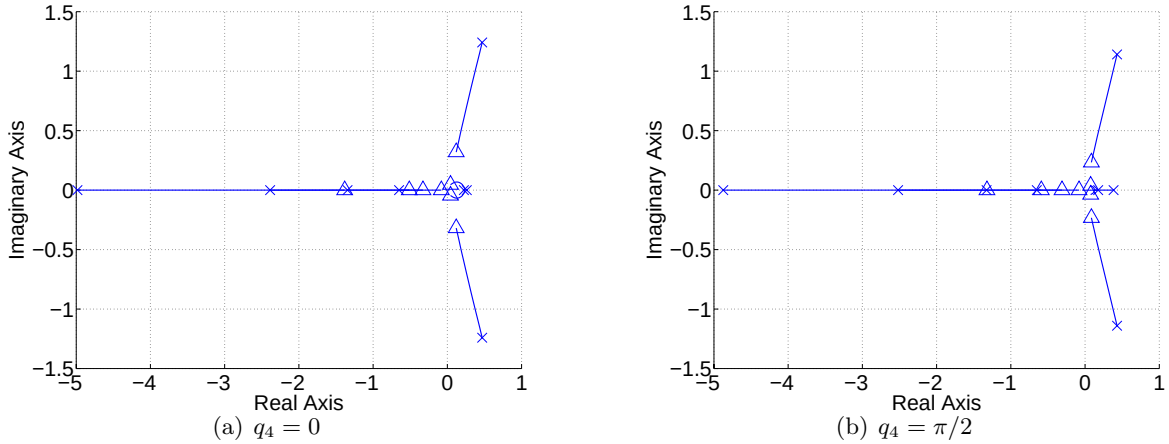

(a) $q_4 = 0$ (b) $q_4 = \pi/2$

Figure 3.5: Pole Trace: Varying Rotor Speed

The trace plots in Figure 3.5 start with the poles for the Platform system with a main rotor speed ratio of $\check{\Omega} = 1.15$, denoted by the cross symbol ($\times$). This represents a system operating with a fifteen percent increase in the main rotor speed relative to the BALANCED/UAV configuration, while maintaining the same trim condition with $\rho_w = 0.046$ m. The triangle symbol ($\triangle$) marks the poles for the Platform system with a main rotor speed ratio of $\check{\Omega} = 0.3$ and the counter weight set at $\rho_w = 1.049$ m, representing a seventy percent decrease in the main rotor speed relative to that of the BALANCED/UAV configuration. The effect of the helicopter heading relative to the platform (q_4) is minimal as the pole movement are similar for the two cases shown in Figure 3.5. The movement of the poles tends uniformly towards the origin as the main rotor speed is reduced. This means as the main rotor speed is reduced, the system dynamic response would also slow down. An alternate interpretation of this is that as the main rotor speed is reduced, (3.26) dictates that the counter weight be moved further and further away from the elbow (q_2) joint. That has a net effect analogous to those of increasing the mass and inertia of the platform linkages as shown in Figure 3.3. Whereas the influence by changes

in the link mass and inertia is dependent on the helicopter heading, changes in the main rotor speed affect the system dynamics uniformly regardless of the heading.

The pole trace plots shown in Figure 3.5 illustrates the effects on the system modes by changing the rotor speed while maintaining the same trim condition through the counter weight location. This provides a guideline on how to compensate for variation in rotor speed with weight configurations and vice versa.

Parameter Values for the Different Configurations

Configuration	Description/Highlight
UAV	• Served as the reference helicopter setup. • Main rotor speed: $\Omega = 1761$ RPM.
BALANCED	• UAV setup with a physical platform. • Same main rotor speed as UAV: $\Omega = 1761$ RPM. • Platform counter weight is setup for gravity balance: $m_w = 5.7$ kg.
REDUCED	• BALANCED configuration operated with reduced rotor speed. • Same counter weight as the BALANCED case, but with location changes to compensate for the reduced rotor speed: $m_w = 5.7$ kg. • Main rotor speed: $\Omega = 875$ RPM.
HANGAR	• REDUCED configuration operated with different counter weight. • Heavier counter weight mass: $m_w = 14.8$ kg. • Main rotor speed: $\Omega = 875$ RPM.

Table 3.2: Comparison between Configurations

Three Platform system configurations have been introduced thus far: the UAV, the BALANCED and the REDUCED configurations. There is a fourth configuration, referred to as the HANGAR [1] configuration, defined in Appendix E. Recall the REDUCED configuration for the Platform system has been introduced to address the need for a reduced main rotor speed within the indoor laboratory environment. While the REDUCED configuration is obtained from the BALANCED configuration by adjusting the location (ρ_w) of the counter weight mass ($m_w = 5.7$ kg) as the main rotor speed is varied; the HANGAR configuration uses a different counter weight mass ($m_w = 14.8$ kg) to achieve the trade-off balancing. The reason for this is that the parameter values for the HANGAR configuration listed in Appendix E are obtained from

[1] HANGAR stands for the Helicopter Autonomous Navigation and Guidance Applied Research, a reference to the laboratory in which this research originated.

the actual experimentation setup in the laboratory for this research. The primary constraint here is the limited power available through the electric motor. In this case, the main rotor speed is constrained to operate at 875 RPM (Rotation-Per-Minute). The counter weight configuration is then setup in such a way that the rotor running at 875 RPM can generate enough thrust for the helicopter on the platform to lift off from its *home* position. This yields the values of

$$m_w = 14.8 \text{ kg} \qquad \text{and} \qquad \rho_w = 0.36 \text{ m},$$

as listed in Appendix E for the HANGAR configuration. Substituting the parameter values for the HANGAR configuration into (3.26) would yield a main rotor speed ratio of

$$\check{\Omega} = 0.5,$$

which explains how the main rotor speed value for the BALANCED/UAV configuration defined in Appendix E is obtained.

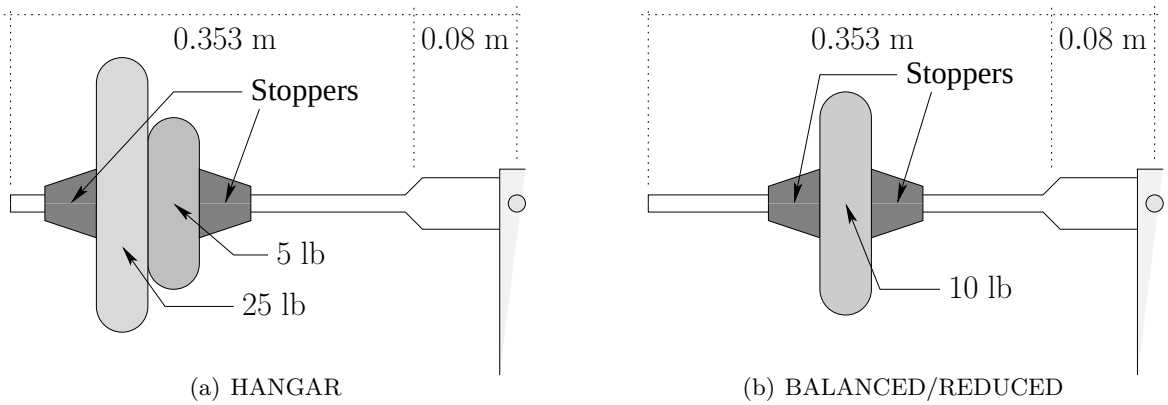

(a) HANGAR (b) BALANCED/REDUCED

Figure 3.6: Counter Weight Configuration Diagram

In the HANGAR case, the value for the counter weight mass of $m_w = 14.8$ kg is realized as a combination of two separate weights secured on the platform main boom by two stoppers. The two weights used have weights of 5 lb (2.3 kg) and 25 lb (11.3 kg), with the heavier of the two located further away from the elbow (q_2) joint. Each stopper has a mass of 0.6 kg. Figure 3.6(a) illustrates this counter weight arrangement. To obtain the BALANCED configuration from this

counter weight setting would result in

$$\rho_w = 0.12 \text{ m},$$

which would have put the weight assembly illustrated in Figure 3.6(a) too close to the elbow joint for practical realization. As a result, the two-weight arrangement illustrated in Figure 3.6(a) is replaced by a single (10 lb) weight arrangement shown in Figure 3.6(b) for the BALANCED and the REDUCED configurations. Parameter values for the BALANCED and REDUCED configurations found in Appendix E corresponds to this single (10 lb) weight arrangement. Although the main rotor speed is the same for both the REDUCED and the HANGAR configurations, they are defined separately to distinguish between the two counter weight settings used. In particular, the REDUCED configuration, with $m_w = 5.7$ kg and $\check{\Omega} = 0.5$, requires $\rho_w = 0.92$ m, which is again out of bound for practical realization. Table 3.2 highlights the difference between the four configurations introduced in this thesis.

REDUCED and HANGAR Configurations

Applying the linearization around the hover trim point ($q_4 = 0$) for the REDUCED configuration would yield the following eigenvalues for the linearized system matrix $\bar{\boldsymbol{A}}_{\mathrm{D}}$:

$$\mathrm{eig}(\bar{\boldsymbol{A}}_{\mathrm{D}}) = \begin{bmatrix} \vec{\mathbf{0}}_{4\times 1} \\ 0.2 \pm 0.53\, j \\ 0.07 \pm 0.06\, j \\ -2.24 \\ -0.9 \\ -0.54 \\ -0.15 \end{bmatrix}. \tag{3.28}$$

These poles has been plotted in Figure 3.1(c). The corresponding eigenvalues for the linearized system matrix $\bar{\boldsymbol{A}}_{\mathrm{H}}$ for the HANGAR configuration is given by

$$\mathrm{eig}(\bar{\boldsymbol{A}}_{\mathrm{H}}) = \begin{bmatrix} \vec{\mathbf{0}}_{4\times 1} \\ 0.2 \pm 0.53\ j \\ 0.09 \pm 0.05\ j \\ -2.21 \\ -0.95 \\ -0.57 \\ -0.21 \end{bmatrix}. \tag{3.29}$$

These poles are plotted in Figure 3.1(d). As has been observed from Figure 3.5, the primary effect of reducing the main rotor speed is in the migration of the poles towards the origin. The difference between the REDUCED and HANGAR configurations is minimal, indicating that the change in the counter weight settings is not significant. There is a slight reduction in the magnitude of the poles for the HANGAR configuration when compared to the REDUCED case. This can be attributed to the net increase in the platform linkage mass due to the change in the counter weight.

The poles for the REDUCED configuration around the hover trim point for the case $q_4 = \pi/2$ is given by

$$\mathrm{eig}(\bar{\boldsymbol{A}}_{\mathrm{D}}) = \begin{bmatrix} \vec{\mathbf{0}}_{4\times 1} \\ 0.15 \pm 0.41\ j \\ 0.12 \pm 0.02\ j \\ -2.14 \\ -1.02 \\ -0.52 \\ -0.15 \end{bmatrix}. \tag{3.30}$$

The corresponding poles for the HANGAR configuration is given by

$$\text{eig}(\bar{\boldsymbol{A}}_{\text{H}}) = \begin{bmatrix} \vec{\mathbf{0}}_{4\times 1} \\ 0.17 \pm 0.45\, j \\ 0.13 \\ 0.11 \\ -2.14 \\ -1.04 \\ -0.55 \\ -0.21 \end{bmatrix}. \tag{3.31}$$

These poles are plotted in Figure 3.2(c) and Figure 3.2(d) respectively. Similarly observations to the $q_4 = 0$ case can be made here.

3.5 Limitations on the use of the Platform System

One of the objectives of this research is to investigate the possibility of utilizing the Platform system as a tool for UAV research. It is therefore desirable to relate the Platform system behaviour to that of the UAV system. While Theorem 2.1 provides a theoretical basis for obtaining the UAV system model from the Platform model, it is not directly applicable to the physical system since it is not practical to reduce the mass and inertia of the platform linkages to zero. A more relevant approach is to seek a set of conditions for the Platform system so that its dynamic behaviour becomes equivalent to those of the UAV system.

Dimensional analysis can be used to achieve such dynamic equivalence between two systems [48]. Ghanekar [48] illustrated the use of dimensional analysis to achieve scaling and dynamic equivalence for robot manipulator systems similar to the Platform system employed in this research. The key to obtaining the dynamic equivalence condition between two robot manipulator systems of interest is in the matching of their corresponding non-dimensional models. The non-dimensional model represents the normalized behaviour of each system. The actual system response is scaled from the non-dimensional model through the characteristic force and torque of the system. In the case of robot manipulators, the characteristic force can be represented by the product between the base link mass m_1, the radius of gyration k_1 [39] of the base link

and a system characteristic frequency Ω: $m_1 k_1 \Omega^2$ [48]. The corresponding characteristic torque is represented by $m_1 k_1^2 \Omega^2$. By matching the non-dimensional models through the characteristic force and torque, two systems can be made of different materials, or of different dimensions, or even be operated under different gravitational effect (as in operating on a different planet, such as on Mars instead of on Earth), dynamic equivalence between them can still be achieved. Dimensional analysis is used extensively in the aerospace literature, especially pertaining to wind tunnel research [49]. In regards to a helicopter, the characteristic thrust and torque are defined by the product $\rho A_{\text{disc}}(\Omega R)^2$ and $\rho A_{\text{disc}}(\Omega R)^2 R$ respectively. Because of the dual nature of the Platform system, which includes both the robot manipulator and the helicopter dynamics, and to facilitate comparison with the UAV system, the characteristic thrust and torque for the helicopter rotor, namely $\rho A_{\text{disc}}(\Omega R)^2$ and $\rho A_{\text{disc}}(\Omega R)^2 R$, have been chosen and applied for normalization in Chapter 2. The dimensional factor for mass, length, inertia and time are derived from the characteristic thrust and torque as:

$$\text{Mass} : \rho A_{\text{disc}} R; \qquad \text{Length} : R; \qquad \text{Inertia} : \rho A_{\text{disc}} R^3; \qquad \text{Time} : \frac{1}{\Omega}.$$

Applying the dynamic equivalence condition to the Platform system means matching the non-dimensional Platform model defined in (2.106) to that of the UAV system in (3.9). While the dynamics of the UAV model are independent of the position and the heading of the helicopter (assuming environmental conditions, such as wind speed, remains uniform within the range of operation), the same cannot be said for the Platform system. For instance, as the helicopter operates further away from the base of the Platform, the inertia property about the base joint (q_1) will increase due to the increase in the slider joint variable q_3. This effect manifests in the mass-inertia matrix $\hat{\hat{\boldsymbol{M}}}(\hat{\hat{\boldsymbol{q}}})$, for example in $\hat{m}_{11}$ (from Appendix D):

$$\begin{aligned}\hat{m}_{11} = {} & \hat{I}_{zz_1} + \hat{I}_{zz_4} + (\hat{I}_{xx_2} + \hat{I}_{xx_3}) S_{\hat{q}_2}^2 + (\hat{I}_{yy_2} + \hat{I}_{yy_3} + m_2 \hat{\rho}_2^2 + \hat{m}_3 \hat{\rho}_3^2 + \hat{m}_4 \hat{l}_3^2) C_{\hat{q}_2}^2 \\ & + \hat{m}_b (\hat{l}_s + \hat{q}_3 + \hat{l}_3 C_{\hat{q}_2})^2 + \hat{I}_{xx_\text{b}} S_{\hat{q}_5}^2 + (\hat{I}_{yy_\text{b}} S_{\hat{q}_6}^2 + \hat{I}_{zz_\text{b}} C_{\hat{q}_6}^2) C_{\hat{q}_5}^2 + 2 \hat{I}_{xz_\text{b}} C_{\hat{q}_6} S_{\hat{q}_5} C_{\hat{q}_5}.\end{aligned} \tag{3.32}$$

In fact, based on the geometry of the Platform system, any possible equivalence with the UAV system can only be achieved when the elbow (q_2) and the slider (q_3) joints remain constant. This narrows to either point-to-point equivalence (such as during hover) or equivalence between operating in a constant height circular flight path around the base (q_1) joint. Furthermore, when

comparing the two models closely, it can be concluded that equivalence between the Platform and UAV systems cannot be achieved by adjusting the configuration parameters alone. This can be illustrated by comparing the $\hat{m}_{22}$ entry of the mass-inertia matrix $\hat{\bar{\boldsymbol{M}}}$ of both systems (from Appendix D):

$$\hat{m}_{22} = \hat{I}_{zz_2} + \hat{I}_{zz_3} + \hat{m}_2\hat{\rho}_2^2 + \hat{m}_3\hat{\rho}_3^2 + (\hat{m}_4 + \hat{m}_b)\hat{l}_3^2, \tag{3.33}$$

$$\hat{m}_{22_{\mathrm{U}}} = \hat{m}_b\hat{l}_3^2. \tag{3.34}$$

With the mass of the helicopter body $\hat{m}_b$ being constrained by the $\hat{m}_{33}$ entry (see Appendix D),

$$\hat{m}_{33} = \hat{m}_b,$$

the equivalence condition between the two $\hat{m}_{22}$ entries reduces to

$$\hat{I}_{zz_2} + \hat{I}_{zz_3} + \hat{m}_2\hat{\rho}_2^2 + \hat{m}_3\hat{\rho}_3^2 + \hat{m}_4\hat{l}_3^2 = 0, \tag{3.35}$$

which is impossible to satisfy for any physical systems whose mass and inertia are positive (non-zero). As a result, due to the difference in the model structures (that is, changes in the configuration parameters) between the Platform and the UAV system, direct dynamic equivalence cannot be achieved through the means of non-dimensional scaling as in the case of the robot manipulator systems [48]. Although the Platform configuration parameters (such as the mass and location of the counter weight on the main boom) can be adjusted according to the payload equation in (3.12) to match the operating point, additional means will be needed to achieve dynamic equivalence. In particular, the source of the discrepancy between the Platform and the UAV systems is the additional mass and inertia of the platform linkages. As such, a possible approach to achieve equivalence is to add servo control torque to the joints to *compensate* for the additional mass and inertia. This requires changes to be made to the Platform system presented in this research and is therefore out-of-scope here. A brief discussion on such an approach will be presented in Chapter 5.

3.6 Summary

In this chapter, four configurations of the Platform model have been defined and compared. These four configurations are related through the payload equation, which constrains their operating point to remain at the same hover trim point. The UAV configuration is the benchmark system to which the remaining configurations are compared. The BALANCED configuration is the case where the counter weight arrangement is set to statically gravity balance the platform link mass about the elbow (q_2) joint. This represents the ideal setup configuration for the Platform system as the effect of the platform linkages on the system dynamics is kept to a minimum. The REDUCED configuration is defined to address the need for reduced rotor speed operation within the indoor laboratory environment. It explores the trade-off between counter weight arrangement and the main rotor speed. Finally, the HANGAR configuration is obtained to reflect the physical limitation of the Platform system in the laboratory. It is set up with a counter weight large enough so that the Platform system is able to lift off using the reduced main rotor speed.

Through linearization, the hover modes for each of the four configurations have been obtained. It has been shown that while the hover dynamics of the UAV system is independent of the helicopter position and heading, the same is not true about the BALANCED case. In particular, the helicopter heading orientation relative to the platform linkages determines how the longitudinal and lateral modes of the helicopter are affected by the link mass and inertia. Furthermore, it has been shown that the platform linkage effect becomes dominant as the link mass and inertia are increased. Similar effect is observed when the main rotor speed is reduced. Both of these results conform to the intuition that the Platform system dynamics is dictated by the relative prominence between the main rotor and the platform linkage dynamics. If the platform linkage is massive relative to the thrust generated by the main rotor, the platform dynamics will be dominant and vice versa.

Finally, through the use of dimensional analysis, it has been concluded that dynamic equivalence between the Platform and the UAV systems cannot be achieved through adjustment in configuration parameters alone. An approach that modifies the Platform system to achieve equivalence will be presented in Chapter 5 as a possible future research topic.

In summary, the contributions presented in this chapter are:

- derived the payload equation, which defines the trim equivalence condition;
- derived the rotor speed trade-off condition for the Platform system, which allows for comparison to be made between the UAV system and the reduced rotor speed operation within the indoor laboratory environment;
- examined the effect that the main rotor speed and the link mass and inertia have on the system dynamics;
- established the limitation on using the Platform system for direct model equivalence with the UAV system.

Chapter 4

Platform Control Strategy

The objective of this chapter is to outline the Virtual Joint Control strategy for the Platform system. Through simulation, it will be shown that this control method represents not only a viable control strategy for the Platform system but it can also be viewed as an alternate control strategy for stand alone helicopter (UAV) systems.

4.1 Motivation

The stand alone helicopter (UAV) system is inherently unstable [10, 12], as indicated by the presence of the unstable phugoid and side slip modes near hover (see Figure 3.1(b)). Although the effect of the platform link mass and inertia in the Platform system causes the system modes to shift away from those in the UAV system, as illustrated in Figure 3.3, the unstable modes remained. To perform experimentation on either system therefore requires the use of a stabilizing controller. For the purpose of comparison and extension of the research results obtained on the Platform system to the UAV system, it is desirable to devise a control strategy that is applicable to both systems, despite the differences in their system dynamics.

4.1.1 Conventional Helicopter Flight Control

Numerous flight control strategies have been proposed in the literature for helicopter flight control. The type and complexity of the controller depend largely on the intended application. With its unstable, coupled and complex dynamics, the helicopter has been used as

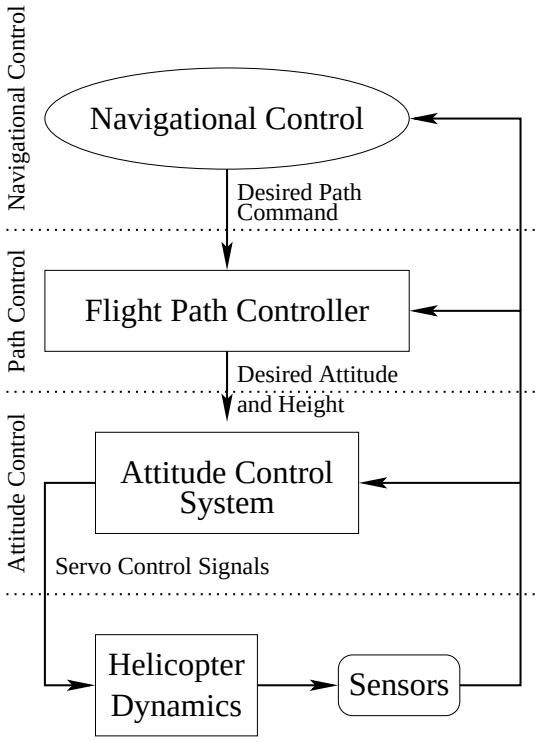

Figure 4.1: Helicopter Hierarchical Control

case study for various control laws throughout the years, such as adaptive control [50, 7, 31], $\mathcal{H}_\infty$ robust control [19, 51, 52, 53, 54, 55, 44], predictive control [56, 13], sliding mode control [57, 58], Lyapunov-based backstepping technique [59, 30, 60], Linear Quadratic Gaussian/Regulator (LQG/LQR) control [18, 43], Input-Output linearization [34, 14], fuzzy logic and neural network [61, 37, 62, 63, 64, 43, 34], and vision based tracking [65]. Due to the nature of the helicopter dynamics, it is common to divide the overall control strategy into three layers: navigational control, path/trajectory control, and attitude control. Such control hierarchy is illustrated in Figure 4.1.

Navigational Control

In the context of *autonomous* helicopter flight control, the function of the navigation controller is to oversee the operation of the system with the aim to reach the intended mission target. Recall navigational tasks include path and trajectory planning [66, 67, 3, 68], object and collision avoidance [22, 69] and multi-vehicle cooperation [70]. Often, a navigation control strategy is

divided into a hierarchical structure with the upper-most level composed of decision-making directives and the lower-most level being the stabilization system, responsible for path, position and attitude control. Naturally, the emphasis in navigational control is on the design of the overall control structure (the hierarchy) as well as in the high level intelligence that is responsible for the planning and execution of the various actions taken by the system. Since the goal of the Platform research is to provide feasible testing facility for the investigation and control of the system dynamics, which corresponds to the lower level control strategies such as for attitude and path control, navigational control issues will be deferred to future research and will not be addressed here.

Path Control

As the name suggests, the objective of the Flight Path Controller (FPC) is path control, such as moving the helicopter from one location to another location with desired way-points in between. This problem is multi-faceted. For instance, Frezza [27] viewed the tracking problem as an approximation task. Frezza [27] approximated the desired trajectory by choosing among a set of feasible trajectories. At each sample instance, a local feasible trajectory, called a connecting contour, is chosen such that it connects the current location of the helicopter to the desired trajectory. Linear feedback control is then applied to control the helicopter along the connecting contour. The effective trajectory is the envelope of all of the connecting contours.

Another approach to path control focuses on the input-output characteristics of the system as a whole. Koo and Sastry [14] take the nonlinear system dynamics and apply an input-output feedback linearization algorithm for path control. Koo and Sastry find that a direct input-output feedback linearization applied to the rigid body dynamics of the helicopter yields a linearized system with non-minimum phase zero dynamics. This means that when the feedback control law is implemented, some of the internal states may oscillate despite stable outputs. For example, the helicopter may be rolling and pitching (oscillating) while tracking the desired path. The source of the oscillations comes from the couplings between the rolling (pitching) moments and lateral (longitudinal) accelerations. To overcome this problem, Koo and Sastry propose to approximately linearize the system by neglecting the coupling terms. The end result is an extended system that is minimum phase. Bounded tracking has been shown in simulations using the approximate linearization technique. However, practical issues such as actuator saturation,

which can pose a problem in the implementation of the feedback linearization controller [71], have not been addressed by Koo and Sastry.

Alternatively, Mahony and Lozano [26] approach the coupling problem by manipulating the mass distributions on the helicopter. The location of the control electronics, such as computers and sensors, is adjusted such that the moment of inertia around the first two principal axes (the roll and pitch axes) are equal. This simplifies the rotation dynamics and results in a linearized model that has no zero dynamics. The idea is that control law design based on such a simplified model would yield almost exact tracking control.

In addition to focusing on either the characteristic of the flight path [27] or on the system input-output behaviour [14, 26], Frazzoli *et al.* [60] look at yet another aspect of path control: attitude representation. Rigid body attitude is commonly parameterized through the Euler (roll, pitch and yaw) angles. For the 3-2-1 Euler angle representation [40] employed in this research (see Appendix A.1.1), singularities occur when the pitch angle θ is at $\pm 90^\circ$. This corresponds to the situation when the helicopter is pointing vertically up or down. This singularity is *artificial* since it arises from the mathematical representation instead of from physical constraints. According to Euler's theorem [39], general rotation can be parameterized by a rotation about a fixed axis. Such a representation does not suffer from the singularities present in the Euler angle representation. Frazzoli *et al.* [60] use this alternate form of attitude description and are able to show, in simulation, autonomous path control of a helicopter executing complex manoeuvres, such as looping, that are otherwise impossible for control laws with an Euler angle attitude representation because of the presence of kinematic singularities.

The Platform system poses a slightly different set of problems for path control. First, its operation is limited to within the reachable workspace of the platform linkages. Second, the singularities are materialized by the physical constraints of the system. Finally, contrary to the uniform dynamics exhibited by the UAV system with respect to its position and orientation, the dynamics of the Platform system varies within the reachable workspace, as illustrated in Figure 3.1 and Figure 3.2. All of these reasons necessitate an alternate control strategy for path control on the Platform system. For the purpose of this research, path control focuses on regulating the helicopter system to follow through a set of pre-defined way-points. The paths through these way-points are assumed to be feasible and the issue of path generation will not be addressed.

Attitude Control System (ACS)

The objective in attitude control is to stabilize the helicopter in the air. Since the hover state can be approximated using a tether (or be simulated by mounting the helicopter on a platform like in this research) for safe operation and does not require a large flying field, hover control has been studied most extensively in the literature. A majority of strategies on hover control revolve around linearizing the nonlinear system model about the equilibrium point and using the linearized model in the control design [8, 20, 28]. In particular, Shim *et al.* [20] show that a linear multi-loop control strategy (with only proportional controllers) is capable of hover control for a small-scale helicopter. Other approaches include robust control [16, 19, 51, 56, 52], model-following adaptive control [50, 72] and control through feedback linearization [32, 30].

In addition to using linearized models, decoupled or reduced order models are often considered for attitude control design near hover [8, 7, 37, 34]. This is because the coupling between the longitudinal, lateral and yaw dynamics of the helicopter are weaker near hover [10, 12]. With this assumption, controllers for the different subsystems can be designed and tested separately. To facilitate the testing of the individual subsystems, test platforms with various configurations are employed [73, 61, 74, 75]. With the ability to secure (lock down) each of its six joints independently, different combinations of subsystem testing can be performed on the Platform system utilized in this research. This makes the Platform system particularly suitable for attitude control research.

As in the case of the path control, the varying dynamics with respect to the position and heading orientation of the helicopter motivates the search for an alternate attitude control strategy.

4.1.2 Robot Manipulator Control

Although the structure of the Platform system defined in (2.106),

$$\hat{\bar{\boldsymbol{M}}}(\hat{\bar{\boldsymbol{q}}})\ddot{\hat{\bar{\boldsymbol{q}}}} + \hat{\bar{\boldsymbol{h}}}(\hat{\bar{\boldsymbol{q}}}, \dot{\hat{\bar{\boldsymbol{q}}}}) = \hat{\bar{\boldsymbol{\tau}}}(\hat{\bar{\boldsymbol{q}}}, \dot{\hat{\bar{\boldsymbol{q}}}}, \vec{\boldsymbol{u}}), \tag{2.106}$$

is similar to those for a typical robot manipulator system [40, 41], their actuation mechanisms, represented by the term $\hat{\bar{\boldsymbol{\tau}}}(\bar{\boldsymbol{q}}, \dot{\hat{\bar{\boldsymbol{q}}}}, \vec{\boldsymbol{u}})$, are quite different. While most robot manipulator systems are

actuated at the joints by servo motors, the joints of the Platform system utilized in this research are not actuated. The actuation in the Platform system comes indirectly from the rotor thrust through the helicopter body connection to the platform linkages. This means conventional control strategies for robot manipulator systems cannot be applied directly to the Platform system.

Nonetheless, the concept of applying robot manipulator control to the Platform system is appealing due to the well established stability results available in the literature. This provides motivation for a *virtual joint control* scheme where the helicopter control signals are generated in such a way that the resulting torque generated indirectly at the joints of the Platform system by the rotor thrust would *mimic* those computed by joint control laws intended for a similarly configured robot manipulator system. The term *virtual* here makes reference to the indirect control of the joint torque of the Platform system through the helicopter rotor input. With the result of Theorem 2.1, such *virtual joint control* scheme are equally applicable to the UAV system, provided the coordinate change defined in Lemma 2.1 is utilized. Therefore, *virtual* can also be referring to the control scheme for a stand alone helicopter attached to a *virtual* platform, such as in the UAV system explored previously. A *stable* control scheme for the Platform system can then be obtained by defining a stable manipulator joint control law as the *mimicking* target for the *virtual joint controller*. Since linear joint PD control law with positive gains has been shown capable of stabilizing the nonlinear dynamics of rigid link robot manipulator systems [76, 40], a virtual joint PD control law will be derived and investigated for both the Platform and the UAV systems.

4.2 Virtual Joint PD Control

The Virtual Joint Proportional-Derivative (PD) Control strategy consists of two steps: desired joint torque generation and joint torque approximation. A block diagram for the closed-loop Virtual Joint PD Control method applied to the Platform system is shown in Figure 4.2. The desired torque generation step, represented by the first sub-block in Figure 4.2, is relatively straight forward. The desired joint torque experienced by each of the platform joints are computed from independent linear PD control laws. The use of PD control laws is motivated by the well established stability result pertaining to the control of rigid link robot manipulator systems [40]: when PD control signals are applied at the joints, the resulting system dynamic behaviour

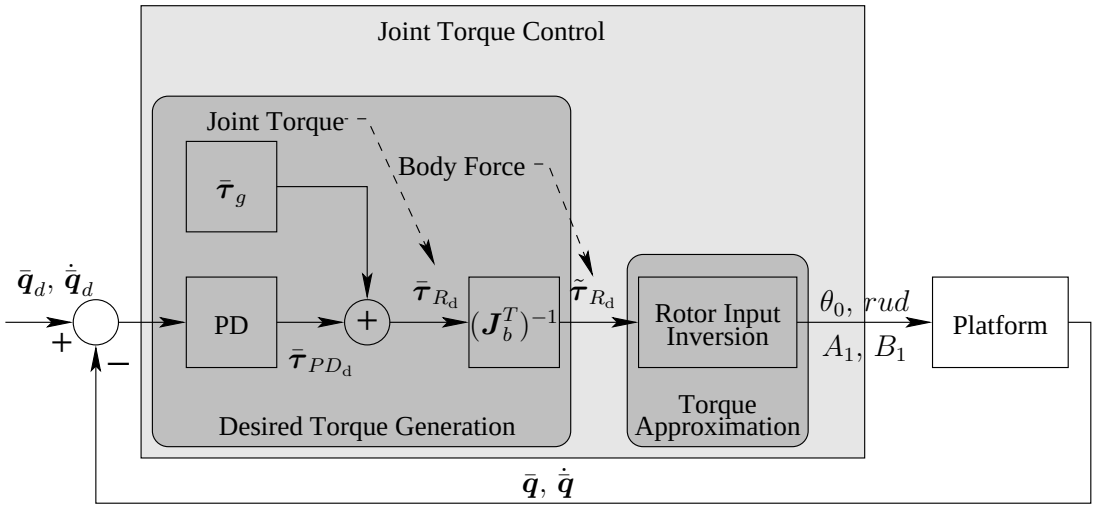

Figure 4.2: Joint PD Control

would be analogous to having springs and dampers mounted at the joints. This provides stability to the system as energy is dissipated through the dampers over time. As a result, if the helicopter rotor can be controlled to generate thrust whose projection to the joints matches *exactly* to those computed from the linear PD control laws, the Virtual Joint PD Control strategy should provide a stable control law for the Platform system.

However, due to the coupling constraints imposed by the helicopter dynamics, exact matching between the desired and the actual joint torque is achievable only under limited conditions. An illustration of such coupling constraints can be observed through the main rotor cyclic inputs of the helicopter. Both the helicopter side forces ($\hat{X}_{\mathrm{R}}$ and $\hat{Y}_{\mathrm{R}}$ in (2.52) and (2.53)) and rotation (rolling and pitching) moments ($\hat{L}_{\mathrm{R}}$ and $\hat{M}_{\mathrm{R}}$ in (2.55) and (2.56)) are controlled through the cyclic inputs (through $\hat{C}_{\mathrm{lon}}$ and $\hat{C}_{\mathrm{lat}}$ in (2.42) and (2.43)). This means, in general, the side force cannot be specified independently from the moments. The root cause for this stemmed from the helicopter system being under-actuated, having six Degree-Of-Freedom (DOF) but only four control inputs are available:

$$(\theta_0, A_1, B_1, \theta_{\mathrm{tail}}) \longrightarrow (\hat{X}_{\mathrm{R}}, \hat{Y}_{\mathrm{R}}, \hat{Z}_{\mathrm{R}}, \hat{L}_{\mathrm{R}}, \hat{M}_{\mathrm{R}}, \hat{N}_{\mathrm{R}}).$$

Therefore, special provision has to be developed in the joint torque approximation step for computing the rotor control inputs that would permit the resulting joint torque to *mimic* the

$$(\bar{\boldsymbol{q}}_1, \bar{\boldsymbol{q}}_2, \bar{\boldsymbol{q}}_3, \bar{\boldsymbol{q}}_4, \bar{\boldsymbol{q}}_5, \bar{\boldsymbol{q}}_6) + (\dot{\bar{\boldsymbol{q}}}_1, \dot{\bar{\boldsymbol{q}}}_2, \dot{\bar{\boldsymbol{q}}}_3, \dot{\bar{\boldsymbol{q}}}_4, \dot{\bar{\boldsymbol{q}}}_5, \dot{\bar{\boldsymbol{q}}}_6)$$

$$\downarrow \text{Step 1: desired joint torque generation}$$

$$(\hat{X}_{R_\mathrm{d}}, \hat{Y}_{R_\mathrm{d}}, \hat{Z}_{R_\mathrm{d}}, \hat{L}_{R_\mathrm{d}}, \hat{M}_{R_\mathrm{d}}, \hat{N}_{R_\mathrm{d}})$$

$$\downarrow \text{Step 2: joint torque approximation}$$

$$(\theta_0, A_1, B_1, \theta_{\mathrm{tail}})$$

Figure 4.3: Virtual Joint PD Control Algorithm Overview

desired PD control values as close as possible. An overview of the Virtual Joint PD Control algorithm is depicted in Figure 4.3.

There is one particular case under which exact matching of the desired joint torque can be realized. It is when the system is at trim, where the net body force and moment acting on the helicopter is zero. Recall the trim computation from Section 3.1, in addition to having the inputs set to their trim values ($\hat{\vec{\boldsymbol{u}}}_\mathrm{e}$), the roll and pitch angles of the helicopter are required to be maintained at a specific trim level (ϕ_e and θ_e) to achieve trim:

$$(\hat{X}_{R_\mathrm{d}}, \hat{Y}_{R_\mathrm{d}}, \hat{Z}_{R_\mathrm{d}}, \hat{L}_{R_\mathrm{d}}, \hat{M}_{R_\mathrm{d}}, \hat{N}_{R_\mathrm{d}}) \longrightarrow (\theta_0, A_1, B_1, \theta_{\mathrm{tail}}) + (\phi_\mathrm{e}, \theta_\mathrm{e}).$$

Consequently, the desired joint torque should be generated in a way that would drive the system towards the trim condition to ensure close approximation of the desired joint torque can be attained. This corresponds to setting the reference/desired joint angles and rates of the PD control law to their corresponding trim values.

4.2.1 Desired PD Joint Torque

For a rigid link 6 DOF robot manipulator system similar to the Platform system, a linear PD control law specifying the desired decoupled servo torque to be generated at the joints can be written as

$$\bar{\boldsymbol{\tau}}_{PD_\mathrm{d}} = \begin{bmatrix} K_{p_1} & & \vec{\mathbf{0}} \\ & \ddots & \\ \vec{\mathbf{0}} & & K_{p_6} \end{bmatrix} \begin{bmatrix} \Delta q_1 \\ \vdots \\ \Delta q_6 \end{bmatrix} + \begin{bmatrix} K_{d_1} & & \vec{\mathbf{0}} \\ & \ddots & \\ \vec{\mathbf{0}} & & K_{d_6} \end{bmatrix} \begin{bmatrix} \Delta \dot{q}_1 \\ \vdots \\ \Delta \dot{q}_6 \end{bmatrix}, \tag{4.1}$$

where $\Delta q_i \triangleq q_{i_\mathrm{d}} - q_i$ are the difference between the desired (q_{i_d}) and the actual (q_i) joint angles; $\Delta \dot{q}_i \triangleq \dot{q}_{i_\mathrm{d}} - \dot{q}_i$ are the difference between the desired ($\dot{q}_{i_\mathrm{d}}$) and the actual ($\dot{q}_i$) joint rate; and K_{p_i} and K_{d_i} are the proportional and derivative gains respectively.

As mentioned previously, it is desirable to use the trim values for the joint angles and rates as the reference quantities to allow for close approximation to be achieved by the rotor thrust. This means when controlling the helicopter for hover or slow moving operations, the desired/reference joint rates are set to zero:

$$\dot{\boldsymbol{q}}_{i_\mathrm{d}} = 0.$$

While the trim values for the roll and pitch angles are used as the reference for q_6 and q_5 respectively, the reference values for the position and heading orientation of the helicopter are set according to the control objectives. In the case of hover, the reference position and heading orientation (q_1 to q_4) would be constant. If the control objective is for path/way-point following, the desired trajectory will be used as the reference.

Recall the PD controllers are analogous to springs and dampers at the joints for the robot manipulator system. This means that the system will be stable for all positive PD gain values [40] with the upper-bound limit imposed by actuator saturation. In the context of the virtual joint PD control, actuator saturation represents the maximum joint torque achievable through the rotor thrust projection, which is a complex function of the rotor stall conditions [10, 12]. As such, contrary to the robot manipulator case, determination of the torque saturation limit for the Platform system is not trivial. However, for hover or slow moving operations, with sufficiently small PD gains, the Platform system should remain stable without reaching the saturation limit.

The desired PD joint torque $\bar{\boldsymbol{\tau}}_{PD_\mathrm{d}}$, combined with the gravitational compensation term $\bar{\boldsymbol{\tau}}_\mathrm{g}$, forms the total desired joint torque $\bar{\boldsymbol{\tau}}_{R_\mathrm{d}}$ to be generated by the rotors:

$$\bar{\boldsymbol{\tau}}_{R_\mathrm{d}} = \bar{\boldsymbol{\tau}}_{PD_\mathrm{d}} + \bar{\boldsymbol{\tau}}_\mathrm{g}. \tag{4.2}$$

Recall the gravitational component in the Platform model is dependent on the configuration

setting through the apparent weight W_{p} and the elbow joint angle q_2:

$$\bar{\boldsymbol{\tau}}_{\mathrm{g}} = \begin{bmatrix} 0 \\ W_{\mathrm{p}} l_3 \cos(q_2) \\ 0 \\ 0 \\ 0 \\ 0 \end{bmatrix}, \tag{4.3}$$

where W_{p} is defined in (3.6).

Once the desired joint torque $\bar{\boldsymbol{\tau}}_{R_{\mathrm{d}}}$ has been obtained, it is then projected to the body-fixed frame of the helicopter through the transpose of the Jacobian matrix inverse $(\boldsymbol{J}_{\mathrm{b}}^T)^{-1}$ to obtain the corresponding desired rotor force and moment $\tilde{\boldsymbol{\tau}}_{R_{\mathrm{d}}}$ acting on the helicopter body:

$$\tilde{\boldsymbol{\tau}}_{R_{\mathrm{d}}} = (\boldsymbol{J}_{\mathrm{b}}^T)^{-1} \bar{\boldsymbol{\tau}}_{R_{\mathrm{d}}}. \tag{4.4}$$

4.2.2 Joint Torque Approximation

The body force and moment obtained from (4.4), combined with the rotor force equations in (2.52)–(2.57), specify six desired conditions to be satisfied by the four rotor control inputs:

$$(\hat{X}_{\mathrm{R}}, \hat{Y}_{\mathrm{R}}, \hat{Z}_{\mathrm{R}}, \hat{L}_{\mathrm{R}}, \hat{M}_{\mathrm{R}}, \hat{N}_{\mathrm{R}}) \longrightarrow (\theta_0, A_1, B_1, \theta_{\mathrm{tail}}).$$

As mentioned, such condition can only be satisfied when the system is at trim (that is, its roll and pitch are at ϕ_{e} and θ_{e} respectively). The objective of the torque approximation step, represented by the second sub-block in Figure 4.2, is to define a *rotor input inversion algorithm* that computes the rotor inputs from the desired body force and moment ($\tilde{\boldsymbol{\tau}}_{R_{\mathrm{d}}}$) in such a way that the resulting joint torque experienced by the Platform would match the desired joint torque when the system is at trim and remain *close* to them when the system is deviated from trim.

There are many ways to define the rotor input inversion algorithm. For instance, the rotor control inputs $\vec{\boldsymbol{u}}$ can be obtained by posing the task of rotor input inversion as an optimization problem where the objective (cost) function is represented by the error function defined as the norm of the difference between the desired body force and moment vector ($\tilde{\boldsymbol{\tau}}_{R_{\mathrm{d}}}$) and the

computed values from the rotor inputs ($\tilde{\boldsymbol{\tau}}_{\mathrm{R}}$),

$$Error = ||\tilde{\boldsymbol{\tau}}_{R_{\mathrm{d}}} - \tilde{\boldsymbol{\tau}}_{\mathrm{R}}||. \tag{4.5}$$

The norm in the above error function represents a *size* measurement of how close the computed body force and moment are in mimicking the desired values. From (2.52)–(2.57) and the rotor equations derived in Appendix B.2, it can be seen that this represents a nonlinear global optimization problem, which are typically solved by nonlinear programming methods such as simulated annealing or genetic algorithms. However, there are three issues with solving for the rotor input inversion as a global optimization problem: computational complexity, local optimum solution, and lack of physical intuition. Due to the coupling and nonlinear nature of the rotor dynamics, the computational complexity involved in solving for the optimal solution to the rotor input inversion problem is necessarily high. This makes global optimization methods a poor choice for computing the rotor control inputs as the computation is to be repeated at every sampling period. Second, although the use of a local optimal (or sub-optimal) solution for rotor control does not contradict the requirement of *close* approximation as specified by the Virtual Joint Control scheme, the existence of multiple local optimal solutions poses the challenge of defining appropriate criteria for selection among these solutions. This leads to the third issue of the lack of physical intuition associated with global optimization solutions. Each of the possible global optimization solutions (optimal or otherwise sub-optimal/local) represents an approximation to the desired control effort applied to the Platform system. However, given two possible solutions, there is no direct correlation between the effect on the physical control objective, such as the amount of control effort involved for the individual joints, and the degree of proximity to the desired behaviour. This motivates the derivation of an alternate approach for solving the rotor input inversion problem.

From the structure of the rotor input inversion problem, the difficulty in obtaining a solution lies in the under-actuated nature of the problem: there are six objective criteria to be satisfied via four available control inputs. If the number of objective criteria can be reduced to match the number of available control inputs, that is choosing only four of the possible six criteria in formulating a solution, such a reduced problem could potentially be solved efficiently either analytically (albeit with a highly nonlinear and complex solution) or numerically (via

iterative numerical methods or look-up table heuristics). With this approach, the solution from the reduced problem can then be updated or adjusted to obtain a *close* approximation of the desired control behaviour in that the residual error associated with the two remaining criteria are bounded. Although this would result in a suboptimal solution to the rotor input inversion problem, depending on the combination of the criteria chosen, physical insight and intuition can be employed explicitly in the setting of the trade-off between multiple possible solutions.

In the subsequent sections, two of the fifteen possible combinations ($\binom{6}{4} = \frac{6!}{4!2!} = 15$) of selecting any four equations out of the six objective criteria, represented by the body force and moment equations in (2.52)–(2.57), will be explored due to their apparent physical interpretations. The first combination corresponds to selecting the desired force for the body z axis ($\hat{Z}_{R_\mathrm{d}}$) in (2.54), together with the three desired body moments ($\hat{L}_{R_\mathrm{d}}$, $\hat{M}_{R_\mathrm{d}}$ and $\hat{N}_{R_\mathrm{d}}$) in (2.55)–(2.57). This choice places emphasis on matching the force and moment associated with the attitude orientation and height of the helicopter. This is analogous to the control objectives of a typical Attitude Control System (ACS), as illustrated in Figure 4.1, in the helicopter control literature [8, 34, 18, 77, 54, 46]. The second combination corresponds to selecting the three linear desired forces ($\hat{X}_{R_\mathrm{d}}$, $\hat{Y}_{R_\mathrm{d}}$ and $\hat{Z}_{R_\mathrm{d}}$) in (2.52)–(2.54), together with the direction moment of the helicopter ($\hat{N}_{R_\mathrm{d}}$) in (2.57). The emphasis in this case is placed on trajectory or path tracking. This is analogous to the control objectives of a Flight Path Control (FPC) system in the literature [15, 53, 14]. The overall rotor input inversion algorithm will then be obtained by combining the solutions of these two options through a weighting factor (ζ). The weighting factor provides an explicit parameter for scaling the relative emphasis of the input between attitude and path control.

Rotor Input Inversion Algorithm - Attitude Tracking Option

In terms of solving for the four control inputs (θ_0, A_1, B_1 and θ_{tail}) from the four desired criteria represented by the body force $\hat{Z}_{R_\mathrm{d}}$ and the moments $\hat{L}_{R_\mathrm{d}}$, $\hat{M}_{R_\mathrm{d}}$ and $\hat{N}_{R_\mathrm{d}}$,

$$(\hat{Z}_{R_\mathrm{d}}, \hat{L}_{R_\mathrm{d}}, \hat{M}_{R_\mathrm{d}}, \hat{N}_{R_\mathrm{d}}) \longrightarrow (\theta_0, A_1, B_1, \theta_{\mathrm{tail}})$$

in the Attitude Tracking option, notice that (2.54)–(2.57) are implicit functions of the control inputs through the rotor coefficients, such as $\hat{C}_{\mathrm{T}}$ and $\hat{C}_{T_{\mathrm{tail}}}$, as the intermediate variables,

$$(\hat{Z}_{R_{\mathrm{d}}}, \hat{L}_{R_{\mathrm{d}}}, \hat{M}_{R_{\mathrm{d}}}, \hat{N}_{R_{\mathrm{d}}}) \longrightarrow (\hat{C}_{\mathrm{T}}, \hat{C}_{\mathrm{lon}}, \hat{C}_{\mathrm{lat}}, \hat{C}_{\mathrm{Q}}, \hat{C}_{T_{\mathrm{tail}}}, \hat{C}_{lon_{\mathrm{tail}}}, \hat{C}_{lat_{\mathrm{tail}}}, \hat{C}_{Q_{\mathrm{tail}}}) \longrightarrow (\theta_0, A_1, B_1, \theta_{\mathrm{tail}}).$$

From the definitions of the rotor coefficients given by (2.40), (2.42), (2.43) and (2.45), together with the definitions of the various rotor state variables, such as the inflow factor λ_1 in (2.35) and the rotor flapping coefficients a_0, $a_{1,\mathrm{s}}$ and $b_{1,\mathrm{s}}$ defined in Appendix B, it can be seen that the rotor input inversion problem is coupled and highly nonlinear. Although an analytical solution to this problem is feasible, the closed form solution has not been obtained due to the prohibitively expensive complexity involved in computing it. Instead, an alternate approach through iteration would be employed.

The desired body force and moments in (2.54)–(2.57) are affine in the rotor coefficients. This can be exploited by solving for an analytical solution for a subset of the rotor coefficients. In the iteration process, the rotor coefficients are divided into two groups. In the first step of the iteration, initial values are chosen for the first group of rotor coefficients ($\hat{C}_{\mathrm{Q}}$, $\hat{C}_{Q_{\mathrm{tail}}}$, $\hat{C}_{lon_{\mathrm{tail}}}$, $\hat{C}_{lat_{\mathrm{tail}}}$). These initial values, together with the desired body force and moment values, are then substituted into (2.54)–(2.57) to obtain intermediate values for the second group of the rotor coefficients ($\hat{C}_{\mathrm{T}}$, $\hat{C}_{\mathrm{lon}}$, $\hat{C}_{\mathrm{lat}}$, $\hat{C}_{T_{\mathrm{tail}}}$). In the second step, the values of the first group of rotor coefficients are updated by solving the corresponding rotor coefficient equations (from (2.40), (2.42), (2.43) and (2.45)) with the computed values of the second group of rotor coefficients. The iteration process then repeats until the coefficients converged to within a specified tolerance level. Figure 4.4 shows an overview of this iterative rotor input inversion algorithm.

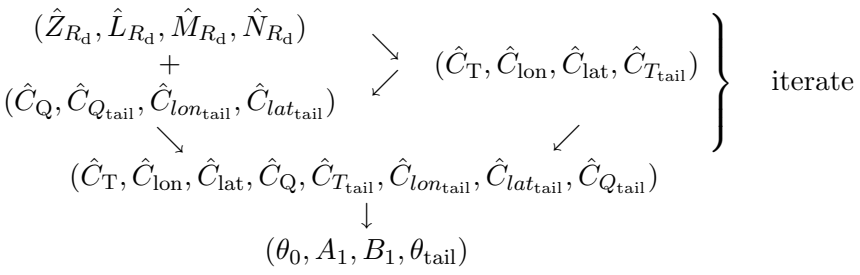

Figure 4.4: Rotor Input Inversion – Attitude Tracking (Overview)

In this case, after the initial values are assigned to the first group of rotor coefficients ($\hat{C}_{\mathrm{Q}}$, $\hat{C}_{Q_{\mathrm{tail}}}$, $\hat{C}_{lon_{\mathrm{tail}}}$, $\hat{C}_{lat_{\mathrm{tail}}}$), the values of the second group of the rotor coefficients ($\hat{C}_{\mathrm{T}}$, $\hat{C}_{\mathrm{lon}}$, $\hat{C}_{\mathrm{lat}}$, $\hat{C}_{T_{\mathrm{tail}}}$) are obtained by solving for them from (2.54)–(2.57):

$$\hat{C}_{\mathrm{T}} = -\hat{Z}_{R_{\mathrm{d}}} + \hat{A}(\hat{\Omega}\hat{R})^2\big[\hat{C}_{lon_{\mathrm{tail}}}\sin(\eta_t) + \hat{C}_{lat_{\mathrm{tail}}}\cos(\eta_t)\big] \tag{4.6}$$

$$\begin{aligned}\hat{C}_{\mathrm{lon}} = {} & \frac{\cos(\eta_m)}{\hat{h}_{\mathrm{M}}}(\hat{M}_{R_{\mathrm{d}}} - \hat{l}_{\mathrm{M}}\hat{Z}_{R_{\mathrm{d}}}) - \frac{\sin(\eta_m)}{\hat{l}_{\mathrm{T}}\hat{h}_{\mathrm{M}} - \hat{l}_{\mathrm{M}}\hat{h}_{\mathrm{T}}}\big[\hat{l}_{\mathrm{T}}\hat{L}_{R_{\mathrm{d}}} + \hat{h}_{\mathrm{T}}(\hat{N}_{R_{\mathrm{d}}} + \hat{C}_{\mathrm{Q}})\big] \\ & + \hat{A}(\hat{\Omega}\hat{R})^2\hat{R}\frac{\cos(\eta_m)}{\hat{h}_{\mathrm{M}}}\Big[\hat{C}_{Q_{\mathrm{tail}}} - \hat{C}_{lon_{\mathrm{tail}}}\Big(\big[\hat{l}_{\mathrm{T}} - \hat{l}_{\mathrm{M}}\big]\sin(\eta_t) + \hat{h}_{\mathrm{T}}\cos(\eta_t)\Big) \\ & \qquad - \hat{C}_{lat_{\mathrm{tail}}}\Big(\big[\hat{l}_{\mathrm{T}} - \hat{l}_{\mathrm{M}}\big]\cos(\eta_t) - \hat{h}_{\mathrm{T}}\sin(\eta_t)\Big)\Big]\end{aligned} \tag{4.7}$$

$$\begin{aligned}\hat{C}_{\mathrm{lat}} = {} & \frac{\sin(\eta_m)}{\hat{h}_{\mathrm{M}}}(-\hat{M}_{R_{\mathrm{d}}} + \hat{l}_{\mathrm{M}}\hat{Z}_{R_{\mathrm{d}}}) - \frac{\cos(\eta_m)}{\hat{l}_{\mathrm{T}}\hat{h}_{\mathrm{M}} - \hat{l}_{\mathrm{M}}\hat{h}_{\mathrm{T}}}\big[\hat{l}_{\mathrm{T}}\hat{L}_{R_{\mathrm{d}}} + \hat{h}_{\mathrm{T}}(\hat{N}_{R_{\mathrm{d}}} + \hat{C}_{\mathrm{Q}})\big] \\ & + \hat{A}(\hat{\Omega}\hat{R})^2\hat{R}\frac{\sin(\eta_m)}{\hat{h}_{\mathrm{M}}}\Big[-\hat{C}_{Q_{\mathrm{tail}}} + \hat{C}_{lon_{\mathrm{tail}}}\Big(\big[\hat{l}_{\mathrm{T}} - \hat{l}_{\mathrm{M}}\big]\sin(\eta_t) + \hat{h}_{\mathrm{T}}\cos(\eta_t)\Big) \\ & \qquad + \hat{C}_{lat_{\mathrm{tail}}}\Big(\big[\hat{l}_{\mathrm{T}} - \hat{l}_{\mathrm{M}}\big]\cos(\eta_t) - \hat{h}_{\mathrm{T}}\sin(\eta_t)\Big)\Big]\end{aligned} \tag{4.8}$$

$$\hat{C}_{T_{\mathrm{tail}}} = \frac{\hat{l}_{\mathrm{M}}\hat{L}_{R_{\mathrm{d}}} + \hat{h}_{\mathrm{M}}(\hat{N}_{R_{\mathrm{d}}} + \hat{C}_{\mathrm{Q}})}{\hat{A}(\hat{\Omega}\hat{R})^2(\hat{l}_{\mathrm{T}}\hat{h}_{\mathrm{M}} - \hat{l}_{\mathrm{M}}\hat{h}_{\mathrm{T}})}. \tag{4.9}$$

Next, the updated value for the main rotor torque coefficient $\hat{C}_{\mathrm{Q}}$ is obtained by first computing the intermediate control inputs (θ_0, A_1 and B_1) for the main rotor from (2.40), (2.42) and (2.43) using the values of $\hat{C}_{\mathrm{T}}$, $\hat{C}_{\mathrm{lon}}$ and $\hat{C}_{\mathrm{lat}}$ obtained from (4.6)–(4.8),

$$(\hat{C}_{\mathrm{T}}, \hat{C}_{\mathrm{lon}}, \hat{C}_{\mathrm{lat}}) \longrightarrow (\theta_0, A_1, B_1).$$

This coupled and nonlinear inverse mapping is solved analytically using Maple™ [1]. The intermediate control inputs are then substituted into (2.45) to obtain the updated $\hat{C}_{\mathrm{Q}}$ value. The corresponding calculation for the tail rotor would use (2.40) to compute the θ_{tail} input with the value of $\hat{C}_{T_{\mathrm{tail}}}$ obtained from (4.9). The updated value for the tail planar force coefficients $\hat{C}_{lon_{\mathrm{tail}}}$ and $\hat{C}_{lat_{\mathrm{tail}}}$, and the torque coefficient $\hat{C}_{Q_{\mathrm{tail}}}$, are then computed from (2.42), (2.43) and (2.45) with the cyclic input for the tail rotor set to zero. This iterative process is summarized in Figure 4.5.

[1] Maple™ is a symbolic mathematical tool made by Maplesoft. Maple™ is a trademark of Waterloo Maple Inc.

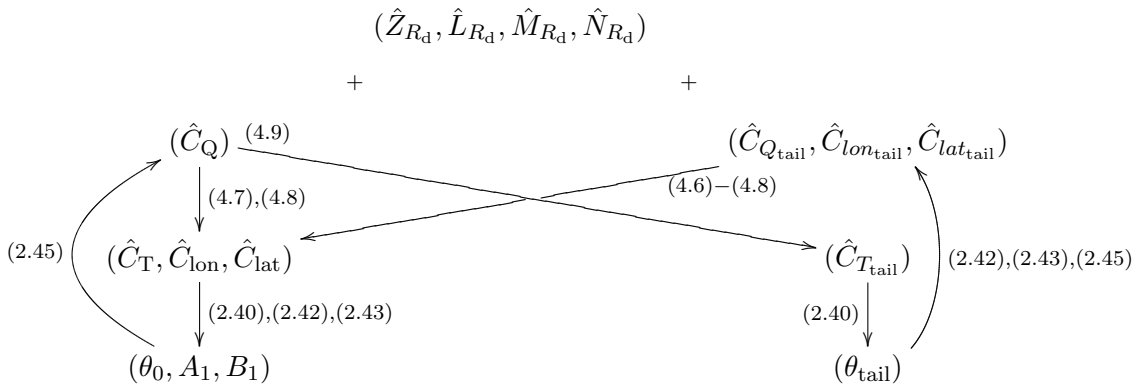

Figure 4.5: Rotor Input Inversion – Attitude Tracking (Expanded)

The choice of the rotor coefficients used in the reverse computation of the rotor control inputs is motivated by their physical interpretation. The thrust coefficients $\hat{C}_\mathrm{T}$ and $\hat{C}_{T_\mathrm{tail}}$ are selected since they have a direct correlation with the collective inputs of the two rotors θ_0 and θ_tail. The main rotor planar force coefficients $\hat{C}_\mathrm{lon}$ and $\hat{C}_\mathrm{lat}$ are used because of their similar relationship with the cyclic inputs A_1 and B_1.

Rotor Input Inversion Algorithm - Position Tracking Option

The difference between the Position Tracking option and the Attitude Tracking option is in the selection of the desired criteria. In the Position Tracking option, the desired criteria are represented by the linear body forces $\hat{X}_{R_\mathrm{d}}$, $\hat{Y}_{R_\mathrm{d}}$ and $\hat{Z}_{R_\mathrm{d}}$, and the direction moment $\hat{N}_{R_\mathrm{d}}$,

$$(\hat{X}_{R_\mathrm{d}}, \hat{Y}_{R_\mathrm{d}}, \hat{Z}_{R_\mathrm{d}}, \hat{N}_{R_\mathrm{d}}) \longrightarrow (\theta_0, A_1, B_1, \theta_\mathrm{tail}).$$

The iteration steps for the Position Tracking option are identical to those for the Attitude Tracking option with the exception of using (2.52)–(2.54) and (2.57) instead of (2.54)–(2.57) when solving for the rotor coefficients ($\hat{C}_\mathrm{T}$, $\hat{C}_\mathrm{lon}$, $\hat{C}_\mathrm{lat}$, $\hat{C}_{T_\mathrm{tail}}$). The resulting expressions of the

rotor coefficients are given by:

$$\hat{C}_{\mathrm{T}} = -\hat{Z}_{R_{\mathrm{d}}} + \hat{A}(\hat{\Omega}\hat{R})^2\big[\hat{C}_{lon_{\mathrm{tail}}}\sin(\eta_t) + \hat{C}_{lat_{\mathrm{tail}}}\cos(\eta_t)\big] \tag{4.10}$$

$$\begin{aligned}\hat{C}_{\mathrm{lon}} = \cos(\eta_m)\Big(&- \hat{X}_{R_{\mathrm{d}}} + \hat{A}(\hat{\Omega}\hat{R})^2\big[\hat{C}_{lat_{\mathrm{tail}}}\sin(\eta_t) - \hat{C}_{lon_{\mathrm{tail}}}\cos(\eta_t)\big]\Big) \\ &+ \frac{\sin(\eta_m)}{\hat{l}_{\mathrm{M}} - \hat{l}_{\mathrm{T}}}(\hat{l}_{\mathrm{T}}\hat{Y}_{R_{\mathrm{d}}} + \hat{N}_{R_{\mathrm{d}}} + \hat{C}_{\mathrm{Q}})\end{aligned} \tag{4.11}$$

$$\begin{aligned}\hat{C}_{\mathrm{lat}} = \sin(\eta_m)\Big(&\hat{X}_{R_{\mathrm{d}}} + \hat{A}(\hat{\Omega}\hat{R})^2\big[\hat{C}_{lon_{\mathrm{tail}}}\cos(\eta_t) - \hat{C}_{lat_{\mathrm{tail}}}\sin(\eta_t)\big]\Big) \\ &+ \frac{\cos(\eta_m)}{\hat{l}_{\mathrm{M}} - \hat{l}_{\mathrm{T}}}(\hat{l}_{\mathrm{T}}\hat{Y}_{R_{\mathrm{d}}} + \hat{N}_{R_{\mathrm{d}}} + \hat{C}_{\mathrm{Q}})\end{aligned} \tag{4.12}$$

$$\hat{C}_{T_{\mathrm{tail}}} = -\frac{\hat{N}_{R_{\mathrm{d}}} + \hat{l}_{\mathrm{M}}\hat{Y}_{R_{\mathrm{d}}} + \hat{C}_{\mathrm{Q}}}{\hat{A}(\hat{\Omega}\hat{R})^2(\hat{l}_{\mathrm{M}} - \hat{l}_{\mathrm{T}})}. \tag{4.13}$$

The rotor input inversion algorithm for the Position Tracking case is summarized in Figure 4.6. Comparing the iterative algorithms for the Attitude and Position tracking options presented in

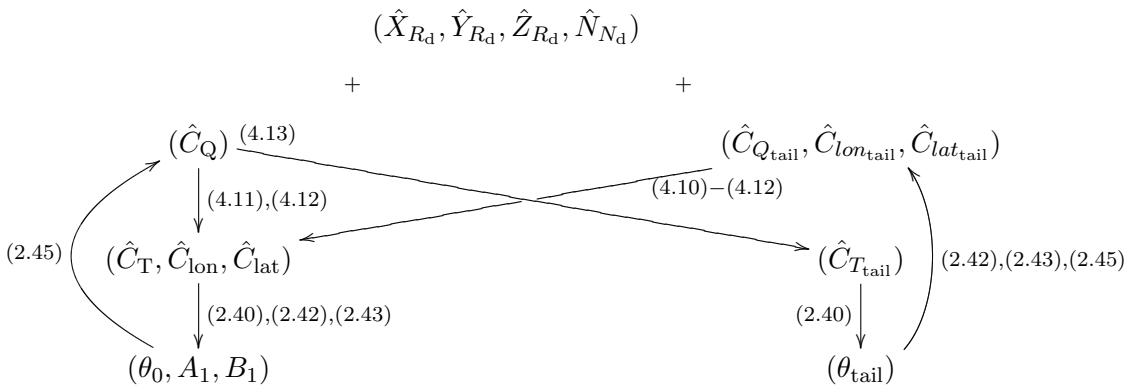

Figure 4.6: Rotor Input Inversion – Position Tracking (Expanded)

Figure 4.5 and Figure 4.6 respectively, it can be seen that the difference in the choice of the desired criteria affects only the equations used in computing the rotor coefficients ($\hat{C}_{\mathrm{T}}$, $\hat{C}_{\mathrm{lon}}$, $\hat{C}_{\mathrm{lat}}$, $\hat{C}_{T_{\mathrm{tail}}}$). For example, instead of using (4.6) to solve for $\hat{C}_{\mathrm{T}}$, (4.10) is used in the Position tracking option.

Rotor Input Inversion Algorithm - Weighted Scale Option

The control inputs obtained from both of the options introduced previously ignore two of the six desired criteria. In the case of the Attitude Tracking option, the criteria on the planar forces $\hat{X}_{R_\mathrm{d}}$ and $\hat{Y}_{R_\mathrm{d}}$ are not utilized; for the Position Tracking option, it is the criteria on the rolling and pitching moment $\hat{L}_{R_\mathrm{d}}$ and $\hat{M}_{R_\mathrm{d}}$. The effect of this is that while the system would track the selected criteria closely by design, the performance regarding the tracking of the remaining criteria can vary depending on the operating condition of the system. For example, in the Attitude Tracking option, since the planar forces of the helicopter are not controlled directly, the helicopter could drift horizontally while maintaining a constant attitude and orientation. As a result, a weighted scale option is derived to utilize all six of the desired criteria.

In the Weighted Scale option, the same iteration procedure, shown in Figure 4.5, for the Attitude Tracking option is first carried out to obtain a set of converged values for the eight rotor coefficients. Let this set of converged rotor coefficient values be designated with the subscript ZLMN to indicate they are obtained from the Attitude Tracking option by solving (2.54)–(2.57):

$$(\hat{C}_\mathrm{T}, \hat{C}_\mathrm{lon}, \hat{C}_\mathrm{lat}, \hat{C}_\mathrm{Q}, \hat{C}_{T_\mathrm{tail}}, \hat{C}_{lon_\mathrm{tail}}, \hat{C}_{lat_\mathrm{tail}}, \hat{C}_{Q_\mathrm{tail}})_\mathrm{ZLMN}.$$

Next, this set of coefficients are separated into three groups:

$$(\hat{C}_{T_\mathrm{tail}}, \hat{C}_{lon_\mathrm{tail}}, \hat{C}_{lat_\mathrm{tail}})_\mathrm{ZLMN}, (\hat{C}_\mathrm{lon}, \hat{C}_\mathrm{lat})_\mathrm{ZLMN}, (\hat{C}_\mathrm{T}, \hat{C}_\mathrm{Q}, \hat{C}_{Q_\mathrm{tail}})_\mathrm{ZLMN}.$$

The first group, $(\hat{C}_{T_\mathrm{tail}}, \hat{C}_{lon_\mathrm{tail}}, \hat{C}_{lat_\mathrm{tail}})_\mathrm{ZLMN}$, together with the desired planar forces $(\hat{X}_{R_\mathrm{d}}, \hat{Y}_{R_\mathrm{d}})$, are substituted into (4.14) and (4.15) to obtain updated values of the main rotor planar coefficients $(\hat{C}_\mathrm{lon}, \hat{C}_\mathrm{lat})_\mathrm{XY}$,

$$\begin{aligned}(\hat{C}_\mathrm{lon})_\mathrm{XY} = \cos(\eta_m)\Big(&- \hat{X}_{R_\mathrm{d}} + \hat{A}(\hat{\Omega}\hat{R})^2\big[\hat{C}_{lat_\mathrm{tail}}\sin(\eta_t) - \hat{C}_{lon_\mathrm{tail}}\cos(\eta_t)\big]\Big) \\ &- \sin(\eta_m)\big[\hat{Y}_{R_\mathrm{d}} + \hat{A}(\hat{\Omega}\hat{R})^2\hat{C}_{T_\mathrm{tail}}\big] \qquad (4.14)\\ (\hat{C}_\mathrm{lat})_\mathrm{XY} = \sin(\eta_m)\Big(&\hat{X}_{R_\mathrm{d}} + \hat{A}(\hat{\Omega}\hat{R})^2\big[\hat{C}_{lon_\mathrm{tail}}\cos(\eta_t) - \hat{C}_{lat_\mathrm{tail}}\sin(\eta_t)\big]\Big) \\ &- \cos(\eta_m)\big[\hat{Y}_{R_\mathrm{d}} + \hat{A}(\hat{\Omega}\hat{R})^2\hat{C}_{T_\mathrm{tail}}\big]. \qquad (4.15)\end{aligned}$$

The expressions for $\hat{C}_\mathrm{lon}$ and $\hat{C}_\mathrm{lat}$ in (4.14) and (4.15) are obtained by solving for them from

(2.52) and (2.53). At this point, there are two sets of main rotor longitudinal and lateral planar force coefficients: one set is from the second group of rotor coefficients obtained from the Attitude Tracking option calculations, denoted by $(\hat{C}_{\text{lon}}, \hat{C}_{\text{lat}})_{\text{ZLMN}}$; the second set, denoted as $(\hat{C}_{\text{lon}}, \hat{C}_{\text{lat}})_{\text{XY}}$, is obtained from (4.14) and (4.15) where the desired planar force criteria $\hat{X}_{R_{\text{d}}}$ and $\hat{Y}_{R_{\text{d}}}$ are utilized. These two sets of main rotor planar force coefficients are then combined through a scaling factor ζ to obtained a weighted average value:

$$(\hat{C}_{\text{lon}})_{\text{Scaled}} = \zeta(\hat{C}_{\text{lon}})_{\text{XY}} + (1-\zeta)(\hat{C}_{\text{lon}})_{\text{ZLMN}} \tag{4.16}$$

$$(\hat{C}_{\text{lat}})_{\text{Scaled}} = \zeta(\hat{C}_{\text{lat}})_{\text{XY}} + (1-\zeta)(\hat{C}_{\text{lat}})_{\text{ZLMN}} \tag{4.17}$$

where the scaling factor ζ has value between 0 and 1:

$$0 \leq \zeta \leq 1.$$

The scaled value of the main rotor planar force coefficients $(\hat{C}_{\text{lon}}, \hat{C}_{\text{lat}})_{\text{Scaled}}$ are then combined with the main rotor thrust coefficient $(\hat{C}_{\text{T}})_{\text{ZLMN}}$ from the third rotor coefficient group of the Attitude Tracking option to solve for the main rotor control inputs (θ_0, A_1, B_1) from (2.40), (2.42) and (2.43). Finally, the control input for the tail rotor θ_{tail} is computed from (2.40) based on the tail rotor thrust coefficient value $(\hat{C}_{T_{\text{tail}}})_{\text{ZLMN}}$ obtained from the Attitude Tracking option. An overview of this Weighted Scale option is depicted in Figure 4.7.

Notice from Figure 4.7 that the Weighted Scale option extends the Attitude Tracking option by modifying the computation of the rotor control inputs $(\theta_0, A_1, B_1, \theta_{\text{tail}})$ using the updated weighted average value of the planar coefficients $(\hat{C}_{\text{lon}}, \hat{C}_{\text{lat}})_{\text{Scaled}}$; while keeping the values for the rotor thurst coefficients $(\hat{C}_{\text{T}}, \hat{C}_{T_{\text{tail}}})_{\text{ZLMN}}$ obtained from the Attitude Tracking iterations constant during the computation. In doing so, the rotor force and moment generated from these rotor control inputs would not satisfy all six of the desired criteria represented by (2.52)–(2.57) exactly. Instead, only (2.54) for $\hat{Z}_{R_{\text{d}}}$ would be satisfied exactly, as it does not depend on the planar coefficients $(\hat{C}_{\text{lon}}, \hat{C}_{\text{lat}})$. For the rest of the criteria, the agreement between the desired and generated force and moment would depend on the value of the scaling factor ζ. When $\zeta = 0$, the update steps in (4.16) and (4.17) would effectively be turned off and the Weighted Scale option is reverted back to the Attitude Tracking case, where the desired criteria for $\hat{Z}_{R_{\text{d}}}$, $\hat{L}_{R_{\text{d}}}$, $\hat{M}_{R_{\text{d}}}$ and $\hat{N}_{R_{\text{d}}}$ in (2.54)–(2.57) are satisfied; while (2.52) and (2.53) for $\hat{X}_{R_{\text{d}}}$ and $\hat{Y}_{R_{\text{d}}}$ are not. On

the other hand, for $\zeta = 1$, the resulting body force and moment would satisfy (2.52)–(2.54) for $\hat{X}_{R_\mathrm{d}}$, $\hat{Y}_{R_\mathrm{d}}$ and $\hat{Z}_{R_\mathrm{d}}$; but not for $\hat{L}_{R_\mathrm{d}}$, $\hat{M}_{R_\mathrm{d}}$ and $\hat{N}_{R_\mathrm{d}}$ in (2.55)–(2.57). The behaviour in this case would be similar to the Position Tracking option. For other values of ζ, the degree of agreement between the resulting and the desired body force and moment would fall between the Attitude Tracking and the Position Tracking cases. For control purposes, the scaling factor ζ provides an explicit tuning parameter in selecting the trade-off between Attitude Tracking and Position Tracking.

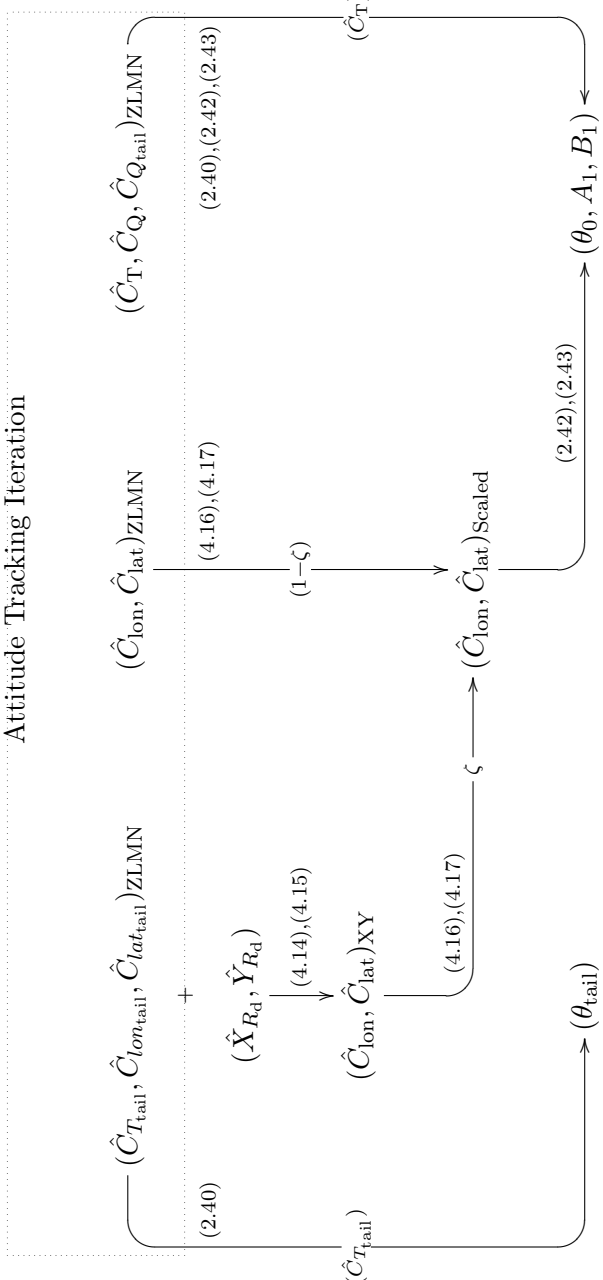

Figure 4.7: Rotor Input Inversion – Weighted Scale (Expanded)

4.3 Extension to Virtual Joint Control

The central theme in the Virtual Joint PD Control technique presented in the previous section is the idea of approximating stable joint control torques by the rotor generated forces and torques. In that case, the desired stable joint control torques are computed through independent linear joint PD control laws with constant gains. The choice of PD control laws is motivated by its stability characteristic with respect to the platform linkage system [40]. In Ravichandran [78], a general class of nonlinear controller of the form:

$$\bar{\boldsymbol{\tau}} = \bar{\boldsymbol{\tau}}_{\mathrm{ff}}(\bar{\boldsymbol{q}}) + \bar{\boldsymbol{\tau}}_{\mathrm{fb}}(\bar{\boldsymbol{q}}, \dot{\bar{\boldsymbol{q}}}, \bar{\boldsymbol{q}}_{\mathrm{d}}, \dot{\bar{\boldsymbol{q}}}_{\mathrm{d}}), \tag{4.18}$$

has been shown to provide stable control for a class of rigid body robot manipulator system that includes the platform structure employed in this research. The $\bar{\boldsymbol{\tau}}_{\mathrm{ff}}$ component represents the feed-forward term; while the $\bar{\boldsymbol{\tau}}_{\mathrm{fb}}$ component represents the feedback term. The PD control law presented in the previous section is a special case of this class of nonlinear controller where the feed-forward term corresponds to the gravitational term $\bar{\boldsymbol{\tau}}_{\mathrm{g}}$ defined in (4.3):

$$\bar{\boldsymbol{\tau}}_{\mathrm{ff}} = \bar{\boldsymbol{\tau}}_{\mathrm{g}}. \tag{4.19}$$

The feedback term corresponds to the desired PD joint torque defined in (4.1):

$$\bar{\boldsymbol{\tau}}_{\mathrm{fb}} = \bar{\boldsymbol{\tau}}_{PD_{\mathrm{d}}}. \tag{4.20}$$

For the purpose of this research, another special sub-class of nonlinear PD controllers described by (4.18) will be considered for extending the Virtual Joint Control scheme. The gains of this sub-class of nonlinear controllers have the following form:

$$K_{P_{\mathrm{i}}}(\Delta q_i) = \frac{k_{p_{\mathrm{i}}}}{a_i + |\Delta q_i|} \qquad \text{and} \qquad K_{D_{\mathrm{i}}}(\Delta q_i, \Delta \dot{q}_i) = \frac{k_{d_{\mathrm{i}}}}{(b_i + |\Delta q_i|)(c_i + |\Delta \dot{q}_i|)}, \tag{4.21}$$

where the gains are time varying functions of the system states ($\bar{\boldsymbol{q}}$ and $\dot{\bar{\boldsymbol{q}}}$). For positive values of the parameters a_i, b_i and c_i ($a_i > 0$, $b_i > 0$ and $c_i > 0$), the resulting control torque generated

by this nonlinear PD control law will be bounded, that is,

$$\left|\frac{\Delta q_i}{a_i + |\Delta q_i|}\right| < 1 \qquad \text{and} \qquad \left|\frac{\Delta \dot{q}_i}{c_i + |\Delta \dot{q}_i|}\right| < 1. \tag{4.22}$$

With this choice of gain structure, the values of the parameters can be optimized for performance objectives while the actuator saturation limits can be satisfied through the selection of appropriate nominal gain values k_{p_i} and k_{d_i} [78]. This form of gain structure provides *nonlinear* damping (through the derivative gains) to the system. When the error signals (Δq_i and $\Delta \dot{q}_i$) are large, the effective damping will be small; conversely, when the system is near the desired operating point, the increased effective damping will provide a settling characteristic similar to those of over-damped systems. For the proportional gains, they provide large control action when nearing the desired operating point to improve the speed of the output response but reduce the control effort when far away from the operating point to avoid actuator saturation. As such, this property could be employed in the desired torque generation step to address the rotor torque saturation issue through parameter and gain adjustments.

4.4 Simulation

4.4.1 Test Scenarios

Three test scenarios have been implemented in simulation to illustrate the performance of the Virtual Joint Control strategy proposed earlier in this chapter. The first test scenario is a simple hover test where the Platform system starts with an initial condition slightly deviated from the trim point. The goal here is to illustrate the controller's ability to stabilize the system around its trim condition. In the second test scenario, a desired trajectory in the form of a square in the horizontal plane is specified for the Platform system to follow. This highlights the controller's ability for path following while maintaining a constant heading. In addition, the sharp corners of the square path would induce a step-like response of the system for observation. Finally, in the third test scenario, the Platform system is tasked to follow a trajectory resembling the shape of a Figure-8. The Figure-8 trajectory will reside on a plane tilted 45° from the horizontal plane so that the platform helicopter is required to track both horizontal position and height. Furthermore, the desired heading of the helicopter is set tangent to the path. As such, this

test requires the controller to track both the position and attitude of the helicopter along the trajectory. Details of each of these scenarios are given in the following sections.

Hover with Initial Perturbation

The initial condition for this test is obtained by changing the roll and pitch trim values from Table 3.1 by ten percent to

$$q_5 = -0.058 \text{ rad} \approx -3.3^\circ \qquad \text{and} \qquad q_6 = 0.058 \text{ rad} \approx 3.3^\circ. \tag{4.23}$$

The goal of the controller is to compensate for this initial disturbance and restore the helicopter back to its hover trim state as given by Table 3.1:

$$q_{5_e} = -0.053 \text{ rad} \approx -3.0^\circ \qquad \text{and} \qquad q_{6_e} = 0.053 \text{ rad} \approx 3.0^\circ. \tag{4.24}$$

The desired position and heading for the PD joint controllers are set to the Platform home position and heading:

$$q_1 = 0 \text{ rad}, \qquad q_2 = 0 \text{ rad}, \qquad q_3 = 0 \text{ rad}, \qquad q_4 = 0 \text{ rad}. \tag{4.25}$$

The corresponding desired joint rates are all set to zero for hover.

Horizontal Tracking of a Square path

Joint	q_1	q_2	q_3	q_4	q_5	q_6
Value (rad)	0	0	0	0	-0.053	0.053

Table 4.1: Initial Condition – Square Path

In this test, the helicopter starts at trim from its home position, which corresponds to the joint angle settings listed in Table 4.1.

The desired trajectory first leads the helicopter forward for 30 cm. Then the helicopter will slide abruptly sideways to the right for 30 cm. From there, the helicopter will fly backward for another 30 cm before sliding sideways to the left back to the home position. The heading of the helicopter is to be kept pointing forward ($\psi = 0^\circ$) during this manoeuvre. Figure 4.8

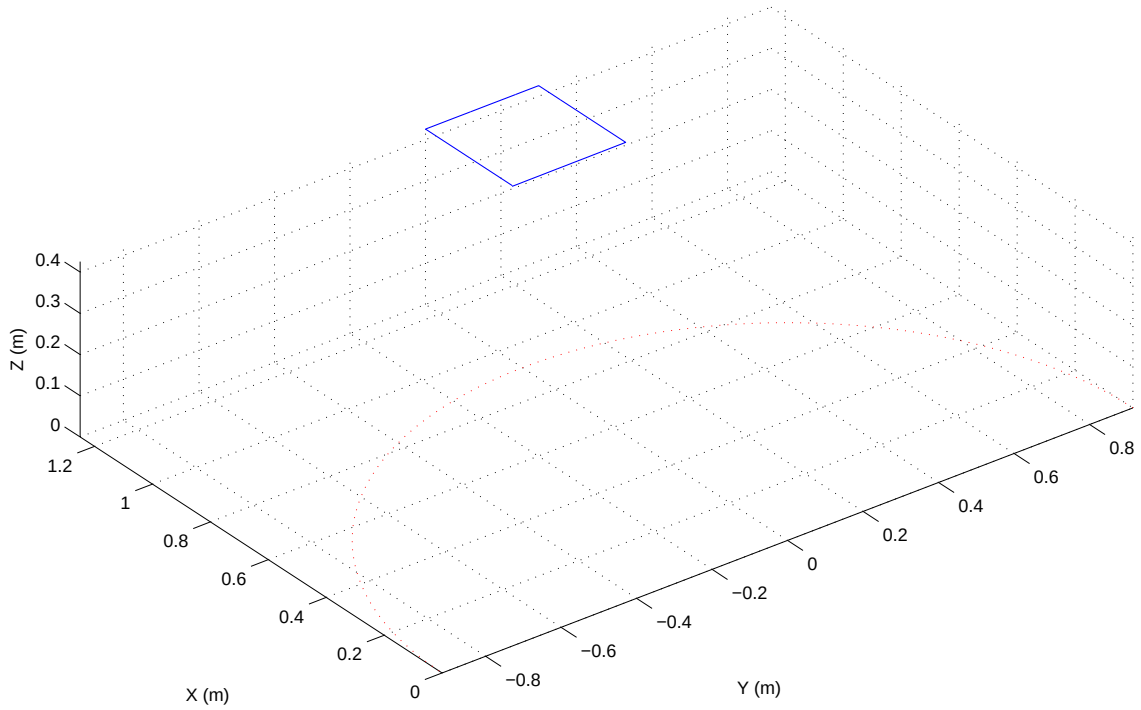

Figure 4.8: Horizontal Square Trajectory

shows this desired square trajectory in a three dimensional (3-D) plot. The dotted semi-circle line represents the projected trajectory of the tip of the main boom onto the ground plane as the base joint (q_1) changes from $-90°$ to $90°$. It is shown in the plot to provide a reference to the ground plane. The desired x and y traces of the helicopter with respect to the platform base (the origin) over time are shown in Figure 4.9. In Figure 4.9, two sets of reference trajectories are shown. The solid line represents the square trajectory with step changes while the dash-dotted line represents the trajectory that changes with a linear slope. Both sets of trajectories will be applied to highlight the effects of the abrupt change in the step reference trajectory. For the desired x position shown in Figure 4.9(a), the step reference (solid line) starts initially at 1.25m, which is 30 cm away from the helicopter initial home position. This is contrasted with the sloped reference (dash-dotted line) where it varies from 0.95 m to 1.25 m (a length of 30 cm) in the first 25 seconds. At around the 60 seconds mark, the reference x position is returned back to 0.95 m via a corresponding step or linear slope change. The reference x position will remain at 0.95 m until the end of the simulation. The desired y position, shown in Figure 4.9(b), follows a similar pattern.

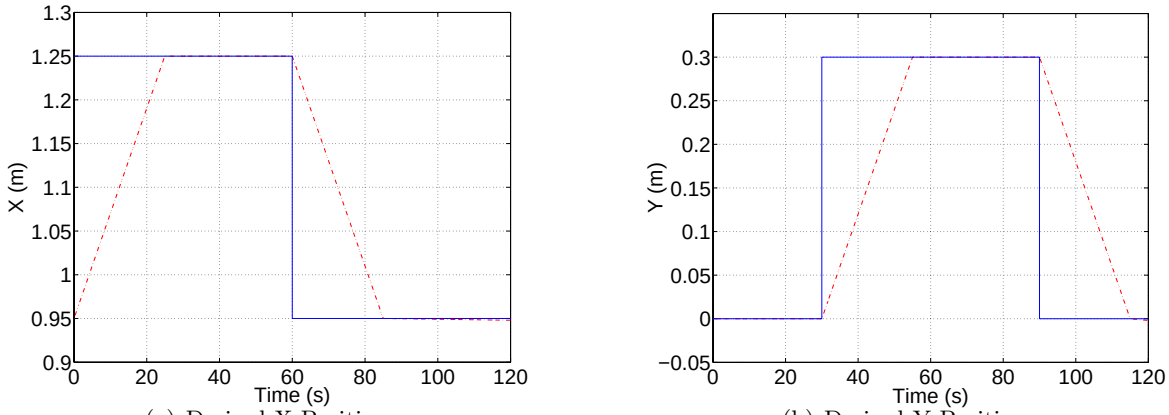

(a) Desired X Position (b) Desired Y Position

Figure 4.9: Reference X and Y Position of the Desired Planar Square Trajectory

The corresponding joint values for these desired Cartesian coordinates are shown in Figure 4.10. Once again, the solid line denotes the reference trajectories for the step change case; while the dash-dotted line denotes the linear slope change case. Here the horizontal planar motion is described through the base (q_1), the slider (q_3) and the yaw (q_4) joints. The x and y position is defined through q_1 and q_3; while the desired heading $\psi = 0°$ is maintained by adjusting the desired Yaw joint angle q_4 so that $\psi = q_1 + q_4 = 0°$. The desired values for the rest of the joints (q_2, q_5 and q_6) are kept to remain the same as their initial values listed in Table 4.1. The desired values for the joint rates are all set to zero.

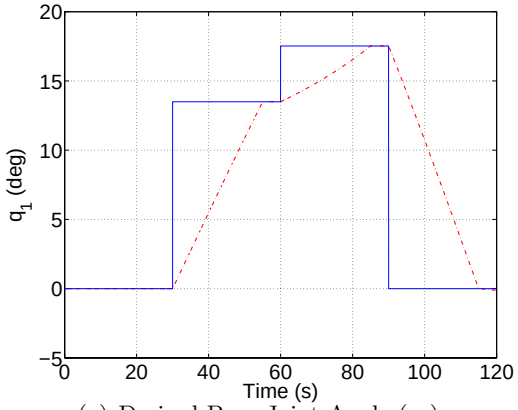

(a) Desired Base Joint Angle (q_1)

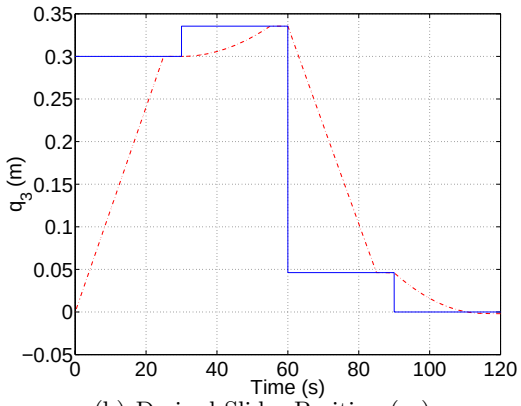

(b) Desired Slider Position (q_3)

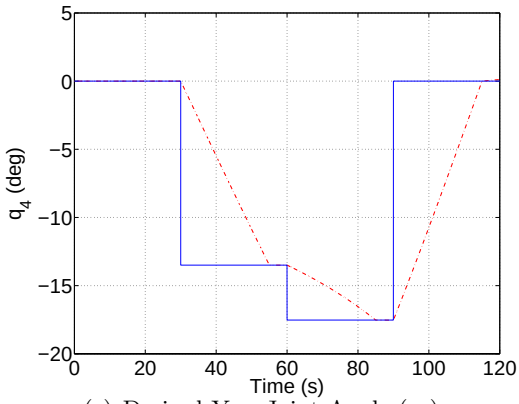

(c) Desired Yaw Joint Angle (q_4)

Figure 4.10: Reference q_1, q_3, q_4 of the Desired Planar Square Trajectory

Figure-8 with changing Heading and Height

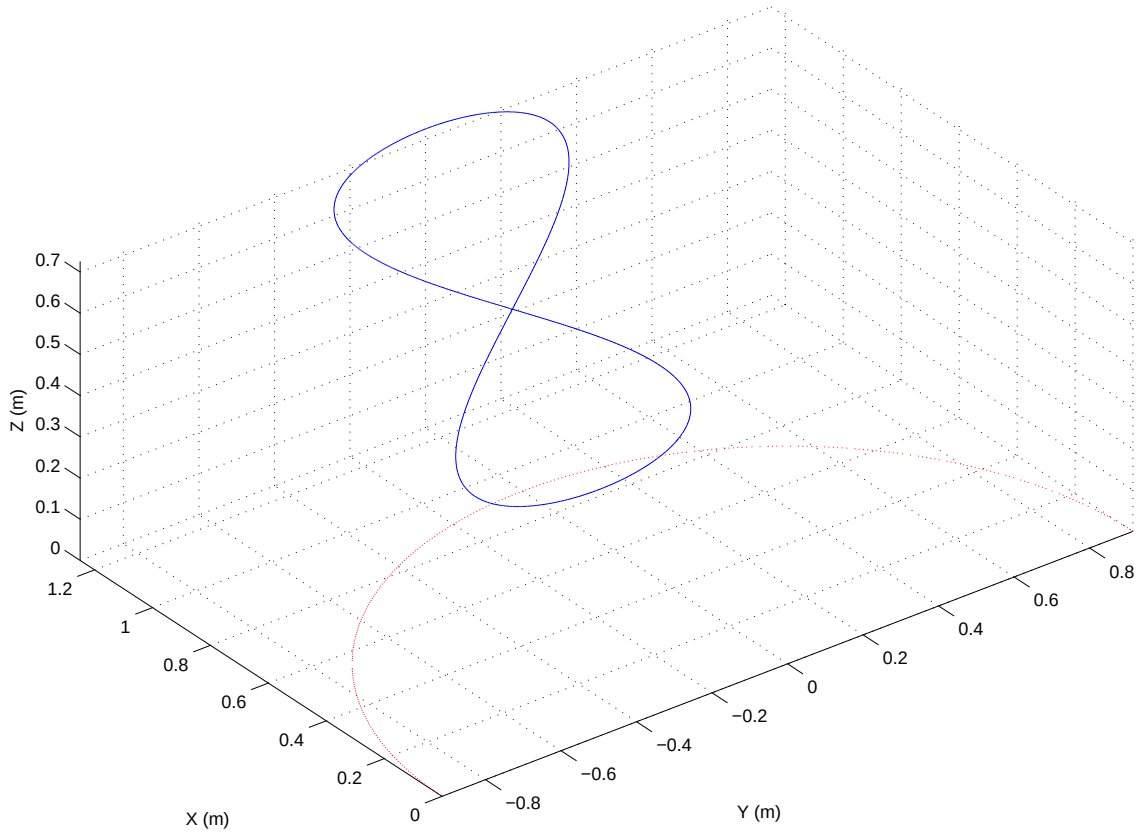

Figure 4.11: Figure-8 Trajectory

In this test, the helicopter again starts at trim from its home position, which corresponds to the joint angle settings listed in Table 4.2. Here, the initial Yaw joint angle q_4 is set so that the helicopter path is tangent to the desired trajectory. The initial point of the helicopter is located at the middle point in the Figure-8 trajectory. The plane on which the Figure-8 trajectory is defined is tilted at 45° about the y-axis so that the height of the helicopter, in addition to its x and y position and heading ψ, will vary as it moves along the path. The 3-D plot of the Figure-8 trajectory is shown in Figure 4.11. Figure 4.12 shows the time histories of the desired x, y, z and ψ values for this Figure-8 trajectory. As the helicopter starts out facing in the positive y-axis direction, it moves up along the z-axis while following the Figure-8 curve. Its heading is maintained to remain tangent to the desired trajectory throughout the manoeuvre. After reaching the highest point at the tip of the Figure-8 (at 30 cm above and 30 cm along

Joint	q_1	q_2	q_3	q_4	q_5	q_6
Value (rad)	0	0	0	$\frac{\pi}{2}$	-0.053	0.053

Table 4.2: Initial Condition – Figure-8 Path

the positive x-axis from the initial position), it starts to descend back to the initial position. As the helicopter passes back through the home position, the desired trajectory brings it to the opposite end of the Figure-8 (at 30 cm below and 30 cm along the negative x-axis from the initial position). The Figure-8 loop trajectory is completed when the helicopter returns back to the initial position. The duration of this manoeuvre is 120 seconds. The time histories of the corresponding desired platform joint values are shown in Figure 4.13. In this case, all four lower joints of the platform are utilized in defining the desired trajectory. The desired values for the remaining roll (q_6) and pitch (q_5) joints are kept at their hover trim values. The desired rates for all of the joints are set to zero as before.

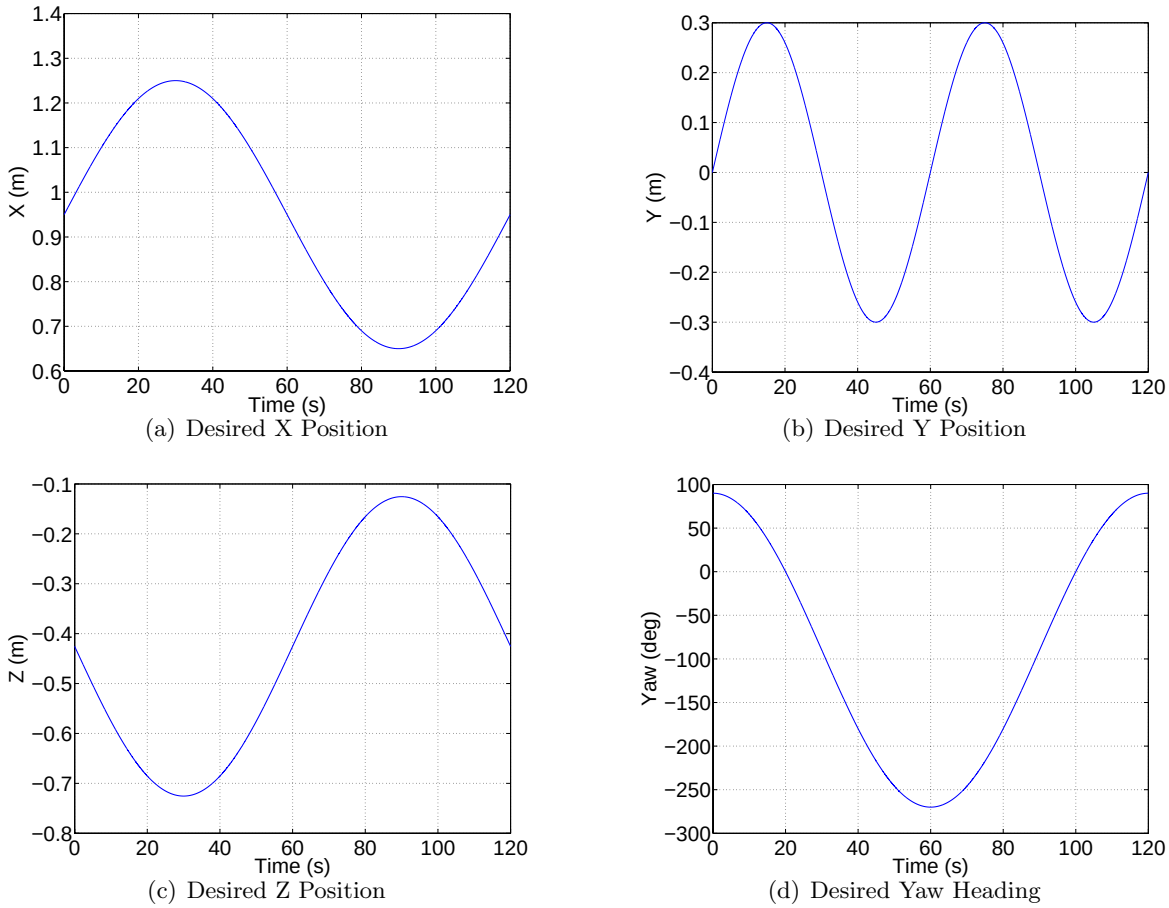

(a) Desired X Position

(b) Desired Y Position

(c) Desired Z Position

(d) Desired Yaw Heading

Figure 4.12: Reference Position and Heading of the Desired Figure-8 Trajectory

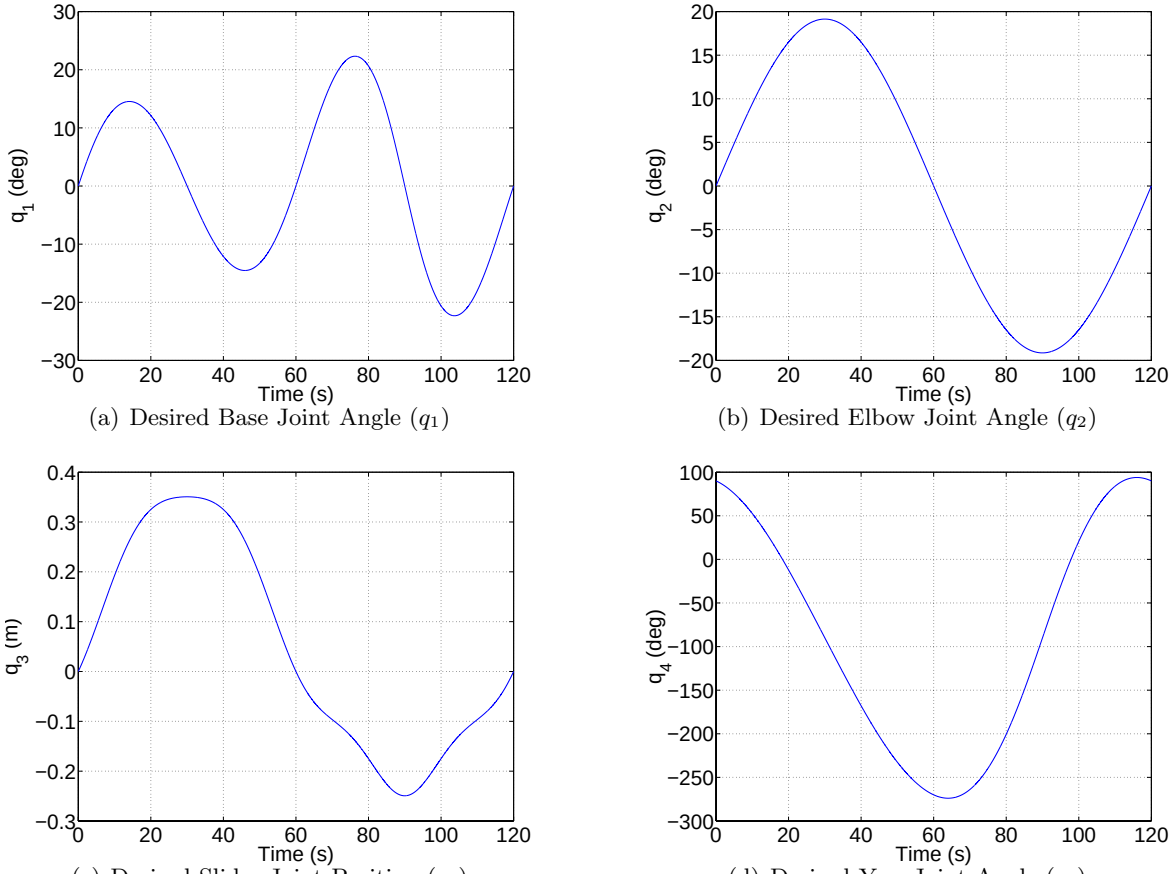

(a) Desired Base Joint Angle (q_1)

(b) Desired Elbow Joint Angle (q_2)

(c) Desired Slider Joint Position (q_3)

(d) Desired Yaw Joint Angle (q_4)

Figure 4.13: Reference Joint Values of the Desired Figure-8 Trajectory

4.4.2 Results

The three test scenarios defined previously have been applied to both the HANGAR and the UAV configurations, defined in Chapter 3, of the Platform system to illustrate the applicability of the Virtual Joint Control technique to the Platform system as well as a stand alone helicopter system. The parameter values used for the simulations can be found in Appendix E.

For each test scenario, three values for the weight scaling factor ζ of the Virtual Joint PD controller are used for comparison. Recall that a value of $\zeta = 0$ corresponds to the Attitude Control option (ACS), which is expected to be able to maintain the attitude orientation and heading of the helicopter but not perform well for position/path tracking tasks. A value of $\zeta = 1$ represents the opposite end of the spectrum where position/path tracking can be achieved at the expense of attitude regulation. The result for a third value of $\zeta = 0.5$ is shown as a representative of the trade-off between Attitude and Path tracking. From (4.16) and (4.17), the value of $\zeta = 0.5$ represents taking the average values of the desired main rotor planar force coefficients ($\hat{C}_{\text{lon}}$ and $\hat{C}_{\text{lat}}$) obtained from the attitude and position tracking criteria defined by (2.52)–(2.57).

An additional set of tests utilizing the nonlinear PD control (NPD) structure defined in Section 4.3 instead of the linear PD controller for the desired torque generation is also shown. This represents an extension to the proposed Virtual Joint Control scheme by using a different stable joint control strategy for the desired joint torque generation. A value of $\zeta = 0.5$ for the weight scaling factor is used for the nonlinear PD controller tests.

		HANGAR			UAV		
	Test Cases / ζ	Hover Test	Square Path	Figure-8	Hover Test	Square Path	Figure-8
PD	0.0	✖	✖	✖	✖	✖	✖
	0.5	❍	❍	❍	❍	❍	❍
	1.0	❑	❑	❑	❑	❑	❑
NPD	0.5	❍	❍	❍	❍	❍	❍

Table 4.3: Summary of Simulation Test Results

The results of the various test cases are summarized in Table 4.3. The circle symbol ❍ indicates a satisfactory tracking in all of the position, heading and attitude of the helicopter has been observed in that test run. The cross symbol ✖ indicates the overall tracking performance is not satisfactory. The square symbol ❑ indicates some aspect of the tracking performance is not satisfactory.

Overall, the results are consistent between the different test scenarios regardless of the Platform configuration. For instance, the results from the Joint PD control with ACS option ($\zeta = 0.0$) are not satisfactory for all three test scenarios under both the HANGAR and UAV configurations; while those from the Joint PD control with the averaging option ($\zeta = 0.5$) yield satisfactory results for all of the test scenarios.

From the results, it can be seen that the averaging option ($\zeta = 0.5$) provides the best overall performance of the cases considered. This is expected since the averaging option represents a trade-off between the Attitude Tracking (ACS) and the Position Tracking (FPC) options. Furthermore, the consistency in the results shown across the two platform configurations (HANGAR and UAV) illustrates that the proposed Virtual Joint Control scheme is indeed applicable to both platform and stand alone helicopter systems. Finally, all three tests scenarios utilizing the nonlinear PD (NPD) control law for desired torque generation produced satisfactory results under both platform configurations. This illustrates the possibility of extending the proposed Virtual Joint Control scheme to use different stable joint control strategies.

Hover with Initial Perturbation

As stated previously, the purpose of this test is to illustrate the controller's ability to stabilize the system after initial perturbation from the equilibrium point. Figure 4.14 shows a set of four three-dimensional (3-D) plots of the position of the helicopter with the HANGAR configuration for the four control options. The four control options are the three values (0.0, 0.5 and 1.0) of the weight scale factor ζ for the linear PD control case and the one nonlinear PD (NPD) control case (with $\zeta = 0.5$). With the exception of the case of the linear PD (PD) with ACS option ($\zeta = 0.0$), the helicopter remained close to the starting *home* position despite the initial attitude perturbation.

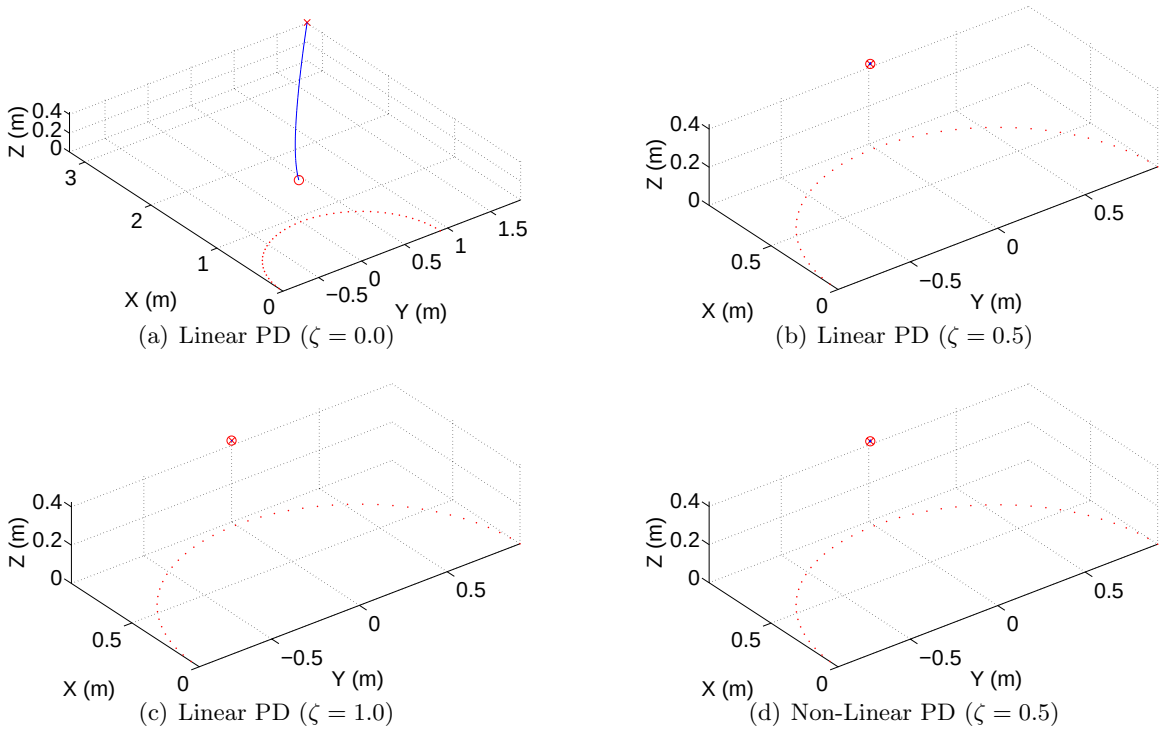

(a) Linear PD ($\zeta = 0.0$)

(b) Linear PD ($\zeta = 0.5$)

(c) Linear PD ($\zeta = 1.0$)

(d) Non-Linear PD ($\zeta = 0.5$)

Figure 4.14: Helicopter 3-D Positions for Hover Tests with HANGAR Configuration

The observed result for the case of PD with ACS option is consistent with the expected performance by the controller. The weight scale factor value of zero ($\zeta = 0.0$) places no emphasis on the helicopter position tracking performance in the controller objective. Instead, the emphasis is placed on tracking the desired attitude of the helicopter. As a consequence, the helicopter position is not regulated by this control strategy. The effect of such emphasis can be observed from the time response plot of the joint variables and their associated rates shown in Figure 4.15. Given the initial perturbation in the helicopter roll and pitch angles, defined in (4.23), the controller is able to achieve steady state tracking with respect to the attitude angles (q_4, q_5 and q_6) within a relatively short duration (about 10 seconds). However, during this transient period, the helicopter has gained translational velocities through the coupled roll and pitch dynamics. This, in turn, causes the position of the helicopter to drift indefinitely.

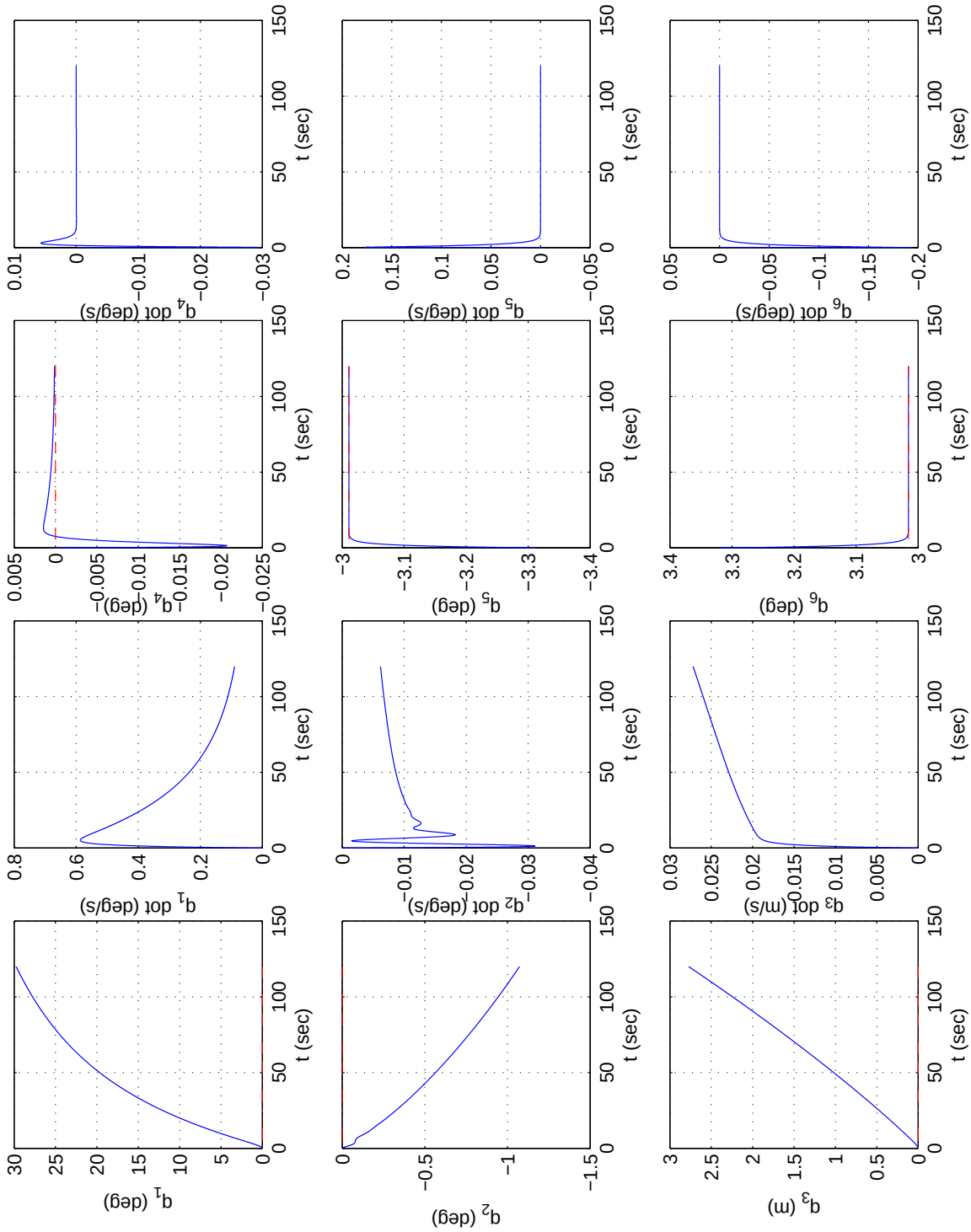

Figure 4.15: Joint Plots for Hover Test with HANGAR configuration using PD ($\zeta = 0.0$)

On the other hand, the value of $\zeta = 1.0$ in the case of PD with FPC option places emphasis in the position tracking performance. As such, the controller in this case is able to maintain the helicopter around its starting *home* position. However, judging the overall performance of the controller by looking at just the 3-D plot in Figure 4.14 is deceptive as it does not provide information on the attitude tracking performance. Mirroring the response of the PD with ACS option (shown in Figure 4.15), Figure 4.16 portrays a split in the emphasis on the performance between position and attitude tracking for the case of PD with FPC option. In this case, while steady state is achieved for the position tracking, excessive oscillations, albeit damped, are observed for the attitude angles (q_4, q_5 and q_6). This contrasts with the ACS option in that while the position of the helicopter is regulated by the controller, the response in the attitude angles are not regulated. Instead of being allowed to drift, like the position in the ACS option, the attitude angles here is constrained to oscillate back and forth by the desired joint torque for position regulation.

This also illustrates the inherent inner-outer loop dynamic characteristics that is typical of helicopter systems. The inner loop consists of the faster attitude (angular) dynamics; while the outer loop consists of the typically slower position (linear) dynamics. It is precisely this inner-outer loop dynamics that motivates the use of hierarchical control structures for helicopter flight control in the literature, such as those found in [4, 23, 20]. With this context, the proposed Virtual Joint Control strategy with the weight scale factor ζ provides a simple and explicit mechanism for shifting the emphasis between the inner and outer loop dynamic performance based on mission objective.

Furthermore, the oscillatory response in Figure 4.16 would suggest it is the same phenomenon that Koo and Sastry [14] observed when direct input-output feedback linearization is applied. Recall the objective of the approximate input-output feedback linearization strategy proposed by Koo and Sastry [14] is to avoid excessive (unstable) oscillations in the internal dynamics of the feedback system. This implies that by adjusting the value of the weight scale factor ζ, the proposed Virtual Joint Control strategy is functionally similar to the approximate input-output feedback linearization strategy proposed by Koo and Sastry [14]. Additional research efforts can be made to establish such potential equivalence between these two strategies in the future.

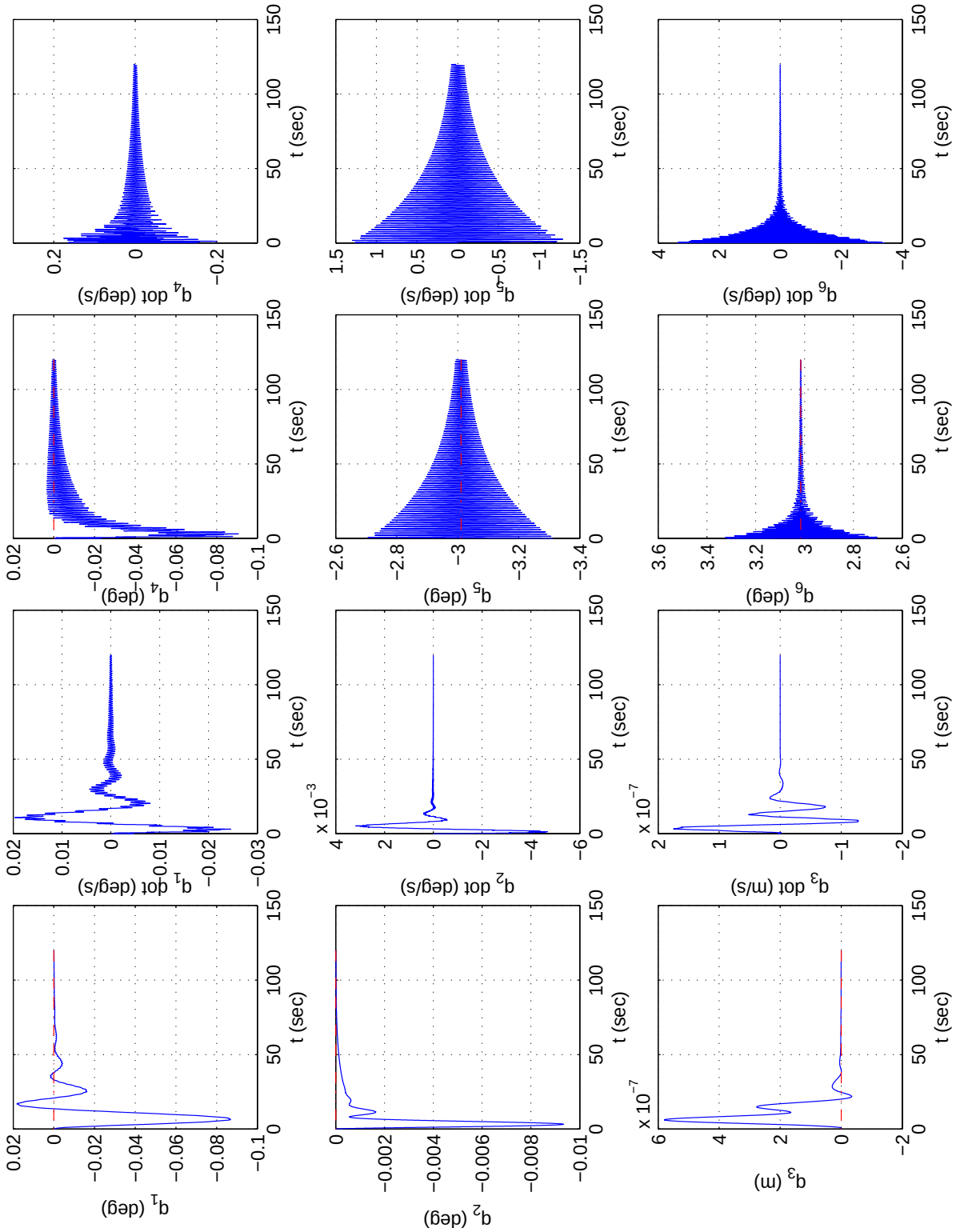

Figure 4.16: Joint Plots for Hover Test with HANGAR configuration using PD ($\zeta = 1.0$)

Figure 4.17 contains the position tracking responses for the UAV configuration. Overall, the results mirror the corresponding cases for the HANGAR configuration. Recall the UAV configuration is defined such that it is equivalent to the stand alone helicopter system mounted on a virtual platform. The results in Figure 4.17 shows that the proposed Virtual Joint Control scheme is applicable to a stand alone helicopter system as well.

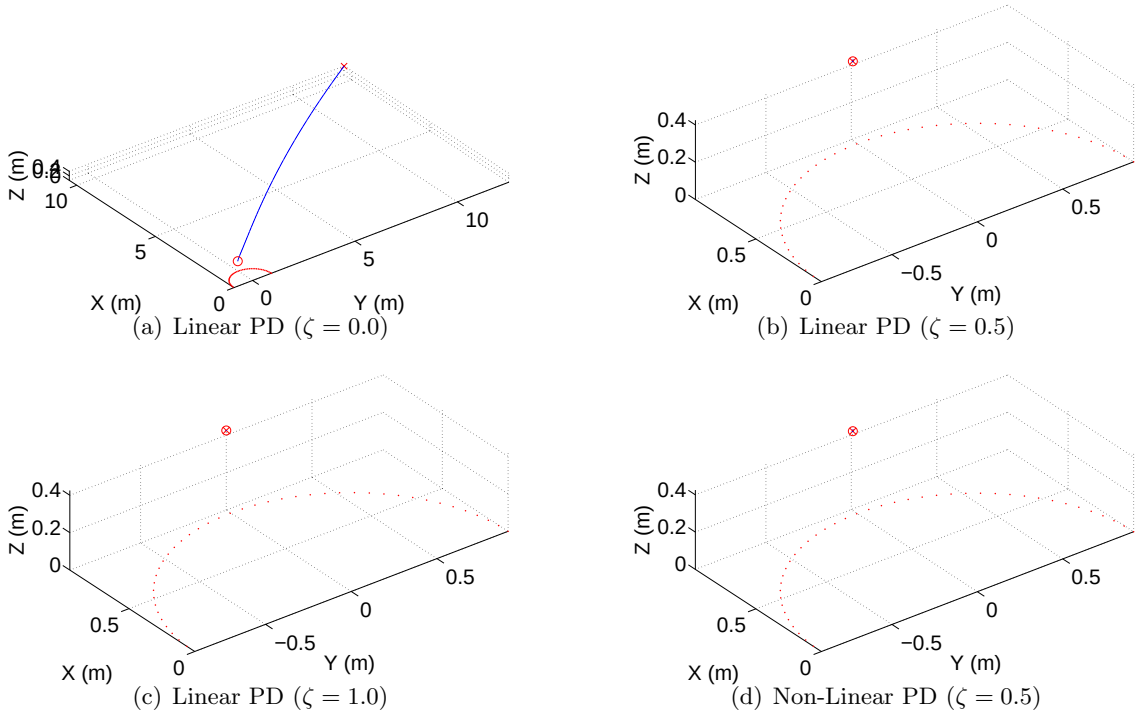

(a) Linear PD ($\zeta = 0.0$)

(b) Linear PD ($\zeta = 0.5$)

(c) Linear PD ($\zeta = 1.0$)

(d) Non-Linear PD ($\zeta = 0.5$)

Figure 4.17: Helicopter 3-D Positions for Hover Tests with UAV Configuration

Finally, the results shown in Figure 4.14 and Figure 4.17 show that for $\zeta = 0.5$, both the linear PD (PD) and nonlinear PD (NPD) controls are equally applicable. Recall the difference between them is in the desired joint torque generation. Figure 4.18 shows the desired torque [2] for the six joints on the platform. The dash-dotted line represents the desired torque generated by the linear PD control scheme; while the solid line represents those generated by the nonlinear PD (NPD) control scheme.

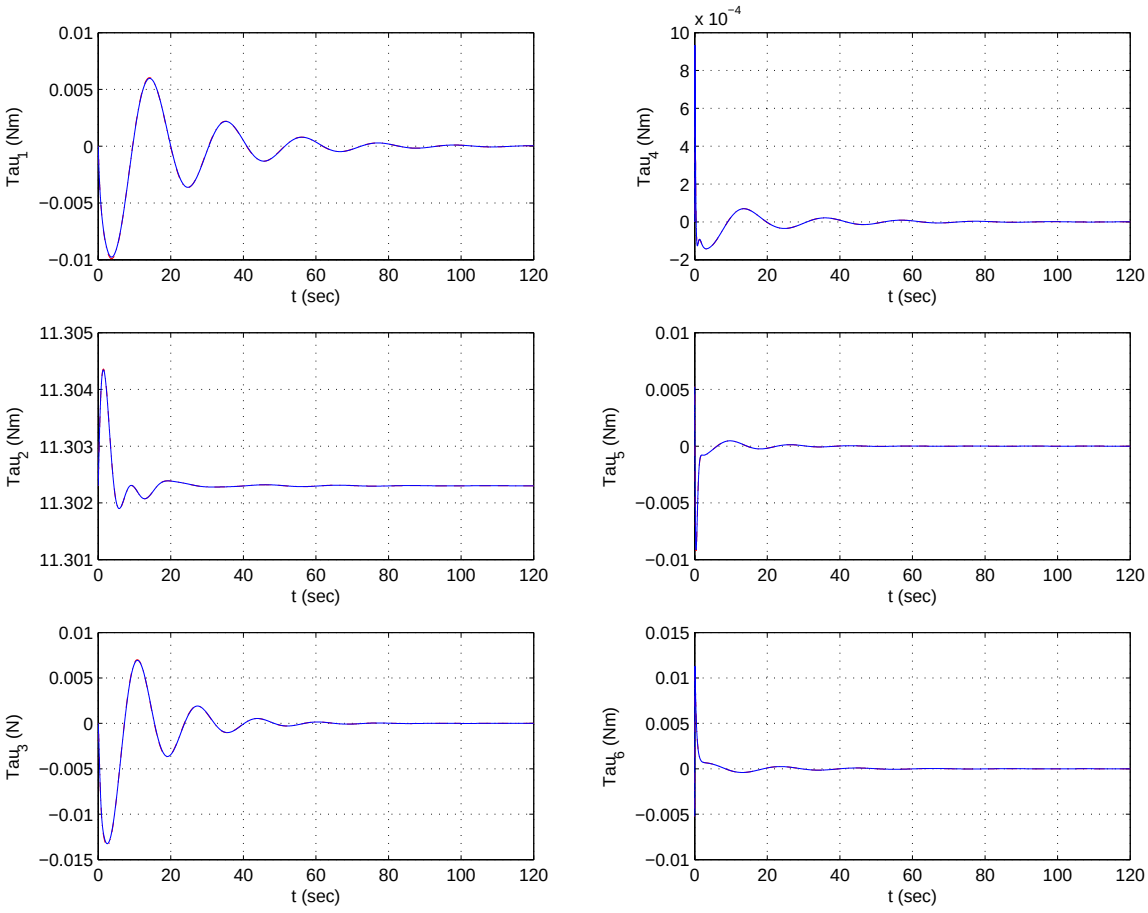

Figure 4.18: Desired Joint Torque Comparison: PD vs NPD (Hover, HANGAR, $\zeta = 0.5$)

[2]Notice that for Joint 3, the slider joint, the reference/desired control τ_3 refers to the linear force along the slider instead of a joint torque. However, for simplicity, all of the desired joint controls are referred to as joint torque, with exceptions to be noted separately when necessary.

From Figure 4.18, it can be seen that the desired control joint torque is nearly identical between the two cases. The is due to the chosen value of the parameters a_i, b_i and c_i. In this case, the values for all three of these parameters are set to 1.0 (see Appendix E). Recall the definition of the nonlinear gains in (4.21), the effective gains for small errors (in both the joint angles and rates), such as in this case, will be dominated by the ratio of the nominal gains (k_{p_i} and k_{d_i}) and the controller parameters (a_i, b_i and c_i):

$$K_{P_i}(\Delta q_i) \approx \frac{k_{p_i}}{a_i} \qquad\qquad K_{D_i}(\Delta q_i, \Delta \dot{q}_i) \approx \frac{k_{d_i}}{b_i c_i} \tag{4.26}$$

For comparison, the values of the nominal gains for the nonlinear PD controllers have been chosen to match their corresponding values for the PD controllers (see Appendix E). As such, the observed similarity in the test results between the PD and the NPD cases are expected for this test scenario.

Figure 4.19 compares the transient yaw (ψ) angle responses of the platform helicopter with the HANGAR configuration under both the PD and the NPD control for a test with large initial error in the yaw angle. In this test, all of the states of the helicopter are set to their trim values at the beginning of the simulation, except for the initial yaw angle. The initial value of the helicopter yaw (ψ) angle is set to 60° to the right. The controllers are instructed to return the yaw angle back to 0° while keeping the helicopter hover at its starting (home) position. When the error is large, the yaw angle under NPD control, denoted by the solid line in Figure 4.19, converges towards the desired value faster than the corresponding case under PD control, denoted by the dash-dotted line. Later, when the yaw angle approaches the desired value, the rate of convergence for the yaw angle is slower under NPD control than it is under PD control. This illustrates the nonlinear damping effect inherent in the NPD control strategy. Despite the smaller initial damping, the magnitude of the initial desired control torque for yaw (corresponds to τ_1 and τ_4) demanded by the NPD controller (denoted by the solid line)

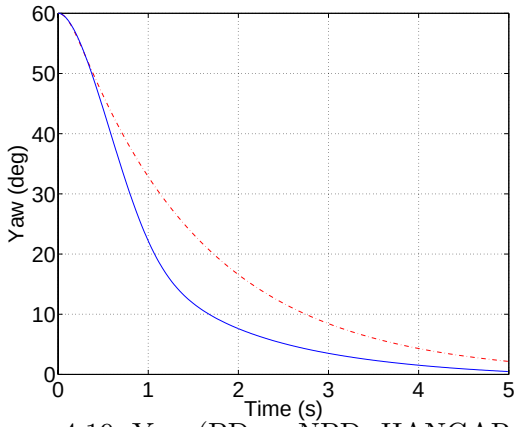

Figure 4.19: Yaw (PD vs NPD, HANGAR, $\zeta = 0.5$)

are smaller when compared to those demanded by the PD controller (denoted by the dash-dotted line), as shown in Figure 4.20. In fact, for the rest of the control torques, the initial joint torque for the NPD controller are either very close to (e.g. τ_2 and τ_3) or smaller than (e.g. τ_5 and τ_6) those for the PD controller. Such behaviour is a direct consequence of the chosen nonlinear gain structure. The degree to which the desired control torque are different can be adjusted through the NPD parameters a_i, b_i and c_i.

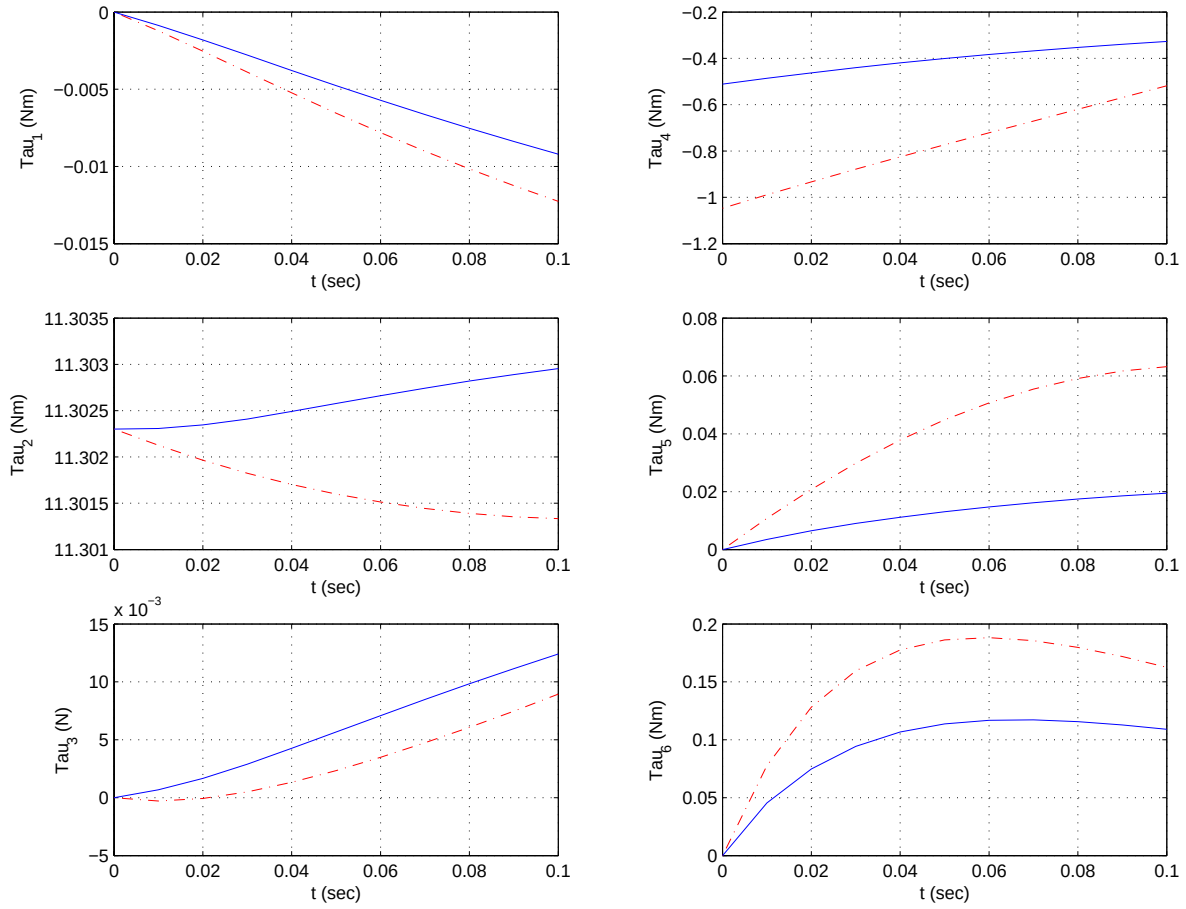

Figure 4.20: Desired Joint Torque Comparison: PD vs NPD (Yaw Turn, HANGAR, $\zeta = 0.5$)

Horizontal Tracking of a Square Path

For the horizontal square path tracking, the objective is to test the controller's ability to both track a planar trajectory as well as handle discontinuity in the desired position trajectory, represented by the corners of the square path. Two sets of square path tests have been performed. In the first set, shown in Figure 4.21, the reference planar square path, denoted by the dash-dotted line, is specified with step changes. Similar to the hover test scenario, the square path test has been applied to the same four control options (three for PD and one for NPD). Overall, the observed responses are consistent with those obtained in the hover case, namely that reasonable path tracking has been observed for all of the options except for the PD with ACS ($\zeta = 0.0$) option. Due to the large initial change in the position reference, all three of the remaining control

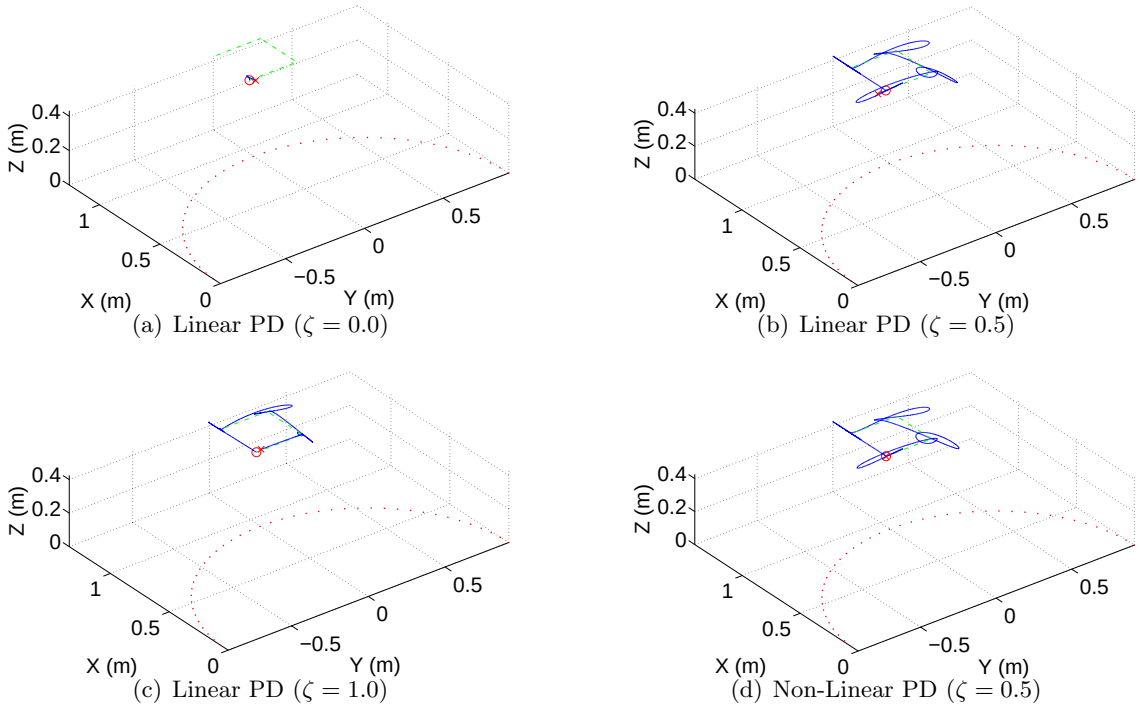

(a) Linear PD ($\zeta = 0.0$)

(b) Linear PD ($\zeta = 0.5$)

(c) Linear PD ($\zeta = 1.0$)

(d) Non-Linear PD ($\zeta = 0.5$)

Figure 4.21: Helicopter 3-D Positions for Square (Step) Path Tests with HANGAR Config.

options produced overshoot in the tracking results. Slight improvement in the position tracking performance (less overshoot) can be observed in the PD with FPC option ($\zeta = 1.0$) over the other two options (both with $\zeta = 0.5$). This reflects the relative emphasis placed on the position tracking for the $\zeta = 1.0$ case when compared to the cases with $\zeta = 0.5$.

When looking at the joint plot for the PD with FPC option ($\zeta = 1.0$), shown in Figure 4.22, it reveals that the trade-off for the improved position tracking performance is in the excessive oscillations for the attitude (q_5 and q_6) of the helicopter.

Figure 4.23 shows the comparison between the desired joint torque produced by the PD and NPD control options (with both option having $\zeta = 0.5$). The peak values of the PD generated desired joint torque (dash-dotted line) is observed to be slightly higher than those generated by the NPD option (solid line). This is again consistent with the expected behaviour of the chosen nonlinear PD gain structure.

Figure 4.24 shows the tracking responses of the second set of square path test, where the step changes in the position reference have been replaced with a linear slope change. The objective of this test is to illustrate that given a sufficiently slow varying path reference trajectory, reasonable position tracking performance can be achieved with the proposed Virtual Joint Control scheme. From Figure 4.24, the overall position tracking performance have indeed been improved for all of the options (except for the $\zeta = 0.0$, PD with ACS option).

Finally, the results of applying the square path tracking test with linear slope changes to the Platform system using the UAV configuration are shown in Figure 4.25. In general, the results for the UAV configuration are consistent with their counterpart for the HANGAR configuration. This re-enforces the idea that, despite the changes in the configuration, the proposed Virtual Joint Control scheme applies equally well to both configurations and is capable of producing consistent results in both cases.

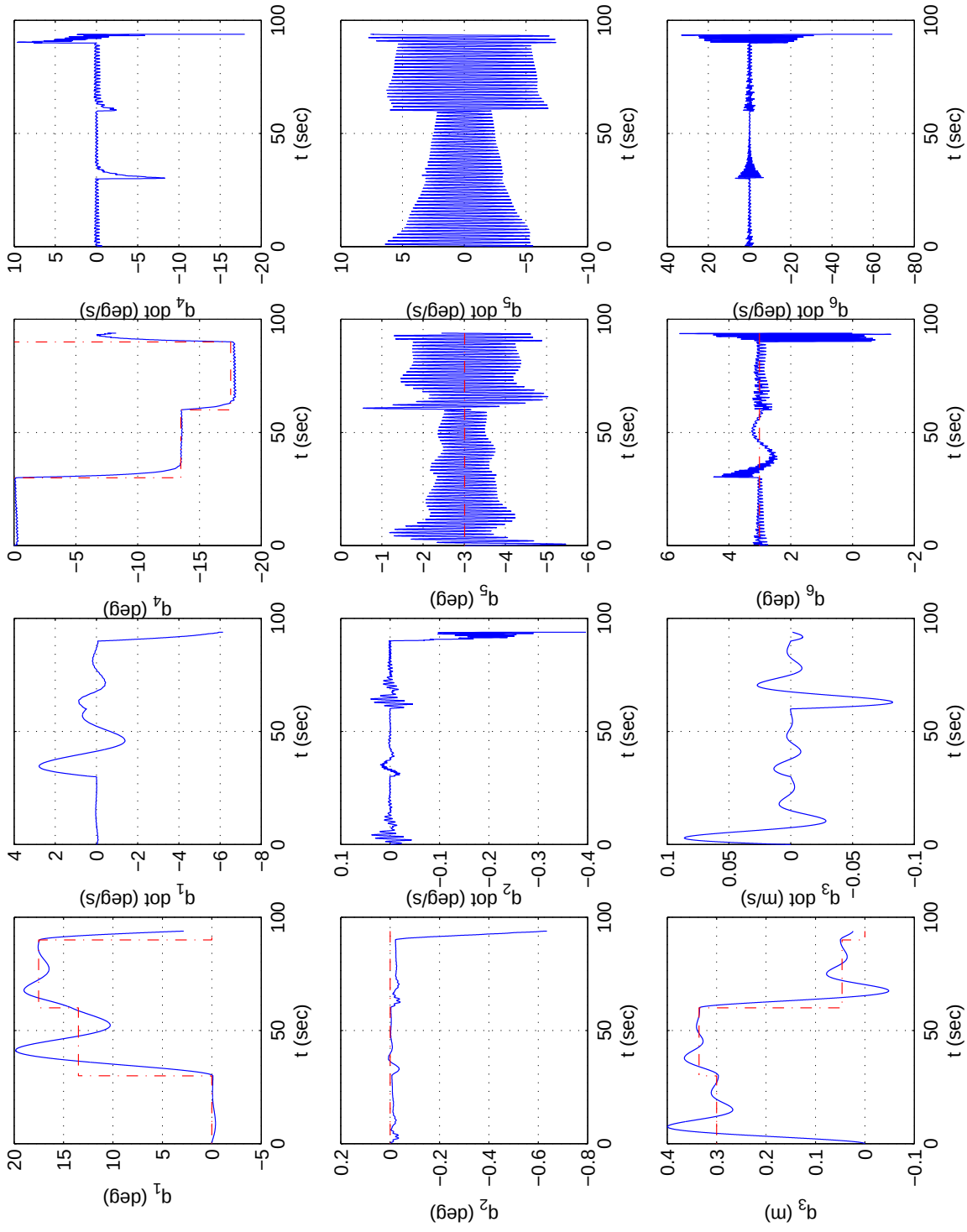

Figure 4.22: Joint Plots: Square (Step) test with HANGAR config. using PD ($\zeta = 1.0$)

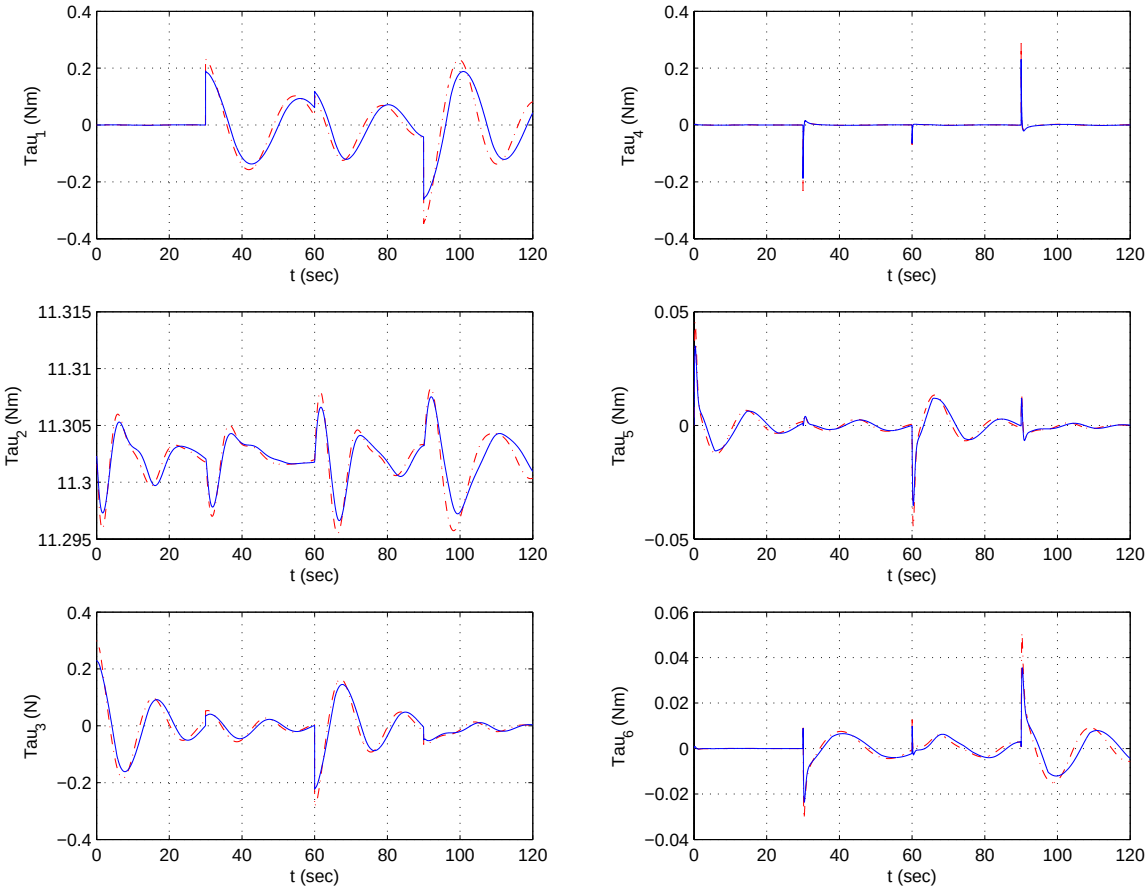

Figure 4.23: Desired Torque Comparison: PD vs NPD (Square Step, HANGAR, $\zeta = 0.5$)

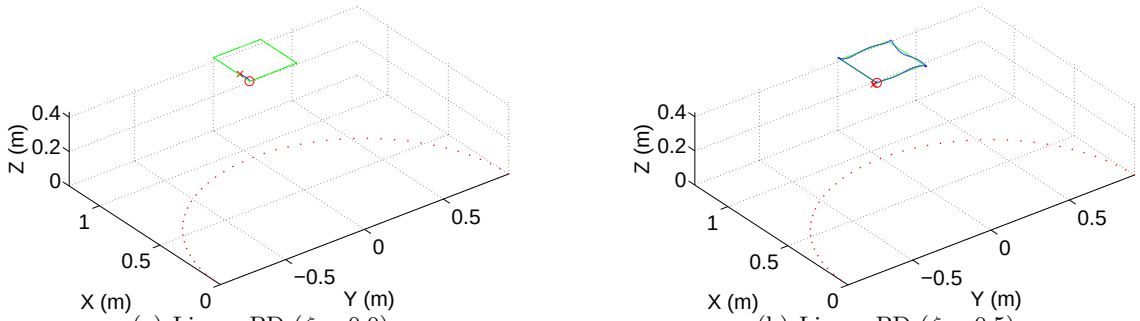

(a) Linear PD ($\zeta = 0.0$)

(b) Linear PD ($\zeta = 0.5$)

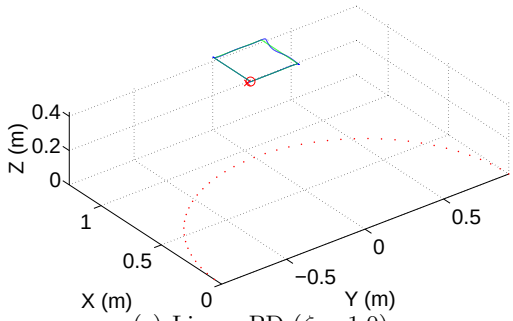

(c) Linear PD ($\zeta = 1.0$)

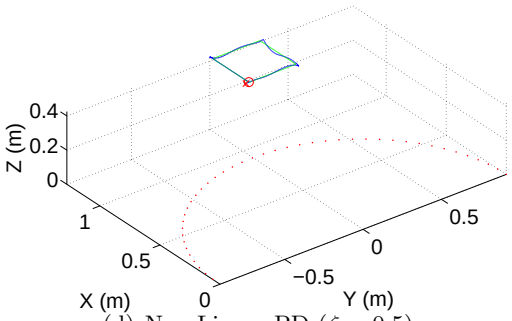

(d) Non-Linear PD ($\zeta = 0.5$)

Figure 4.24: Helicopter 3-D Positions for Square Path Tests with HANGAR Configuration

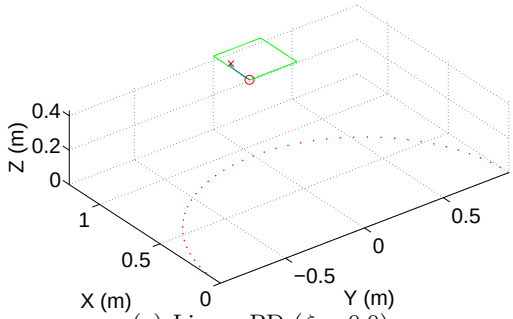

(a) Linear PD ($\zeta = 0.0$)

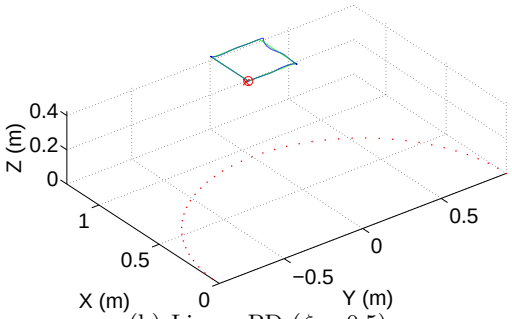

(b) Linear PD ($\zeta = 0.5$)

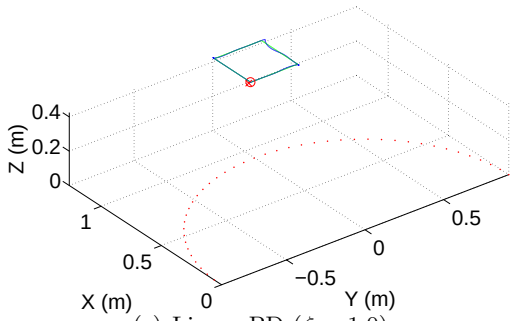

(c) Linear PD ($\zeta = 1.0$)

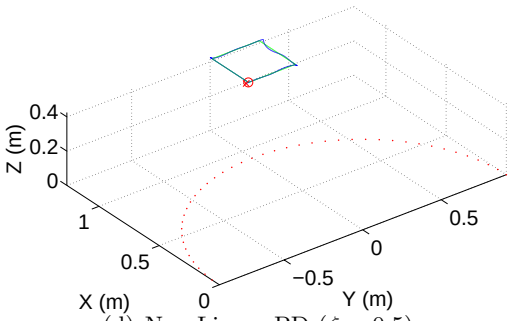

(d) Non-Linear PD ($\zeta = 0.5$)

Figure 4.25: Helicopter 3-D Positions for Square Path Tests with UAV Configuration

Figure-8 with changing Heading and Height

While the Square path test was designed to examine the step response of the controller, the Figure-8 test expands the reference trajectory from a planar 2-D motion to include movement in 3-D space, as well as combining changes in the helicopter heading. The resulting trajectories of the helicopter under the four sets of control options are shown in Figure 4.26. Overall, the results of the Figure-8 test are consistent with the responses observed in the previous two test scenarios. The linear PD with ACS ($\zeta = 0.0$) option once again produces unsatisfactory path tracking performance while the rest of the control options produce varying degree of satisfactory position tracking responses.

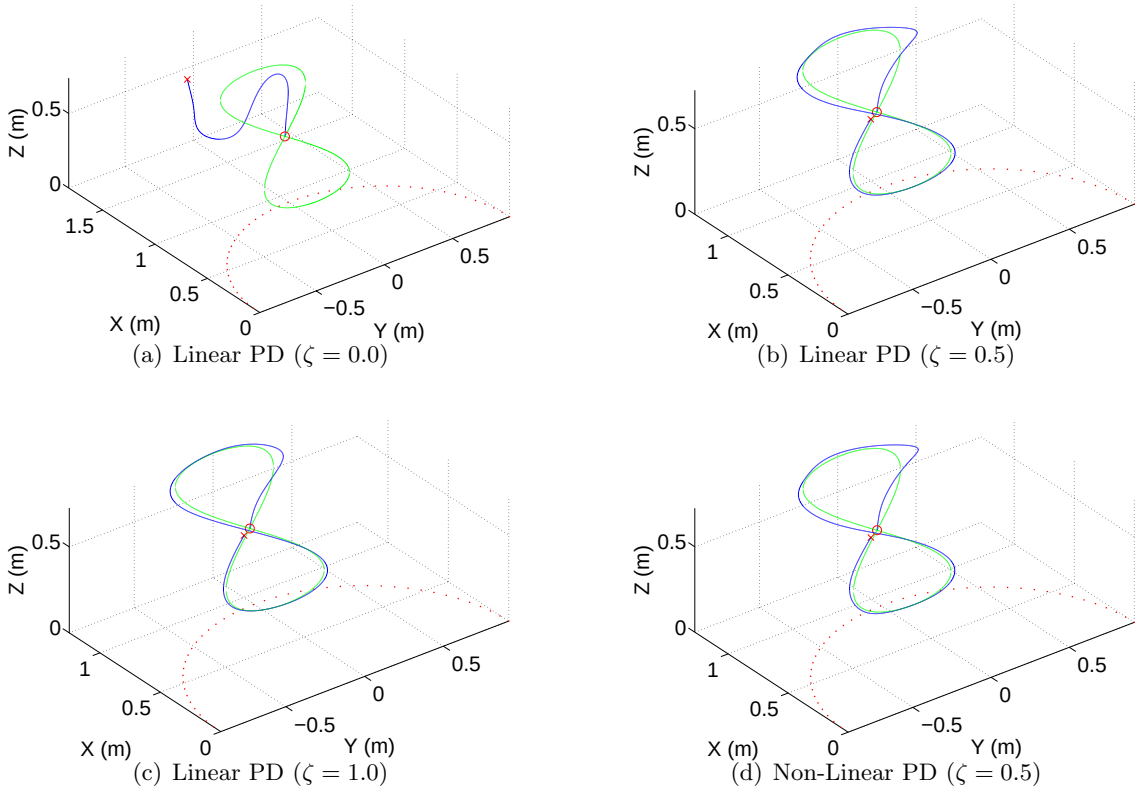

(a) Linear PD ($\zeta = 0.0$)

(b) Linear PD ($\zeta = 0.5$)

(c) Linear PD ($\zeta = 1.0$)

(d) Non-Linear PD ($\zeta = 0.5$)

Figure 4.26: Helicopter 3-D Positions for Figure-8 Tests with HANGAR Configuration

The trade-off in obtaining a slight improvement in the path trajectory for the FPC option ($\zeta = 1.0$, shown in Figure 4.26(c)) when compare to the averaged option ($\zeta = 0.5$, shown in Figure 4.26(b)) can be observed when examining the plots of the joint variables for the FPC

option, shown in Figure 4.27. From there, oscillations occur once again in the roll (q_6) and pitch (q_5) angles while satisfactory tracking performance are obtained for the remaining joints.

Similar responses are obtained when the control options are applied to the Platform system with the UAV configuration, as shown in Figure 4.28. Recall the UAV configuration differs from the HANGAR configuration in that the dynamics of the UAV configuration is uniform across the workspace of the platform while it is non-uniform for the HANGAR configuration. This indicates the proposed Virtual Joint Control scheme can provide a consistent testing facility to perform comparison between the two platform configurations.

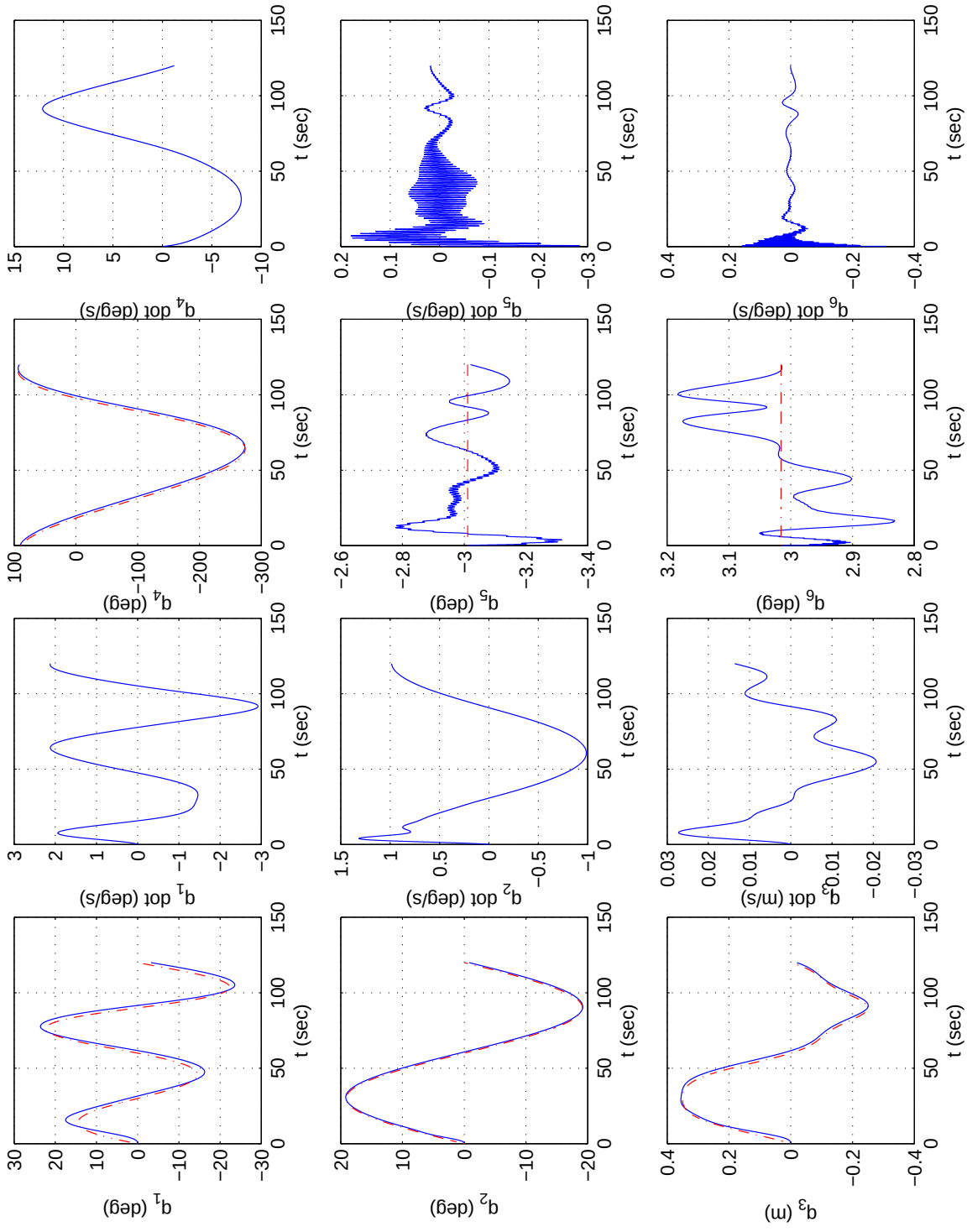

Figure 4.27: Joint Plots for Figure-8 test with HANGAR configuration using PD ($\zeta = 1.0$)

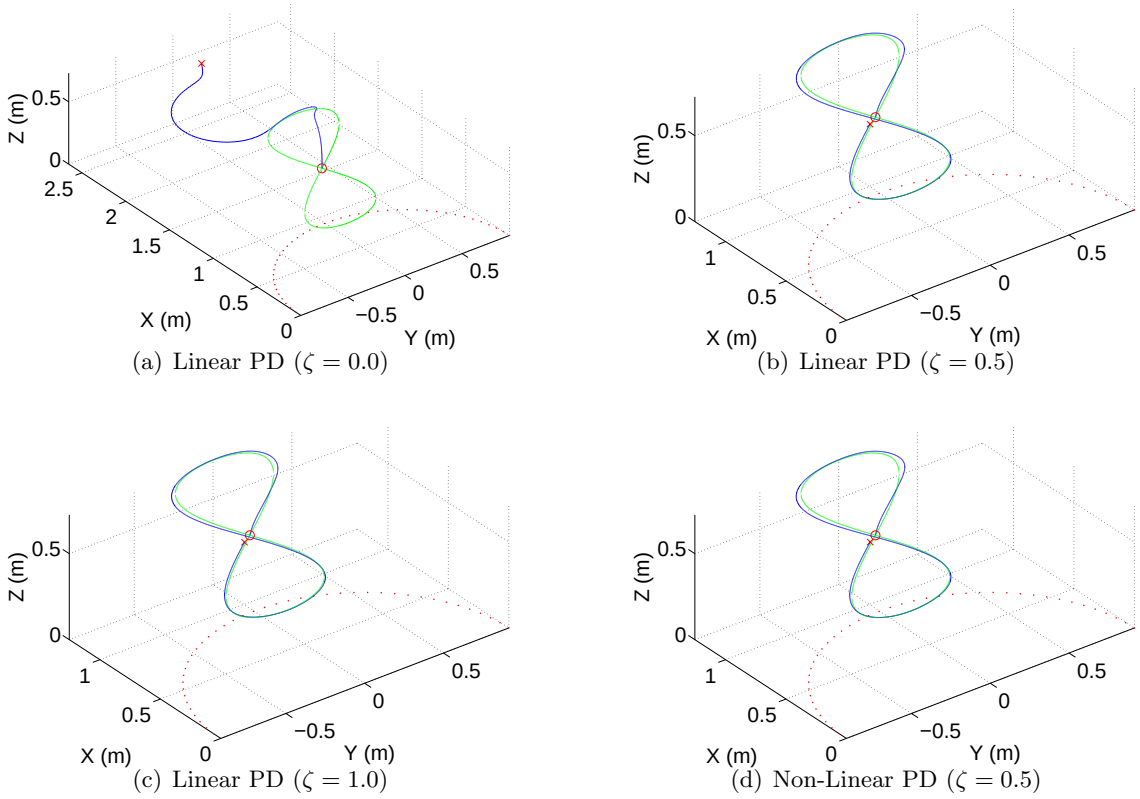

(a) Linear PD ($\zeta = 0.0$)

(b) Linear PD ($\zeta = 0.5$)

(c) Linear PD ($\zeta = 1.0$)

(d) Non-Linear PD ($\zeta = 0.5$)

Figure 4.28: Helicopter 3-D Positions for Figure-8 Tests with UAV Configuration

4.5 Summary

The Virtual Joint Control scheme has been introduced for the purpose of providing an alternate control strategy that is applicable to both Platform and stand alone helicopter (UAV) systems. The fundamental theme of the Virtual Joint Control scheme lies in the rotor input inversion algorithm that computes the rotor control input to generate torque at the platform joint that would mimic those computed from stable platform joint controllers. The weight scale factor ζ in the rotor input inversion algorithm provides an explicit tuning mechanism for determining the degree of trade-off between attitude and path tracking.

Three simulation test scenarios have been designed to highlight various aspects of the proposed Virtual Joint Control scheme. The hover with initial disturbance test is designed to illustrate the controllers' ability to stabilize the system within the proximity of the hover trim condition. The planar square path test shows the step responses of the controllers, as well as their tracking performances along the horizontal plane. The Figure-8 test expands the path tracking requirement to include a reference trajectory and heading defined in the three-dimensional (3-D) space.

The results of the simulation tests illustrate how the selection of the weight scale factor ζ can indeed affect the relative emphasis placed between attitude control and path tracking control. When $\zeta = 0.0$, the controller's emphasis is placed completely on tracking the reference attitude while ignoring the reference position. On the other hand, when $\zeta = 1.0$, position/path tracking is maintained at the cost of excessive oscillations in the attitude of the helicopter. The $\zeta = 0.5$ case is a representative of how adjusting the value of ζ can provide a trade-off effect between having satisfactory tracking performances in both position and attitude.

Finally, two desired joint torque generation control strategies have been applied for the proposed Virtual Joint Control scheme. The simulation tests demonstrated the feasibility of extending the proposed Virtual Joint Control scheme to utilize different stable joint control strategies. Such extension would expose the wealth of stable joint control strategies available in the robot manipulator control literature for helicopter flight consideration.

In summary, the contributions presented in this chapter are:

- proposed a new Virtual Joint Control scheme for helicopter flight control using two variants

of desired joint torque generation techniques: linear PD (PD) and nonlinear PD (NPD);

- illustrated the feasibility of applying the proposed Virtual Joint Control scheme to the test Platform system through simulation with both HANGAR and UAV configuration settings;
- demonstrated the potential extension of the Virtual Joint Control scheme to utilize different stable joint control strategies for desired joint torque generation, which could make the class of stable robot manipulator joint control strategies available for helicopter flight control research.

Chapter 5

Conclusions

The research presented in this thesis is motivated by the desire to utilize a test platform system for helicopter studies. The results obtained from this study provide a foundation for achieving this goal. A summary of the results will be given in this chapter. In addition, the novel contributions of the research will be presented, followed by a list of proposed future research areas.

5.1 Summary

In this thesis, a nonlinear six degree-of-freedom (6 DOF) model for the Platform system has been derived from the Principle of Virtual Power [38]. The model derivation has been verified mathematically using the Maple™ symbolic tool to avoid manipulation errors. The Platform model utilizes a quasi-steady rotor model [12], together with the rigid body dynamics for both the helicopter body and the platform linkages, to formulate the system dynamics. The resulting model has a complexity equivalent to a Level 1 model [11, 12], which is suitable for control design and analysis. Through the use of the Principle of Virtual Power, a mapping between the Platform model and the stand alone helicopter (UAV) model has been derived and presented through Theorem 2.1 and Lemma 2.1. Theorem 2.1 shows that the UAV model can be recovered from the Platform model by setting the mass and inertia of the linkages to zero. Lemma 2.1 then defines the coordinate transformation mapping between the helicopter body frame and the platform joint space. Taken together, Theorem 2.1 and Lemma 2.1 provide the basic framework for utilizing the Platform system for UAV research.

Using the mapping relationship between the Platform and UAV model, the expression for the *apparent payload* $\hat{W}_p$, which defines the hover trim condition for the Platform system, has been derived. An application of the *apparent payload* expression is to derive the matching criteria for the hover trim conditions between different Platform configurations, as well as with other UAV systems. With the hover trim conditions matched, linearization can be applied to various Platform configurations for analysis and comparisons. Four Platform configurations have been introduced in Chapter 3: UAV, BALANCED, REDUCED, and HANGAR. The UAV configuration represents a system in which a stand alone helicopter is attached to a *virtual* platform whose link mass and inertia are set to zero. The BALANCED configuration represents a Platform system set up in such a way that the effects of the mass and inertia of the linkages around the elbow joint (q_2) are statically balanced out by the counter weights. This has an effect of matching its hover trim condition with the one in the UAV configuration for comparisons. The REDUCED configuration represents a Platform setup with a slower rotor operation speed. This is defined to address physical implementation constraints, such as availability of rotor power and safety concerns. The rotor speed and counter weight trade-off constraint defined in (3.26) is used to define the counter weight setting for the REDUCED configuration given the reduced rotor speed. Finally, the HANGAR configuration uses the same rotor speed as in the REDUCED configuration, but with a different counter weight combination. This is defined to address the physical limitations imposed by the dimensions of the Platform linkages available for this research.

Comparisons among the linearized models around hover for the four configurations reveal two main observations. First, while the hover dynamics of the UAV system is independent of the helicopter position and heading, the hover dynamics of the BALANCED case varies depending on the helicopter body orientation relative to the Platform linkages. Second, as the Platform linkage mass and inertia increase relative to the force generated by the rotor, they tend to dominate the system dynamics and result in slower responses.

Further examination of the Platform system model through dimensional analysis shows that dynamic equivalence between the Platform and UAV system is unattainable without active control at the Platform joints. Due to the lack of actuators at the Platform system available for this research, this represents a limitation on using the Platform system for direct equivalence comparison with a stand alone UAV system. However, a modification to the Platform system

will be proposed in a later section as a future research topic to extend the Platform system in such a way that dynamic equivalence can be achieved between the Platform and the UAV systems.

Despite the difference in their dynamic behaviour, it is still desirable to apply the same control strategy to both the Platform and UAV systems. As such, a unified Virtual Joint Control scheme is presented. Simulation results show that the Virtual Joint Control scheme can indeed provide a unified stable control strategy for both systems. Two variations on the desired torque generation algorithm for the Virtual Joint Control scheme have been presented: linear Proportional-Derivative (PD) and Nonlinear Proportional-Derivative (NPD) control. These variations illustrate that the Virtual Joint Control scheme can be expanded through the use of different desired joint torque generation algorithms. This enables the wealth of stable joint control strategies available in the robot manipulator control literature [40, 41, 79] to be considered for helicopter flight control applications. Finally, the weight scale factor ζ, defined in the Virtual Joint Control scheme, provides an explicit tuning parameter for adjusting the performance emphasis between position and attitude tracking. For example, when setting $\zeta = 0$, the Virtual Joint Controller exhibits Attitude Control System (ACS) type control behaviour where the attitude and heading of the helicopter are maintained at the expense of uncontrolled drift in its position. On the other hand, when $\zeta = 1$, unstable internal dynamics, similar to the ones reported by Koo and Sastry [14] when performing exact input-output feedback linearization for path control, are observed in the form of excessive oscillations in the attitude (roll and pitch angles) of the helicopter.

5.2 Contributions

The major contributions of this thesis are briefly summarized here:

- derived the trim equivalence condition based on the payload equation, which allows for direct comparisons to be made between various configurations of the test Platform, as well as with UAV systems
- proposed a new Virtual Joint Control scheme for helicopter flight control
- examined the effects of the main rotor speed and the link mass and inertia on the Platform

system dynamics

Other contributions presented include:

- illustrated the feasibility of applying the proposed Virtual Joint Control scheme to the test Platform system through simulation with both the HANGAR and the UAV configuration settings
- demonstrated the extensibility of the proposed Virtual Joint Control scheme by examining the behaviour, in simulation, of two of its variant forms, utilizing different desired torque generation techniques: linear PD (PD) and nonlinear PD (NPD).
- derived the mapping relationship between the Platform system model and the UAV system model
- derived the nonlinear 6 DOF model for the Platform system that is also applicable to stand alone helicopter (UAV) systems

5.3 Future Research

The contributions presented in this thesis provide a theoretical basis for applying the test Platform system to small-scale helicopter modelling and control research. To this end, a list of possible avenues available for future pursuit are presented in the following sections.

5.3.1 Experimentation

For the model presented in Chapter 2, although some of the system parameters, such as mass, can be obtained readily, others, such as inertia, are more difficult to derive. As such, system identification [80] is necessary to obtain model parameters, as well as for verification of the simulation results presented thus far. The Platform model derived in this thesis and its subsequent linearization can provide insight into the system model structure necessary for system identification. There are two main challenges in applying system identification to the test platform system: quality sensor measurements for both joint angles and angular rates, and closed-loop identification. Preliminary experimentation on the test platform shows that the joint angle measurements provided by the potentiometers currently employed are too noisy to provide quality

data for system identification (see Appendix F). Furthermore, to identify the dynamics of the helicopter, rate sensor measurements are needed to improve the system identification results [28]. Due to the unstable dynamics inherent in the helicopter systems, closed-loop system identification [81, 82] is necessary and therefore a stable controller for the system is required. To this end, the Virtual Joint Control scheme proposed in this research can provide a candidate control strategy for performing closed-loop system identification experiment.

Other challenges in performing experimentation on the Test Platform includes identification of the joint friction, which has been neglected in the model presented. Also, real-time implementation of the Virtual Joint Control scheme is non-trivial due to the iterative loop in the torque approximation step.

5.3.2 Model Improvement

Improvements to the Platform model can be obtained by using increased fidelity models for the helicopter dynamics, such as including the joint friction effect, the drag effect caused by the fuselage and body fins, more detailed rotor models to include such effects as rotor aerodynamic moments, servo and blade dynamics (gyroscopic effects and hinge offset) [9, 10, 1, 12]. In particular, the quasi-steady rotor model employed in this research does not take into account the dynamics of the swashplate and the Bell-Hiller flybar assembly [83, 20, 84], which is common for small-scale helicopters and can have a significant effect on the system dynamics for more aggressive manoeuvres [85].

Another possible avenue to explore is to examine the model of platforms with different topologies. Although the parallel link structure employed in the Platform system presented provides a convenient mechanism for counter balance setup, it might be possible to derive similar counter balance trade-off condition for platforms with different topologies.

5.3.3 Further Analysis

The analysis presented in Chapter 3 focuses primarily on the effect of mass and inertia of the Platform linkage and counter weight and how they are related to the rotor speed. Such analysis is designed to address one of the key questions that motivates this research: how does the additional mass and inertia of the Platform system affect the helicopter dynamics. The assumption inherent

in the analysis there is that the same helicopter is used for both the Platform and the stand alone systems. Further analysis can be performed utilizing different helicopter attributes for the two systems. For example, the rotor radius R for the two systems could be made different instead of/in addition to varying the rotor speed Ω.

Another possible extension in the analysis of the Platform model is to perform linearization at an equilibrium point different from hover, such as cruising along a circular path about the base joint at different speed. Comparisons can also be made between the behaviour of the system operating at different radius of such circular paths.

Finally, to address the limitation of using the Platform system for direct dynamic equivalence comparisons with the UAV system, a Servo Assisted Equivalence Algorithm is proposed below. This algorithm calls for the addition of joint servo actuators in order to extend the existing Platform system for UAV research.

Servo Assisted Equivalence Algorithm

Recall the model for the Platform system without actuated joints in (2.106):

$$\hat{\boldsymbol{M}}(\hat{\boldsymbol{q}})\ddot{\hat{\boldsymbol{q}}} + \hat{\boldsymbol{h}}(\hat{\boldsymbol{q}}, \dot{\hat{\boldsymbol{q}}}) = \hat{\boldsymbol{\tau}}(\hat{\boldsymbol{q}}, \dot{\hat{\boldsymbol{q}}}, \vec{\boldsymbol{u}}). \tag{2.106}$$

If servo actuators can be added to the Platform system, the corresponding model would be modified with the additional servo torque input $\hat{\boldsymbol{\tau}}_{\mathrm{s}}(\hat{\boldsymbol{q}}, \dot{\hat{\boldsymbol{q}}}, \vec{\boldsymbol{u}})$ as

$$\hat{\boldsymbol{M}}(\hat{\boldsymbol{q}})\ddot{\hat{\boldsymbol{q}}} + \hat{\boldsymbol{h}}(\hat{\boldsymbol{q}}, \dot{\hat{\boldsymbol{q}}}) - \hat{\boldsymbol{\tau}}_{\mathrm{g}}(\hat{\boldsymbol{q}}) = \hat{\boldsymbol{\tau}}_{\mathrm{R}}(\hat{\boldsymbol{q}}, \dot{\hat{\boldsymbol{q}}}, \vec{\boldsymbol{u}}) + \hat{\boldsymbol{\tau}}_{\mathrm{s}}(\hat{\boldsymbol{q}}, \dot{\hat{\boldsymbol{q}}}, \vec{\boldsymbol{u}}), \tag{5.1}$$

where the generalized gravitational and rotor force components have been separated out into $\hat{\boldsymbol{\tau}}_{\mathrm{g}}$ and $\hat{\boldsymbol{\tau}}_{\mathrm{R}}$ respectively. The generalized gravitational term is defined in (2.100); while the generalized rotor force component is defined in (2.101). The goal of the servo assisted equivalence algorithm is to derive the control law for $\hat{\boldsymbol{\tau}}_{\mathrm{s}}(\hat{\boldsymbol{q}}, \dot{\hat{\boldsymbol{q}}}, \vec{\boldsymbol{u}})$ such that the resulting system would be equivalent to the UAV system in (3.9).

Theorem 5.1 *Assuming the Platform system model described by* (5.1) *is not operating near its*

singularities, when the servo control law defined by

$$\hat{\boldsymbol{\tau}}_s(\hat{\boldsymbol{q}}, \dot{\hat{\boldsymbol{q}}}, \vec{\boldsymbol{u}}) = \hat{\boldsymbol{M}}(\hat{\boldsymbol{q}})\hat{\boldsymbol{\tau}}_c(\hat{\boldsymbol{q}}, \dot{\hat{\boldsymbol{q}}}, \vec{\boldsymbol{u}}) + \hat{\boldsymbol{h}}(\hat{\boldsymbol{q}}, \dot{\hat{\boldsymbol{q}}}) - \hat{\boldsymbol{\tau}}_g(\hat{\boldsymbol{q}}), \tag{5.2}$$

where

$$\hat{\boldsymbol{\tau}}_c(\hat{\boldsymbol{q}}, \dot{\hat{\boldsymbol{q}}}, \vec{\boldsymbol{u}}) = \hat{\boldsymbol{M}}_U(\hat{\boldsymbol{q}})^{-1}\left[\hat{\boldsymbol{\tau}}_{R_U}(\hat{\boldsymbol{q}}, \dot{\hat{\boldsymbol{q}}}, \vec{\boldsymbol{u}}) + \hat{\boldsymbol{\tau}}_{g_U}(\hat{\boldsymbol{q}}) - \hat{\boldsymbol{h}}_U(\hat{\boldsymbol{q}}, \dot{\hat{\boldsymbol{q}}})\right] - \hat{\boldsymbol{M}}(\hat{\boldsymbol{q}})^{-1}\hat{\boldsymbol{\tau}}_R(\hat{\boldsymbol{q}}, \dot{\hat{\boldsymbol{q}}}, \vec{\boldsymbol{u}}), \tag{5.3}$$

is applied to it, the resulting closed-loop system dynamics will be equivalent to the UAV system model in (3.9).

Proof: Theorem 5.1

Applying (5.2) to (5.1) would yield

$$\hat{\boldsymbol{M}}(\hat{\boldsymbol{q}})\ddot{\hat{\boldsymbol{q}}} + \hat{\boldsymbol{h}}(\hat{\boldsymbol{q}}, \dot{\hat{\boldsymbol{q}}}) - \hat{\boldsymbol{\tau}}_{\mathrm{g}}(\hat{\boldsymbol{q}}) = \hat{\boldsymbol{\tau}}_{\mathrm{R}}(\hat{\boldsymbol{q}}, \dot{\hat{\boldsymbol{q}}}, \vec{\boldsymbol{u}}) + \hat{\boldsymbol{M}}(\hat{\boldsymbol{q}})\hat{\boldsymbol{\tau}}_{\mathrm{c}}(\hat{\boldsymbol{q}}, \dot{\hat{\boldsymbol{q}}}, \vec{\boldsymbol{u}}) + \hat{\boldsymbol{h}}(\hat{\boldsymbol{q}}, \dot{\hat{\boldsymbol{q}}}) - \hat{\boldsymbol{\tau}}_{\mathrm{g}}(\hat{\boldsymbol{q}}), \tag{5.4}$$

which can be simplified to

$$\hat{\boldsymbol{M}}(\hat{\boldsymbol{q}})\ddot{\hat{\boldsymbol{q}}} = \hat{\boldsymbol{\tau}}_{\mathrm{R}}(\hat{\boldsymbol{q}}, \dot{\hat{\boldsymbol{q}}}, \vec{\boldsymbol{u}}) + \hat{\boldsymbol{M}}(\hat{\boldsymbol{q}})\hat{\boldsymbol{\tau}}_{\mathrm{c}}(\hat{\boldsymbol{q}}, \dot{\hat{\boldsymbol{q}}}, \vec{\boldsymbol{u}}). \tag{5.5}$$

Substituting in (5.3) and simplifying to yield

$$\hat{\boldsymbol{M}}(\hat{\boldsymbol{q}})\ddot{\hat{\boldsymbol{q}}} = \hat{\boldsymbol{M}}(\hat{\boldsymbol{q}})\Big(\hat{\boldsymbol{M}}_{\mathrm{U}}(\hat{\boldsymbol{q}})^{-1}\big[\hat{\boldsymbol{\tau}}_{R_{\mathrm{U}}}(\hat{\boldsymbol{q}}, \dot{\hat{\boldsymbol{q}}}, \vec{\boldsymbol{u}}) + \hat{\boldsymbol{\tau}}_{g_{\mathrm{U}}}(\hat{\boldsymbol{q}}) - \hat{\boldsymbol{h}}_{\mathrm{U}}(\hat{\boldsymbol{q}}, \dot{\hat{\boldsymbol{q}}})\big]\Big), \tag{5.6}$$

which can be further simplified by left multiplying both sides with the product $\hat{\boldsymbol{M}}_{\mathrm{U}}(\hat{\boldsymbol{q}})\hat{\boldsymbol{M}}(\hat{\boldsymbol{q}})^{-1}$ and recognizing that

$$\hat{\boldsymbol{\tau}}_{\mathrm{U}}(\hat{\boldsymbol{q}}, \dot{\hat{\boldsymbol{q}}}, \vec{\boldsymbol{u}}) = \hat{\boldsymbol{\tau}}_{g_{\mathrm{U}}}(\hat{\boldsymbol{q}}) + \hat{\boldsymbol{\tau}}_{R_{\mathrm{U}}}(\hat{\boldsymbol{q}}, \dot{\hat{\boldsymbol{q}}}, \vec{\boldsymbol{u}}) \tag{5.7}$$

to obtain the desired UAV model in (3.9). ■

Conceptually, the servo assisted equivalence algorithm defined in Theorem 5.1 is similar to the Computed Torque Control Method in the robotics literature [41]. In the Computed Torque Method, the servo control law has the form [41]

$$\vec{\boldsymbol{\tau}} = \boldsymbol{\alpha}\vec{\boldsymbol{\tau}}' + \vec{\boldsymbol{\beta}}, \tag{5.8}$$

where $\boldsymbol{\alpha}$ and $\vec{\boldsymbol{\beta}}$ represent the model-based component; while $\vec{\boldsymbol{\tau}}'$ represents a *desired* system behaviour. The idea is to have the model-based component *cancels* out the nonlinearity in the system model and makes the system behave like a second order linear system to the input $\vec{\boldsymbol{\tau}}'$. Then the input $\vec{\boldsymbol{\tau}}'$ will be defined by the *desired* behaviour [41]. Drawing on the parallel with the Computed Torque Method, the model-based portion of the servo assisted equivalence algorithm defined in Theorem 5.1 is represented by $\hat{\vec{\boldsymbol{\tau}}}_{\mathrm{s}}(\hat{\vec{\boldsymbol{q}}}, \dot{\hat{\vec{\boldsymbol{q}}}}, \vec{\boldsymbol{u}})$ in (5.2) with

$$\boldsymbol{\alpha} = \hat{\boldsymbol{M}}(\hat{\vec{\boldsymbol{q}}}) \qquad \text{and} \qquad \vec{\boldsymbol{\beta}} = \hat{\vec{\boldsymbol{h}}}(\hat{\vec{\boldsymbol{q}}}, \dot{\hat{\vec{\boldsymbol{q}}}}) - \hat{\vec{\boldsymbol{\tau}}}_{\mathrm{g}}(\hat{\vec{\boldsymbol{q}}}), \tag{5.9}$$

while the *desired* behaviour is represented by $\hat{\vec{\boldsymbol{\tau}}}_{\mathrm{c}}(\hat{\vec{\boldsymbol{q}}}, \dot{\hat{\vec{\boldsymbol{q}}}}, \vec{\boldsymbol{u}})$ in (5.3). The principal difference between the servo assisted equivalence algorithm presented here and a conventional Computed Torque Method is in the definition of the *desired* behaviour. It is not surprising that while the typical desired response for robot manipulator systems under Computed Torque Control is a well defined second order behaviour [41], the *desired* behaviour defined by (5.3) represents the dynamics of the UAV system since it is the objective of the equivalence algorithm.

In terms of implementation, in addition to the limitations shared by the Computed Torque Method, such as the need for precise knowledge of the system model parameters and computational complexity [40, 41], the use of the UAV model as the desired behaviour also introduces the need to model the helicopter rotor dynamics adequately for the equivalence algorithm. In particular, the generalized rotor force $\hat{\vec{\boldsymbol{\tau}}}_{\mathrm{R}}(\hat{\vec{\boldsymbol{q}}}, \dot{\hat{\vec{\boldsymbol{q}}}}, \vec{\boldsymbol{u}})$ will need to be computed from the rotor control inputs $\vec{\boldsymbol{u}}$. However, considering that the servo assisted equivalence algorithm is designed to augment any control strategy for the Platform system, it does not represent additional burden with respect to implementation, with the possible exception of added computational complexity.

Finally, the servo assisted equivalence algorithm defined in Theorem 5.1 provides a systematic approach to operate the Platform system so that its dynamic behaviour resembles that of the target UAV system. With this algorithm, as long as the trim conditions are matched, equivalence between the Platform and the UAV system can be extended beyond the point-to-point and constant height circular path cases mentioned previously.

Application to the HANGAR Configuration

Since the main rotor speed represents the normalization factor for time, when the Servo Assisted Equivalence Algorithm defined in Theorem 5.1 is applied to the HANGAR configuration defined previously, the resulting system dynamics is expected to be time scaled due to the change in the main rotor speed. This is illustrated in Figure 5.1, where the servo assisted HANGAR configuration is plotted side-by-side with those for the UAV configuration for comparison.

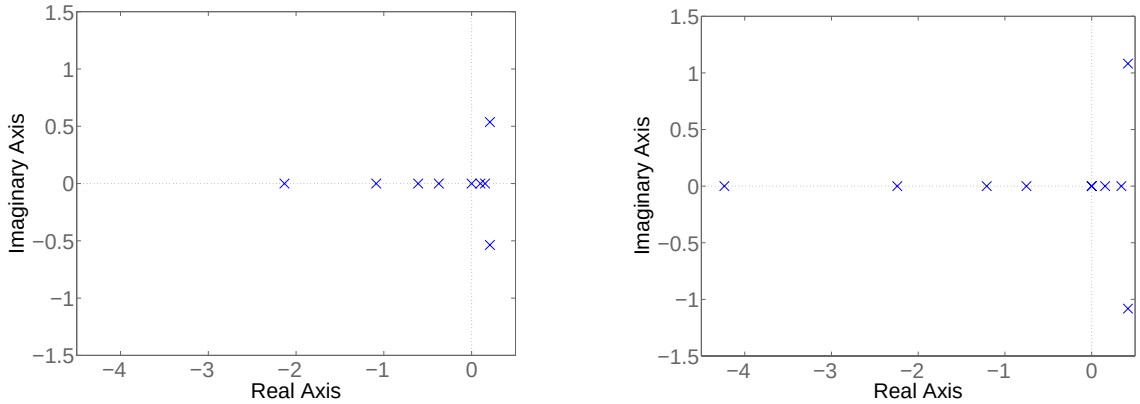

(a) HANGAR (Servo Assisted) (b) UAV

Figure 5.1: HANGAR Poles Around Hover (Servo Assisted)

The eigenvalues of the linearized system matrix $\bar{\boldsymbol{A}}_{H_c}$ of the compensated HANGAR system is given by

$$\text{eig}(\bar{\boldsymbol{A}}_{H_c}) = \begin{bmatrix} \vec{\mathbf{0}}_{4\times 1} \\ 0.21 \pm 0.54\, i \\ 0.15 \\ 0.1 \\ -2.13 \\ -1.09 \\ -0.61 \\ -0.37 \end{bmatrix}. \tag{5.10}$$

Recall, the main rotor speed ratio between the HANGAR and the UAV case is $\breve{\Omega} = 0.5$. When comparing the eigenvalues for the compensated HANGAR configuration in (5.10) to those of the UAV configuration in (3.19), it can be seen that ratio between the corresponding modes are

indeed close to the main rotor speed ratio.

5.3.4 Stability Proof and Extension of Virtual Joint Control Scheme

Due to the nonlinear nature of the proposed Virtual Joint Control scheme, it is not trivial to obtain a stability proof for it. Recall the desired joint torque is computed to drive the system towards the trim condition such that the system behaviour would *minic* those of a robot manipulator system under stable joint control. As such, a possible avenue for obtaining stability condition for the Virtual Joint Control scheme is through examining the error between the desired and the actual torque applied at the joints. Alternatively, for PD based variants (both linear and nonlinear cases), a modified Lyapunov function [71] might be obtainable from the underlying desired joint torque generation algorithms [40, 78].

The nonlinearity in the Virtual Joint Control scheme also poses a challenge for implementation, especially the presence of the iteration loop in the torque approximation step could result in computation time that is too long for real time applications. One possible solution is to replace the iteration loop with a multiple dimensional look-up table for computing the control inputs from the desired rotor force and moment.

More in depth analysis on the effect of the weight scale factor ζ can also be performed to explore the possibility of obtaining an optimal value given a certain mission objectives. Development of an automatic tuning or online adaptive algorithms for adjusting the value of ζ can also be explored. Furthermore, the effects of the gain values in the PD/NPD controller for the desired torque generation can be explored in terms of performance enhancement with respect to specific control objectives.

Finally, the two variant forms of the Virtual Joint Control scheme presented here is only a proof of concept illustration on the extensibility of this control strategy. Other stable robot control laws can also be explored for flight control case studies through this test platform setup.

Appendix A

Rotation Matrix

A.1 General Rotation Matrix

The convention used to define rotation matrices in this document is similar to the one presented in [40]. A rotation matrix $\boldsymbol{R}_a^b$ maps the coordinates of a vector expressed in frame b to the coordinates expressed in frame a:

$$\begin{bmatrix} x_a \\ y_a \\ z_a \end{bmatrix} = \boldsymbol{R}_a^b \begin{bmatrix} x_b \\ y_b \\ z_b \end{bmatrix} \tag{A.1}$$

Here, frame a is interpreted as the initial frame, while frame b is the resulting frame after the rotation is applied. With this definition, the rotation matrices for rotations about the major axes can be defined as follows. The positive sense of the rotation angles is defined by the standard right-hand rule.

Rotation about x-axis by an angle of ϕ:

$$\boldsymbol{R}_{x,\phi} = \begin{bmatrix} 1 & 0 & 0 \\ 0 & \cos\phi & -\sin\phi \\ 0 & \sin\phi & \cos\phi \end{bmatrix} \tag{A.2}$$

Rotation about y-axis by an angle of θ:

$$\boldsymbol{R}_{y,\theta} = \begin{bmatrix} \cos\theta & 0 & \sin\theta \\ 0 & 1 & 0 \\ -\sin\theta & 0 & \cos\theta \end{bmatrix} \tag{A.3}$$

Rotation about z-axis by an angle of ψ:

$$\boldsymbol{R}_{z,\psi} = \begin{bmatrix} \cos\psi & -\sin\psi & 0 \\ \sin\psi & \cos\psi & 0 \\ 0 & 0 & 1 \end{bmatrix} \tag{A.4}$$

A.1.1 Roll, Pitch and Yaw

The orientation of an aircraft is typically measured in terms of the roll (ϕ), pitch (θ) and yaw (ψ) angles that the aircraft body-fixed axes make with the principal inertial axes (see Figure A.1). These angles can be interpreted as the angles of rotation for the inertial frame to transform into the body-fixed frame. As such, a rotation matrix can be obtained for each set of roll-pitch-yaw angles and it is defined as follows:

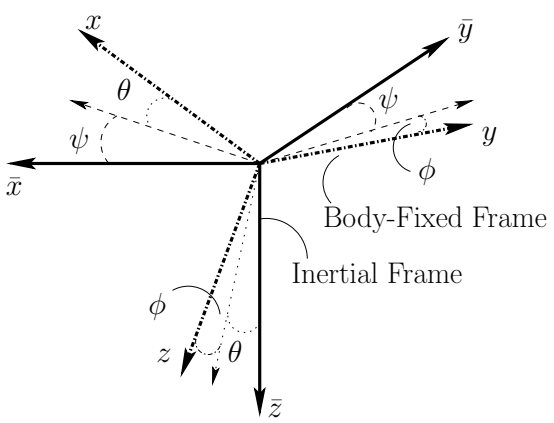

Figure A.1: Roll, Pitch and Yaw angles

$$\boldsymbol{R}_{\psi,\theta,\phi} = \boldsymbol{R}_{z,\psi}\boldsymbol{R}_{y,\theta}\boldsymbol{R}_{x,\phi} \tag{A.5}$$

The above rotation can be interpreted as a series of current-frame [40] rotations:

1. rotates about z-axis by ψ
2. rotates about the resulting y-axis by θ
3. rotates again about the current x-axis by ϕ

Using (A.2) to (A.4), (A.5) can be written as:

$$\boldsymbol{R}_{\psi,\theta,\phi} = \begin{bmatrix} \cos\theta\cos\psi & \sin\phi\sin\theta\cos\psi - \cos\phi\sin\psi & \cos\phi\sin\theta\cos\psi + \sin\phi\sin\psi \\ \cos\theta\sin\psi & \sin\phi\sin\theta\sin\psi + \cos\phi\cos\psi & \cos\phi\sin\theta\sin\psi - \sin\phi\cos\psi \\ -\sin\theta & \sin\phi\cos\theta & \cos\phi\cos\theta \end{bmatrix} \tag{A.6}$$

The above rotation matrix can be used to transform vectors expressed between the body-fixed frame (frame b) and the earth-fixed (inertial) surface frame (frame a):

$$\boldsymbol{R}^{\text{body}}_{\text{inertial}} = \boldsymbol{R}_{\psi,\theta,\phi} \tag{A.7}$$

However, this matrix does not help in obtaining angular rate measurement from the raw data into either frames. The reason is that the rate measurements ($\dot{\phi}$, $\dot{\theta}$, and $\dot{\psi}$) are taken with respect to the intermediate frames. As a result, another transformation is necessary [38]:

$$\begin{bmatrix} p \\ q \\ r \end{bmatrix} = \begin{bmatrix} 1 & 0 & -\sin\theta \\ 0 & \cos\phi & \cos\theta\sin\phi \\ 0 & -\sin\phi & \cos\theta\cos\phi \end{bmatrix} \begin{bmatrix} \dot{\phi} \\ \dot{\theta} \\ \dot{\psi} \end{bmatrix} = \boldsymbol{R}_{\text{Euler}} \begin{bmatrix} \dot{\phi} \\ \dot{\theta} \\ \dot{\psi} \end{bmatrix} \tag{A.8}$$

where p, q and r are the angular rates expressed with respect to the body-fixed frame x, y and z axis respectively (frame b). Notice that the mapping in (A.8) is not an orthogonal rotation matrix. The inverse mapping is given as:

$$\begin{bmatrix} \dot{\phi} \\ \dot{\theta} \\ \dot{\psi} \end{bmatrix} = \begin{bmatrix} 1 & \sin\phi\tan\theta & \cos\phi\tan\theta \\ 0 & \cos\phi & -\sin\phi \\ 0 & \frac{\sin\phi}{\cos\theta} & \frac{\cos\phi}{\cos\theta} \end{bmatrix} \begin{bmatrix} p \\ q \\ r \end{bmatrix} \tag{A.9}$$

A.2 Rotor Frame Rotations

In the derivation of rotor dynamics, two frames are defined for each rotors: hub and hub-wind frame.

A.2.1 Hub Frames

The hub frame for each rotor is defined by aligning the z axis with the direction of air flow through the rotor.

Main Rotor Hub Frame

For the main rotor, the orientation of the hub frame is the same as the body-fixed frame:

$$\boldsymbol{R}_{\text{body}}^{\text{hub}} = \begin{bmatrix} 1 & 0 & 0 \\ 0 & 1 & 0 \\ 0 & 0 & 1 \end{bmatrix} \tag{A.10}$$

Tail Rotor Hub Frame

For the tail rotor, the hub frame is obtained by rotating the body-fixed frame about the x axis by $-\pi/2$:

$$\boldsymbol{R}_{\text{body}}^{\text{hub}} = \begin{bmatrix} 1 & 0 & 0 \\ 0 & \cos\left(-\frac{\pi}{2}\right) & -\sin\left(-\frac{\pi}{2}\right) \\ 0 & \sin\left(-\frac{\pi}{2}\right) & \cos\left(-\frac{\pi}{2}\right) \end{bmatrix} = \begin{bmatrix} 1 & 0 & 0 \\ 0 & 0 & 1 \\ 0 & -1 & 0 \end{bmatrix} \tag{A.11}$$

A.2.2 Hub-Wind Frame

The hub-wind frame for each rotor is obtained by rotating the hub frame about the z axis by the side slip angle (η_m or η_t).

Main Rotor Hub-Wind Frame

Since the main rotor hub frame has the same orientation as the body-fixed frame, the rotation matrix from both the body-fixed and hub frame to the hub-wind frame will be the same:

$$\boldsymbol{R}_{\text{body}}^{\text{hub-wind}} = \boldsymbol{R}_{\text{hub}}^{\text{hub-wind}} = \begin{bmatrix} \cos(\eta_m) & -\sin(\eta_m) & 0 \\ \sin(\eta_m) & \cos(\eta_m) & 0 \\ 0 & 0 & 1 \end{bmatrix} \tag{A.12}$$

Tail Rotor Hub-Wind Frame

From the tail rotor hub frame to the hub-wind frame, it is a simple rotation about the z axis by the side slip angle (η_t):

$$\boldsymbol{R}_{\text{hub}}^{\text{hub-wind}} = \begin{bmatrix} \cos(\eta_t) & -\sin(\eta_t) & 0 \\ \sin(\eta_t) & \cos(\eta_t) & 0 \\ 0 & 0 & 1 \end{bmatrix} \tag{A.13}$$

To go from the body-fixed frame to the tail rotor hub-wind frame, the rotation matrix is obtained by adding the rotation between the body-fixed frame and the tail hub frame:

$$\boldsymbol{R}_{\text{body}}^{\text{hub-wind}} = \boldsymbol{R}_{\text{body}}^{\text{hub}} \boldsymbol{R}_{\text{hub}}^{\text{hub-wind}} = \begin{bmatrix} \cos(\eta_t) & -\sin(\eta_t) & 0 \\ 0 & 0 & 1 \\ -\sin(\eta_t) & -\cos(\eta_t) & 0 \end{bmatrix} \tag{A.14}$$

A.3 Rotation Matrix for the Test Platform

Applying the rotation matrices defined in the previous section to the test platform, the rotation matrices between the Inertial Frame and each of the frames fixed to the platform linkage can be computed. They are listed in the following sections.

A.3.1 Base Rod and Vertical Bar - Frame 1 and Frame 4

The orientation of both Frame 1 and Frame 4 only rotates about the vertical z axis of the inertial frame. So the rotation matrix is just $\boldsymbol{R}_{z,q_1}$:

$$\boldsymbol{R}_0^1 = \boldsymbol{R}_0^4 = \begin{bmatrix} C_{q_1} & -S_{q_1} & 0 \\ S_{q_1} & C_{q_1} & 0 \\ 0 & 0 & 1 \end{bmatrix} \tag{A.15}$$

where the short form for the sine and cosine of the joint angles have been used. For example, S_{q_1} is the short form $\sin q_1$ and C_{q_1} is the short form for $\cos q_1$.

A.3.2 Bottom and Main Boom - Frame 2 and Frame 3

Frame 2 and Frame 3 rotates through both q_1 and q_2. First, it is rotated by q_1 about z. Then, a rotation of -90° about the resulting x axis is performed to align the resulting z axis with z_2. Finally, a rotation of q_2 about z_2 brings the frame to align with Frame 2. As a result, the rotation matrix is given by $\boldsymbol{R}_0^3 = \boldsymbol{R}_{z,q_1}\boldsymbol{R}_{x,-90^\circ}\boldsymbol{R}_{z,q_2}$:

$$\boldsymbol{R}_0^2 = \boldsymbol{R}_0^3 = \begin{bmatrix} C_{q_1}C_{q_2} & -C_{q_1}S_{q_2} & -S_{q_1} \\ S_{q_1}C_{q_2} & -S_{q_1}S_{q_2} & C_{q_1} \\ -S_{q_2} & -C_{q_2} & 0 \end{bmatrix} \tag{A.16}$$

A.3.3 Helicopter Body - Body Frame

When applying the Roll (q_6), Pitch (q_5) and Yaw (q_4) angle rotation of the platform directly into the Euler rotation matrix derived in the previous section, the resulting rotation matrix represents the rotation from Frame 4 (as defined in Figure 2.6) to the helicopter Body Frame.

$$\boldsymbol{R}_4^b = \begin{bmatrix} \cos q_5 \cos q_4 & \sin q_6 \sin q_5 \cos q_4 - \cos q_6 \sin q_4 & \cos q_6 \sin q_5 \cos q_4 + \sin q_6 \sin q_4 \\ \cos q_5 \sin q_4 & \sin q_6 \sin q_5 \sin q_4 + \cos q_6 \cos q_4 & \cos q_6 \sin q_5 \sin q_4 - \sin q_6 \cos q_4 \\ -\sin q_5 & \sin q_6 \cos q_5 & \cos q_6 \cos q_5 \end{bmatrix} \tag{A.17}$$

However, Frame 4 is itself rotated by the motion of the base joint (q_1). Therefore, to obtain the rotation matrix for the helicopter Body Frame from the inertial frame, the Euler Yaw angle is not q_4, but it is actually the sum of q_1 and q_4. The corresponding mappings between the Euler angles and the joint variables are given by:

$$\phi = q_6 \quad \theta = q_5 \quad \psi = (q_1 + q_4) \tag{A.18}$$

The rotation matrix between the Inertial Frame and the Body Frame $\boldsymbol{R}_0^b$ can therefore be obtained by substituting (A.18) into (A.6).

Similarly, the relationship between the body fixed angular rates and the joint rates is given

as:

$$\begin{bmatrix} 1 & 0 & -\sin q_5 \\ 0 & \cos q_6 & \cos q_5 \sin q_6 \\ 0 & -\sin q_6 & \cos q_5 \cos q_6 \end{bmatrix} \begin{bmatrix} \dot{q_6} \\ \dot{q_5} \\ (\dot{q_1} + \dot{q_4}) \end{bmatrix} = \begin{bmatrix} p \\ q \\ r \end{bmatrix} \tag{A.19}$$

From this, the Jacobian for the helicopter body-fixed angular velocity can be defined as:

$$\begin{bmatrix} p \\ q \\ r \end{bmatrix} = \begin{bmatrix} -S_{q_5} & 0 & 0 & -S_{q_5} & 0 & 1 \\ C_{q_5} S_{q_6} & 0 & 0 & C_{q_5} S_{q_6} & C_{q_6} & 0 \\ C_{q_5} C_{q_6} & 0 & 0 & C_{q_5} S_{q_6} & -S_{q_6} & 0 \end{bmatrix} \begin{bmatrix} \dot{q}_1 \\ \dot{q}_2 \\ \dot{q}_3 \\ \dot{q}_4 \\ \dot{q}_5 \\ \dot{q}_6 \end{bmatrix} = \boldsymbol{J}_{\omega_b} \dot{\vec{q}} \tag{A.20}$$

Appendix B

Rotor Aerodynamics

A more detailed derivation of the rotor dynamics is included in this appendix for completeness. The first section illustrates the application of the momentum theory in obtaining the relationship between rotor thrust and the induced velocity.

B.1 Relating Thrust and Induced Velocity

For steady free flight conditions, such as during hover or constant speed cruise flight, the thrust required is approximately equal to the weight of the helicopter body:

$$T \approx m_b g \tag{B.1}$$

From momentum theory, the thrust generated at the rotor disc is equal to the product of the rate of the air mass flow $\rho A_{\text{disc}} v_1$ and the change in the air mass velocity Δv [10]:

$$T = \rho A_{\text{disc}} v_1 \Delta v \tag{B.2}$$

where v_1 is the air velocity at the rotor disc. Let v_0 denote the velocity of air far above the rotor disc and v_2 be that of air far below the rotor disc. The change of air velocity (due to the action of the rotor disc) is then given as the difference between the two velocities:

$$\Delta v = v_2 - v_0 \tag{B.3}$$

Assume that the air velocity far above the rotor disc is zero (calm air), the change in air velocity is therefore equal to $\Delta v = v_2$. The thrust equation then becomes:

$$T = \rho A_{\text{disc}} v_1 v_2 \tag{B.4}$$

To examine how the rotor affects the pressure and velocity of the air stream that passes through it, the principle of conservation of energy is applied to the system that includes the air stream from far above through the rotor disc to the stream far below. This system is treated as a closed system, that is ignoring external disturbance and assuming no loss of energy. For aerodynamics, the conservation of energy is expressed in the form of the Bernoulli's equation [86], which states that the sum of the static and dynamics pressure is constant. Applying Bernoulli's equation to the air stream inflow above the rotor, the static pressure at far above p_∞ is equal to [1]:

$$p_\infty = p_{\text{disc}} + \frac{1}{2}\rho v_1^2 \tag{B.5}$$

where p_{disc} is the static pressure just above the rotor disc. The term $\frac{1}{2}\rho v_1^2$ represents the dynamic pressure at the rotor disc with v_1 being the air velocity at the rotor disc.

For the outflow below the rotor, the Bernoulli's equation becomes:

$$p_{\text{disc}} + \Delta p + \frac{1}{2}\rho v_1^2 = p_\infty + \frac{1}{2}\rho v_2^2 \tag{B.6}$$

The change in pressure resulted from the rotor disc action is denoted as Δp. This equation assumes that the static pressure at far below the rotor disc returns to the same level as that at far above the rotor disc. Substituting the static pressure p_∞ from the Bernoulli's equation for the rotor disc inflow into that for the outflow, the change in the static pressure Δp can be obtained:

$$\Delta p = \frac{1}{2}\rho v_2^2 \tag{B.7}$$

This is the change in air pressure caused by the rotor disc pushing air downward to generate thrust. Therefore, by definition, this change in pressure across the rotor disc is also equal to the

thrust generated across the rotor disc divided by the disc area:

$$\Delta p = \frac{T}{A_{\text{disc}}} = \rho v_1 v_2 \tag{B.8}$$

where the rotor thrust T is given by (B.4). Equating the two expressions for Δp and solve for the outflow air velocity v_2 at far below the rotor disc yields:

$$v_2 = 2v_1 \tag{B.9}$$

This gives the relationship between the thrust T and the air velocity at the rotor disc v_1:

$$T = 2\rho A_{\text{disc}} v_1^2 \qquad \text{or} \qquad v_1 = \sqrt{\frac{T}{2\rho A_{\text{disc}}}} \tag{B.10}$$

The velocity v_1 is called the induced velocity. The implicit assumption here is that both the thrust and the induced velocity are uniformly distributed across the rotor disc.

The expressions for the rotor thrust T and the induced velocity v_1 in (B.10) were derived for hover condition. For general flight condition, they are modified to include the rotor velocity through air due to the motion of the helicopter [12]:

$$T = 2\rho A_{\text{disc}} V_{\text{air}} v_1 \qquad \text{or} \qquad v_1 = \frac{T}{2\rho A_{\text{disc}} V_{\text{air}}} \tag{B.11}$$

where V_{air} is the rotor velocity through air given by:

$$V_{\text{air}} = \sqrt{V_{\text{horizontal}}^2 + (v_1 + V_{\text{vertical}})^2} \tag{B.12}$$

The component of the rotor velocity that lies in the plane of rotation of the blades is denoted as $V_{\text{horizontal}}$; while the perpendicular component is denoted V_{vertical}.

B.2 Rotor Coefficients

For a helicopter hovering in calm air, the relative air velocity along the plane of the rotor disc flowing over the blade air foil is mainly due to the motion of the blade $U_T = \Omega r_{\text{s}}$, where r_{s} is the position of the blade element along the blade span with respect to the rotor hub (See Figure 2.3).

The planar velocity U_T combines with the velocity perpendicular to the rotor disc plane, which is the induced velocity $U_P = v_1$ for the hover case, forms the net air velocity $\vec{\boldsymbol{U}}$ that the blade element experienced. The angle that the net air velocity $\vec{\boldsymbol{U}}$ made with respect to the rotor disc plane is called the inflow angle ϕ:

$$\phi = \arctan\left(\frac{U_P}{U_T}\right) = \arctan\left(\frac{v_1}{\Omega r_s}\right) \tag{B.13}$$

For small inflow angle, it can be approximated by:

$$\phi \approx \frac{U_P}{U_T} = \frac{v_1}{\Omega r_s} \tag{B.14}$$

The difference between the blade pitch θ, measured relative to the rotor disc plane, and the inflow angle ϕ is the effective angle of attack α [1]:

$$\alpha = \theta - \phi \tag{B.15}$$

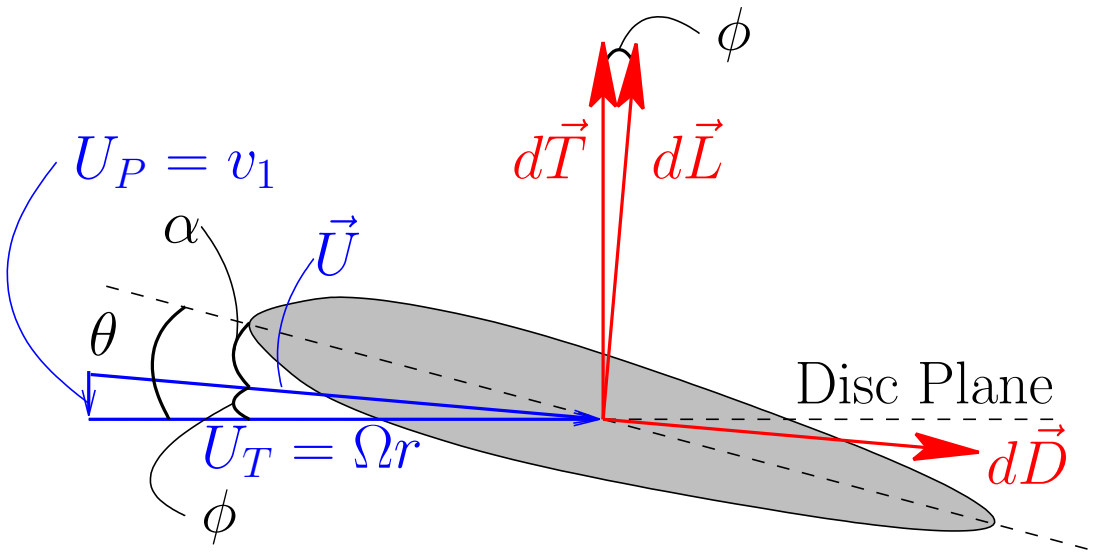

Figure B.1: Force and Velocity Components on a Blade Element

As a lift generating surface, the aerodynamic forces acting on the blade element is similar to those on an air foil of an airplane wing [42]. The force acting on the blade element can be resolved into an incremental lift vector $d\vec{\boldsymbol{L}}$ and an incremental drag vector $d\vec{\boldsymbol{D}}$ components that

are perpendicular to each other. The lift is perpendicular to the net air velocity $\vec{\boldsymbol{U}}$ over the blade element; while the drag component is along that of $\vec{\boldsymbol{U}}$. The direction of these forces on the blade element is shown in Figure B.1. Here, a distinction is made between the lift generated by the blade ($d\vec{\boldsymbol{L}}$) and the rotor thrust ($d\vec{\boldsymbol{T}}$). The rotor thrust is the component of the blade aerodynamic force that is normal to the rotor disc plane.

The magnitude of the lift (drag) force component of the blade element has a general form of a product of three terms: the dynamic pressure $\frac{1}{2}\rho\vec{\boldsymbol{U}}^2$, the lift (drag) coefficient c_L (c_D) and the surface area of the blade element cdr_s:

$$d\vec{\boldsymbol{L}} = \frac{1}{2}\rho\vec{\boldsymbol{U}}^2 c_L c dr_s \qquad \text{and} \qquad d\vec{\boldsymbol{D}} = \frac{1}{2}\rho\vec{\boldsymbol{U}}^2 c_D c dr_s \tag{B.16}$$

The dynamic pressure term $\frac{1}{2}\rho\vec{\boldsymbol{U}}$ describes the force and drag dependency on the air density and the relative air speed. The dimensionless coefficients (c_L and c_D) measures the effectiveness of the blade element at producing lift and drag. When operating with relatively small angle of attack ($\alpha < 20°$), the lift coefficient c_L is proportional to α [42]:

$$c_L = a_L \alpha \tag{B.17}$$

where a_L is the lift curve coefficient and has a nominal value of around 6 for air foil typically use on helicopter rotor blades [1].

Substituting the expressions for the air velocity $\vec{\boldsymbol{U}}$, the lift (drag) coefficient c_L (c_{D}), the angle of attack α and the inflow angle (ϕ) into (B.16), the incremental lift (drag) becomes:

$$d\vec{\boldsymbol{L}} = \frac{1}{2}\rho U_T^2 a_L c \left(\theta - \frac{U_P}{U_T}\right) dr_s \qquad \text{and} \qquad d\vec{\boldsymbol{D}} = \frac{1}{2}\rho U_T^2 a_L c_{\mathrm{D}} c dr_s \tag{B.18}$$

Notice that the air velocity U is approximated by $U \approx U_T$ as the tangential velocity is typically an order of magnitude larger than the normal velocity $U_T >> U_P$ for normal operations. Substituting the tangential and normal air velocity for hover, the incremental lift and drag becomes:

$$d\vec{\boldsymbol{L}} = \frac{1}{2}\rho a c \left[\theta(\Omega r_s)^2 - v_1(\Omega r_s)\right] dr_s \qquad \text{and} \qquad d\vec{\boldsymbol{D}} = \frac{1}{2}\rho a_L c_{\mathrm{D}} c (\Omega r_s)^2 dr_s \tag{B.19}$$

When deriving the incremental lift and drag for general flight, the tangential and normal air

velocity will be modified to include the effect of the rotor velocity due to helicopter motion [1]:

$$U_T = \Omega r + V_{\text{horizontal}} \sin(\Psi) \tag{B.20}$$

$$U_P = v_1 \left[1 + K\frac{r_s}{R}\cos(\Psi)\right] - V_{\text{vertical}} + V_{\text{horizontal}}\beta\cos(\Psi) + r_s\left[\dot{\beta} + p\sin(\Psi) - q\cos(\Psi)\right] \tag{B.21}$$

where v_1 is the averaged induced velocity in hover and K is the velocity dependent factor to account for the non-uniform distribution of the induced velocity due to the motion of the rotor through air [12]:

$$K = \begin{cases} \tan\left(\frac{|\chi|}{2}\right) & |\chi| \leq \frac{\pi}{2} \\ \cot\left(\frac{|\chi|}{2}\right) & \frac{\pi}{2} < |\chi| \end{cases} \tag{B.22}$$

The wake angle χ is defined as:

$$\chi = \arctan\left(\frac{\mu}{\lambda_1 + \lambda_z}\right) \tag{B.23}$$

The first term in the normal velocity equation (B.21) represents the effect of forward speed on the induced velocity. The second term is the component of the incoming velocity (due to the motion of the helicopter) along the rotor shaft axis. The last two terms accounts for the effect of blade flapping [9].

The incremental thrust ($d\vec{\boldsymbol{T}}$) is the sum of the projection of the incremental lift and drag vector normal to the disc plane:

$$d\vec{\boldsymbol{T}} = d\vec{\boldsymbol{L}}\cos(\phi) - d\vec{\boldsymbol{D}}\sin(\phi) \approx d\vec{\boldsymbol{L}} \tag{B.24}$$

The incremental thrust is approximated by the incremental lift because of the small magnitude of the incremental drag vector relative to the incremental lift, as well as the small angle assumption on the inflow angle ϕ. The net rotor thrust $\vec{\boldsymbol{T}}$ is computed by integrating the incremental thrust $d\vec{\boldsymbol{T}}$ along the span (length) of the blade and multiply by the number of blades N_b:

$$\vec{\boldsymbol{T}} = N_b \int_0^R d\vec{\boldsymbol{T}} \tag{B.25}$$

For general flight, such as in forward flight, the incremental thrust needs to be averaged over the

azimuth angle (Ψ) as well to account for the non-uniform induced velocity flow at the rotor:

$$\vec{\boldsymbol{T}} = \frac{N_b}{2\pi}\int_0^R \int_0^{2\pi} d\vec{\boldsymbol{T}} \tag{B.26}$$

Carrying out the integration in (B.25), the thrust for hover is given by:

$$\vec{\boldsymbol{T}} = \frac{1}{2}\rho N_b c R(\Omega R)^2 a_L \left(\frac{\theta_0}{3} - \frac{v_1}{2(\Omega R)}\right) \tag{B.27}$$

The thrust equation can be written in a more compact form using the following non-dimensional factors [10, 1, 9]:

$$\text{Thrust Coefficient} \quad : \hat{C}_{\mathrm{T}} \quad = \frac{T}{\rho A_{\mathrm{disc}}(\Omega R)^2} \tag{B.28}$$

$$\text{Inflow Factor} \quad : \lambda_1 \quad = \frac{v_1}{(\Omega R)} \tag{B.29}$$

$$\text{Solidity} \quad : \sigma \quad = \frac{A_{\mathrm{b}}}{A_{\mathrm{disc}}} = \frac{N_b c R}{\pi R^2} = \frac{N_b c}{\pi R} \tag{B.30}$$

where A_{b} is the total blade area of the rotor.

The hover thrust coefficient is then given as:

$$\hat{C}_{\mathrm{T}} = \frac{\sigma a_L}{4}\left(\frac{2}{3}\theta_0 - \lambda_1\right) \tag{B.31}$$

For general flight, the thrust coefficient becomes:

$$\hat{C}_{\mathrm{T}} = \frac{\sigma a_L}{4}\left[\frac{2}{3}\theta_0\left(1 + \frac{3}{2}\mu^2\right) - (\lambda_1 + \lambda_{\mathrm{z}} + \mu B_1) - \frac{\mu \upsilon_{\mathrm{x}}}{2}\right] \tag{B.32}$$

In addition to the thrust, when the helicopter is in motion (such as in forward flight), the asymmetry in the local angle of attack of the blades also produces net force within the disc plane. This force is called the planar Horizontal Force (H-Force). The component of the H-Force along the direction of flight is called the longitudinal H-Force; the associated perpendicular component is referred to as the lateral H-Force. The incremental longitudinal H-Force $d\vec{\boldsymbol{H}}_{\mathrm{lon}}$ is defined as:

$$d\vec{\boldsymbol{H}}_{\mathrm{lon}} = d\vec{\boldsymbol{L}}\big[\phi \sin(\Psi) - \beta \cos(\Psi)\big] + d\vec{\boldsymbol{D}} \sin(\Psi) \tag{B.33}$$

and the incremental lateral H-Force $d\vec{\boldsymbol{H}}_{\text{lat}}$ is define as:

$$d\vec{\boldsymbol{H}}_{\text{lat}} = -d\vec{\boldsymbol{L}}\big[\phi\cos(\Psi) + \beta\sin(\Psi)\big] - d\vec{\boldsymbol{D}}\cos(\Psi) \tag{B.34}$$

Similar to the rotor thrust, these can be integrated to obtain:

$$\begin{aligned}
\hat{C}_{\text{lon}} &= \frac{\mu\sigma}{4}c_{\text{D}} + a_{1,\text{s}}\hat{C}_{\text{T}} + \frac{a_L\sigma}{4}\Bigg((\lambda_1 + \lambda_{\text{z}} - a_{1,\text{s}}\mu)\left[\theta_0\mu - \frac{1}{2}(a_{1,\text{s}} + \hat{B}_1) - \upsilon_{\text{x}}\right] \\
&\quad +(b_{1,\text{s}} + \hat{A}_1)\left[\frac{a_0}{3} - \frac{\mu}{8}(K\lambda_1 - \upsilon_{\text{y}})\right] + a_0\left[\frac{\mu a_0}{2} + \frac{1}{3}(K\lambda_1 - \upsilon_{\text{y}})\right] \\
&\quad +\upsilon_{\text{x}}\left[\frac{\theta_0}{3} - \frac{3}{8}\mu(a_{1,\text{s}} + \hat{B}_1)\right]\Bigg) \qquad \text{(B.35)} \\
\hat{C}_{\text{lat}} &= -b_{1,\text{s}}\hat{C}_{\text{T}} + \frac{a_L\sigma}{4}\Bigg((\lambda_1 + \lambda_{\text{z}} - a_{1,\text{s}}\mu)\left[3a_0\mu + (K\lambda_1 - \upsilon_{\text{y}}) + \frac{1}{2}(b_{1,\text{s}} + \hat{A}_1)\right] \\
&\quad +(a_{1,\text{s}} + \hat{B}_1)\left[\frac{a_0}{3} + \frac{\mu}{8}(K\lambda_1 - \upsilon_{\text{y}}) + a_0\mu^2\right] - \theta_0\left[\frac{3}{2}a_0\mu + \frac{1}{3}(K\lambda_1 - \upsilon_{\text{y}})\right] \\
&\quad +\upsilon_{\text{x}}\left[\frac{a_0}{3} + \frac{\mu}{8}(b_{1,\text{s}} + \hat{A}_1)\right]\Bigg) \qquad \text{(B.36)}
\end{aligned}$$

where the H-forces have been written in the compact non-dimensional form defined similar to the thrust coefficient as:

$$\hat{C}_{\text{lon}} = \frac{H_{\text{lon}}}{\rho A_{\text{disc}}(\Omega R)^2} \qquad\qquad \hat{C}_{\text{lat}} = \frac{H_{\text{lat}}}{\rho A_{\text{disc}}(\Omega R)^2} \tag{B.37}$$

The expressions for the flapping coefficients a_0, $a_{1,\text{s}}$ and $b_{1,\text{s}}$, defined in (2.25), can be obtained by summing the flapping (out-of-plane) moment on the rotor blade about the rotor hub hinge at equilibrium [9]:

$$a_0 = \frac{\gamma_{\text{L}}}{8}\left[\theta_0(1+\mu^2) - \frac{4}{3}(\lambda_1 + \lambda_{\text{z}} + \mu\hat{B}_1) - \frac{2}{3}\mu\upsilon_{\text{x}}\right] - \frac{3}{2}\frac{g}{\Omega^2 R} \tag{B.38}$$

$$a_{1,\text{s}} = \frac{2\mu}{(1-\mu^2/2)}\left[\frac{4}{3}\theta_0 - (\lambda_1 + \lambda_{\text{z}} + \mu\hat{B}_1)\right] - \frac{\upsilon_{\text{x}}}{(1-\mu^2/2)} - \frac{16\upsilon_{\text{y}}}{\gamma_{\text{L}}(1-\mu^2/2)} - \hat{B}_1 \tag{B.39}$$

$$b_{1,\text{s}} = \frac{-1}{(1+\mu^2/2)}\left[\frac{4}{3}a_0\mu + K\lambda_1 - \upsilon_{\text{y}}\right] - \frac{16\upsilon_{\text{x}}}{\gamma_{\text{L}}(1+\mu^2/2)} - \hat{A}_1 \tag{B.40}$$

where γ_{L} is the Lock Number defined as [10]:

$$\gamma_{\mathrm{L}} = \frac{\rho a c R^4}{I_{\mathrm{blade}}} \tag{B.41}$$

with I_{blade} representing the blade flapping inertia.

Carrying out the same process for computing the rotor torque Q, the incremental torque $d\vec{\boldsymbol{Q}}$ is defined as:

$$d\vec{\boldsymbol{Q}} = r(d\vec{\boldsymbol{L}}\phi + d\vec{\boldsymbol{D}}) \tag{B.42}$$

The torque coefficient for hover, obtained by integrating the incremental torque, is given as:

$$\hat{C}_{\mathrm{Q}} = \frac{\sigma}{8} c_{\mathrm{D}} + \frac{1}{\sqrt{2}} \hat{C}_{\mathrm{T}}^{3/2} \tag{B.43}$$

where the torque coefficient is defined by:

$$\hat{C}_{\mathrm{Q}} = \frac{Q}{\rho A_{\mathrm{disc}} (\Omega R)^2 R} \tag{B.44}$$

The torque coefficient for general flight is:

$$\hat{C}_{\mathrm{Q}} = \frac{\sigma}{8} c_{\mathrm{D}} (1 + 3\mu^2) + (\lambda_1 + \lambda_{\mathrm{z}}) \hat{C}_{\mathrm{T}} - \mu \hat{C}_{\mathrm{lon}} + \frac{a_L \sigma}{\gamma_{\mathrm{L}}} (a_{1,\mathrm{s}} \upsilon_{\mathrm{y}} + b_{1,\mathrm{s}} \upsilon_{\mathrm{x}} + K \lambda_1 \upsilon_{\mathrm{x}}) \tag{B.45}$$

Appendix C

Platform Kinematics

C.1 Position Vectors

The position vectors for the centre of gravity of each of the rigid body of the platform system expressed with respect to the inertial frame are given as follows. The *home* position of the platform system is when all of the joint variables are at zero. The Inertial Frame is defined on the same level as the helicopter centre of gravity when it is at the *home* position. The location of the centre of gravity of each of the rigid body in the platform system and their associated reference frames are indicated in Figure 2.6.

$$\vec{\boldsymbol{r}}_1 = \begin{bmatrix} 0 \\ 0 \\ l_4 + \rho_1 \end{bmatrix} \qquad \vec{\boldsymbol{r}}_2 = \begin{bmatrix} \rho_2 C_{q_1} C_{q_2} \\ \rho_2 S_{q_1} C_{q_2} \\ -(l_1 + \rho_2 S_{q_2}) \end{bmatrix} \qquad \vec{\boldsymbol{r}}_3 = \begin{bmatrix} -\rho_3 C_{q_1} C_{q_2} \\ -\rho_3 S_{q_1} C_{q_2} \\ -(l_1 + l_2 - \rho_3 S_{q_2}) \end{bmatrix}$$

$$\vec{\boldsymbol{r}}_4 = \begin{bmatrix} l_3 C_{q_1} C_{q_2} \\ l_3 S_{q_1} C_{q_2} \\ -(l_1 + \rho_4 + l_3 S_{q_2}) \end{bmatrix} \quad \vec{\boldsymbol{r}}_b = \begin{bmatrix} (l_s + q_3 + l_3 C_{q_2}) C_{q_1} \\ (l_s + q_3 + l_3 C_{q_2}) S_{q_1} \\ -(l_1 + l_2 + l_4 + l_3 S_{q_2}) \end{bmatrix} \tag{C.1}$$

C.2 Velocity Vectors

C.2.1 Linear Velocity Vectors

The linear velocity of each of the rigid body expressed in the inertial frame are given as follows.

$$\vec{\boldsymbol{v}}_1 = \begin{bmatrix} 0 \\ 0 \\ 0 \end{bmatrix} \quad \vec{\boldsymbol{v}}_2 = \begin{bmatrix} -\rho_2(S_{q_1}C_{q_2}\dot{q}_1 + C_{q_1}S_{q_2}\dot{q}_2) \\ \rho_2(C_{q_1}C_{q_2}\dot{q}_1 - S_{q_1}S_{q_1}\dot{q}_2) \\ -\rho_2 C_{q_2}\dot{q}_2 \end{bmatrix} \quad \vec{\boldsymbol{v}}_3 = \begin{bmatrix} \rho_3(S_{q_1}C_{q_2}\dot{q}_1 + C_{q_1}S_{q_2}\dot{q}_2) \\ -\rho_3(C_{q_1}C_{q_2}\dot{q}_1 - S_{q_1}S_{q_1}\dot{q}_2) \\ \rho_3 C_{q_2}\dot{q}_2 \end{bmatrix}$$
$$\vec{\boldsymbol{v}}_4 = \begin{bmatrix} -l_3(S_{q_1}C_{q_2}\dot{q}_1 + C_{q_1}S_{q_2}\dot{q}_2) \\ l_3(C_{q_1}C_{q_2}\dot{q}_1 - S_{q_1}S_{q_1}\dot{q}_2) \\ -l_3 C_{q_2}\dot{q}_2 \end{bmatrix} \quad \vec{\boldsymbol{v}}_b = \begin{bmatrix} -\big[(l_s + q_3 + l_3C_{q_2})S_{q_1}\dot{q}_1 + (S_{q_2}\dot{q}_2 - \dot{q}_3)C_{q_1}\big] \\ (l_s + q_3 + l_3C_{q_2})C_{q_1}\dot{q}_1 - (S_{q_2}\dot{q}_2 - \dot{q}_3)S_{q_1} \\ -l_3 C_{q_2}\dot{q}_2 \end{bmatrix} \tag{C.2}$$

The linear velocity expressed with respect to the associated centre of gravity frame for each rigid body is given as follows.

$$\vec{\boldsymbol{v}}_{l_1} = \begin{bmatrix} 0 \\ 0 \\ 0 \end{bmatrix} \quad \vec{\boldsymbol{v}}_{l_2} = \begin{bmatrix} 0 \\ \rho_2\dot{q}_2 \\ \rho_2 C_{q_2}\dot{q}_1 \end{bmatrix} \quad \vec{\boldsymbol{v}}_{l_3} = \begin{bmatrix} 0 \\ -\rho_3\dot{q}_2 \\ -\rho_3 C_{q_2}\dot{q}_1 \end{bmatrix} \quad \vec{\boldsymbol{v}}_{l_4} = \begin{bmatrix} -l_3 S_{q_2}\dot{q}_2 \\ l_3 C_{q_2}\dot{q}_1 \\ -l_3 C_{q_2}\dot{q}_2 \end{bmatrix}$$
$$\begin{aligned} \vec{\boldsymbol{v}}_{l_b} = {} & (l_s + q_3 + l_3C_{q_2})\dot{q}_1 \begin{bmatrix} S_{q_4}C_{q_5} \\ S_{q_4}S_{q_5}S_{q_6} + C_{q_4}C_{q_6} \\ S_{q_4}S_{q_5}C_{q_6} - C_{q_4}S_{q_6} \end{bmatrix} \\ & - l_3\dot{q}_2 \begin{bmatrix} S_{q_2}C_{q_4}C_{q_5} - C_{q_2}S_{q_5} \\ S_{q_2}(C_{q_4}S_{q_5}S_{q_6} - S_{q_4}C_{q_6}) + C_{q_2}C_{q_5}S_{q_6} \\ S_{q_2}(C_{q_4}S_{q_5}C_{q_6} + S_{q_4}S_{q_6}) + C_{q_2}C_{q_5}C_{q_6} \end{bmatrix} \\ & + \dot{q}_3 \begin{bmatrix} C_{q_4}C_{q_5} \\ C_{q_4}S_{q_5}S_{q_6} - S_{q_4}C_{q_6} \\ C_{q_4}S_{q_5}C_{q_6} + S_{q_4}S_{q_6} \end{bmatrix} \end{aligned} \tag{C.3}$$

C.2.2 Angular Velocity Vectors

The angular velocity of each of the rigid body in the platform system expressed in the inertial frame is given as follows.

$$\vec{\boldsymbol{\omega}}_1 = \begin{bmatrix} 0 \\ 0 \\ \dot{q}_1 \end{bmatrix} \qquad \vec{\boldsymbol{\omega}}_2 = \begin{bmatrix} -S_{q_1}\dot{q}_2 \\ C_{q_1}\dot{q}_2 \\ \dot{q}_1 \end{bmatrix} \qquad \vec{\boldsymbol{\omega}}_3 = \begin{bmatrix} -S_{q_1}\dot{q}_2 \\ C_{q_1}\dot{q}_2 \\ \dot{q}_1 \end{bmatrix} \qquad \vec{\boldsymbol{\omega}}_4 = \begin{bmatrix} 0 \\ 0 \\ \dot{q}_1 \end{bmatrix}$$
$$\vec{\boldsymbol{\omega}}_b = \begin{bmatrix} -\sin(q_1+q_4)\dot{q}_5 + \cos(q_1+q_4)C_{q_5}\dot{q}_6 \\ \cos(q_1+q_4)\dot{q}_5 + \sin(q_1+q_4)C_{q_5}\dot{q}_6 \\ \dot{q}_1 + \dot{q}_4 - S_{q_5}\dot{q}_6 \end{bmatrix} \tag{C.4}$$

The angular velocity of the rigid bodies expressed in the associated local frames are given as follows.

$$\vec{\boldsymbol{\omega}}_{l_1} = \begin{bmatrix} 0 \\ 0 \\ \dot{q}_1 \end{bmatrix} \qquad \vec{\boldsymbol{\omega}}_{l_2} = \begin{bmatrix} -S_{q_2}\dot{q}_1 \\ -C_{q_2}\dot{q}_1 \\ \dot{q}_2 \end{bmatrix} \qquad \vec{\boldsymbol{\omega}}_{l_3} = \begin{bmatrix} -S_{q_2}\dot{q}_1 \\ -C_{q_2}\dot{q}_1 \\ \dot{q}_2 \end{bmatrix} \qquad \vec{\boldsymbol{\omega}}_{l_4} = \begin{bmatrix} 0 \\ 0 \\ \dot{q}_1 \end{bmatrix}$$
$$\vec{\boldsymbol{\omega}}_{l_b} = \tilde{\boldsymbol{\omega}}_b = \begin{bmatrix} -S_{q_5}(\dot{q}_1+\dot{q}_4) + \dot{q}_6 \\ C_{q_5}S_{q_6}(\dot{q}_1+\dot{q}_4) + C_{q_6}\dot{q}_5 \\ C_{q_5}C_{q_6}(\dot{q}_4+\dot{q}_4) - S_{q_6}\dot{q}_5 \end{bmatrix} \tag{C.5}$$

C.3 Jacobian Matrices

C.3.1 Linear Jacobian

The Jacobian matrix mapping between the joint rates and the linear velocity of each of the rigid bodies in the platform system expressed in their associated local frames are listed in the following.

The base rod is fixed to the ground and therefore its linear velocity Jacobian is zero:

$$\boldsymbol{J}_{v_1} = \mathbf{0}_{3\times 6} = \begin{bmatrix} \vec{\boldsymbol{\beta}}_{11} & \vec{\boldsymbol{\beta}}_{12} & \vec{\boldsymbol{\beta}}_{13} & \vec{\boldsymbol{\beta}}_{14} & \vec{\boldsymbol{\beta}}_{15} & \vec{\boldsymbol{\beta}}_{16} \end{bmatrix} \tag{C.6}$$

where the j^{th} column of the Jacobian matrix is the rate projection vector of the velocity vector with respect to the j^{th} generalized coordinate $\vec{\boldsymbol{\beta}}_{1j}$.

For the bottom (Body 2) and main (Body 3) boom:

$$\begin{aligned} \boldsymbol{J}_{v_2} &= \rho_2 \boldsymbol{J}_{v_p} = \left[\begin{array}{cccccc} \vec{\boldsymbol{\beta}}_{21} & \vec{\boldsymbol{\beta}}_{22} & \vec{\boldsymbol{\beta}}_{23} & \vec{\boldsymbol{\beta}}_{24} & \vec{\boldsymbol{\beta}}_{25} & \vec{\boldsymbol{\beta}}_{26} \end{array} \right] \\ \boldsymbol{J}_{v_3} &= -\rho_3 \boldsymbol{J}_{v_p} = \left[\begin{array}{cccccc} \vec{\boldsymbol{\beta}}_{31} & \vec{\boldsymbol{\beta}}_{32} & \vec{\boldsymbol{\beta}}_{33} & \vec{\boldsymbol{\beta}}_{34} & \vec{\boldsymbol{\beta}}_{35} & \vec{\boldsymbol{\beta}}_{36} \end{array} \right] \end{aligned} \tag{C.7}$$

where

$$\boldsymbol{J}_{v_p} = \left[\begin{array}{cccccc} 0 & 0 & 0 & 0 & 0 & 0 \\ 0 & 1 & 0 & 0 & 0 & 0 \\ C_{q_2} & 0 & 0 & 0 & 0 & 0 \end{array} \right] \tag{C.8}$$

and for the vertical bar (Body 4):

$$\boldsymbol{J}_{v_4} = \left[\begin{array}{cccccc} 0 & -l_3 S_{q_2} & 0 & 0 & 0 & 0 \\ l_3 C_{q_2} & 0 & 0 & 0 & 0 & 0 \\ 0 & -l_3 C_{q_2} & 0 & 0 & 0 & 0 \end{array} \right] = \left[\begin{array}{cccccc} \vec{\boldsymbol{\beta}}_{41} & \vec{\boldsymbol{\beta}}_{42} & \vec{\boldsymbol{\beta}}_{43} & \vec{\boldsymbol{\beta}}_{44} & \vec{\boldsymbol{\beta}}_{45} & \vec{\boldsymbol{\beta}}_{46} \end{array} \right] \tag{C.9}$$

Finally, for the helicopter body:

$$\begin{aligned} \boldsymbol{J}_{v_b} &= \left[\begin{array}{ccccc} l_{hp} S_{q_4} C_{q_5} & -l_3 (S_{q_2} C_{q_4} C_{q_5} - C_{q_2} S_{q_5}) & C_{q_4} C_{q_5} & & \\ l_{hp} (S_{q_4} S_{q_5} S_{q_6} + C_{q_4} C_{q_6}) & -l_3 (S_{q_2} r_{12} + C_{q_2} C_{q_5} S_{q_6}) & r_{12} & \boldsymbol{0}_{3\times 3} & \\ l_{hp} (S_{q_4} S_{q_5} C_{q_6} - C_{q_4} S_{q_6}) & -l_3 (S_{q_2} r_{13} + C_{q_2} C_{q_5} C_{q_6}) & r_{13} & & \end{array} \right] \\ &= \left[\begin{array}{cccccc} \vec{\boldsymbol{\beta}}_{b1} & \vec{\boldsymbol{\beta}}_{b2} & \vec{\boldsymbol{\beta}}_{b3} & \vec{\boldsymbol{\beta}}_{b4} & \vec{\boldsymbol{\beta}}_{b5} & \vec{\boldsymbol{\beta}}_{b6} \end{array} \right] \end{aligned} \tag{C.10}$$

where $l_{hp} = (l_s + q_3 + l_3 C_{q_2})$, $r_{12} = C_{q_4} S_{q_5} S_{q_6} - S_{q_4} C_{q_6}$, and $r_{13} = C_{q_4} S_{q_5} C_{q_6} + S_{q_4} S_{q_6}$.

C.3.2 Angular Jacobian

The Jacobian matrix mapping between the joint rates and the angular velocities of the rigid bodies of the platform system are listed in the following.

The motion of the base rod (Body 1) and the vertical bar (Body 4) are constrained by the

parallelogram configuration of the platform so that they have the same angular velocities:

$$\begin{aligned}\boldsymbol{J}_{\omega_1} = \boldsymbol{J}_{\omega_4} &= \begin{bmatrix} 0 & 0 & 0 & 0 & 0 & 0 \\ 0 & 0 & 0 & 0 & 0 & 0 \\ 1 & 0 & 0 & 0 & 0 & 0 \end{bmatrix} \\ &= \begin{bmatrix} \vec{\gamma}_{11} & \vec{\gamma}_{12} & \vec{\gamma}_{13} & \vec{\gamma}_{14} & \vec{\gamma}_{15} & \vec{\gamma}_{16} \end{bmatrix} = \begin{bmatrix} \vec{\gamma}_{41} & \vec{\gamma}_{42} & \vec{\gamma}_{43} & \vec{\gamma}_{44} & \vec{\gamma}_{45} & \vec{\gamma}_{46} \end{bmatrix}\end{aligned} \tag{C.11}$$

Similarly, the main and bottom boom have the same angular velocity:

$$\begin{aligned}\boldsymbol{J}_{\omega_2} = \boldsymbol{J}_{\omega_3} &= \begin{bmatrix} -S_{q_2} & 0 & 0 & 0 & 0 & 0 \\ -C_{q_2} & 0 & 0 & 0 & 0 & 0 \\ 0 & 1 & 0 & 0 & 0 & 0 \end{bmatrix} \\ &= \begin{bmatrix} \vec{\gamma}_{21} & \vec{\gamma}_{22} & \vec{\gamma}_{23} & \vec{\gamma}_{24} & \vec{\gamma}_{25} & \vec{\gamma}_{26} \end{bmatrix} = \begin{bmatrix} \vec{\gamma}_{31} & \vec{\gamma}_{32} & \vec{\gamma}_{33} & \vec{\gamma}_{34} & \vec{\gamma}_{35} & \vec{\gamma}_{36} \end{bmatrix}\end{aligned} \tag{C.12}$$

Finally, the angular Jacobian for the helicopter body is:

$$\boldsymbol{J}_{\omega_b} = \begin{bmatrix} -S_{q_5} & 0 & 0 & -S_{q_5} & 0 & 1 \\ C_{q_5}S_{q_6} & 0 & 0 & C_{q_5}S_{q_6} & C_{q_6} & 0 \\ C_{q_5}C_{q_6} & 0 & 0 & C_{q_5}C_{q_6} & -S_{q_6} & 0 \end{bmatrix} = \begin{bmatrix} \vec{\gamma}_{b1} & \vec{\gamma}_{b2} & \vec{\gamma}_{b3} & \vec{\gamma}_{b4} & \vec{\gamma}_{b5} & \vec{\gamma}_{b6} \end{bmatrix} \tag{C.13}$$

C.3.3 Overall Jacobian

The overall Jacobian is obtained by augmenting the linear and angular Jacobian together. The Jacobians for the rigid bodies of the platform system is therefore defined as:

$$\boldsymbol{J}_1 = \begin{bmatrix} \boldsymbol{J}_{v_1} \\ \boldsymbol{J}_{\omega_1} \end{bmatrix} \quad \boldsymbol{J}_2 = \begin{bmatrix} \boldsymbol{J}_{v_2} \\ \boldsymbol{J}_{\omega_2} \end{bmatrix} \quad \boldsymbol{J}_3 = \begin{bmatrix} \boldsymbol{J}_{v_3} \\ \boldsymbol{J}_{\omega_3} \end{bmatrix} \quad \boldsymbol{J}_4 = \begin{bmatrix} \boldsymbol{J}_{v_4} \\ \boldsymbol{J}_{\omega_4} \end{bmatrix} \quad \boldsymbol{J}_b = \begin{bmatrix} \boldsymbol{J}_{v_b} \\ \boldsymbol{J}_{\omega_b} \end{bmatrix} \tag{C.14}$$

C.4 Acceleration Vectors

C.4.1 Linear Acceleration Vectors

The acceleration vectors of the platform system expressed in the inertial frame is given as follows.

$$\begin{aligned}
\vec{\boldsymbol{a}}_1 &= \begin{bmatrix} 0 \\ 0 \\ 0 \end{bmatrix} \qquad \vec{\boldsymbol{a}}_2 = -\rho_2 \vec{\boldsymbol{a}}_{hp} \qquad \vec{\boldsymbol{a}}_3 = \rho_3 \vec{\boldsymbol{a}}_{hp} \qquad \vec{\boldsymbol{a}}_4 = -l_3 \vec{\boldsymbol{a}}_{hp} \\
\vec{\boldsymbol{a}}_b &= -l_3 \vec{\boldsymbol{a}}_{hp} + \begin{bmatrix} -(l_s + q_3) S_{q_1} \ddot{q}_1 + C_{q_1} \ddot{q}_3 - (l_s + q_3) C_{q_1} \dot{q}_1^2 - 2 S_{q_1} \dot{q}_1 \dot{q}_3 \\ (l_s + q_3) C_{q_1} \ddot{q}_1 + S_{q_1} \ddot{q}_3 - (l_s + q_3) S_{q_1} \dot{q}_1^2 + 2 C_{q_1} \dot{q}_1 \dot{q}_3 \\ 0 \end{bmatrix}
\end{aligned} \tag{C.15}$$

where

$$\vec{\boldsymbol{a}}_{hp} = \begin{bmatrix} S_{q_1} C_{q_2} \ddot{q}_1 + C_{q_1} S_{q_2} \ddot{q}_2 + C_{q_1} C_{q_2} (\dot{q}_1^2 + \dot{q}_2^2) - 2 S_{q_1} S_{q_2} \dot{q}_1 \dot{q}_2 \\ -C_{q_1} C_{q_2} \ddot{q}_1 + S_{q_1} S_{q_2} \ddot{q}_2 + S_{q_1} C_{q_2} (\dot{q}_1^2 + \dot{q}_2^2) + 2 C_{q_1} S_{q_2} \dot{q}_1 \dot{q}_2 \\ C_{q_2} \ddot{q}_2 - S_{q_2} \dot{q}_2^2 \end{bmatrix} \tag{C.16}$$

Appendix D

Platform Matrices

D.1 Inertia Matrices

$$\boldsymbol{I}_1 = \begin{bmatrix} I_{xx_1} & 0 & 0 \\ 0 & I_{yy_1} & 0 \\ 0 & 0 & I_{zz_1} \end{bmatrix} \quad \boldsymbol{I}_2 = \begin{bmatrix} I_{xx_2} & 0 & 0 \\ 0 & I_{yy_2} & 0 \\ 0 & 0 & I_{zz_2} \end{bmatrix} \quad \boldsymbol{I}_3 = \begin{bmatrix} I_{xx_3} & 0 & 0 \\ 0 & I_{yy_3} & 0 \\ 0 & 0 & I_{zz_3} \end{bmatrix}$$

$$\boldsymbol{I}_4 = \begin{bmatrix} I_{xx_4} & 0 & 0 \\ 0 & I_{yy_4} & 0 \\ 0 & 0 & I_{zz_4} \end{bmatrix} \quad \boldsymbol{I}_b = \begin{bmatrix} I_{xx_b} & 0 & -I_{xz_b} \\ 0 & I_{yy_b} & 0 \\ -I_{xz_b} & 0 & I_{zz_b} \end{bmatrix} \tag{D.1}$$

D.2 Mass Matrices

The mass matrix of the platform system expressed in joint space is symmetric and has the form:

$$\bar{\boldsymbol{M}}(\bar{\boldsymbol{q}}) = \begin{bmatrix} m_{11} & 0 & 0 & m_{44} & m_{15} & m_{16} \\ 0 & m_{22} & m_{23} & 0 & 0 & 0 \\ 0 & m_{23} & m_{33} & 0 & 0 & 0 \\ m_{44} & 0 & 0 & m_{44} & m_{15} & m_{16} \\ m_{15} & 0 & 0 & m_{15} & m_{55} & m_{56} \\ m_{16} & 0 & 0 & m_{16} & m_{56} & m_{66} \end{bmatrix} \tag{D.2}$$

where

$$\begin{aligned} m_{11} = {} & I_{zz_1} + I_{zz_4} + (I_{xx_2} + I_{xx_3})S_{q_2}^2 + (I_{yy_2} + I_{yy_3} + m_2\rho_2^2 + m_3\rho_3^2 + m_4 l_3^2)C_{q_2}^2 \\ & + m_b(l_s + q_3 + l_3 C_{q_2})^2 + I_{xx_\mathrm{b}} S_{q_5}^2 + (I_{yy_\mathrm{b}} S_{q_6}^2 + I_{zz_\mathrm{b}} C_{q_6}^2)C_{q_5}^2 + 2I_{xz_\mathrm{b}} C_{q_6} S_{q_5} C_{q_5} \end{aligned} \tag{D.3}$$

$$m_{22} = I_{zz_2} + I_{zz_3} + m_2\rho_2^2 + m_3\rho_3^2 + (m_4 + m_b)l_3^2 \tag{D.4}$$

$$m_{33} = m_b \tag{D.5}$$

$$m_{44} = I_{xx_\mathrm{b}} S_{q_5}^2 + (I_{yy_\mathrm{b}} S_{q_6}^2 + I_{zz_\mathrm{b}} C_{q_6}^2)C_{q_5}^2 + 2I_{xz_b} C_{q_6} S_{q_5} C_{q_5} \tag{D.6}$$

$$m_{55} = I_{yy_b} C_{q_6}^2 + I_{zz_b} S_{q_6}^2 \tag{D.7}$$

$$m_{66} = I_{xx_b} \tag{D.8}$$

$$m_{15} = \left[(I_{yy_b} - I_{zz_b})C_{q_5} C_{q_6} - I_{xz_b} S_{q_5}\right] S_{q_6} \tag{D.9}$$

$$m_{16} = -(I_{xx_b} S_{q_5} + I_{xz_b} C_{q_6} C_{q_5}) \tag{D.10}$$

$$m_{23} = -m_b l_3 S_{q_2} \tag{D.11}$$

$$m_{56} = I_{xz_b} S_{q_6} \tag{D.12}$$

D.3 Centrifugal and Coriolis Terms

The centrifugal and Coriolis vector $\bar{\boldsymbol{h}}(\bar{\boldsymbol{q}}, \dot{\bar{\boldsymbol{q}}})$ can be expressed as a product with the joint rate vector $\dot{\bar{\boldsymbol{q}}}$:

$$\bar{\boldsymbol{h}}(\bar{\boldsymbol{q}}, \dot{\bar{\boldsymbol{q}}}) = \bar{\boldsymbol{C}}(\bar{\boldsymbol{q}}, \dot{\bar{\boldsymbol{q}}})\dot{\bar{\boldsymbol{q}}} \tag{D.13}$$

The $\bar{\boldsymbol{C}}(\bar{\boldsymbol{q}}, \dot{\bar{\boldsymbol{q}}})$ matrix has the following form:

$$\bar{\boldsymbol{C}}(\bar{\boldsymbol{q}}, \dot{\bar{\boldsymbol{q}}}) = \begin{bmatrix} c_{11} & c_{12} & c_{13} & c_{14} & c_{15} & c_{16} \\ c_{21} & 0 & 0 & 0 & 0 & 0 \\ c_{13} & c_{32} & 0 & 0 & 0 & 0 \\ c_{14} & 0 & 0 & c_{14} & c_{15} & c_{16} \\ c_{51} & 0 & 0 & c_{51} & c_{55} & c_{56} \\ c_{61} & 0 & 0 & c_{61} & c_{65} & 0 \end{bmatrix} \tag{D.14}$$

where each of the elements are given by:

$$\begin{aligned} c_{11} = &\Bigg[\Big(I_{xx_2} + I_{xx_3} - \big[I_{yy_2} + I_{yy_3} + m_2\rho_2^2 + m_3\rho_3^2 + (m_4+m_b)l_3^2\big]\Big)C_{q_2} \\ &\quad - m_b l_3(l_s + q_3)\Bigg]S_{q_2}\dot{q}_2 + m_b(l_s + q_3 + l_3 C_{q_2})\dot{q}_3 \\ &+ \big[(I_{xx_\mathrm{b}} - I_{yy_\mathrm{b}}S_{q_6}^2 - I_{zz_6}C_{q_6}^2)S_{q_5}C_{q_5} + I_{xz_\mathrm{b}}(C_{q_5}^2 - S_{q_5}^2)C_{q_6}\big]\dot{q}_5 \\ &+ \big[(I_{yy_b} - I_{zz_b})C_{q_5}C_{q_6} - I_{xz_b}S_{q_5}\big]C_{q_5}S_{q_6}\dot{q}_6 \end{aligned} \tag{D.15}$$

$$\begin{aligned} c_{12} = &\Bigg[\Big(I_{xx_2} + I_{xx_3} - \big[I_{yy_2} + I_{yy_3} + m_2\rho_2^2 + m_3\rho_3^2 + (m_4+m_b)l_3^2\big]\Big)C_{q_2} \\ &\quad - m_b l_3(l_s + q_3)\Bigg]S_{q_2}\dot{q}_1 \end{aligned} \tag{D.16}$$

$$c_{13} = m_b(l_s + q_3 + l_3 C_{q_2})\dot{q}_1 \tag{D.17}$$

$$\begin{aligned} c_{14} = &\big[(I_{xx_\mathrm{b}} - I_{yy_\mathrm{b}}S_{q_6}^2 - I_{zz_6}C_{q_6}^2)S_{q_5}C_{q_5} + I_{xz_\mathrm{b}}(C_{q_5}^2 - S_{q_5}^2)C_{q_6}\big]\dot{q}_5 \\ &+ \big[(I_{yy_b} - I_{zz_b})C_{q_5}C_{q_6} - I_{xz_b}S_{q_5}\big]C_{q_5}S_{q_6}\dot{q}_6 \end{aligned} \tag{D.18}$$

$$\begin{aligned} c_{15} = &\big[(I_{xx_\mathrm{b}} - I_{yy_\mathrm{b}}S_{q_6}^2 - I_{zz_6}C_{q_6}^2)S_{q_5}C_{q_5} + I_{xz_\mathrm{b}}(C_{q_5}^2 - S_{q_5}^2)C_{q_6}\big](\dot{q}_1 + \dot{q}_4) \\ &- \big[(I_{yy_b} - I_{zz_b})S_{q_5}C_{q_6} + I_{xz_b}C_{q_5}\big]S_{q_6}\dot{q}_5 \\ &- \frac{1}{2}\big[I_{xx_\mathrm{b}} - (I_{yy_\mathrm{b}} - I_{zz_\mathrm{b}})(C_{q_6}^2 - S_{q_6}^2)\big]C_{q_5}\dot{q}_6 \end{aligned} \tag{D.19}$$

$$\begin{aligned} c_{16} = &\big[(I_{yy_b} - I_{zz_b})C_{q_5}C_{q_6} - I_{xz_b}S_{q_5}\big]C_{q_5}S_{q_6}(\dot{q}_1 + \dot{q}_4) \\ &- \frac{1}{2}\big[I_{xx_\mathrm{b}} - (I_{yy_\mathrm{b}} - I_{zz_\mathrm{b}})(C_{q_6}^2 - S_{q_6}^2)\big]C_{q_5}\dot{q}_5 + I_{xz_\mathrm{b}}C_{q_5}S_{q_6}\dot{q}_6 \end{aligned} \tag{D.20}$$

$$c_{21} = -c_{12} \tag{D.21}$$

$$c_{31} = -c_{13} \tag{D.22}$$

$$c_{32} = -m_b l_3 C_{q_2}\dot{q}_2 \tag{D.23}$$

$$\begin{aligned} c_{51} = &-\big[(I_{xx_\mathrm{b}} - I_{yy_\mathrm{b}}S_{q_6}^2 - I_{zz_\mathrm{b}}C_{q_6}^2)S_{q_5}C_{q_5} + I_{xz_\mathrm{b}}(C_{q_5}^2 - S_{q_5}^2)C_{q_6}\big](\dot{q}_1 + \dot{q}_4) \\ &+ \frac{1}{2}\Big(\big[I_{xx_\mathrm{b}} + (I_{yy_\mathrm{b}} - I_{zz_\mathrm{b}})(C_{q_6}^2 - S_{q_6}^2)\big]C_{q_5} - 2I_{xz_\mathrm{b}}S_{q_5}C_{q_6}\Big)\dot{q}_6 \end{aligned} \tag{D.24}$$

$$c_{55} = -(I_{yy_\mathrm{b}} - I_{zz_\mathrm{b}})S_{q_6}C_{q_6}\dot{q}_6 \tag{D.25}$$

$$\begin{aligned} c_{56} = &\frac{1}{2}\Big(\big[I_{xx_\mathrm{b}} + (I_{yy_\mathrm{b}} - I_{zz_\mathrm{b}})(C_{q_6}^2 - S_{q_6}^2)\big]C_{q_5} - 2I_{xz_\mathrm{b}}S_{q_5}C_{q_6}\Big)(\dot{q}_1 + \dot{q}_4) \\ &- (I_{yy_\mathrm{b}} - I_{zz_\mathrm{b}})S_{q_6}C_{q_6}\dot{q}_5 + I_{xz_\mathrm{b}}C_{q_6}\dot{q}_6 \end{aligned} \tag{D.26}$$

$$c_{61} = -\Bigg[\big[(I_{yy_{\mathrm{b}}} - I_{zz_{\mathrm{b}}})C_{q_5}C_{q_6} - I_{xz_{\mathrm{b}}}S_{q_5}\big]C_{q_5}S_{q_6}(\dot{q}_1 + \dot{q}_4) + \frac{1}{2}\Big(\big[I_{xx_{\mathrm{b}}} + (I_{yy_{\mathrm{b}}} - I_{zz_6})(C_{q_6}^2 - S_{q_6}^2)\big]C_{q_5} - 2I_{xz_6}S_{q_5}C_{q_6}\Big)\dot{q}_5\Bigg] \tag{D.27}$$

$$c_{65} = -\frac{1}{2}\Big(\big[I_{xx_{\mathrm{b}}} + (I_{yy_{\mathrm{b}}} - I_{zz_6})(C_{q_6}^2 - S_{q_6}^2)\big]C_{q_5} - 2I_{xz_6}S_{q_5}C_{q_6}\Big)(\dot{q}_1 + \dot{q}_4) + (I_{yy_{\mathrm{b}}} - I_{zz_{\mathrm{b}}})S_{q_6}C_{q_6}\dot{q}_5 \tag{D.28}$$

Appendix E

Estimated Parameter Values

The system parameter values used in the numerical simulation results presented in this thesis are obtained either through direct measurements (such as the mass and the length quantities) or from estimation by the geometry of the physical objects (such as the moment and product of inertia).

E.1 Common Parameters Across Configurations

E.1.1 Environmental Parameters

Gravitational acceleration and air density are assumed constant and are estimated as:

$$g = 9.81 \ \frac{\mathrm{m}}{\mathrm{s}^2} \qquad \rho = 1.225 \ \frac{\mathrm{kg}}{\mathrm{m}^3} \tag{E.1}$$

E.1.2 Platform Dimensions

Estimates of the characteristic dimensions for the Platform system:

l_1	=	0.0	m	ρ_2	=	0.4575	m	m_b	=	5.1	kg
l_2	=	0.153	m	h_M	=	0.2	m	I_{xx_b}	=	0.021	$\mathrm{kg}\cdot\mathrm{m}^2$
l_3	=	0.915	m	h_T	=	0.0	m	I_{yy_b}	=	0.13	$\mathrm{kg}\cdot\mathrm{m}^2$
l_4	=	0.2725	m	l_M	=	0.01	m	I_{zz_b}	=	0.13	$\mathrm{kg}\cdot\mathrm{m}^2$
l_s	=	0.035	m	l_T	=	0.68	m	I_{xz_b}	=	$9.5\cdot10^{-3}$	$\mathrm{kg}\cdot\mathrm{m}^2$

E.1.3 Rotor Parameters

Estimated values for the parameters of the main and tail rotors are shown in Table E.1.

Table E.1: Rotor Parameters

Parameters	Main	Tail
R (m)	0.585	0.105
N_b	2	2
c (m)	0.05	0.025
A_{disc} (m^2)	1.08	0.035
A_b (m^2)	0.0585	$5.25\cdot10^{-3}$
σ	0.054	0.15
c_D	0.01	0.01
I_{blade} ($\mathrm{kg}\cdot\mathrm{m}^2$)	$9.7\cdot10^{-3}$	$8.8\cdot10^{-5}$
γ_L	4.45	0.25
a_L	6.0	6.0

E.2 Configuration Parameters

Estimated values for the configuration parameters are shown in Table E.2

Table E.2: System Configuration Parameters

Parameters \ Configurations	HANGAR	REDUCED	BALANCED	UAV
Ω (RPM)	875	875	1761	1761
Ω_{tail} (RPM)	3037	3037	6111	6111
ρ_3 – w/ weight (m)	0.242	0.492	0.092	0.0
ρ_3 – bare boom (m)	−0.314	−0.314	−0.314	0.0
ρ_w (m)	0.36	.92	0.31	0.0
m_2 (kg)	0.442	0.442	0.442	0.0
m_3 – w/ weight (kg)	17.863	8.791	8.791	0.0
m_3 – bare boom (kg)	3.055	3.055	3.055	0.0
m_w (kg)	14.8	5.7	5.7	0.0
m_4 (kg)	0.663	0.663	0.663	0.0
I_{xx_2} (kg $\cdot$ m^2)	$1.23 \cdot 10^{-5}$	$1.23 \cdot 10^{-5}$	$1.23 \cdot 10^{-5}$	0.0
I_{xx_3} – w/ weight (kg $\cdot$ m^2)	0.13	0.034	0.034	0.0
I_{xx_3} – bare boom (kg $\cdot$ m^2)	$4.33 \cdot 10^{-4}$	$4.33 \cdot 10^{-4}$	$4.33 \cdot 10^{-4}$	0.0
$I_{xx_{\text{w}}}$ (kg $\cdot$ m^2)	0.13	0.033	0.033	0.0
I_{yy_2} (kg $\cdot$ m^2)	0.031	0.031	0.031	0.0
I_{yy_3} – w/ weight (kg $\cdot$ m^2)	1.61	3.46	1.19	0.0
I_{yy_3} – bare boom (kg $\cdot$ m^2)	0.4	0.4	0.4	0.0
$I_{yy_{\text{w}}}$ (kg $\cdot$ m^2)	0.071	0.02	0.02	0.0
I_{zz_1} (kg $\cdot$ m^2)	$3.81 \cdot 10^{-4}$	$3.81 \cdot 10^{-4}$	$3.81 \cdot 10^{-4}$	0.0
I_{zz_2} (kg $\cdot$ m^2)	0.031	0.031	0.031	0.0
I_{zz_3} – w/ weight (kg $\cdot$ m^2)	1.61	3.46	1.19	0.0
I_{zz_3} – bare boom (kg $\cdot$ m^2)	0.4	0.4	0.4	0.0
$I_{zz_{\text{w}}}$ (kg $\cdot$ m^2)	0.071	0.02	0.02	0.0

E.3 Controller Parameters

The controller gains for the simulation presented in this thesis are obtained through trial-and-error since the goal is only to obtain a stable controller as benchmark instead of obtaining specific performance criteria through gain adjustments.

E.3.1 Linear PD Controller Gains

The linear PD control law for the i^{th} joint can be expressed as:

$$u_i = k_{p_i}\Delta q_i + k_{d_i}\Delta \dot{q}_i \tag{E.2}$$

where the position (Δq_i) and rate ($\Delta \dot{q}_i$) errors are defined as:

$$\Delta q_i \triangleq q_{i_d} - q_i$$
$$\Delta \dot{q}_i \triangleq \dot{q}_{i_d} - \dot{q}_i$$

Table E.3 lists the proportional (k_{p_i}) and derivative (k_{d_i}) gains for each of the six linear joint controllers for desired torque generation. .

Joint	k_{p_i}	k_{d_i}
1	1	1.5
2	5	4
3	1	1.5
4	1	1.5
5	1	1.5
6	1	1.5

Table E.3: Linear PD Gains

E.3.2 Nonlinear PD Controller Gains

The nonlinear PD control law for the i^{th} joint can be expressed as:

$$u_i = \frac{k_{p_i}}{(a_i + |\Delta q_i|)}\Delta q_i + \frac{k_{d_i}}{(b_1 + |\Delta q_i|)(c_i + |\Delta \dot{q}_i|)}\Delta \dot{q}_i \tag{E.3}$$

where Δq_i and $\Delta \dot{q}_i$ are as defined previously.

Table E.4 lists the proportional (k_{p_i}) and derivative (k_{d_i}) gains, together with the controller parameters (a_i, b_i and c_i) for each of the six nonlinear joint controllers for desired torque generation.

Joint	k_{p_i}	a_i	k_{d_i}	b_i	c_i
1	1	1	1.5	1	1
2	5	1	4	1	1
3	1	1	1.5	1	1
4	1	1	1.5	1	1
5	1	1	1.5	1	1
6	1	1	1.5	1	1

Table E.4: Nonlinear PD Gains

Appendix F

System Identification

An overview of the Comprehensive Identification From FrEquency Responses (CIFER) technique is given here. Preliminary testing of applying the CIFER technique to the test platform system has been performed. A brief comment on these early results will be given at the end of this appendix.

F.1 Comprehensive Identification From FrEquency Responses (CIFER)

The *Comprehensive Identification from FrEquency Responses* (CIFER) technique computes a parametric state-space or transfer function model through a set of non-parametric input-to-output frequency responses identified from the measurement data [85]. The procedure is divided into three main steps. First, frequency responses for each of the input-output pair in the system (for the multiple-input, multiple-output case) are computed as the ratio [85]:

$$G(j\omega_k) = \frac{S_{YU}(j\omega_k)}{S_{UU}(j\omega_k)} \tag{F.1}$$

where $S_{YU}(j\omega)$ and $S_{UU}(j\omega_k)$ are the input-output cross-spectral density and the input auto-spectral density estimates respectively. The spectral densities are defined as [87]:

$$\begin{aligned} S_{YU}(j\omega_k) &= Y(k)\overline{U(k)} \\ S_{UU}(j\omega_k) &= U(k)\overline{U(k)} \\ S_{YY}(j\omega_k) &= Y(k)\overline{Y(k)} \end{aligned} \tag{F.2}$$

where $U(k)$ and $Y(k)$ are the Discrete Fourier Transform (DFT) of the input and output signals respectively. The over-bar denotes the complex conjugate of the signals. The DFT of the input and output signals is computed using the Chirp-Z transform algorithm. The Chirp-Z transform is a flexible Fast Fourier Transform (FFT) algorithm [85, 88]. It allows the transforms to be computed within a user-selectable frequency range ("zoom" in) and requires less restrictions on the number of data points used (data length does not need to be power of 2).

Typically when computing frequency transforms for finite length data records, a windowing technique is used to reduce the effect of leakage error [89]. The full data record of length T is divided into N sub-records or "windows". The length of each sub-records is the window size ($T_w = T/N$). The frequency spectrum for the data is then computed as the average of the spectrum from the N sub-records. For a given total number of data records, the window size determines the number of sub-records available for averaging. To minimize the effect of noise and random error, the spectral densities should be averaged over as many sub-records as possible. However, the minimum frequency $\omega_{\min}$ in the spectrum identifiable from a finite length record T_w is given by $\omega_{\min} = 1/T_w$ (the maximum frequency is limited by the Nyquist frequency, which is half of the sampling frequency ω_s). As a result, there is a trade-off between the frequency range and the number of windows available for averaging.

To solve this problem, the CIFER algorithm introduces a method to combine spectrum estimations computed using different window sizes to obtain an improved frequency response estimate. The spectrum curves are combined using a nonlinear, least-squares optimization method applied to the cost function [85]:

$$J_f = \sum_{i=1}^{n_w} W_i \left[\left(\frac{S_{UU_c} - S_{UU_i}}{S_{UU_i}} \right)^2 + \left(\frac{S_{YY_c} - S_{YY_i}}{S_{YY_i}} \right)^2 + \left(\frac{S_{UY_c} - S_{UY_i}}{S_{UY_i}} \right)^2 + 5.0 \left(\frac{\gamma_c^2 - \gamma_i^2}{\gamma_i^2} \right)^2 \right] \tag{F.3}$$

where the subscript i denotes the individual window results and the subscript c denotes the combined (composite) window results. Notice that for implementation, the complex cross-spectrum term (second last term in (F.3)) is separated into real and imaginary parts. The weighting W_i is tailored to each individual window's frequency range. Up to five sets of frequency response functions ($n_w = 5$) can be used in the optimization for each input-output pair, corresponding to five different choices of the window size. The coherence function γ^2 is defined as [87, 89, 90]:

$$\gamma^2(\omega) = \frac{|S_{UY}(j\omega)|^2}{S_{UU}(j\omega)S_{YY}(j\omega)} \tag{F.4}$$

and it measures how much of the output power is *coherent* (linearly related) with the input power. The coherence function estimates associated with each window size provide a good indication on the quality of the identified frequency spectrum. The spectrum with a higher coherence estimate is weighted more favourably in the optimization process through the cost function (F.3) [85].

Once the input-output frequency responses are identified, the final step is to identify the parametric models (transfer function or state-space models) from these frequency responses. A nonlinear least-squares optimization method is applied to the cost function [91]:

$$J_{tf} = \frac{20}{n}\sum_{\omega_1}^{\omega_n} W_\gamma \left[W_g \left(|T_{\text{data}}| - |T_{\text{model}}| \right)^2 + W_p \left(\angle T_{\text{data}} - \angle T_{\text{model}} \right)^2 \right] \tag{F.5}$$

where n is the number of frequency points; ω_1 and ω_n are the starting and ending frequencies of the fit, and W_γ, W_g and W_p are the weighting factors for coherence, gain error and phase error respectively. T_{data} is the transfer function (magnitude and phase) obtained from the previously identified frequency responses. T_{model} is the transfer function model to be identified. The parameters of T_{model} are expressed in coefficient form:

$$T_{\text{model}} = \frac{(b_0 s^m + b_1 s^{m-1} + \cdots + b_m)e^{-\tau s}}{s^n + a_1 s^{n-1} + \cdots + a_n} \tag{F.6}$$

Due to the weighted "averaging" effect through the coherence function in the computation, improved frequency response estimates can be obtained over the basic Empirical Transfer Function Estimate (ETFE) method, as is reported by Lai *et al.* [92].

F.2 Preliminary Results

The preliminary system identification results of applying the CIFER technique to the individual attitude channels (roll, pitch and yaw) have all indicated to have dynamics similar to that of a second order integrator, i.e. $\frac{1}{s^2}$. These results are consistent with the observations obtained from the analysis of the platform system presented in Chapter 3. In particular, due to the type of sensors currently available on the test platform system, i.e. angular readings through potentiometers at the joints, the identified dynamics correspond to the integral kinematic relationships of the attitude angles. The noise effects inherent in the potentiometer readings have prevented the use of numerical differentiation on the data to identify the system modes associated with the rates. As a result, additional rate sensor measurements are needed to identify the other rate related modes present in the system for future work.

Bibliography

[1] J. Seddon, *Basic Helicopter Aerodynamics*. AIAA, 1990.

[2] H. Hellman, *Helicopters and other VTOL's*. Garden City, New York: Doubleday & Company, Inc., 1970.

[3] T. J. Koo, F. Hoffmann, H. Shim, B. Sinopoli, and S. Sastry, "Hybrid control of an autonomous helicopter," in *IFAC Workshop on Motion Control*, pp. 265–270, IEEE, Sept. 1998.

[4] C. P. Sanders, P. A. DeBitetto, E. Feron, H. F. Vuong, and N. Leveson, "Hierarchical control of small autonomous helicopters," in *Conference on Decision and Control*, (Tampa, Florida, USA), pp. 3629–3634, IEEE, Dec. 1998.

[5] V. Gavrilets, A. Shterenberg, M. A. Dahleh, and E. Feron, "Avionics system for a small unmanned helicopter performing aggressive manoeuvres," in 19^{th} *Digital Avionics Systems Conference*, IEEE, Oct. 7–13 2000.

[6] J. F. Montgomery and G. A. Bekey, "Learning helicopter control through 'teaching by showing'," in 37^{th} *Conference on Decision and Control*, (Tampa, Florida, USA), pp. 3647–3652, IEEE, Dec. 1998.

[7] J. E. Corban, A. J. Calise, and J. V. R. Prasad, "Implementation of adaptive nonlinear control for flight test on an unmanned helicopter," in 37^{th} *Conference on Decision and Control*, (Tampa, Florida, USA), pp. 3641–3646, IEEE, Dec. 1998.

[8] E. H. Lee, H. Shim, H. Park, and K. I. Lee, "Design of hovering attitude controller for a model helicopter," in *SICE*, (Kanazawa), pp. 1385–1390, SICE, Aug. 4–6 1993.

[9] A. Bramwell, *Helicopter Dynamics*. London, U.K.: Edward Arnold, 1976.

[10] R. W. Prouty, *Helicopter Performance, Stability, and Control*. Boston: PWS Publishers, 1986.

[11] D. J. Murray-Smith, "Modelling limitations for helicopter flight control system design," in *EUROSIM '95*, pp. 397–402, 1995.

[12] G. D. Padfield, *Helicopter Flight Dynamics: The Theory and Application of Flying Qualities and Simulation Modelling*. Education Series, Reston, VA, USA: AIAA, 1996.

[13] E. A. Wan and A. A. Bogdanov, "Model predictive neural control with applications to a 6 DOF helicopter model," in *American Control Conference*, (Arlington, VA), pp. 488–493, IEEE, June 25–27 2001.

[14] T. J. Koo and S. Sastry, "Output tracking control design of a helicopter model based on approximation linearization," in 37^{th} *Conference on Decision and Control*, (Tampa, Florida, USA), pp. 3635–3640, IEEE, Dec. 1998.

[15] M. F. Weilenmann, U. Christen, and H. P. Geering, "Robust helicopter position control at hover," in *American Control Conference*, (Baltimore, Maryland, USA), pp. 2491–2495, IEEE, June 1994.

[16] D. J. Walker, M. C. Turner, A. J. Smerlas, M. E. Strange, and A. W. Gubbels, "Robust control of the longitudinal and lateral dynamics of the BELL 205 helicopter," in *American Control Conference*, (San Diego, California, USA), pp. 2742–2746, IEEE, June 1999.

[17] J. V. R. Prasad, A. J. Calise, Y. Pei, and J. E. Corban, "Adaptive nonlinear controller synthesis and flight test evaluation on an unmanned helicopter," in *International Conference on Control Applications*, (Kohala Coast-Island of Hawaii, Hawaii, USA), pp. 137–142, IEEE, Aug. 22–27 1999.

[18] J. J. Bink, I. Sharf, P. C. A. van Gool, and J. A. Mulder, "Design of stability augmentation system for a model helicopter," in *American Helicopter Society Annual Forum*, (Washington, D.C.), AHS, May 20–22 1998.

[19] S. Mammar and G. Duc, "Loop shaping $\mathcal{H}_\infty$ design applied to the robust stabilization of a helicopter," in *Conference on Control Applications*, vol. 2, pp. 806–811, IEEE, Sept. 13–16 1992.

[20] D. H. Shim, H. J. Kim, and S. Sastry, "Control system design fo rotorcraft-based unmanned aerial vehicles using time-domain system identification," in *International Conference on Control Applications*, (Anchorage, Alaska, USA), pp. 808–813, IEEE, Sept. 25–27 2000.

[21] B. Mettler, M. B. Tischler, and T. Kanade, "System identification of small-size unmanned helicopter dynamics," in *American Helicopter Society* 55^{th} *Forum*, American Helicopter Society, May 25–27 1999.

[22] S. M. Rock, E. W. Frew, H. Jones, E. A. LeMaster, and B. R. Woodley, "Combined CDGPS and vision-based control of a small autonomous helicopter," in *American Control Conference*, (Philadelphia, Pennsylvania), pp. 694–698, IEEE, June 1998.

[23] G. Lai, K. Fregene, and D. Wang, "A control structure for autonomous model helicopter," in *Canadian Conference on Electrical and Computer Engineering*, (Halifax, Nova Scotia, Canada), pp. 103–107, IEEE, May 2000.

[24] E. Frazzoli, M. A. Dahleh, and E. Feron, "A hybrid control architecture for aggressive manoeuvring of autonomous helicopters," in *Conference on Decision and Control*, (Phoenix, Arizona, USA), pp. 2471–2476, IEEE, Dec. 1999.

[25] E. Frazzoli, M. A. Dahleh, and E. Feron, "Robust hybrid control for autonomous vehicle motion planning," tech. rep., Massachusetts Institute of Technology, 1999.

[26] R. Mahony and R. Lozano, "(Almost) exact path tracking control for an autonomous helicopter in hover manoeuvres," in *International Conference on Robotics and Autonomous*, (San Francisco, CA, USA), pp. 1245–1250, IEEE, Apr. 2000.

[27] R. Frezza, "Path following for air vehicles in coordinated flight," in *International Conference on Advanced Intelligent Mechatronics*, (Atlanta, USA), pp. 884–889, IEEE/ASME, Sept. 19–23 1999.

[28] J. C. Morris, M. van Nieuwstadt, and P. Bendotti, "Identification and control of a model helicopter in hover," in *American Control Conference*, (Baltimore, Maryland), pp. 1238–1242, IEEE, June 1994.

[29] S. Devasia, "Output tracking with nonhyperbolic and near nonhyperbolic internal dynamics: Helicopter hover control," in *American Control Conference*, (Albuquerque, New Mexico), pp. 1439–1446, IEEE, June 1997.

[30] R. Mahony, T. Hamel, and A. Dzul, "Hover control via lyapunov control for an autonomous model helicopter," in 38^{th} *Conference on Decision and Control*, (Phoenix, Arizona, USA), pp. 3490–3495, IEEE, Dec. 1999.

[31] C. Tournes and C. D. Johnson, "Helicopter hover control using linear adaptive control techniques," in *Thirty-Fourth Southeastern Symposium on System Theory*, (Huntsville, AL, USA), pp. 479–483, IEEE, Mar. 18–19 2002.

[32] S. Rebeschieß and M. Roloff, "Position control by feedback linearization for a simplified helicopter model," in *International Conference on Control Applications*, (Kohala Coast-Island of Hawaii, Hawaii, USA), pp. 143–145, IEEE, Aug. 22–27 1999.

[33] H. K. Khalil, *Nonlinear Systems*. Prentice Hall, second ed., 1996.

[34] H. Shim, T. J. Koo, F. Hoffmann, and S. Sastry, "A comprehensive study of control design for an autonomous helicopter," in 37^{th} *Conference on Decision and Control*, (Tampa, Florida, USA), pp. 3653–3658, IEEE, Dec. 1998.

[35] G. Ma, S. Zein-Sabatto, and M. J. Malkani, "Intelligent flight control design for helicopter yaw control," in 30^{th} *Southeastern Symposium on System Theory*, pp. 184–188, IEEE, Mar. 1998.

[36] C.-T. Lin and C. S. G. Lee, *Neural Fuzzy Systems: A Neuro-Fuzzy Synergism to Intelligent Systems*. Upper Saddle River, NJ, USA: Prentice Hall, 1996.

[37] M. Sasaki, H. Ishida, T. Katsuno, and A. Ogasawara, "Learning fuzzy logic controller for hovering a helicopter," in *Conference of the North American Fuzzy Information Processing Society – NAFIPS*, pp. 25–28, IEEE, Aug. 20–21 1998.

[38] F. C. Moon, *Applied Dynamics with Applications to Multibody and Mechatronic Systems*. John Wiley & Sons, Inc., 1998.

[39] J. H. Ginsberg, *Advanced Engineering Dynamics*. Cambridge University Press, second ed., 1998.

[40] M. W. Spong and M. Vidyasagar, *Robot Dynamics and Control*. John Wiley & Sons, Inc., 1989.

[41] J. J. Craig, *Introduction to Robotics*. Addison-Wesley, second ed., 1989.

[42] B. L. Stevens and F. L. Lewis, *Aircraft Control and Simulation*. John Wiley & Sons, Inc., 1992.

[43] D. McLean and H. Matsuda, "Helicopter station-keeping: comparing lqr, fuzzy-logic and neural-net controllers," *Engineering Applications of Artificial Intelligence*, vol. 11, pp. 411–418, 1998.

[44] C.-C. Luo, R.-F. Liu, C.-D. Yang, and Y.-H. Chang, "Helicopter h_∞ control design with robust flying quality," *Aerospace Science and Technology*, vol. 7, pp. 159–169, 2003.

[45] B. Mettler, C. Dever, and E. Feron, "Scaling effects and dynamic characteristics of miniature rotorcraft," *Journal of Guidance, Control, and Dynamics*, vol. 27, no. 3, pp. 466–478, 2004.

[46] B. Kim, Y. Chang, J. Keh, H. Ha, and M. Lee, "Design of 6-dof attitude controller of hovering model helicopter," in 30^{th} *Annual Conference of the IEEE Industrial Electronics Society*, (Busan, Korea), pp. 104–110, IEEE, Nov. 2–6 2004.

[47] M. T. Frye, S. Bhandari, and R. D. Colgren, "The raptor 50 6-DOF simulation environment for flight control research," in *American Control Conference*, (Minneapolis, Minnesota, USA), pp. 1038–1043, IEEE, June 2006.

[48] M. Ghanekar, *Dynamic Equivalence Conditions and Controller Scaling Laws for Robotic Manipulators*. PhD thesis, University of Waterloo, Waterloo, ON, 1997.

[49] J. D. Singleton and Yeager, Jr., William T., "Important scaling parameters for testing model-scale helicopter rotors," *AIAA Paper*, no. AIAA-98-2881, 1998.

[50] Q. M. Lam and J. P. Hill, "Investigation of robust adaptive control laws for flight control system implementation," in *Conference on Control Applications*, vol. 2, pp. 608–610, IEEE, Sept. 13–16 1992.

[51] J.-S. Young and C. E. Lin, "Refined $\mathcal{H}_\infty$-optimal approach to rotorcraft flight control – a simulation on time responses," in *Conference on Control Applications*, vol. 2, pp. 818–824, IEEE, Sept. 13–16 1992.

[52] I. Postlethwaite and D. J. Walker, "The design of helicopter flight control systems using advanced $\mathcal{H}_\infty$ control," in *American Control Conference*, (Baltimore, Maryland, USA), pp. 3193–3197, IEEE, June 1994.

[53] G. J. W. Dudgeon and J. J. Gribble, "Helicopter translational rate command using individual channel analysis and design," *Control Engineering Practice*, vol. 6, pp. 15–23, 1998.

[54] C.-D. Yang, W.-H. Liu, and C.-C. Kung, "Robust nonlinear h_∞ decoupling control of flight vehicle in hovering," in *Conference on Decision and Control*, (Las Vegas, Nevada, USA), pp. 4486–4491, IEEE, Dec. 2002.

[55] C.-C. Kung, C.-D. Yang, D.-W. Chiou, and C.-C. Luo, "Nonlinear h_∞ helicopter control," in *Conference on Decision and Control*, (Las Vegas, Nevada, USA), pp. 4468–4473, IEEE, Dec. 2002.

[56] Y. Aslan, D. Beauvois, and J. A. Rossiter, "A predictive multivariable helicopter robust design," in *Conference on Control Applications*, vol. 2, pp. 812–817, IEEE, Sept. 13–16 1992.

[57] H. Sira-Ramire, M. Zribi, and S. Ahmad, "Dynamic sliding mode control approach for vertical flight regulation in helicopter," in *Control Theory Applications*, no. 1, pp. 19–24, IEE, Jan. 1994.

[58] D. Y. Maharaj, *The Application of Nonlinear Control Theory to Robust Helicopter Flight Control*. PhD thesis, Department of Aeronautics, Imperial College of Science, Technology, and Medicine, 1994.

[59] J. Kaloust, C. Ham, and Z. Qu, "Nonlinear autopilot control design for a 2-DOF helicopter model," in *Control Theory Applications*, vol. 144, pp. 612–616, IEE, Nov. 1997.

[60] E. Frazzoli, M. A. Dahleh, and E. Feron, "Trajectory tracking control design for autonomous helicopters using a backstepping algorithm," in *American Control Conference*, (Chicago, Illinois), pp. 4102–4107, IEEE, June 2000.

[61] S. Zein-Sabatto and Y. Zheng, "Intelligent flight controllers for helicopter control," in *International Conference on Neural Networks*, vol. 2, (Houston, TX, USA), pp. 617–621, IEEE, June 9-12 1997.

[62] R. Enns and J. Si, "Helicopter flight control design using a learning control approach," in *Conference on Decision and Control*, (Sydney, Australia), pp. 1754–1759, IEEE, Dec. 2000.

[63] K. Tanaka, M. Iwasaki, and H. O. Wang, "Switching control of an R/C hovercraft: Stabilization and smooth switching," *IEEE Transactions on Systems, Man and Cybernetics – Part B: Cybernetics*, vol. 31, pp. 853–863, Dec. 2001.

[64] T. G. B. Amaral and M. M. Crisóstomo, "Neuro-fuzzy controller for helicopter motion control," in *International Fuzzy Systems Conference*, pp. 594–597, IEEE, 2001.

[65] C.-H. Oertel, "Machine vision-based sensing for helicopter flight control," *Robotica*, vol. 18, pp. 299–303, May–June 2000.

[66] M. A. Lewis, A. H. Fagg, and G. A. Bekey, "The usc autonomous flying vehicle: An experiment in real-time behaviour-based control," in *International Conference on Robotics and Automation*, vol. 2, pp. 422–429, IEEE, May 2–6 1993.

[67] A. H. Fagg, M. A. Lewis, J. F. Montgomery, and G. A. Bekey, "The USC autonomous flying vehicle: An experiment in real-time behaviour-based control," in *Proceedings of the 1993 IEEE/RSJ International Conference on Intelligent Robots and Systems*, (Yokohama, Japan), pp. 1173–1180, IEEE, July 26–30 1993.

[68] T. J. Koo, D. H. Shim, O. Shakernia, B. Sinopoli, F. Hoffmann, and S. Sastry, "Hierarchical hybrid system design on berkeley UAV," in *International Aerial Robotics Competition (IARC)*, (Richland, Washington, USA), AUVS, Aug. 1998.

[69] J. F. Montgomery, "The USC autonomous flying vehicle (AFV) project: Year 2000 status," Tech. Rep. IRIS-00-390, University of Southern California, Sept. 20 2000.

[70] I. Y. Eom and S. Jung, "A novel force tracking control approach to an autonomous unmanned helicopter system," in *Proceedings of the 2005 IEEE/RSJ International Conference on Intelligent Robots and Systems*, (Edmonton, Alberta), pp. 376–381, IEEE, Aug. 2–6 2005.

[71] J.-J. E. Slotine and W. Li, *Applied Nonlinear Control*. Prentice Hall, 1991.

[72] M. Trentini and J. K. Pieper, "Model-following control of a helicopter in hover," in *Proceedings of the 1996 IEEE International Conference on Control Applications*, (Dearborn, MI), pp. 7–12, IEEE, Sept. 15–18 1996.

[73] M. F. Weilenmann and H. P. Geering, "Test bench for rotorcraft hover control," *Journal of Guidance, Control, and Dynamics*, vol. 17, pp. 729–736, July–Aug. 1994.

[74] K. Tanaka, H. Ohtake, and T. Hori, "Stable control for R/C helicopter," in *IFSA World Congress*, vol. 4, (Vancouver, B.C., Canada), pp. 2056–2061, IEEE, July 25–28 2001.

[75] J. Zhang, J. Chen, C. C. Ko, B. M. Chen, and S. S. Ge, "A web-based laboratory on control of a two-degree-of-freedom helicopter," in *Conference on Decision and Control*, (Orlando, Florida, USA), pp. 2821–2826, IEEE, Dec. 2001.

[76] M. Takegaki and S. Arimoto, "A new feedback method for dynamic control of manipulators," *Transactions of the ASME. Journal of Dynamic Systems, Measurement and Control*, vol. 103, pp. 119–125, June 1981.

[77] D. Park, M.-S. Park, and S.-K. Hong, "A study on the 3-DOF atitude control of free-flying vehicle," in *International Symposium on Industial Electronics (ISIE)*, vol. 2, (Pusan, Korea), pp. 1260–1265, IEEE, June 12–16 2001.

[78] T. Ravichandran, *Simultaneous Plant/Controller Design Optimization with Applications to Serial Robots*. PhD thesis, University of Waterloo, Waterloo, ON, 2005.

[79] R. Kelly and R. Carelli, "A class of nonlinear PD-type controllers for robot manipulators," *Journal of Robotic Systems*, vol. 13, no. 12, pp. 793–802, 1996.

[80] L. Ljung, *System Identification: Theory for the User*. Prentice-Hall, Inc., second ed., 1999.

[81] T. Söderström and P. Stoica, *System Identification*. Prentice-Hall, 1988.

[82] U. Forssell, *Closes-Loop Identification: Methods, Theory, and Applications*. PhD thesis, Department of Electrical Engineering, Linköping University, 1999.

[83] S. A. Bortoff, "The University of Toronto RC helicopter: A test bed for nonlinear control," in *IEEE International Conference on Control Applications*, (Kohala Coast-ISland of Hawaii, Hawaii, USA), pp. 333 – 338, IEEE, Aug. 22–27 1999.

[84] B. Mettler, T. Kanade, and M. B. Tischler, "System identification modelling of a model-scale helicopter," Tech. Rep. CMU-RI-TR-00-03, Carnegie Mellon University, 2000.

[85] M. B. Tischler and M. G. Cauffman, "Frequency-response method for rotorcraft system identification: Flight applications to BO-105 coupled fuselage/rotor dynamics," *Journal of the American Helicopter Society*, vol. 37, no. 3, pp. 3–17, 1992.

[86] R. C. Nelson, *Flight Stability and Automatic Control*. McGraw-Hill, second ed., 1998.

[87] R. E. Challis and R. I. Kitney, "Tutorial paper: Biomedical signal processing (in four parts). part 3: The power spectrum and coherence function," *Medical & Biological Engineering & Computing*, vol. 29, pp. 225–241, May 1991.

[88] R. E. Challis and R. I. Kitney, "Tutorial paper: Biomedical signal processing (in four parts). part 2: The frequency transforms and their inter-relationships," *Medical & Biological Engineering & Computing*, vol. 29, pp. 1–17, Jan. 1991.

[89] R. Pintelon and J. Schoukens, *System Identification: A Frequency Domain Approach*. IEEE Press, 2001.

[90] J. A. Cadzow and O. M. Solomon, "Linear modelling and the coherence function," *IEEE Transactions on Acoustics, Speech, and Signal Processing*, vol. ASSP-35, pp. 19–28, Jan. 1987.

[91] M. B. Tischler, "Frequency-domain modelling and testing throughout the flight vehicle development cycle." AHS Forum 58 Short Course, Montreal, Canada, June 10 2002.

[92] G. M. Y. Lai, K. Ziaei, D. W. L. Wang, and G. R. Heppler, "Application of an advanced frequency domain identification method for modelling of flexible-link manipulators," in *ASME International Mechanical Engineering Congress & Exposition*, (Washington, D. C., USA), ASME, Nov. 16–21 2003.

Nomenclature

Acronyms

ACS	:	Attitude Control System
AUV	:	Autonomous Unmanned Vehicle
C.G.	:	Centre of Gravity
CIFER	:	Comprehensive Identification from FrEquency Responses technique
DC	:	Direct Current
DOF	:	Degree Of Freedom
FPC	:	Flight Path Controller
HANGAR	:	Helicopter Autonomous Navigation and Guidance Applied Research
LQG	:	Linear Quadratic Gaussian
MIMO	:	Multiple Input, Multiple Output
MISO	:	Multiple Input, Single Output
NN	:	Neural Network
PD	:	Proportional-Derivative Controller
PI	:	Proportional-Integral Controller
PID	:	Proportional-Integral-Derivative Controller
R-C	:	Radio-Controlled
RPM	:	Rotation/Revolution-Per-Minute
SISO	:	Single Input, Single Output
UAV	:	Unmanned Aerial Vehicle
WARG	:	Waterloo Aerial Robotics Group

Typeset Notations

$\vec{\boldsymbol{v}}$	:	Vector quantity.
$\tilde{\boldsymbol{v}}$	:	Vector expressed in helicopter body-fixed frame.
$\bar{\boldsymbol{v}}$	:	Vector expressed with respect to platform joint coordinates.

Typeset Notations (continued)		
$\boldsymbol{R}$	:	Matrix quantity.
$\dot{x}$	:	Time derivative (absolute).
[ ]	:	Matrix or Vector elements.
$\hat{x}$	:	Normalized quantity.

Operators

∂	:	Partial Derivative operator.
$\times$	:	Cross Product for Vector. Multiplication for Scalar.
S_{q_k}, C_{q_k}	:	Short form for $\sin q_k$ and $\cos q_k$.
$\left[\quad\right]^T$	:	Matrix or Vector transpose.
$\left[\quad\right]^{-1}$	:	Matrix or Vector inverse.

List of Symbols

$\mathbf{0}_{n\times m}$	:	Zero matrix of dimension $n \times m$.
A_1, B_1	:	Lateral (A_1) and Longitudinal (B_1) Cyclic Pitch Input. (rad)
A_b	:	Blade area. (m^2). $A_\mathrm{b} = N_b c R$
A_disc, A_{disc_tail}	:	Rotor Disc Area (Main and Tail). (m^2). $A_\mathrm{disc} = \pi R^2$
$\hat{A}$	:	Ratio between main and tail rotor disc area. $\hat{A} = \frac{A_{disc_\mathrm{tail}}}{A_\mathrm{disc}}$
$\tilde{\boldsymbol{C}}$, $\bar{\boldsymbol{C}}$	:	Coriolis and centrifugal matrix for UAV model ($\tilde{\boldsymbol{C}}$) and Platform model ($\bar{\boldsymbol{C}}$) respectively.
$\hat{C}_\mathrm{lat}$, $\hat{C}_{lat_\mathrm{tail}}$	:	Lateral Rotor Coefficients (Main and Tail).
$\hat{C}_\mathrm{lon}$, $\hat{C}_{lon_\mathrm{tail}}$	:	Longitudinal Rotor Coefficients (Main and Tail).
$\hat{C}_\mathrm{Q}$, $\hat{C}_{Q_\mathrm{tail}}$	:	Rotor Torque Coefficients (Main and Tail).
$\hat{C}_\mathrm{T}$, $\hat{C}_{T_\mathrm{tail}}$	:	Rotor Thrust Coefficients (Main and Tail).
F_lat, F_{lat_tail}	:	Lateral Planar Horizontal Force (H-Force). (N)
F_lon, F_{lon_tail}	:	Longitudinal Planar Horizontal Force (H-Force). (N)
$\bar{\boldsymbol{F}}_\mathrm{main}$, $\tilde{\boldsymbol{F}}_\mathrm{main}$	:	Main rotor force vector in joint ($\bar{\boldsymbol{F}}_\mathrm{main}$) and body-fixed ($\tilde{\boldsymbol{F}}_\mathrm{main}$) coordinates.
$\bar{\boldsymbol{F}}_\mathrm{tail}$, $\tilde{\boldsymbol{F}}_\mathrm{tail}$	:	Tail rotor force vector in joint ($\bar{\boldsymbol{F}}_\mathrm{tail}$) and body-fixed ($\tilde{\boldsymbol{F}}_\mathrm{tail}$) coordinates.
$\vec{\boldsymbol{F}}_i^a$	:	Total active external force acting on the i^th rigid body of the Test Platform. (N)
$\vec{\boldsymbol{H}}_i$	:	Angular momentum about the centre of gravity for the

List of Symbols (continued)

		i^{th} rigid body of the Test Platform. $\vec{\boldsymbol{H}}_i = \boldsymbol{I}_i \vec{\boldsymbol{\omega}}_{\boldsymbol{l_i}}$
$\boldsymbol{I}_{n\times n}$	:	Identity matrix of dimension $n \times n$.
$\boldsymbol{I}_i$	:	Inertia matrix about the centre of gravity for the i^{th} rigid body of the Test Platform.
I_{blade}	:	Blade flapping inertia about the hub. $(\text{kg} \cdot \text{m}^2)$.
I_{xx_i}, I_{yy_i}, I_{zz_i}	:	Moment of inertia about the x, y, and z axis of the i^{th} rigid body of the Test Platform. $(\text{kg} \cdot \text{m}^2)$. $I_{xx} = \int\limits_{\text{body}} (y^2 + z^2)\, dm$
I_{xy_i}, I_{xz_i}, I_{yz_i}	:	Product of inertia in the $x-y$, $x-z$, and $y-z$ plane of the i^{th} rigid body of the Test Platform. $(\text{kg} \cdot \text{m}^2)$. $I_{xy} = \int\limits_{\text{body}} xy\, dm\ , \quad I_{xz} = \int\limits_{\text{body}} xz\, dm\ , \quad I_{yz} = \int\limits_{\text{body}} yz\, dm$
$\boldsymbol{J}_{v_i}$, $\boldsymbol{J}_{\omega_i}$	:	Jacobian matrices for the linear $\vec{\boldsymbol{v}}_{l_i}$ and angular $\vec{\boldsymbol{\omega}}_{l_i}$ velocities.
K	:	Rotor inflow factor distribution factor.
K_{coll}, K_{rud}	:	Rotor servo gain coefficients (collective and rudder).
K_{lon}, K_{lat}	:	Rotor servo gain coefficients (cyclic).
K_P, K_D	:	Proportional and Derivative gain of a controller.
L, M, N	:	Scalar component of the net moment about the body fixed x, y and z axis. $(\text{N} \cdot \text{m})$
$\tilde{\boldsymbol{M}}$	:	Mass-inertia matrix of UAV expressed in body-fixed frame.
$\bar{\boldsymbol{M}}_{\text{main}}$, $\tilde{\boldsymbol{M}}_{\text{main}}$	:	Main rotor moment in joint ($\bar{\boldsymbol{M}}_{\text{main}}$) and body-fixed ($\tilde{\boldsymbol{M}}_{\text{main}}$) frames.
$\bar{\boldsymbol{M}}_{\text{tail}}$, $\tilde{\boldsymbol{M}}_{\text{tail}}$	:	Tail rotor moment in joint ($\bar{\boldsymbol{M}}_{\text{tail}}$) and body-fixed ($\tilde{\boldsymbol{M}}_{\text{tail}}$) frames.
$\vec{\boldsymbol{M}}_i^a$	:	The total active external moment/torque acting on the i^{th} rigid body of the Test Platform. $(\text{N} \cdot \text{m})$
N_b	:	Number of Blades.
Q_{main}, Q_{tail}	:	Main and Tail rotor torque. $(\text{N} \cdot \text{m})$
$\boldsymbol{R}_{\text{Euler}}$	:	Mapping matrix from Euler rate to Body-Fixed rate. $\begin{bmatrix} p & q & r \end{bmatrix}^T = \boldsymbol{R}_{\text{Euler}} \begin{bmatrix} \dot{\phi} & \dot{\theta} & \dot{\psi} \end{bmatrix}^T$
$\boldsymbol{R}_{\psi,\theta,\phi}$	:	Inertial to Body-Fixed Frame Rotation matrix.
$\boldsymbol{R}_i^k$	:	Rotation between Frame i and Frame k. $\vec{\boldsymbol{v}}_i = \boldsymbol{R}_i^k \vec{\boldsymbol{v}}_k$
R, R_{tail}	:	Rotor blade radius (Main and Tail rotor). (m)
$\hat{R}$	:	Ratio between main and tail rotor radius. $\hat{R} = \frac{R_{\text{tail}}}{R}$
$\boldsymbol{S}(\vec{\boldsymbol{\omega}})$	:	Skew symmetric matrix for angular rate vector $\vec{\boldsymbol{\omega}}$.
T, T_{main}, T_{tail}	:	Rotor thrust magnitude (Main and Tail rotor). (N)
U_P, U_T	:	Perpendicular and planar relative air speed of blade. $(\frac{\text{m}}{\text{s}})$

List of Symbols (continued)

$\vec{\boldsymbol{U}}$	:	Net velocity experienced by the rotor blade element. $\lvert\vec{\boldsymbol{U}}\rvert = \sqrt{v_1^2 + (\Omega r_s)^2}$
V_{air}	:	Net rotor disc speed. ($\frac{\text{m}}{\text{s}}$)
$V_{\text{horizontal}}$, V_{vertical}	:	Planar ($V_{\text{horizontal}}$) and perpendicular (V_{vertical}) rotor disc speed. ($\frac{\text{m}}{\text{s}}$)
X, Y, Z	:	Scalar component of the net force in the body fixed x, y, and z direction. (N)
a_0	:	Blade coning angle. (rad)
$a_{1,\text{s}}$, $b_{1,\text{s}}$	:	Longitudinal and Lateral blade flapping angle of the rotor. (rad)
a_L	:	Lift Curve Slope. Nominal value for helicopter blades [1]: $a_L = 6.0$
a_i, b_i, c_i	:	Parameters of Nonlinear PD controller.
$\vec{\boldsymbol{a}}_{l_i}$	:	Acceleration of the centre of gravity (w.r.t. local frame) of the i^{th} rigid body of the Test Platform. ($\frac{\text{m}}{\text{s}^2}$)
a_x	:	Net acceleration of the rigid body in the x direction. ($\frac{\text{m}}{\text{s}^2}$)
c	:	Blade chord length. (m)
c_L, c_D	:	Lift and Drag coefficient for the blade element. $c_L = a_{\text{L}}\alpha$
c_{ik}	:	The i,k element of the matrix $\boldsymbol{C}(\bar{\boldsymbol{q}}, \dot{\bar{\boldsymbol{q}}})$.
g	:	Gravitational acceleration. ($\frac{\text{m}}{\text{s}^2}$). $g = 9.81$
$\tilde{\boldsymbol{h}}$, $\bar{\boldsymbol{h}}$	:	Coriolis and centrifugal vector for UAV $\tilde{\boldsymbol{h}}$ and Platform $\bar{\boldsymbol{h}}$ models.
h_M, h_T	:	Vertical (z axis) offset of the main and tail rotor from C.G. (m)
j	:	Imaginary number. $j = \sqrt{-1}$
k_{p_i}, k_{d_i}	:	Proportional (P) and derivative (D) gains of joint controllers.
l_2, l_3, l_4, l_s	:	Test Platform linkage lengths and offsets. (m)
l_M, l_T	:	Horizontal (x axis) offset of the main and tail rotor from C.G. (m)
m_1, m_2, m_3, m_4	:	Mass of the Test Platform linkages. (kg)
m_b	:	Total mass of the helicopter. (kg)
m_{ik}	:	The i,k element of the inertia matrix $\boldsymbol{M}(\bar{\boldsymbol{q}})$.
n	:	Number of rigid bodies on the Test Platform. $n = 5$
p_∞, p_{disc}	:	Static air pressure at and far below the rotor disc. ($\frac{\text{N}}{\text{m}^2}$)
p, q, r	:	Scalar component of the angular rate vector in the body fixed x, y, and z axis.
$\bar{\boldsymbol{q}}$	:	Generalized coordinate vector for the Test Platform. $\bar{\boldsymbol{q}} = \begin{bmatrix} q_1 & q_2 & q_3 & q_4 & q_5 & q_6 \end{bmatrix}^T$

List of Symbols (continued)

q_k	:	k^{th} generalized coordinate.
r_s	:	Blade element span position. (m)
$r(t)$	:	Reference input signal.
$\vec{\boldsymbol{r}}_i$	:	Position vector of the i^{th} rigid body of the Test Platform.
t	:	Time. (s)
u, v, w	:	Scalar component of the linear velocity in the body fixed x, y and z axis. ($\frac{\text{m}}{\text{s}}$)
$\vec{\boldsymbol{u}}$	:	Rotor Input Vector. $\vec{\boldsymbol{u}} = \left[\ \theta_0, A_1, B_1, \theta_{\text{tail}} \ \right]^T$
v_0, v_2, v_∞	:	Air velocity far above and below rotor disc. ($\frac{\text{m}}{\text{s}}$)
v_1	:	Induced velocity. ($\frac{\text{m}}{\text{s}}$)
$\vec{\boldsymbol{v}}_i$	:	Linear velocity vector (w.r.t. inertial frame) of the centre of gravity of the i^{th} rigid body of the Test Platform. ($\frac{\text{m}}{\text{s}}$)
$\vec{\boldsymbol{v}}_{l_i}$	:	Linear velocity vector (w.r.t. local frame) of the centre of gravity of the i^{th} rigid body of the Test Platform. ($\frac{\text{m}}{\text{s}}$)
x, y, z	:	x, y, and z axis coordinate. (m)
α	:	Angle of attack. (rad)
β	:	Blade flapping angle. (rad)
$\vec{\boldsymbol{\beta}}_{ik}$	:	Projection vector for the linear velocity $\vec{\boldsymbol{v}}_i$ onto the generalized coordinate $\dot{q}_k$. $\vec{\boldsymbol{\beta}}_{ik} = \frac{\partial \vec{\boldsymbol{v}}_i}{\partial \dot{q}_k}$
δ_{coll}, δ_{lat}, δ_{lon}, δ_{rud}	:	Rotor servo inputs. (V)
η_m, η_t	:	Side slip angle (Main and Tail rotor). (rad)
γ_L	:	Lock number. $\gamma = \frac{\rho c a_L R}{I_{\text{blade}}}$
$\vec{\boldsymbol{\gamma}}_{ik}$	:	Projection vector for the angular velocity $\vec{\boldsymbol{\omega}}_i$ onto the generalized coordinate $\dot{q}_k$. $\vec{\boldsymbol{\gamma}}_{ik} = \frac{\partial \vec{\boldsymbol{\omega}}_i}{\partial \dot{q}_k}$
η_m, η_t	:	Side slip angle (Main and Tail rotor). (rad)
λ_1	:	Inflow factor. $\lambda_1 = \frac{v_1}{\Omega R}$
λ_{z}, $\lambda_{z_{\text{tail}}}$	:	Normalized perpendicular rotor disc velocity. $\lambda_{\text{z}} = \frac{V_{\text{vertical}}}{\Omega R}$
μ, μ_{tail}	:	Advanced ratio (Main and Tail rotor).
$\dot{\tilde{\boldsymbol{\Phi}}}$	:	Generalized body-fixed rate vector. $\dot{\tilde{\boldsymbol{\Phi}}} = \left[\ u \quad v \quad w \quad p \quad q \quad r \ \right]^T$
ϕ	:	Inflow angle. (rad). $\phi \approx \frac{v_1}{\Omega r}$
Ψ	:	Azimuth angle of the rotor. (rad)
ρ	:	Air density. ($\frac{\text{kg}}{\text{m}^3}$). $\rho = 1.225$
ρ_1, ρ_2, ρ_3, ρ_4, ρ_w	:	Centre of mass location of the test platform linkages. (m)
ϕ, θ, ψ	:	Roll, Pitch and Yaw Euler angles. (rad)

List of Symbols (continued)

σ, σ_{tail}	:	Main and Tail rotor solidity. $\sigma = \frac{N_b c}{\pi R}$
$\bar{\boldsymbol{\tau}}$	:	Generalized force vector for the Test Platform in joint space.
$\tilde{\boldsymbol{\tau}}$	:	Generalized force vector for the helicopter in body fixed frame. $\tilde{\boldsymbol{\tau}} = \begin{bmatrix} X & Y & Z & L & M & N \end{bmatrix}^T$
$\bar{\boldsymbol{\tau}}_{\text{g}}$, $\tilde{\boldsymbol{\tau}}_{\text{g}}$	:	Gravity vector in joint ($\bar{\boldsymbol{\tau}}_{\text{g}}$) and body-fixed ($\tilde{\boldsymbol{\tau}}_{\text{g}}$) coordinates.
$\bar{\boldsymbol{\tau}}_{\text{R}}$, $\tilde{\boldsymbol{\tau}}_{\text{R}}$	:	Net rotor force in joint ($\bar{\boldsymbol{\tau}}_{\text{R}}$) and body-fixed ($\tilde{\boldsymbol{\tau}}_{\text{R}}$) coordinates.
θ	:	Rotor blade pitch angle. (rad)
θ_0	:	Main Rotor Collective Input. (rad)
θ_{tail}	:	Tail Rotor Collective Input. (rad)
$\vec{\boldsymbol{\Theta}}$	:	Generalized position vector for the UAV. $\vec{\boldsymbol{\Theta}} = \begin{bmatrix} x & y & z & \phi & \theta & \psi \end{bmatrix}^T$
Ω, Ω_{tail}	:	Helicopter Rotor Rotation Speed (Main and Tail). ($\frac{\text{rad}}{\text{s}}$)
$\hat{\Omega}$	:	Ratio between main and tail rotor speed. $\hat{\Omega} = \frac{\Omega_{\text{tail}}}{\Omega}$
$\check{\Omega}$	:	Ratio between the main rotor speed of the HANGAR and UAV configurations. $\check{\Omega} = \frac{\Omega_{\text{H}}}{\Omega_{\text{U}}}$
$\vec{\boldsymbol{\omega}}_i$	:	Angular rate vector (w.r.t. inertial frame) of the i^{th} rigid body of the Test Platform. ($\frac{\text{rad}}{\text{s}}$)
$\vec{\boldsymbol{\omega}}_{l_i}$	:	Angular rate vector (w.r.t. local frame) of the i^{th} rigid body of the Test Platform. ($\frac{\text{rad}}{\text{s}}$)
υ_{x}, υ_{y}, υ_{z}	:	Normalized rotor disc angular rate.
ζ	:	Virtual joint PD control scale factor.
ζ_{p}	:	Platform link mass and inertia scaling factor. Usage: m_i/ζ_{p}.

List of Subscripts

B, H, U	:	BALANCED, HANGAR, and UAV configuration quantities.
T, Q	:	Thrust and torque.
w, b	:	Quantities for Platform Counter Weight (w) and Helicopter rigid body (b).
lon, lat	:	Longitudinal and lateral quantity.
m, main	:	Main rotor quantity.
t, tail	:	Tail rotor quantity.
e	:	Quantity at equilibrium.
g	:	Gravity component.
l	:	Quantity expressed with respect to the local frame.
x, y, z	:	x, y, z direction.